Title
Investigation and Control of Ultrafast Magnetic Phenomena

Author
Pattabi, Akshay Bhimesh

Publication Date
2020

Peer reviewed|Thesis/dissertation

Investigation and Control of Ultrafast Magnetic Phenomena

By

Akshay Bhimesh Pattabi

A dissertation submitted in partial satisfaction of the

requirements for the degree of

Doctor of Philosophy

in

Electrical Engineering and Computer Sciences

in the

Graduate Division

of the

University of California, Berkeley

Committee in charge:

Professor Jeffrey Bokor, Chair

Professor Sayeef Salahuddin

Professor Roger Falcone

Summer 2020

Investigation and Control of Ultrafast Magnetic Phenomena

Abstract

Investigation and Control of Ultrafast Magnetic Phenomena

by

Akshay Bhimesh Pattabi

Doctor of Philosophy in Electrical Engineering and Computer Sciences

University of California, Berkeley

Professor Jeffrey Bokor, Chair

Spintronic devices have shown a lot of promise in low power and non-volatile memory applications. However, conventional spintronic devices are limited by the speed of equilibrium magnetization reversal. For more than two decades, the field of ultrafast magnetism, wherein magnetic processes in (sub)picosecond timescales are triggered by the ultrafast non-equilibrium heating of magnetic thin films with femtosecond laser pulses, has provided us with the tantalizing prospect of controlling magnetism in unprecedentedly fast timescales. This dissertation will detail the research conducted over the last 6 years in understanding ultrafast magnetic phenomena, and in controlling and integrating them with conventional spintronic processes to realize fast, non-volatile spintronic devices.

The first part of the dissertation will focus on work done to understand the fundamental limitations of some spintronic and ultrafast magnetic phenomena. This will include experiments on detecting the current induced spin accumulation due to the spin-orbit effects in heavy metals directly on the heavy metal surface using an optical technique called the magnetization-induced second harmonic generation (MSHG). Insight into the dynamics and timescales of current induced spin accumulation in conventional spin-orbit torque (SOT) devices gained from these experiments will help understand the speed limitations of such devices. The dissertation then focuses on the ultrafast helicity-independent all-optical switching (HI-AOS) in ferrimagnetic GdFeCo and GdTbCo alloys. These experiments shed a light on the underlying mechanism of such a process, and unravel the complex interplay of exchange coupling, elemental damping and other parameters in ultrafast magnetization switching events. The upper limit for the pulse duration of optical excitation that triggers HI-AOS, which has important implications when it comes to integrating these processes on-chip, is also studied.

The second part of the dissertation will introduce ways to build up on the experimental results of the first part, thereby moving towards the integration of ultrafast magnetic phenomena into conventional spintronic devices. Experiments performed to extend the ultrafast HI-AOS capabilities of GdFeCo to Co/Pt multilayers by controlling the exchange interaction between these two films are presented.

This is of technological significance because HI-AOS had thus far only been reported in Gd-based ferrimagnetic films, which are not very attractive for device integration due to their ferrimagnetic nature. Co/Pt multilayers, on the other, are ferromagnetic and are well suited for application in spintronic devices. Then, the ultrafast control of magnetism by picosecond heat current and electrical current pulses will be introduced. Finally, the dissertation will present recent results on demonstrating the deterministic spin-orbit torque switching of a Co/Pt ferromagnet by short, 6 ps electrical pulses.

To my family.

"Beyond the horizon of the place we lived when we were young
In a world of magnets and miracles"

Contents

List of Figures

List of Tables

Acknowledgements

Research does not happen in a vacuum (despite the ultra-high vacuum systems that are integral for modern technical research). This dissertation was possible because of the support of several people and I hope to do justice to some of them here.

First, I want to express my enormous gratitude to my advisor Jeff Bokor, scientist and engineer extraordinaire, for mentoring me, for giving me scientific freedom to explore exciting and challenging problems, and for helping me grow as a researcher and as a person over the last six years. From Jeff I learned how to approach challenges from several perspectives – especially the whacky ones, and that is a skill that I will seek to build on throughout my life. My experience under his wing in his group was gloriously delightful and magnificent, and I wouldn't trade a second of it for anything else.

I will forever be grateful for the professors in my dissertation and qualifying exam committees. Prof Sayeef Salahuddin, the Chair of my qualifying exam committee, was a constant source of advice, support and encouragement, providing great feedback to my work whenever needed. He was always open to me collaborating with his group and using his facilities, and was an excellent teacher for his EE230C course that I thoroughly enjoyed. I am thankful to Prof Roger Falcone and Prof Eli Yablonovitch for being part of my committees and for always being supportive and available, despite their busy schedules.

The work presented here is the result of collaborations with several people throughout the world. From the Salahuddin group, I want to thank Dr Charles-Henri Lambert and Dr OukJae Lee for all their help with sample growth and characterization. I thank Alex Ceballos and Prof Frances Hellman from the Physics department at Berkeley for a fruitful collaboration on exciting material systems. I am thankful to Dr Sergiu Ruta, Dr Richard Evans and Prof Roy Chantrell at the University of York for helping us with cutting-edge atomistic simulations that I was previously unaware of. In the spring of 2019 I had a wonderful experience as a visiting researcher at the Institut Jean Lamour at Nancy. I thank Prof Stéphane Mangin for hosting me there, for showing me the awe-inspiring facilities at Nancy, and for scintillating discussions of research. From his group, I also thank Dr Jon Gorchon and Kaushal Jhuria for a great collaboration and for making me feel welcome for the short time I was there.

During my time at Berkeley, I had the privilege to take courses and learn from the best teachers and mentors one could ask for. I want to express my gratitude to my teachers at Berkeley: Prof Ali Javey, Prof Vivek Subrahmanian (I count myself lucky to have taken EE230B while he was still at Cal), Prof Sayeef Salahuddin, Prof Eli Yablonovitch, Prof Elke Arenholz, Prof Ming Wu, Prof Elke Arenholz and Prof Dave Attwood. I also thank Dr Mohan Dunga for his mentorship at Western Digital. On the same note, I am also grateful to have been given the opportunity to teach (especially through Prof Javey's EE143) the curious, bright and diligent students of Berkeley. Thank you also to my mentees Sarah Stevenson and Tray Capers for helping me learn by teaching and guiding.

Throughout grad school, I was funded by the National Science Foundation Center for Energy Efficient Electronics Science (E3S), which coincidentally concludes its 10 year run as I graduate. E3S has given me great opportunities to share research and knowledge, and this has been a significant factor in my growth as a scientist, and for that I am grateful. My gratitude will always be with the E3S

Executive Director, Michael Bartl and Director of Diversity and Outreach, Kedrick Perry for their help and support, especially through the rough patches of grad school. I want to thank Ms Charlotte Jones for being a great source of encouragement, joy, cheer and gossip day in and day out. Seeing her first thing when I got into the office (offices were a thing back in the before times) everyday was something I would always look forward to. A big thanks to the administrative staff at the EECS department – especially Shirley Salanio – who toiled to make grad school as smooth as possible for us. I am also grateful to the staff of the Marvell Nanofabrication Lab, Sutardja Dai Hall and Cory Hall, and the technical team at Coherent for their support.

When I look back at my time in grad school, most of my highlights will lie with the people of the Bokor group. My gratitude will always be with every single person I worked and interacted with in the group. I was fortunate to share my grad school path with JP – we both started and ended our PhD's at roughly the same time and even had our qualifying exams on the same day, and all throughout, we were there to support and gently push each other like academic brothers-in-arm. I thank Dr Jon Gorchon for being a great mentor to me at the start of my PhD, and for hosting me at Nancy towards the end. Jon was a patient teacher, an excellent researcher and an even better friend, and I will always be grateful to have crossed paths with him. Over my six years at the Bokor group, I had the great honor to work with and learn from several wonderful post-docs and grad students. I am privileged in that a lot of them even ended up becoming good friends of mine. I want to thank Dr Maite Goiriena, Dr Hyejin Jang, Dr Amal El-Ghazaly, Dr Roberto Lo Conte, Dr Rich Wilson, Dr Jyotirmoy Chatterjee, Dr Hanuman Singh, Dr Zafer Mutlu, Dr Sucheta Mondal, Dr Debanjan Polly, Rohit Braganza, Tyler Reichenadter, Dr Patrick Bennett, Dr Yang Yang, Dr Jeongmin Hong and Dr Zheng Gu.

My grad school experience would not have been half as memorable as it is if not for the friends I made along the way. I thank my "Gossip Girl" cohort – Carlos, Jodi, Ben, Lety, Nils, JP and others for always having my back. They would never hesitate to cheer me up or just chat about the most inconsequential things when I needed them. I will look back fondly on watching movies with Carlos and having unplanned lunches with Jodi. I thank Maite for conversations, experiences and memories that will resonate with me beyond grad school. I am also thankful to my friends at Bias Busters for providing a welcome distraction outside of research. I am grateful to Caitlin, for cheering me on for more than two-thirds of my PhD. She has been a rock – an ever-reliable supporter, confidante and a bassist's bassist. Her words of encouragement before talks, exams and conference presentations – although she hardly understood what I was doing – went a long way in easing my infamous nerves. My thanks also to her family: Susan, Dylan, Bruce and Mary. The times I spent with my friends at Berkeley and the adventures I've gotten into with them will remain etched in my (secondary) memory for a long, long time. The person I am today owes a huge deal to these friendships.

I will remain indebted to the city of Berkeley. Its rolling hills and cool, dark waters shaped me in ways that I could never have imagined coming in as a scrawny, doe-eyed South Indian lad of just twenty-two. The grad school journey, famously, has highs and lows. Berkeley has been a splendid place to savor the highs, and it has been a perfect backdrop to pick myself up from the lows. The city of Berkeley and its surroundings, with its rich history and culture has been a magnificent place for me to grow and learn as I lived away from family for the first time.

My getting into Berkeley for a PhD was made possible because of my teachers, friends and supporters from way before grad school. I am thankful to my teachers at the National Institute of Technology Karnataka for inculcating in me a thirst for knowledge and a love for fundamental research. I also owe a tremendous amount of gratitude to Dr Jagadeesh Moodera and Prof Markus Münzenberg for introducing me to the fields of spintronics and ultrafast magnetism. I thank Ajay Anna, Abhin Anna, Anuroopa Akka and Ajji for their unwavering support and faith in me since day one. My friends from India will always have my appreciation for always cheering loudly even when I didn't believe in myself: Hitesh, Vishnu, Arjun, Mallick, Bharati, Jehu, Inchara, Ramya, Darryl, Roshan, Don and others.

Finally, I want to express my gratitude to my parents and my sister. One of the drawbacks of being away from home for grad school was missing out on my baby sister Ashitha going on her own journey of graduating from high school and college. I thank her for her snarky, sisterly support and for inspiring me with her own progress as a student and a researcher. I am grateful to my parents for instilling in me a deep and profound admiration, respect and passion for science. Appa and Amma have been a source of inspiration since I can remember, and I always sought to emulate them and their ideals. They taught me to be uncompromising when it comes to knowledge and education, and I am beyond thankful to them for that. I am thankful for their unflinching, unconditional support and love as I pursued my PhD halfway across the globe from them. Their dedication and sacrifices for more than twenty eight years have made this dissertation a reality.

Chapter 1. Introduction

We live in an era of information, and every dimension of our lives is affected to varying degrees by data and the technological infrastructure that stores and processes this data. At the time of writing of this introduction – July 2020 – the SARS-CoV-2 coronavirus continues to hamper livelihoods and ravage healthcare systems in unprecedented ways as the COVID-19 pandemic brings normal life around the globe to a standstill. This bizarre and unexpected scenario has led humankind to adapt in various resourceful ways. Technology has come to the forefront in ensuring a semblance of normalcy as larger swaths of the population are using computers, smartphones, online services and cloud-based infrastructures in larger volumes and with great effectiveness from the relative safety of their homes. More importantly, technology has proven to be a great resource in healthcare and other sectors at the frontlines. A tremendous amount of data has been used for undertakings such as contact-tracing of infected persons, scheduling of virus tests, analysis of infection epicenters and spread and location-based targeting of public health policy with great success. It has become clear that as humankind moves forward to face the tremendous challenges of the future, like fighting the pandemic for the next couple of years and solving larger, slower problems like the large scale global effects of climate change, the role that technology will play as a tool to aid these challenges will become exponentially more important.

The technological growth of the past few decades has been fuelled by the persistent scaling of the size of Si metal-oxide-semiconductor field effect transistors (MOSFETs) in complementary metal-oxide-semiconductor (CMOS) technology, as dictated by Moore's law[1]. As transistors scale, they get faster, consume less power and become cheaper to produce, leading to advancements in the technology. Since transistors cannot be shrunk indefinitely, the demise of the Moore's law has been predicted for decades. Advances in CMOS technology have successfully warded off such fears so far; in 2019 TSMC began limited production of CMOS at the 5 nm technology node (although it must be kept in mind that the node number does not necessarily mean the transistor gate length). However, for gate lengths below 10 nm, it is inevitable that at some point physical limits will be hit, preventing further scaling. Indeed, signs of hitting these physical limits have existed since the early 2000's, with the saturation of the operating voltage and frequency of CMOS processors (Figure 1.1). The total power dissipated in a CMOS transistor can be calculated at the sum of the dynamic power (arising from the switching of a transistor) and the static power (arising due to the leakage from a constant drain voltage V_{DD} required to power a transistor). At longer channel lengths L of the transistor, the power dissipation in a chip is dominated by the dynamic power, which depends on the density of transistors, the switching frequency and the square of V_{DD}. The scaling of the transistor channel length L at longer L allowed the scaling of V_{DD} linearly, thereby enabling the clock frequencies (processor speed) to increase with each technology node. But for short channel length transistors, the V_{DD} scaling is limited by the physics of the transistor operation. The rate of change of the drain current of a MOSFET with respect to the control gate voltage during the on-off transition of the transistor, called the subthreshold swing, is at best 60 mV/decade due to the Boltzmann limit of the MOSFET operation[2, 3]. Given this limit of the subthreshold swing, in order to limit the MOSFET off-current (thereby limiting static power consumption to manageably low levels) while still enjoying large on-currents, the MOSFET has to be operated at relatively high operating voltage V_{DD}. CMOS scaling has therefore resulted in larger transistor densities at the similar operating voltages. Therefore the clock frequency of processors has

been stuck at ~3 GHz since 2005 so that the total power dissipation of the device does not increase with each generation.

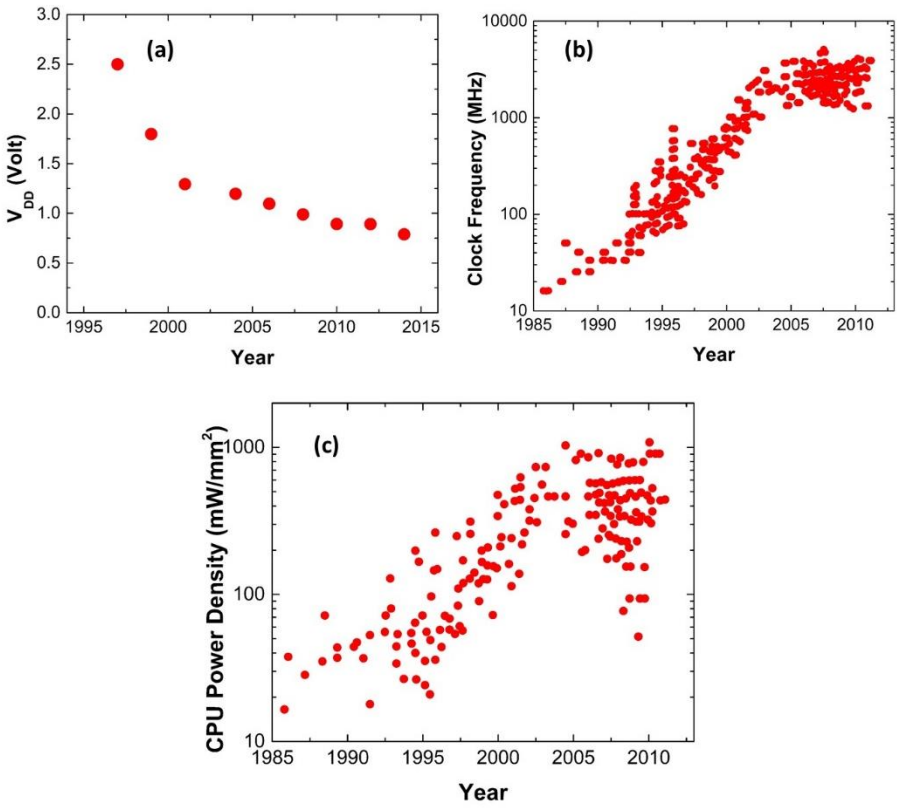

Figure 1.1. Effects of CMOS transistor scaling over the years on CPU performance.
(a) Scaling enables reduction of operation voltage V_{DD}, but the effect has saturated. (b) CPU clock frequencies have saturated since 2005. (c) The power consumption in CPUs has saturated due to the saturation of clock frequency and V_{DD} (Figure adapted from Refs [2, 4]).

The ubiquity of CMOS technology is seen in not only in logic processors, but also in different levels of memory. MOSFETs are used in different cache memory levels and different kinds of random access memory. A static random access memory (SRAM) cell comprises of two CMOS pairs and dynamic random access memory (DRAM) cell contains a MOSFET and a capacitor. The scaling and energy issues of CMOS discussed above apply to these memory systems as well. These limitations to transistor scaling have fuelled the search for viable long-term alternatives and complements to CMOS technology. Various "beyond CMOS" technologies have been touted and floated around for decades, with varying degrees of success. Among these, one of the most promising technologies is spintronics, a subfield of magnetism which involves the use of magnets and spin currents to store and process information. While spintronics has a huge advantage over CMOS technology when it comes to energy dissipation, its strengths are dealt a heavy blow by the slow switching speed of its magnetic bits.

Ultrafast magnetism (or femtomagnetism) is another subfield of magnetism and involves the study and control of magnetism at unprecedented fast picosecond (ps) and sub-picosecond timescales by heating magnets with short femtosecond laser pulses[5]. Ultrafast magnetism by itself is infeasible for application in technology owing to the need for bulky femtosecond-capable laser systems. An

understanding of the field, however, offers an avenue for speeding up spintronic devices. This dissertation will focus heavily on unraveling the complex physics and mechanisms of ultrafast magnetization processes through various experiments, keeping in mind its feasibility in application and the requirements of technology. Armed with this knowledge, the dissertation will then tackle problems on the integration of these processes with conventional spintronics, thereby creating a new subfield we call ultrafast spintronics.

This introduction chapter serves to provide a high-level overview of spintronics, its need and its speed limitations, and a brief introduction to the field of ultrafast magnetism.

1.1 Magnets and magnetism for device applications

Magnetic materials have been used by humankind since times immemorial for applications such as compasses for navigation, magnetic metal separators, motors, generators and, more recently, for the storage and processing of data. A magnetic material can loosely be defined as any material that has magnetic order even in the absence of an external magnetic field[6]. Magnetic order in a material arises from the arrangement of the magnetic moments in the material.

Atomically, magnetism and other magnetic properties in materials arise from the angular momentum (a type of momentum arising from circular or rotational motion of objects) of the electrons in the atoms of these materials. This angular momentum results in a magnetic moment $\boldsymbol{m}$, sometimes also referred to as the magnetic dipole moment, in the atom which consists of two contributions.

The first contributor is the orbital angular momenta of the electrons circulating around the nucleus. This is analogous to current circulating in a coiled electrical wire leading to the generation of a magnetic field in an electromagnet. The orbital magnetic moment of a single electron in an atom is given by $\boldsymbol{m}_{l,e} = IA$ where I is the current due to the circular motion of the electron and A is the area of the loop of the electron around the nucleus. This magnetic moment can be thought of as being similar to the Oersted field generated around a current carrying conductor. The orbital magnetic moment $\boldsymbol{m}_l$ of the atom is the vector sum of the orbital magnetic moments of all the electrons in that atom.

The second contributor to the magnetic moment $\boldsymbol{m}$ of an atom is the spin angular momentum, simply referred to as "spin", of its electrons. The spin of an electron is an intrinsic, quantum mechanical property that can be understood if we visualize the electrons to be spinning around a central axis, akin to the rotation of the earth around an axis. In reality, the origin of spin is purely quantum mechanical and does not arise from any observable physical property of the electron. In the presence of a magnetic field, the spin of an electron is quantized as either "up" (parallel to the field) or "down" (antiparallel to the field). The spin of electrons results in a spin magnetic moment $\boldsymbol{m}_s$ in an atom, which is derived from the vector sum of the spins of all the electrons in that atom. Note that the symbol $\boldsymbol{\sigma}$ is also sometimes used to denote the spin magnetic moment (instead of $\boldsymbol{m}_s$) or the spin angular momentum of an atom. The net magnetic moment $\boldsymbol{m}$ of an atom is then given by $\boldsymbol{m} = \boldsymbol{m}_l + \boldsymbol{m}_s$, the vector sum of the orbital and spin magnetic moments.

Non-magnetic materials have atoms with zero magnetic moment $\boldsymbol{m}$. Magnetic materials order comprise of atoms that have non-zero magnetic moments, and, as mentioned before, have magnetic arising from the arrangement of these magnetic moments. The magnetic moments of atoms in these

materials typically arise from unpaired electrons in their outer shells. It turns out that the contribution of the orbital magnetic moment in most of the commonly used magnetic materials is negligibly small compared to the contribution of the spin magnetic moment[7]. Based on the arrangement of their magnetic moments in equilibrium, magnetic materials are classified into different types, the most common of which are ferromagnets, antiferromagnets and ferrimagnets. Ferromagnets are magnetic materials in which neighboring moments tend to align parallel to each other due to a strong exchange field. Ferromagnets are the most common class of magnetic materials, and is probably what a layman means when they use the word "magnet". Co/Pt ferromagnets are extensively studied in this thesis, and will be the main material focused on in Chapter 5 and Chapter 7. A moment in an antiferromagnet is equal and opposite to its neighboring moments, leading to a net zero moment in such a material. A ferrimagnet is a magnet with opposite but unequal moments, resulting in a net non-zero moment that is typically lower than that of a ferromagnet. Thin films Gd-based rare-earth transition metal ferrimagnetic alloys will be the focus of a bulk of this dissertation (Chapter 3 -Chapter 6).

The density of magnetic moments in a magnetic material or object is a property known as its magnetization. The magnetization $\boldsymbol{M}$ of a magnetic material is therefore the vector sum of the magnetic moment $\boldsymbol{m}$ of all its atoms divided by its volume V, given by $\boldsymbol{M} = \Sigma \boldsymbol{m}/V$.

Magnetic anisotropy refers to the dependence of magnetic properties on the direction along which they are measured. Ferromagnets and ferrimagnets typically have directions or axes along which their magnetic moments (and therefore their magnetization) prefer to align. A direction along which it is energetically favorable for the magnetization of a magnet to orient is called the easy axis of that magnet, and a direction where it is energetically unfavorable for magnetization alignment is called a hard axis. Magnetic thin films that are used as bits to store information in magnetic devices are usually engineered to have only one easy axis, such that the magnetization is bi-stable and prefers to orient along only two opposite directions on that axis (they have "uniaxial anisotropy"). These two directions of magnetization act as the 0 and 1 in binary data storage (Figure 1.2). Most of the magnetic films presented in this dissertation show perpendicular magnetic anisotropy (PMA), which means that their easy axis lies perpendicular to the plane of the film with their magnetization preferring to point either into or out of the plane of the sample surface.

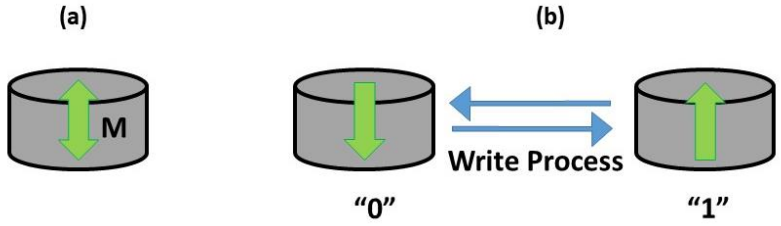

Figure 1.2 Magnetic bits for data storage.
(a) A magnet with uniaxial anisotropy can has two stable opposite states of magnetization. (b) The two opposite states of a magnetic bit store the "0" and "1" of binary data. The dynamic power of a magnetic device depends on the energy required to change the bit from one state to another.

A great advantage of storing binary data using the two opposite magnetization directions of a magnetic film is the non-volatility of magnetic bits. This means that a magnet can retain its state indefinitely without the need for an external power supply as in a semiconductor based static random access

memory (SRAM) or dynamic random access memory (DRAM) cell. Magnetic RAMs (MRAMs) therefore have a static leakage power of zero, accounting for the better energy efficiency of spintronic devices compared to their semiconductor counterparts[8, 9]. Thermal fluctuations can cause loss of the stored state over time, but in most magnetic devices this takes a long period of time, of the order of years[10]. Indeed, a vast majority of information storage systems – from cassette tapes to hard drives in personal computers and cloud storage – rely on magnetic memory.

The energy consumption of a magnetic device depends on the energy required to write a magnetic bit, i.e., to switch its magnetization from one bi-stable state to the other. Early magnetic devices relied on an external magnetic field for writing the magnetic bits[10]. This field was applied as an Oersted field around a current carrying wire (called a "write line" or "word line") in early magnetic random access memories (MRAMs). The final switched magnetic state is controlled by the strength and direction of the applied field, which in turn depends on the strength and direction of the write current. Such a scheme requires relatively large write currents that can create stray fields that switch undesired bits, thereby making scaling of the bits quite infeasible.

1.2 Spintronic devices: spin-transfer torque switching of magnets

Spintronics (short for *spin-tr*ansfer-electr*onics*) is the subfield of magnetism and electronics that involves the control of the spin degree of freedom of an electron (in addition to its charge) in order to manipulate the magnetic states in a magnetic device. Spintronics allows for the electrical control of magnetism of an individual bit without the need for a local external magnetic field, allowing for easier scaling and lower energy compared to traditional field-based MRAMs[10].

Over the last couple of decades, the spin-transfer torque (STT) has emerged as an alternative to an external field for writing magnetic bits in spintronic devices[11, 12]. The schematic of STT is shown in Figure 1.3. The "free layer" represents a magnet that acts as a magnetic bit, and magnetization can be switched between two states that correspond to the "0" and "1" of binary data. The "fixed layer" is a magnetic film with large anisotropy that cannot be switched within the typical operating parameters of the device, and separated from the free layer by a nonmagnetic spacer. When a charge current is flowed from the free layer to the fixed layer (the electrons flow from left to right in the Figure 1.3 (a)), the fixed layer acts as a spin filter because of the different mobilities for electrons with the two spin directions as they flow through a magnetic film with fixed magnetization. The transmitted conduction electrons therefore get polarized along the magnetization of the fixed layer (Figure 1.3 (a)), generating spin currents with a spin moment of $\boldsymbol{\sigma}$. These spins then get absorbed in the free layer and transfer their angular momentum onto the magnetic moment $\boldsymbol{m}$ of the free layer. A torque, called the spin-transfer torque (STT), is then exerted on $\boldsymbol{m}$, which is given by $\boldsymbol{\tau_{STT}} \sim \boldsymbol{m} \times \boldsymbol{m} \times \boldsymbol{\sigma}$. Larger the current, larger is the $\boldsymbol{\sigma}$, and therefore larger the $\boldsymbol{\tau_{STT}}$. In the scenario shown in Figure 1.3 (a), the free layer and fixed layers are magnetized anti-parallel, and the $\boldsymbol{m}$ and $\boldsymbol{\sigma}$ are initially perfectly antiparallel to each other, resulting in zero $\boldsymbol{\tau_{STT}}$ in the beginning. However, as thermal fluctuations tip $\boldsymbol{m}$ slightly away from the axis of $\boldsymbol{\sigma}$, an STT sets in and torques $\boldsymbol{m}$ away from its original direction and tends to align it along the direction of $\boldsymbol{\sigma}$. More the deviation of $\boldsymbol{m}$ from its initial orientation, larger is the STT, ultimately switching the $\boldsymbol{m}$ for a large enough $\boldsymbol{\tau_{STT}}$ (i.e., for a large enough current).

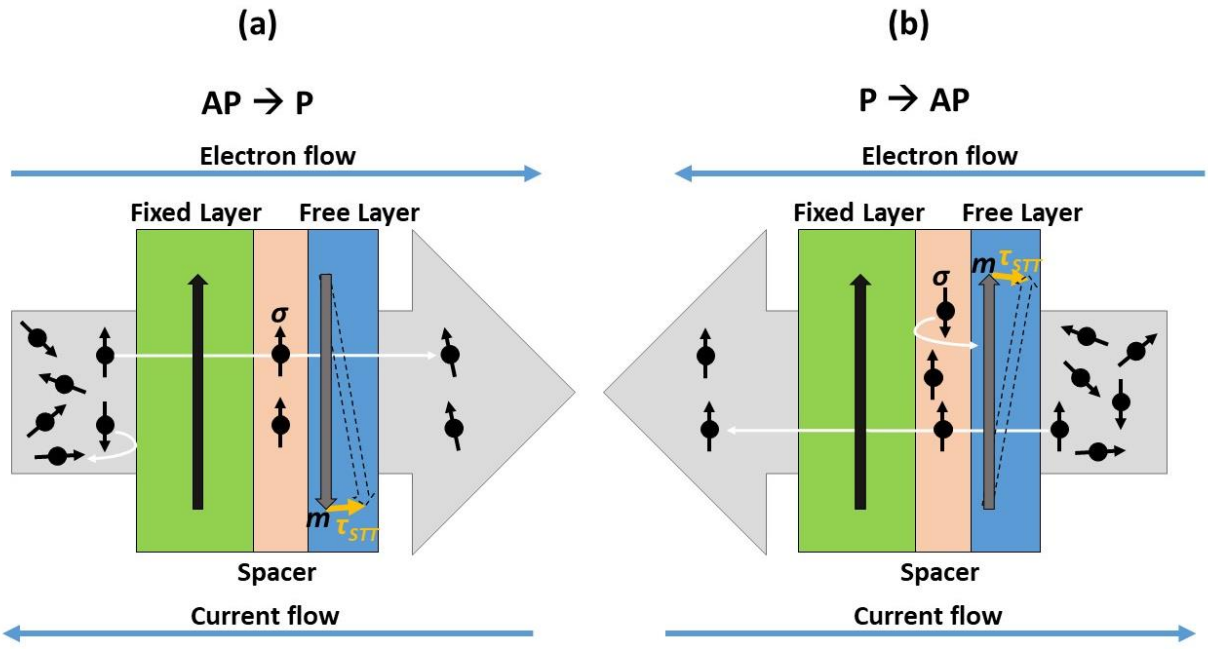

Figure 1.3 Schematic of the spin transfer torque (STT).
(a) Electrons flowing from the fixed layer to the free layer switch the free layer from the antiparallel (AP) to the parallel (P) configuration by the STT from the transmitted spins. (b) Electrons flowing from the free layer to the fixed layer switch the free layer from the parallel (P) to the parallel (P) configuration by the STT from the spins reflected at the fixed layer.

In the scenario shown in Figure 1.3 (b), the current is flowed in the opposite direction (electrons flow from the free layer to the fixed layer – right to left). The fixed layer again acts as spin filter and the reflected spins are oriented opposite to the first case. These back-reflected spins $\boldsymbol{\sigma}$, with moment again apply an STT $\boldsymbol{\tau_{STT} \sim m \times m \times \sigma}$ as before. This causes the free layer from being switched from being parallel to the fixed layer to being antiparallel. It can therefore be seen that the final switched state of the free layer can be set by choosing the direction of write current. It must be noted that the magnitude of the minimum write currents required for switching from parallel to antiparallel configurations of the free and fixed layers (P → AP) and from antiparallel to parallel (AP → P) are different because the latter works with the spin current transmitted through the fixed layer, and the former utilizes the spin current reflected from the fixed layer.

The STT mechanism is the underlying principle of the spin-transfer torque magnetic random access memory (STT-MRAM). Although STT devices are more energy efficient than field-based devices, the critical current needed for switching is still high[11]. Moreover, in a spintronic device, the spacer layer is typically a thin layer of MgO that acts as a tunnel barrier between the fixed and free layers, and the trilayer structure of the fixed layer, spacer and free layer is called a magnetic tunnel junction (MTJ, discussed further in Section 1.4). Passing the large write currents through the MTJ stack in an STT device degrades the MgO tunnel barrier, eventually causing device failure.

1.3 Spin-orbit torque based spintronic devices

The spin-orbit torque (SOT) mechanism has recently emerged as an energy efficient, low current alternative to the STT for switching magnetic bits in an MRAM. In SOT devices, the spin orbit coupling of heavy metals creates a non-equilibrium density of spin polarized conduction electrons when a charge current is flowed through a wire of such a heavy metal[13, 14, 15, 16, 17]. This non-equilibrium of spin polarized electrons causes an accumulation of spin polarization at the surfaces and interfaces of the current carrying heavy metal wire (Figure 1.4). The accumulated spins can then be absorbed by a ferromagnet (or any magnetic film) grown over the heavy metal wire, leading to a transfer of angular momentum and exertion a torque called the spin-orbit torque, similar to the STT. The SOT in heavy metal/ferromagnet bilayers has two possible origins. First is the Rashba effect, wherein an asymmetric crystal field profile is generated across the thickness of the ferromagnet due to the asymmetry between the bottom (heavy metal) and top (oxide, different heavy metal, air etc) layers of the stack. This results in an electric field called the Rashba field[14]. When a charge current J_C flows along such a stack, the conduction electrons in motion experience this electric field as a magnetic field due to relativistic effects, creating a net polarization of the spins of the conduction electrons which then exerts the SOT on the magnetization of the ferromagnet. The non-equilibrium in spin density across the cross-section causes a spin current with density J_S and the accumulation of spins at the surfaces and interfaces where the Rashba field is non-continuous. The second possible origin of the SOT is the spin-Hall effect, which is seen in materials with high spin-orbit coupling, including heavy metals like Pt, Ta and W. When an unpolarized charge current flows through a heavy metal wire, the spin-orbit coupling causes the electrons with spin opposite polarization orientations to spatially separate in opposite directions across the thickness of the layer. This leads to a spin current J_S perpendicular to the direction of the charge current. This, too, causes a spin imbalance, resulting in the accumulation of spin moments at the surfaces and interfaces of the wire. The origin spin-Hall effect could either be intrinsic[18] and linked to the band structure of a material, or extrinsic[13] and dependent on impurities and defects through mechanisms like side-jump or skew scattering. Irrespective of the exact mechanism, both the Rashba and spin-Hall effects have a spin current J_S and a spin accumulation $\boldsymbol{\sigma}$ that are perpendicular to each other and to the direction of the charge current J_C as shown in the Figure 1.4. The strength of a heavy metal wire used for SOT is given by the spin-Hall angle, which is given by $\theta_{SH} = J_S/J_C$. For the rest of this thesis, the terms current-induced spin accumulation and spin-Hall effect will be used interchangeably, without consideration for the actual mechanism behind the spin accumulation. The speed of this spin accumulation in SOT devices will be the focus of Chapter 2 and Chapter 7 of this thesis.

The SOT applied on the magnetic moment $\boldsymbol{m}$ of the ferromagnetic layer on top of the heavy metal by the transfer of angular momentum from the accumulated spins, like the STT, is given by $\boldsymbol{\tau_{SOT}} \sim \boldsymbol{m} \times \boldsymbol{m} \times \boldsymbol{\sigma}$. Changing the direction and magnitude of the charge current J_C changes the direction and magnitude of $\boldsymbol{\sigma}$ and, therefore, also of $\boldsymbol{\tau_{SOT}}$. As in the case of STT, large currents with the right direction can create a large enough torque to switch the magnetization of a free layer of an MTJ. The final switched state of the magnet can be set deterministically for a current over a certain threshold just by the direction of the charge current J_C, all else being equal. In the schematic shown in Figure 1.4, the SOT is utilized to switch the magnetization of a film magnetized with PMA, magnetized along the z-direction with a moment $\boldsymbol{m} = \boldsymbol{m_Z}$. The current J_C applied along the x-axis leads to spins σ_Y accumulating along the y-axis at the heavy metal/magnet interface. $\boldsymbol{\tau_{SOT}}$ then works to align $\boldsymbol{m}$ along

σ_Y and we have $\boldsymbol{m} = \boldsymbol{m_Y}$. After this, in order for the magnet to be to be torqued towards either the –z or +z direction, an external field $\boldsymbol{H_X}$ – referred to as the symmetry breaking field – along the x-axis (parallel or antiparallel to the charge current) is needed. This then exerts a torque $\boldsymbol{\tau_H} \sim \boldsymbol{m_Y} \times \boldsymbol{H_X}$ that torques the magnet along either –z or +z, depending on whether $\boldsymbol{H_X}$ is positive or negative. The $\boldsymbol{\tau_{SOT}}$ described here is typically called the damping-like torque. SOT devices have an additional torque called the field-like torque $\boldsymbol{\tau_{FL}} \sim \boldsymbol{m} \times \boldsymbol{\sigma}$ which could be essential in the SOT switching of some systems[19, 20]. The damping-like and field-like SOTs will be discussed again in Section 1.5.

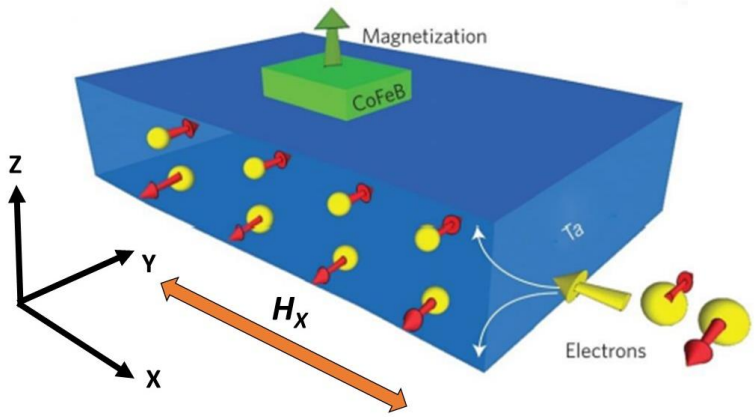

Figure 1.4 Current-induced spin accumulation in a wire of Ta heavy metal.
The orientation of the accumulated spins (along the y-axis), the spin current (z-axis) and charge current (x-axis) are transverse to each other. The accumulated spins exert a spin orbit torque (SOT) on the magnetization of a CoFeB ferromagnetic film on the top of the Ta wire. The symmetry breaking field H_X is required for switching a PMA magnet (Figure from Ref [21]).

SOT devices have reduced switching currents compared to STT devices. Additionally, since the write current only passes through the heavy metal wire, the degradation of the MgO tunnel barrier of the MTJ bit by the passing of large currents across it can be avoided.

The potential for the low power consumption of SOT and STT based MRAMs, in addition to their non-volatility, make them great candidates for the replacement of semiconductor based volatile SRAMs and DRAMs. Traditionally, memory elements farther from the processor core in the memory hierarchy – like secondary storage and external storage – rely on non-volatile memory. The primary concern here is the long retention of data and not necessarily the speed of the memory. Memory elements closer to the processor core are built using fast, volatile devices. The cache memory closest to the processor typically relies on SRAM cells. SRAM cells of cache memory occupy a large area and consume enormous power owing to their large static leakage current (volatility). Recently, the last level of cache has been implemented by DRAM. DRAM cells, too, have a large leakage current. Moreover, they need a periodic refresh operation which adds to the power consumption. MRAMs have the promise of replacing SRAM and DRAM, resulting in lower energy cache operations. Efforts to reduce the write current, for example by using SOT instead of STT, can further improve the efficiency of these MRAMs for use in higher level memory systems. However, cache and other high level energy systems need to be fast enough to keep up with the processor speed. As will be seen from the discussion in Section 1.5, conventional STT and SOT based devices are limited in speed due to the limitations of the precessional switching speed of magnets in equilibrium. This thesis will work

towards building a toolbox for integrating certain phenomena from the field of ultrafast magnetism – which will enable the reversal of magnetization in fast ps and sub-ps timescales – with conventional spintronics schemes like the SOT to allow the ultrafast control of magnetism in spintronic devices. Certain considerations for this will be introduced in the upcoming sections (Sections 1.5 and 1.6) of this chapter.

1.4 Magnetic tunnel junctions and tunnel magnetoresitance

The state of a magnetic bit in a spintronic device must be read electrically in order to enable on-chip integration. This is done by using a magnetic tunnel junction (MTJ) to store the magnetic data. As mentioned in Section 1.2, an MTJ is a trilayer stack of a thin tunnel barrier (spacer) sandwiched between two ferromagnetic layers. A schematic of the MTJ is shown in Figure 1.5 (a). The tunnel barrier is usually a thin insulating layer of crystalline MgO, although other insulators, like an amorphous film of Al_2O_3 have also been used as the tunnel barrier. The free ferromagnetic layer has a magnetization that can be switched between its two opposite bistable states, corresponding to the bit storing a "0" and a "1". The fixed ferromagnetic layer has a magnetization that cannot be switched within the routine operation of the device. The fixed and free layers are typically made from transition metal ferromagnetic elements and their alloys, like Fe, Ni, CoFeB etc. The parallel (P) and antiparallel (AP) configurations of the magnetizations of the fixed and free layers therefore encode, say, the "0" and "1" respectively of the binary data. The P and AP configurations differ in the resistance across the MTJ, a phenomenon known as the tunnel magneto-resistance (TMR)[22]. This difference in resistance can be sensed electrically by sending a small read current through the junction and measuring the corresponding voltage drop.

To understand the basic principle of TMR, let us assume that the fixed and free layers have in-plane magnetization (schematic of Figure 1.5 (a)) and are made of similar magnetic materials with the same band structure. The magnetization of transition metal ferromagnetic materials arises from their itinerant 3d electrons. A magnetized transition metal ferromagnetic film will therefore will have an asymmetry in the densities of its spin "up" and spin "down" 3d electrons. The majority spins determine the magnetization direction of the ferromagnet. In the case of the schematic of Figure 1.5 (a), the magnetization of the fixed layer always points to the right. Let us assume that this means the fixed layer always has a majority of spin "up" electrons as shown in the band structure schematic of Figure 1.5 (b). The spins of the conduction electrons of a charge current, say the read current, passed through the MTJ can be resolved into two opposite directions along the magnetization of the fixed layer – "up" spins (left-pointing blue spins in Figure 1.5 (c)) oriented parallel to the fixed layer magnetization, and "down" spins (right-pointing red spins in Figure 1.5 (c)) oriented antiparallel to the fixed layer magnetization. This explanation neglects the role of the MgO tunnel barrier for the sake of simplicity. It must be noted that crystalline (100) MgO conserves the coherence of electron wave functions during tunneling, such that only conduction electrons whose wave functions are symmetrical with respect to the barrier normal have a high tunneling probability[23, 24, 25].

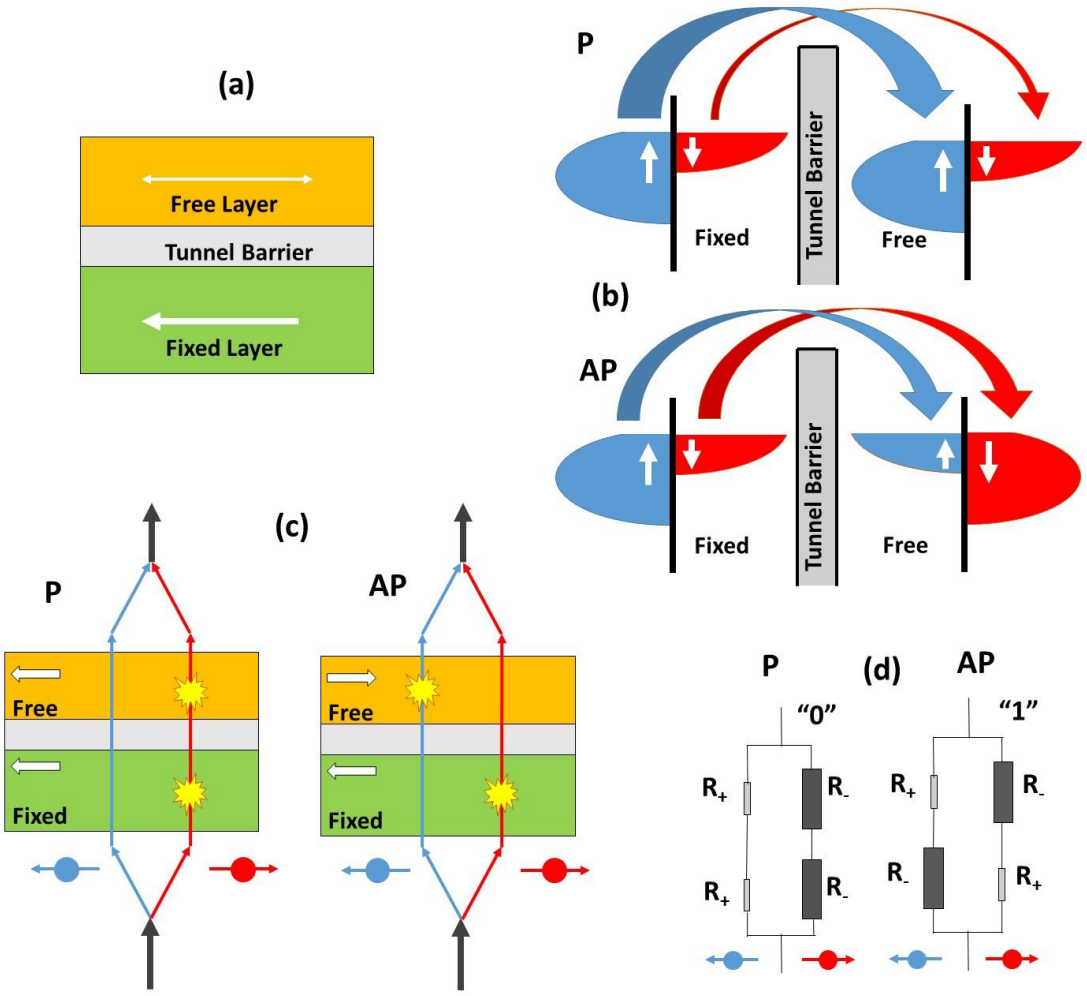

Figure 1.5 Magnetic tunnel junction (MTJ) and tunnel magnetoresistance (TMR).
(a) Schematic of an MTJ with in-plane magnetized fixed and free layers. The fixed layer is always magnetized to the left. (b) The asymmetry in density of the spin up and spin down 3d electrons of the fixed and free layers causes a difference in scattering rates for the spin up and down conduction electrons for the parallel (P, top) and antiparallel (AP, bottom) alignments of the two layers. In this example, the fixed and free layers have the same band structure. (c) Schematic showing the scattering of spin up (blue) and down (red) conduction electrons for the P (left) and AP (right) configurations of the MTJ. (d) Simple circuit schematic for the P (left) and AP (right) configurations of the MTJ.

In the case of the parallel (P) configuration of the fixed and free layers, the spin down electrons (red) get scattered at a large rate by the of large density of empty spin down (minority) 3d states at the Fermi level of the fixed layer[6, 22]. This results in the spin down electrons experiencing a large resistance R_- from the fixed layer. Similarly, these electrons experience the same large resistance R_- from the parallel magnetized free layer as well (we are assuming that the resistances from the fixed and free layers are the same for a fixed magnetization direction). The spin up electrons (blue), on the other hand, experience a lower scattering rate because the majority spin up 3d electrons of the fixed and free layers do not offer a lot of free states at the Fermi level for the conduction electrons to scatter into. As a result, the spin up electrons experience a low resistance of R_+ each from the free and fixed layers. It

must now be noted that the difference in scattering rate of the up and down spins by a magnet with a given fixed magnetization is also the principle of the spin filtering of the write current by the fixed layer in STT devices mentioned in Section 1.2. The circuit schematic for this parallel configuration is shown in Figure 1.5 (d). The resistance R_P of this configuration is then given by equation (1.1).

$$(1.1)\ R_P = \frac{2R_+R_-}{R_+ + R_-}$$

Similarly, for the antiparallel (AP) alignment of the fixed and free layer magnetizations, the spin down (red) conduction electrons of the read current experience the same large resistance R_- from the fixed layer (because its magnetization direction – and hence its spin density asymmetry – is the same as in the P case), and a small resistance R_+ from the switched free layer, which is now a majority spin down magnet. Going by the same argument, the blue spin up electrons experience a low resistance R_+ and a large resistance R_- from the fixed and free layers respectively, leading to a circuit schematic as shown in Figure 1.5 (d), whose total resistance R_{AP} is given by equation (1.2).

$$(1.2)\ R_{AP} = \frac{R_+ + R_-}{2}$$

It can be seen from equations (1.1) and (1.2) that $R_{AP} \neq R_P$, and this phenomenon is called the tunnel magnetoresistance (TMR). TMR can be characterized by a number called the TMR ratio, which is given by

$$(1.3)\ TMR = \frac{R_{AP} - R_P}{R_P} = \frac{(R_- - R_+)^2}{4R_+R_-}$$

As can be seen from equation (1.3), TMR > 0, which means that $R_{AP} > R_P$. This is true for any MTJ where the fixed and free layers are made from similar materials. The difference in resistance of the MTJ between the two states of the free layer enables the determination of the bit state by the voltage drop induced by a constant read current. Larger the difference between R_{AP} and R_P, larger is the TMR ratio, and easier the distinction between the two states. Standard ferromagnet based spintronic MTJs have high TMR ratios > 100%. CoFeB/MgO/CoFeB MTJs with in-plane magnetized CoFeB have TMR of ~700% at room temperature[26]. Chapter 5 and Chapter 7 will touch upon the possibility of having an electrical TMR readout in an ultrafast spintronic device by integrating a ferromagnet based MTJ with the device.

1.5 Speed limit of conventional spintronic devices

Consider a magnet with magnetization $\boldsymbol{M}$ in magnetic field $\boldsymbol{H}$. The magnetization experiences a torque $\boldsymbol{\tau} \sim \boldsymbol{M} \times \boldsymbol{H}$. This torque, which will be referred to as the field torque, causes the magnetization to precess around $\boldsymbol{H}$ as given by the equation (1.4).

$$(1.4)\ \frac{d\vec{M}}{dt} = -\gamma\mu_0\left(\vec{M} \times \vec{H}\right)$$

Here μ_0 is the permeability of vacuum and γ is the gyromagnetic ratio – the ratio of magnetic moment to the angular momentum, which for a single electron spin is given by equation (1.5).

$$(1.5)\ \gamma = \frac{g q_e}{2m_e} = \frac{g\mu_B}{\hbar}$$

Here g is the gyromagnetic splitting factor and is approximately equal to 2 for an electron spin. $\hbar = h/2\pi$ where h is the Planck's constant. q_e and m_e are the magnitude of the charge and the mass of an electron, respectively and $\mu_B = q_e/2m_e$ is the Bohr magneton. For a single free electron spin, $\gamma \approx 28$ GHz/T.

The energy of the magnetic system is $E \sim -\boldsymbol{M.H}$ and for the energy to be minimized, the magnetization needs to be aligned along the direction of the field. This means that the precessions of equation (1.4) cannot go on indefinitely. The system will relax to its minimum energy state with its magnetization pointing along an effective magnetic field $\boldsymbol{H_{eff}}$ by the dissipation of energy and angular momentum. This leads to the modification of the equation (1.4) by the addition of a damping term, leading to the Landau-Lifshitz-Gilbert (LLG) equation (Equation (1.6)).

$$(1.6)\ \frac{d\vec{M}}{dt} = -\gamma\mu_0\left(\vec{M} \times \vec{H}_{eff}\right) + \frac{\alpha}{M_s}\left(\vec{M} \times \frac{d\vec{M}}{dt}\right)$$

Here M_S is the saturation magnetization of the magnetic system and a is its damping parameter. The effect of these two torques on the magnetization $\boldsymbol{M}$ is depicted in Figure 1.6 (a). The first term is arises from the field torque, which as mentioned before leads to the precessional dynamics of the magnet around $\boldsymbol{H_{eff}}$ as shown by the green circle in Figure 1.6 (a), depicting the precessional motion of the magnetization. The second damping term originates from a torque called the damping torque and damps these precessions, and over time aligns $\boldsymbol{M}$ along $\boldsymbol{H_{eff}}$ as is required by energy considerations. The damping torque in conjunction with the field torque leads to the magnet to precess along a spiral that damps towards $\boldsymbol{H_{eff}}$ as depicted by the teal dotted line in Figure 1.6 (a).

The effective field is a sum of the anisotropy field of the magnet $\boldsymbol{H_A}$ (arising from its magnetocrystalline, interfacial and/or shape anisotropies), the demagnetization field (arising from the stray fields outside the magnet due to its magnetization) and any external or applied field $\boldsymbol{H}$. For a magnet that has a uniaxial anisotropy along the z-axis, $\boldsymbol{H_{eff}}$ can be written as equation (1.7).

$$(1.7)\ \vec{H}_{eff} = \begin{bmatrix} H_x \\ H_y \\ H_z + \left(\frac{2K_z}{\mu_0 M_s} - M_s\right) m_z \end{bmatrix}$$

Here H_X, H_Y and H_Z, are the x, y, and z-components of the external field H, K_Z is the perpendicular anisotropy constant, and $\vec{M} = M_s[m_X \quad m_Y \quad m_Z]^T$. The $-M_S m_Z$ term in the z-direction is the demagnetization field due to thin-film shape anisotropy, and $H_A = \frac{2K_z}{\mu_0 M_s} m_z$.

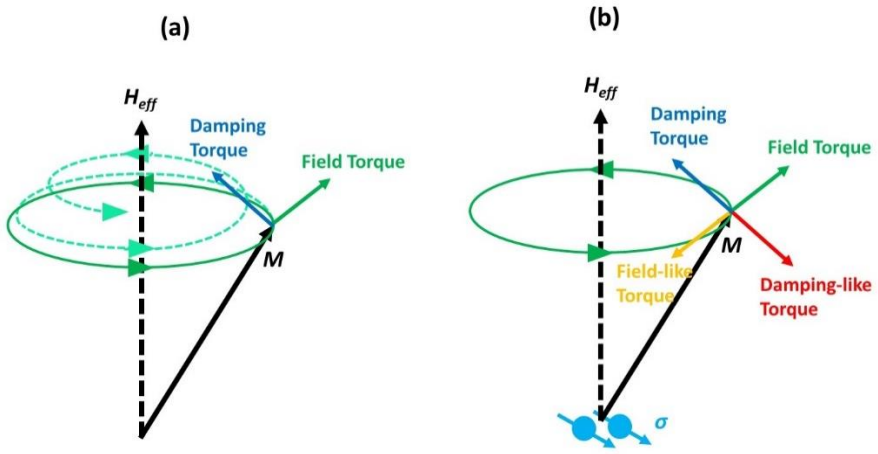

Figure 1.6 Precessional dynamics of magnetization in a conventional spintronic device. (a) The field and damping torques acting on a magnet with magnetization $\boldsymbol{M}$ due to a field $\boldsymbol{H_{eff}}$. The green circle represents the precessions caused of the field torque, and the teal spiral denotes the effective motion of $\boldsymbol{M}$ in the presence of both torques. (b) A spin current with spin moment $\boldsymbol{\sigma}$ adds the damping-like and field-like torques to $\boldsymbol{M}$ in a conventional spintronic device. The precessions are governed by the net effect of all four torques on $\boldsymbol{M}$.

In an STT or SOT spintronic device, spins with moment $\boldsymbol{\sigma}$ are applied onto the magnet as discussed in Sections 1.2 and 1.3. In an SOT device, these spins exert a damping-like SOT $\boldsymbol{\tau_{DL}} \sim \boldsymbol{M} \times \boldsymbol{M} \times \boldsymbol{\sigma}$ (sometimes also called the Slonczewski torque, or simply the spin transfer torque) and a field-like SOT $\boldsymbol{\tau_{FL}} \sim \boldsymbol{M} \times \boldsymbol{\sigma}$. These two terms can be added to the LLG equation as equation (1.8).

$$(1.8)\ \frac{d\vec{M}}{dt} = -\gamma\mu_0\left(\vec{M} \times \vec{H}_{eff}\right) + \frac{\alpha}{M_s}\left(\vec{M} \times \frac{d\vec{M}}{dt}\right) - \theta_{SH}^{DL}\frac{C_s}{M_s}\left(\vec{M} \times \left(\vec{M} \times \vec{\sigma}\right)\right) + \theta_{SH}^{FL}C_s\left(\vec{M} \times \vec{\sigma}\right)$$

where

$$(1.9)\ C_s = \frac{\mu_B}{q_e}\frac{J_c}{d_0}\frac{1}{M_s}$$

Here J_C is the charge current density, θ_{SH}^{DL} is the damping-like spin Hall angle, θ_{SH}^{FL} is the field-like spin Hall angle and d_0 is the thickness of the magnetic layer. As is quite obvious, the third term in the right hand side of equation (1.8) comes from $\boldsymbol{\tau_{DL}}$ and the fourth term arises from $\boldsymbol{\tau_{FL}}$. The directions of the damping-like and field-like torques are depicted in Figure 1.6 (b). Depending on the spin orientation direction $\boldsymbol{\sigma}$, the damping-like (field-like) torque can be either parallel or antiparallel to the damping (field) torque.

The damping-like torque can cause the switching of the magnet if it opposes the damping torque and has a higher magnitude. There is some debate on the relative strengths of $\boldsymbol{\tau_{DL}}$ and $\boldsymbol{\tau_{FL}}$, and on their respective roles in SOT switching in different material systems[20, 27, 28]. However, irrespective of the role their roles in switching, both these torques are still limited by the precessional dynamics of the

magnetization. From Figure 1.6, it can be visualized that the zero-crossing of the magnetization during a reversal process (***M*** crossing the equatorial plane on the sphere defined by its vector) can happen at best in a quarter of a precession period. In conventional spintronic devices, the precession frequency is of the order of a few GHz. This means that the fastest switching speed in such a device will be limited to a few 100s of ps. Indeed, at the time of writing, the fastest conventional SOT device was reported by Garello et al.[29] who were able to switch the magnetization in a Pt(3 nm)/Co(0.6 nm)/AlO_X stack by current pulses with durations down to 180 ps. In the case of STT devices, one of the fastest switching experiments was performed by Lee et al.[30] who demonstrated switching in Cu(6 nm)/ Py(5 nm)/Cu(12 nm)/Py(20 nm) layers (where Py = $Ni_{80}Fe_{20}$) by 50 ps current pulses. With the exception of the Lee STT experiment, most conventional spintronic devices need 100s of ps (if not ns) wide current pulses for switching.

1.6 Introduction to ultrafast magnetism

The field of ultrafast magnetism (femtomagnetism) offers an avenue for speeding up the reversal process of a magnet. This field was discovered in 1996 by Beaurepaire et al.[5] when they observed that the magnetization of a ferromagnetic Ni film was quenched by ~50% within a ps when it was irradiated with a short 60 fs pulse from a mode locked dye laser at 620 nm wavelength (Figure 1.7). This initial rapid ("ultrafast") quenching of magnetism is orders of magnitude faster than the magnetization change by precessional dynamics, and cannot be explained within a conventional understanding of electromagnetism. In the several picoseconds after the initial quenching, the magnetization of Ni reverts back along its original direction as the system begins to cool down. The remarkable observation of the ultrafast demagnetization of Ni galvanized the magnetism community that has since studied ultrafast magnetic processes in a wide range of magnetic materials [31, 32, 33, 34, 35, 36, 37] with different theories for the origin of these processes. Although the exact mechanism of ultrafast demagnetization is still debated, it has been understood that it is caused by the heating of magnetic materials in really short (femtosecond to sub-picosecond) timescales.

When a magnetic material is heated in ultrafast timescales by a short optical pulse, the energy of that laser pulse is first absorbed by the electronic system of the material. In the femtoseconds and picoseconds that follow, the material is in a state of great non-equilibrium and can be best represented by dividing it into three baths – the electrons, the phonons (or lattice) and the spins, as shown in the schematic of Figure 1.8 (a). The laser energy initially absorbed by the electrons is then distributed between the three baths as described by the three temperature model, which describes the temperature evolution of the electrons, phonons and spins with time as equation (1.10).

$$(1.10)\ C_e \frac{dT_e}{dt} = g_{ep}(T_p - T_e) + g_{es}(T_s - T_e) + P(t)$$

$$C_p \frac{dT_p}{dt} = g_{ep}(T_e - T_p) + g_{ps}(T_s - T_p)$$

$$C_s \frac{dT_s}{dt} = g_{es}(T_e - T_s) + g_{ps}(T_p - T_s)$$

Here T_i and C_i are the temperature and heat capacity, respectively, of the bath i (i = e, p and s for electrons, phonons and spins respectively), and g_{ij} is the coupling constant between baths i and j. $P(t)$

is the absorbed power from the laser. The fact that the laser power is absorbed completely by the electron bath is reflected by the absence of the *P(t)* term in the equations for the phonon and spin systems. The estimated T_e, T_p and T_s for the first ultrafast demagnetization experiment of Beaurepaire et al.[5] is shown in Figure 1.8 (b). The time $t = 0$ on the x-axis of this graph corresponds to the time of arrival of the laser pulse on the sample surface.

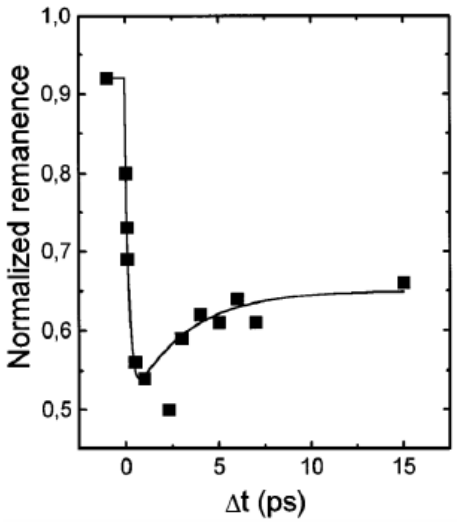

Figure 1.7 Ultrafast demagnetization of Ni by fs laser pulses.
The normalized remanence (M/M_S) of ferromagnetic Ni quenches by ~50% following irradiation by a 60 fs laser pulse, indicating the ultrafast loss of magnetic order (Figure from Ref [5]).

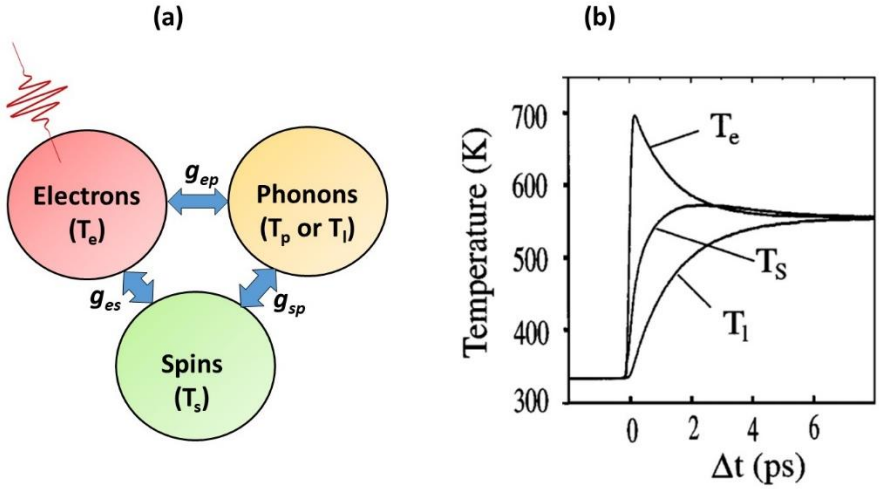

Figure 1.8 The three temperature model for ultrafast magnetism.
(a) The electron, spin and phonon (or lattice) baths of the magnetic system and their corresponding temperatures T_i and coupling parameters g_{ij}. The optical energy of the laser pulse is initially absorbed by the electron bath. (b) The transient temperature response of the three baths (Figure from Ref [5]).

The series of events that takes place in the first femtoseconds and picoseconds after a magnet is heated by a short laser pulse is shown in Figure 1.9. First, the optical energy of the laser excites a few electrons

of the system by ~eV energies dictated by the laser wavelength. This leads to a highly non-equilibrium state wherein the excited electrons have a nonthermal distribution (Figure 1.9 (a)). This means that the concentration of electrons cannot be described by the Fermi-Dirac statistics $f(E) = 1/(1+\exp\{(E-E_F)/kT_e\})$, where E denotes electron energy, E_F is the Fermi level and k is the Boltzmann constant. During these timescales, other non-equilibrium phenomena like superdiffusive spin currents may also be present[33]. In the next few hundred fs, the electrons thermalize and equilibrate with each other and their distribution can be well described by Fermi-Dirac statistics with a single electron temperature T_e that can be as high as 1000-2000 K (Figure 1.9 (b)), much higher than the room temperature T_0. At this point, while the electrons are in equilibrium with each other, the three baths are still in a highly non-equilibrium state with vastly differing T_e, T_p and T_s. Then, over the next few ps the electrons, spins and phonons exchange energy governed by the exchange constants g_{ij} from the three temperature model of equation (1.10) (Figure 1.9 (c)). The exchange of energy between the electron and phonon baths through electron-phonon scattering processes like the Elliot-Yafet scattering[31], wherein the spin of an electron flips upon scattering with a phonon, is believed to play a central role in the thermalization of the electron and phonon baths. Once the three baths are thermalized and are at equilibrium with each other (~few ps), the system can be described by a single equilibrium temperature T. The rate at which the system cools then governs the remagnetization of the magnet (Figure 1.9 (d)), as given by the popular Curie-Weiss law[6] given by equation (1.11).

$$M_s(T) = M_s(0)\left[1 - (T/T_c)^{\zeta}\right] \quad (1.11)$$

Here $M_S(T)$ is the magnetization at equilibrium temperature T (shared temperature of the three baths, and not necessarily the room temperature) and ζ is the critical exponent which depends on the material system.

It must now be noted that the initial non-thermal distribution of electrons is not a necessary condition for triggering ultrafast magnetic phenomena (see discussion in Section 6.8). However, these phenomena do require that there be an initial highly non-equilibrium state between the electron and phonon baths. Conventional spintronic devices under normal operation conditions, even at elevated temperatures, are characterized by the equilibrium (same temperature) between their electrons and phonons, because of which their switching dynamics are still governed by the precessional motion given by the LLG equation.

The microscopic origins of the ultrafast demagnetization process is still hotly debated[31, 33, 38, 39]. One of the important open questions in the field of ultrafast magnetism is the mechanism of loss of angular momentum of the magnetic system in such short timescales, while conserving the angular momentum of the system as a whole. The ultrafast loss of magnetic order has mainly been explained by two different mechanisms. First is the Elliot-Yafet type spin-flip scattering between electrons and phonons[31, 38]. Second is the non-local transfer of angular momentum from the excited regions by fast, superdiffusive spin currents[33]. While both these theories have had relative success in explaining ultrafast demagnetization in many magnetic systems, an overarching theory that explains every observed phenomenon is lacking. Indeed, even though two decades have elapsed since the discovery of the subfield, the biennial Ultrafast Magnetism Conferences are characterized by lively (and sometimes *heated*) discussions and debates about the underlying mechanisms of these exciting processes.

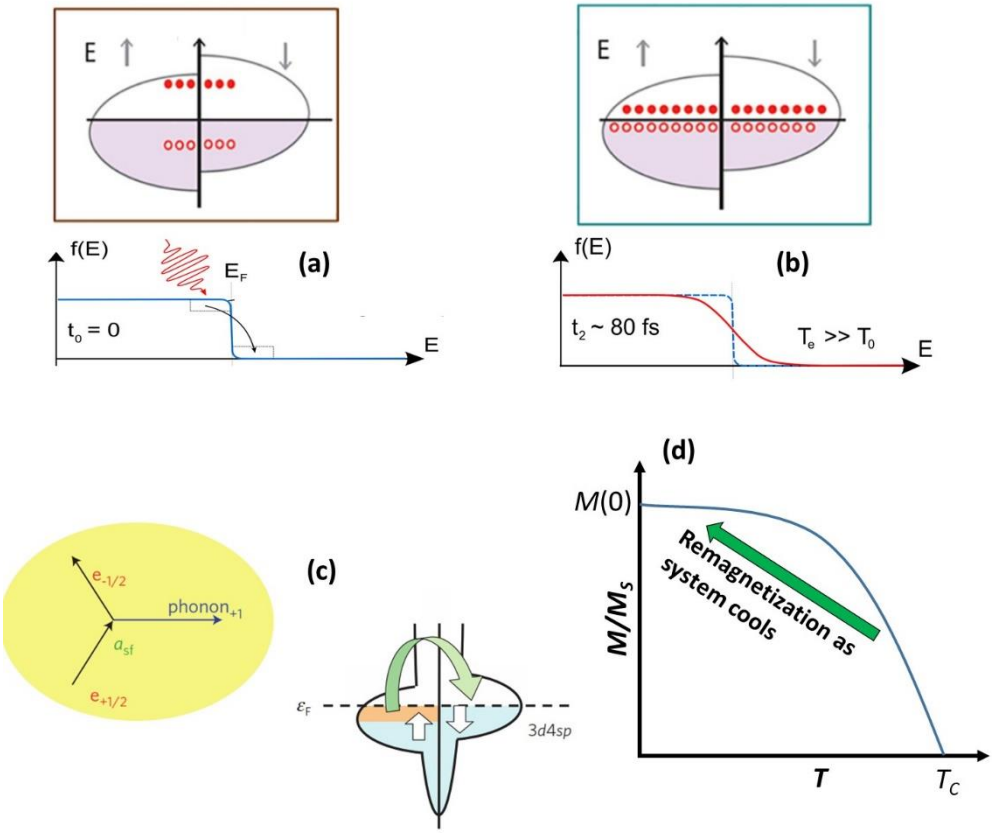

Figure 1.9 Mechanism of ultrafast demagnetization.
(a) Initial (up to ~100 fs after excitation) non-thermal distribution of electrons (bottom) due to the excitation of a few electrons to eV energies (top) by optical absorption. (b) Thermalization of excited electrons (top) yielding a Fermi-Dirac distribution of electrons with large T_e (bottom) in the next few hundred fs (~100 fs to ~1 ps). (Figures (a) and (b) adapted from Ref [40]) (c) Spin-flip scattering of electrons with the lattice through the Elliot-Yafet scattering (up to ~10 ps) (Figure from Ref [31]). (d) Equilibration of the three baths and remagnetization as the system cools back to room temperature.

Despite this lack of complete understanding, ultrafast magnetism offers the potential to drastically increase the speed of precession-limited conventional spintronic devices. One of the most fascinating phenomena studied extensively by groups that focus on ultrafast magnetism is the helicity-independent all optical switching (HI-AOS) exhibited by certain ferrimagnets[37, 41]. It was observed that when a ferrimagnetic GdFeCo thin film is irradiated with a short ~100 fs laser pulse, the magnetization of the film under the laser pulse switches. A second laser pulse switches back the magnetization to its original state. Successive laser pulses then cause the magnetization of the film to toggle between its two stable states. Interestingly, this process occurs even without the presence of an external magnetic field, and is independent of the angular momentum of the laser pulse (i.e., it is independent of the helicity – right-circular or left-circular polarization – of the pulse). Even linearly polarized pulses can trigger this toggle switching, and therefore HI-AOS is understood to be caused purely by the ultrafast heating of the GdFeCo by the optical pulse. Surprisingly, the magnetization of GdFeCo was seen to switch in an ultrafast manner – within a couple of ps of laser pulse excitation. The ultrafast reversal

of GdFeCo magnetization by the HI-AOS can potentially be exploited to demonstrate a spintronic device that switches in timescales much faster than the precession-limited devices. This thesis extensively focuses on HI-AOS experiments on various magnetic systems (refer Chapter 3 -Chapter 5).

1.7 Ultrafast spintronics: towards on-chip integration

While ultrafast magnetic processes – especially the HI-AOS of GdFeCo in a couple ps – offer an exciting avenue for increasing the speed of magnetic devices, their integration on-chip poses several practical challenges. Femtosecond optical pulses are typically generated by bulky laser systems. For example, the Ti: Sapphire Coherent RegA 9050 regeneratively amplified laser at the Bokor lab at UC Berkeley used for a lot of the experiments in this dissertation is $\sim 1.5 \times 0.5 \times 0.25$ m^3 in size. The complete laser system additionally consists of a Ti: Sapphire laser oscillator (Coherent Mantis) that seeds the RegA and a stretcher-compressor system that stretches and compresses the pulses before and after the RegA respectively. The oscillator and stretcher/compressor units are also similarly sized as the RegA. These considerations make it infeasible to have femtosecond optical pulses on-chip. It must now be noted that integrated on-chip mode-locked lasers do exist. However, a fully integrated mode-locked laser requires mirrors to form the cavity, an active amplifier waveguide, a saturable absorber, a passive waveguide, and a transition from the active waveguide to the passive waveguide, all of which must be available on-chip. As a result, integrated mode-locked laser systems are also bulky, with dimensions larger than 100s of μm[42, 43]. Such lasers emit pulses of a few ps duration, but their peak power is typically low[43]. Additionally, these mode-locked lasers operate at a fixed repetition rate, typically a few GHz[42, 43], and will be unable to output single optical pulses as needed for switching, as is required for any practical magnetic device. Moreover, coupling the optical output of an integrated laser into a small (nm scale) magnetic bit may be extremely challenging. Spintronics, on the other hand, is not limited by these considerations because the use of charge and spin currents easily facilitates integration with other on-chip technologies, and application of controlled single pulses.

However, as mentioned in the previous section, the HI-AOS is purely triggered by the ultrafast heating of GdFeCo. A potential source for heating GdFeCo in ps (not fs) timescales is the Joule heating by a ps current pulse. Intense fs current pulse sources are unavailable, but it is very much possible to generate intense ps current pulses on-chip. Indeed, picosecond-ready CMOS transistors exist in commercial technology since 2007[44], based on the demonstration of 5 ps gate delay transistors by researchers at Intel. If it were to be possible to reverse the magnetization of GdFeCo (or any magnetic system, for that matter) in ultrafast timescales by heating it with ps optical pulses, it would mean that ps electrical pulses could also potentially achieve the same ultrafast switching. The work done in this dissertation aims to build a toolbox that can be used to combine the advantages of spintronics and ultrafast magnetism to come up with a new subfield we want to call ultrafast spintronics, wherein the magnetization of devices is manipulated in fast ps timescales by the Joule heating from ps electrical pulses.

The use of ps electrical pulses will help with the on-chip integration for the write process. For complete integration, it is also necessary to read the binary state of the magnetic bit of an ultrafast spintronic device electrically. This would need the integration of an MTJ with the magnetic bit to enable electrical readout through the TMR effect.

Finally, since the primary attraction of spintronic devices is their energy efficiency, the ultrafast spintronic device should ideally also exhibit switching energies comparable to, or lower than, existing conventional spintronic devices. To summarize, in the energy vs switching speed graph of Figure 1.10, which includes data for various conventional STT and SOT devices, our device should be located in the lower left quadrant. It must be noted that the data in this figure is taken from Ref [45], which surveyed the switching energy details reported in different cherry-picked journal publications and conferences. The devices presented in this figure have varying dimensions (mostly in the 10s of nm size), material stacks, and configurations of the magnetic stack (in-plane magnetization, out-of-plane magnetizations, a hybrid of in-plane and out-of-plane etc). This accounts for the reduction in switching energy density with the current pulse width. For a given magnetic device with a fixed size, the switching energy is expected to increase with decreasing pulsewidth τ_P for pulsewidths lower than ~0.5-10 ns, arising from an increase in the switching current density J_C (J_C is inversely proportional to τ_P at small τ_P), for both STT[46] and SOT[47] schemes. For magnetic devices larger than ~50 nm, it has been estimated that for τ_P > ~0.5 – 10 ns, the J_C depends weakly on τ_P, and varies as $\log(1/\tau_P)$. As a result, in these timescales, the energy dissipation $E \sim J_C^2\tau_P$ is fairly linear with τ_P, and a reduction of τ_P leads to a reduction in the energy dissipation. The crossover of the dependence of J_C on τ_P can occur at different pulse durations (ranging from 0.5 ns to 10 ns)[46, 47] for different devices. This can additionally explain the reduction in switching energy with τ_P in Figure 1.10.

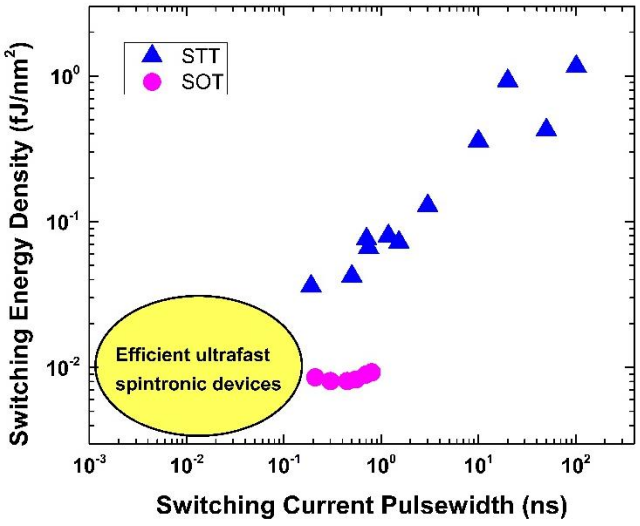

Figure 1.10 Switching energy and switching current pulse durations for different STT and SOT devices.
Data acquired from Ref [45].

1.8 Thesis organization

The chapters of this thesis can roughly be organized into two parts. The first part – comprising of Chapter 2 throughChapter 4 – will deal with understanding the underlying physics and some basic limitations of phenomena like current-induced spin accumulation in heavy metals and HI-AOS in Gd-based rare-earth transition metal ferrimagnetic alloys. Armed with this knowledge, the second part – Chapter 5 through Chapter 7 – will focus on experiments that will have a direct impact on the working of an ultrafast spintronic device, and finally demonstrating a prototype for an ultrafast SOT device.

Chapter 2 will focus on directly observing the current-induced spin accumulation on the surface of wires of high spin-orbit coupling heavy metals like Pt and Ta – without a magnet grown on top – using an optical technique called the magnetization-induced second harmonic generation (MSHG). The technique is then used to study the speed of the spin accumulation following a 2 ns charge current pulse, which will act as a fundamental speed limit for an ultrafast spintronic device.

Chapter 3 deals with experiments to study the HI-AOS phenomenon in GdFeCo. The ability of GdFeCo to undergo HI-AOS with ps heat sources is tested by varying the pulse duration of the optical pulses from 70 fs up to 15 ps. Existing theories for HI-AOS are questioned and an alternate mechanism is proposed.

Chapter 4 details further experiments done to understand the underlying mechanism of HI-AOS by studying the HI-AOS in alloys of $Gd_{22-x}Tb_xCo$. The effects of systematically varying the relative composition of the Gd and Tb rare earth atoms and of the annealing the film on the HI-AOS are studied by monitoring the switching speed and critical fluence required. Simulations based on the atomistic spin dynamics are used to identify the parameters that determine the ability of a ferrimagnetic film to exhibit HI-AOS.

Chapter 5 works on extending the HI-AOS capabilities of ferrimagnetic GdFeCo on to multilayers of Co/Pt. Ferromagnetic Co/Pt are grown on top of GdFeCo and the magnitude and direction of the RKKY exchange interaction between these two layers is controlled by changing the thickness of a Pt spacer layer. The depth-resolved MOKE technique is utilized, so that the magnetizations of these two layers can be independently monitored. The tool is then used to verify whether the exchange interaction extends the ultrafast HI-AOS capabilities of GdFeCo on to the ferromagnet.

Chapter 6 is a broad overview of experimental work conducted, both in the Bokor group and outside, to trigger ultrafast magnetic processes without direct optical excitations. This overview spans experiments on ultrafast demagnetization with free-space THz pulses, and demagnetization and reversal with short electronic heat currents (remote heating). This chapter also introduces Auston switch and transmission line devices used to demonstrate ultrafast reversal of GdFeCo with ps electrical pulses.

Chapter 7 focuses on the demonstration of a prototype ultrafast SOT device, where a ferromagnetic Co/Pt film is switched by the SOT from 6 ps electrical current pulses, and the corresponding analysis of the different SOTs acting in the material system.

1.9 References

1. Moore, G. E. Cramming More Components Onto Integrated Circuits. *Proc. IEEE* **86,** 82–85 (1998). https://doi.org/10.1109/JPROC.1998.658762
2. Danowitz, A., Kelley, K., Mao, J., Stevenson, J. P. & Horowitz, M. CPU DB: recording microprocessor history. *Commun. ACM* **55,** 55–63 (2012). https://doi.org/10.1145/2133806.2133822
3. Salahuddin, S. & Datta, S. Use of Negative Capacitance to Provide Voltage Amplification for Low Power Nanoscale Devices. *Nano Lett.* **8,** 405–410 (2008). https://doi.org/10.1021/nl071804g
4. Bhowmik, D. Spin orbit torque driven magnetic switching for low power computing and memory. (2015).

5. Beaurepaire, E., Merle, J.-C., Daunois, A. & Bigot, J.-Y. Ultrafast Spin Dynamics in Ferromagnetic Nickel. *Phys. Rev. Lett.* **76,** 4250–4253 (1996). https://doi.org/10.1103/PhysRevLett.76.4250
6. Coey, J. M. D. Magnetism and Magnetic Materials. 633
7. Spaldin, N. *Magnetic Materials: Fundamentals and Applications*. (Cambridge University Press, 2010).
8. Behin-Aein, B., Datta, D., Salahuddin, S. & Datta, S. Proposal for an all-spin logic device with built-in memory. *Nature Nanotech* **5,** 266–270 (2010). https://doi.org/10.1038/nnano.2010.31
9. Žutić, I., Fabian, J. & Das Sarma, S. Spintronics: Fundamentals and applications. *Rev. Mod. Phys.* **76,** 323–410 (2004). https://doi.org/10.1103/RevModPhys.76.323
10. Bhatti, S., Sbiaa, R., Hirohata, A., Ohno, H., Fukami, S. & Piramanayagam, S. N. Spintronics based random access memory: a review. *Materials Today* **20,** 530–548 (2017). https://doi.org/10.1016/j.mattod.2017.07.007
11. Ralph, D. C. & Stiles, M. D. Spin transfer torques. *Journal of Magnetism and Magnetic Materials* **320,** 1190–1216 (2008). https://doi.org/10.1016/j.jmmm.2007.12.019
12. Nikonov, D. E. & Young, I. A. Overview of Beyond-CMOS Devices and a Uniform Methodology for Their Benchmarking. *Proc. IEEE* **101,** 2498–2533 (2013). https://doi.org/10.1109/JPROC.2013.2252317
13. Hirsch, J. E. Spin Hall Effect. *Physical Review Letters* **83,** (1999).
14. Mihai Miron, I., Gaudin, G., Auffret, S., Rodmacq, B., Schuhl, A., Pizzini, S., Vogel, J. & Gambardella, P. Current-driven spin torque induced by the Rashba effect in a ferromagnetic metal layer. *Nature Mater* **9,** 230–234 (2010). https://doi.org/10.1038/nmat2613
15. Liu, L., Pai, C.-F., Li, Y., Tseng, H. W., Ralph, D. C. & Buhrman, R. A. Spin-Torque Switching with the Giant Spin Hall Effect of Tantalum. *Science* **336,** 555–558 (2012). https://doi.org/10.1126/science.1218197
16. Zhang, S. Spin Hall Effect in the Presence of Spin Diffusion. *Phys. Rev. Lett.* **85,** 393–396 (2000). https://doi.org/10.1103/PhysRevLett.85.393
17. Manchon, A. & Zhang, S. Theory of spin torque due to spin-orbit coupling. *Phys. Rev. B* **79,** 094422 (2009). https://doi.org/10.1103/PhysRevB.79.094422
18. Tanaka, T., Kontani, H., Naito, M., Naito, T., Hirashima, D. S., Yamada, K. & Inoue, J. Intrinsic spin Hall effect and orbital Hall effect in 4 d and 5 d transition metals. *Phys. Rev. B* **77,** 165117 (2008). https://doi.org/10.1103/PhysRevB.77.165117
19. Lee, J. M., Kwon, J. H., Ramaswamy, R., Yoon, J., Son, J., Qiu, X., Mishra, R., Srivastava, S., Cai, K. & Yang, H. Oscillatory spin-orbit torque switching induced by field-like torques. *Commun Phys* **1,** 2 (2018). https://doi.org/10.1038/s42005-017-0002-3
20. Manchon, A., Železný, J., Miron, I. M., Jungwirth, T., Sinova, J., Thiaville, A., Garello, K. & Gambardella, P. Current-induced spin-orbit torques in ferromagnetic and antiferromagnetic systems. *Rev. Mod. Phys.* **91,** 035004 (2019). https://doi.org/10.1103/RevModPhys.91.035004
21. Bhowmik, D., You, L. & Salahuddin, S. Spin Hall effect clocking of nanomagnetic logic without a magnetic field. *Nature Nanotech* **9,** 59–63 (2014). https://doi.org/10.1038/nnano.2013.241
22. Miyazaki, T. & Jin, H. *The Physics of Ferromagnetism*. **158,** (Springer Berlin Heidelberg, 2012). https://doi.org/10.1007/978-3-642-25583-0
23. Yuasa, S., Nagahama, T., Fukushima, A., Suzuki, Y. & Ando, K. Giant room-temperature magnetoresistance in single-crystal Fe/MgO/Fe magnetic tunnel junctions. *Nature Mater* **3,** 868–871 (2004). https://doi.org/10.1038/nmat1257
24. Parkin, S. S. P., Kaiser, C., Panchula, A., Rice, P. M., Hughes, B., Samant, M. & Yang, S.-H. Giant tunnelling magnetoresistance at room temperature with MgO (100) tunnel barriers. *Nature Mater* **3,** 862–867 (2004). https://doi.org/10.1038/nmat1256

25. Mathon, J. & Umerski, A. Theory of tunneling magnetoresistance of an epitaxial Fe/MgO/Fe(001) junction. *Phys. Rev. B* **63,** 220403 (2001). https://doi.org/10.1103/PhysRevB.63.220403
26. Ikeda, S., Hayakawa, J., Ashizawa, Y., Lee, Y. M., Miura, K., Hasegawa, H., Tsunoda, M., Matsukura, F. & Ohno, H. Tunnel magnetoresistance of 604% at 300K by suppression of Ta diffusion in CoFeB/MgO/CoFeB pseudo-spin-valves annealed at high temperature. *Appl. Phys. Lett.* **93,** 082508 (2008). https://doi.org/10.1063/1.2976435
27. Hoffmann, A. Spin Hall Effects in Metals. *IEEE Trans. Magn.* **49,** 5172–5193 (2013). https://doi.org/10.1109/TMAG.2013.2262947
28. Ou, Y., Pai, C.-F., Shi, S., Ralph, D. C. & Buhrman, R. A. Origin of fieldlike spin-orbit torques in heavy metal/ferromagnet/oxide thin film heterostructures. *Phys. Rev. B* **94,** 140414 (2016). https://doi.org/10.1103/PhysRevB.94.140414
29. Garello, K., Avci, C. O., Miron, I. M., Baumgartner, M., Ghosh, A., Auffret, S., Boulle, O., Gaudin, G. & Gambardella, P. Ultrafast magnetization switching by spin-orbit torques. *Appl. Phys. Lett.* **105,** 212402 (2014). https://doi.org/10.1063/1.4902443
30. Lee, O. J., Ralph, D. C. & Buhrman, R. A. Spin-torque-driven ballistic precessional switching with 50 ps impulses. *Appl. Phys. Lett.* **99,** 102507 (2011). https://doi.org/10.1063/1.3635782
31. Koopmans, B., Malinowski, G., Dalla Longa, F., Steiauf, D., Fähnle, M., Roth, T., Cinchetti, M. & Aeschlimann, M. Explaining the paradoxical diversity of ultrafast laser-induced demagnetization. *Nature Mater* **9,** 259–265 (2010). https://doi.org/10.1038/nmat2593
32. Bigot, J.-Y., Vomir, M. & Beaurepaire, E. Coherent ultrafast magnetism induced by femtosecond laser pulses. *Nature Phys* **5,** 515–520 (2009). https://doi.org/10.1038/nphys1285
33. Battiato, M., Carva, K. & Oppeneer, P. M. Superdiffusive Spin Transport as a Mechanism of Ultrafast Demagnetization. *Phys. Rev. Lett.* **105,** 027203 (2010). https://doi.org/10.1103/PhysRevLett.105.027203
34. Malinowski, G., Dalla Longa, F., Rietjens, J. H. H., Paluskar, P. V., Huijink, R., Swagten, H. J. M. & Koopmans, B. Control of speed and efficiency of ultrafast demagnetization by direct transfer of spin angular momentum. *Nature Phys* **4,** 855–858 (2008). https://doi.org/10.1038/nphys1092
35. Bergeard, N., Hehn, M., Mangin, S., Lengaigne, G., Montaigne, F., Lalieu, M. L. M., Koopmans, B. & Malinowski, G. Hot-Electron-Induced Ultrafast Demagnetization in Co / Pt Multilayers. *Phys. Rev. Lett.* **117,** 147203 (2016). https://doi.org/10.1103/PhysRevLett.117.147203
36. El Hadri, M. S., Pirro, P., Lambert, C.-H., Petit-Watelot, S., Quessab, Y., Hehn, M., Montaigne, F., Malinowski, G. & Mangin, S. Two types of all-optical magnetization switching mechanisms using femtosecond laser pulses. *Phys. Rev. B* **94,** 064412 (2016). https://doi.org/10.1103/PhysRevB.94.064412
37. Ostler, T. A., Barker, J., Evans, R. F. L., Chantrell, R. W., Atxitia, U., Chubykalo-Fesenko, O., El Moussaoui, S., Le Guyader, L., Mengotti, E., Heyderman, L. J., Nolting, F., Tsukamoto, A., Itoh, A., Afanasiev, D., Ivanov, B. A., Kalashnikova, A. M., Vahaplar, K., Mentink, J., Kirilyuk, A., Rasing, Th. & Kimel, A. V. Ultrafast heating as a sufficient stimulus for magnetization reversal in a ferrimagnet. *Nat Commun* **3,** 666 (2012). https://doi.org/10.1038/ncomms1666
38. Koopmans, B., Ruigrok, J. J. M., Longa, F. D. & de Jonge, W. J. M. Unifying Ultrafast Magnetization Dynamics. *Phys. Rev. Lett.* **95,** 267207 (2005). https://doi.org/10.1103/PhysRevLett.95.267207
39. Schellekens, A. J. & Koopmans, B. Comparing Ultrafast Demagnetization Rates Between Competing Models for Finite Temperature Magnetism. *Phys. Rev. Lett.* **110,** 217204 (2013). https://doi.org/10.1103/PhysRevLett.110.217204

40. El-Ghazaly, A., Gorchon, J., Wilson, R. B., Pattabi, A. & Bokor, J. Progress towards ultrafast spintronics applications. *Journal of Magnetism and Magnetic Materials* **502,** 166478 (2020). https://doi.org/10.1016/j.jmmm.2020.166478
41. Radu, I., Vahaplar, K., Stamm, C., Kachel, T., Pontius, N., Dürr, H. A., Ostler, T. A., Barker, J., Evans, R. F. L., Chantrell, R. W., Tsukamoto, A., Itoh, A., Kirilyuk, A., Rasing, Th. & Kimel, A. V. Transient ferromagnetic-like state mediating ultrafast reversal of antiferromagnetically coupled spins. *Nature* **472,** 205–208 (2011). https://doi.org/10.1038/nature09901
42. Kärtner, F. X., Callahan, P., Shtyrkova, K., Li, N., Singh, N., Xin, M., Ravi, K., Notaros, J., Magden, S., Vermeulen, D., Ippen, E. P. & Watts, M. Integrated rare-Earth doped mode-locked lasers on a CMOS platform. in *Silicon Photonics: From Fundamental Research to Manufacturing* (eds. Baets, R. G., O'Brien, P. & Vivien, L.) 14 (SPIE, 2018). https://doi.org/10.1117/12.2318010
43. Davenport, M. L., Liu, S. & Bowers, J. E. Integrated heterogeneous silicon/III–V mode-locked lasers. *Photon. Res.* **6,** 468 (2018). https://doi.org/10.1364/PRJ.6.000468
44. Mistry, K., Chau, R., Choi, C.-H. et al. A 45nm Logic Technology with High-k+Metal Gate Transistors, Strained Silicon, 9 Cu Interconnect Layers, 193nm Dry Patterning, and 100% Pb-free Packaging. in *2007 IEEE International Electron Devices Meeting* 247–250 (IEEE, 2007). https://doi.org/10.1109/IEDM.2007.4418914
45. Wong, H.-S. P. Stanford Memory Trends. at <https://nano.stanford.edu/stanford-memory-trends>
46. Diao, Z., Li, Z., Wang, S., Ding, Y., Panchula, A., Chen, E., Wang, L.-C. & Huai, Y. Spin-transfer torque switching in magnetic tunnel junctions and spin-transfer torque random access memory. *J. Phys.: Condens. Matter* **19,** 165209 (2007). https://doi.org/10.1088/0953-8984/19/16/165209
47. Cubukcu, M., Boulle, O., Mikuszeit, N., Hamelin, C., Bracher, T., Lamard, N., Cyrille, M.-C., Buda-Prejbeanu, L., Garello, K., Miron, I. M., Klein, O., de Loubens, G., Naletov, V. V., Langer, J., Ocker, B., Gambardella, P. & Gaudin, G. Ultra-Fast Perpendicular Spin–Orbit Torque MRAM. *IEEE Trans. Magn.* **54,** 1–4 (2018). https://doi.org/10.1109/TMAG.2017.2772185

Chapter 2. Direct optical detection of current induced spin accumulation dynamics in heavy metals

State-of-the-art spintronic devices use spin polarized currents to exert torques to switch the magnetization of magnetic bits in high-density memory and logic systems. Strong spin currents with the right orientation can switch magnetic bits with charge currents that are orders of magnitude lower than traditional Oersted field switching[1]. Most spintronic devices in large scale production in industry today operate on the principle of spin transfer torque (STT)[2]. In these devices, a spin current is generated when the charge current flowing across a magnetic tunnel junction (MTJ), which also acts as the magnetic bit, gets spin polarized by the magnetization of the fixed magnetic layer. The spin current then exerts a spin transfer torque on the magnetization of the free magnetic layer of the magnetic tunnel junction. The free layer can switch its magnetization direction at a high enough spin torque, given the right orientation of the spins, relative to the free layer magnetization. Spin transfer torque devices rely on large currents being passed through the thin MgO tunneling oxide barrier of the magnetic tunnel junctions, which can lead to junction degradation over time.

2.1 Current induced spin accumulation in heavy metals

Over the last decade, the spin-orbit torque has emerged as a potential alternative to the spin transfer torque in spintronic devices. The spin-orbit torque effect[3], typically called the spin-Hall effect [4, 5, 6, 7], is the generation of a transverse spin current to an applied charge current in materials with strong spin orbit coupling. This leads to the accumulation of spins at the surfaces and interfaces of the charge current carrier, with the spins oriented such that they are transverse to the directions of both the spin current and the applied charge current (Figure 1.4). These accumulated spins can then exert a torque on the magnetization of a magnetic thin film grown on top of the charge current carrier, called the spin-orbit torque (SOT), and, like the STT, can switch the magnetic film. Since such a scheme does not involve passing large write currents across the MgO layer of the MTJ, degradation of the MTJ is mitigated. The origin of the spin-orbit torque effect is understood to be either the Rashba-splitting of spin states[3] at interfaces or the spin-Hall effect[6]. The origin of the spin-Hall effect could either be intrinsic[7] and linked to the band structure of a material, or extrinsic[5] and dependent on impurities and defects through mechanisms like side-jump or skew scattering. Regardless of their physical origins, both the Rashba and the spin-Hall effects lead to current-induced spin accumulation at the surfaces of high spin-orbit coupling materials, which can then be used to switch an adjacent magnetic device through the spin-orbit torque. Therefore, within the context of this thesis, the terms "spin-Hall effect" and "spin-orbit torque effect" and "current-induced spin accumulation" will be used interchangeably. The spin-Hall effect has been extensively studied in heavy metals with high spin-orbit coupling like Pt, Ta and W which are promising candidates for use in mass-produced SOT devices. The discovery of the giant spin-Hall effect in the highly resistive β phases of Ta and W[8], and the switching of the CoFeB free layer of an MTJ by the spin-orbit torque from β-Ta[6], opened up the possibility of a commercial SOT based spintronic device. The write current in an SOT device need only flow through the heavy metal wire, and not across the MTJ tunnel barrier as in an STT device. This minimizes the damage to the MTJ in an SOT device, thereby making SOT devices more appealing than their STT counterparts.

The transverse spin accumulation that arises from a charge current is usually quantified by the spin-Hall angle[6] $\theta_{sH} = J_S/J_C$ where J_C is the charge current density and J_S is the transverse spin current density. Large spin-Hall angles, up to 30%, have been measured in heavy metals such as Pt[9], β-Ta[6] and β-W[8]. Although optical techniques have been used to detect and measure the current induced spin accumulation in semiconductors such as AlGaAs[10], GaAs[11, 12] and strained InGaAs[12], until recently the effect in metals was studied exclusively by electronic methods[13] or by the study of its interaction with a magnet[6, 9, 14]. These studies and measurements are indirect in that they study spin-orbit effects in the heavy metal by the response of an adjacent ferromagnet to the spin-orbit torque. A majority of these studies assume 100% transmission of the spin current across the heavy metal – magnet interface. In reality, not all the spins that accumulate at the heavy metal – magnet interface get transmitted into the magnet because of mismatch of bands at the interface, interface roughness and other non-idealities. Moreover, indirect measurements of the spin-Hall effect are limited by the response of the magnet and cannot access the inherent physics of the spin accumulation, including the speed of accumulation following an applied charge current pulse. A study of the dynamics of spin accumulation will help elucidate the speed limits of an ultrafast spintronic device operating on the principle of the spin-orbit torque.

In this chapter, I will detail experimental work performed to detect the current-induced spin accumulation directly on the surfaces of heavy metals using an optical technique called the magnetization-induced second harmonic generation (MSHG)[15]. Several control experiments are performed on a high spin-Hall angle Pt sample to verify that the MSHG setup is sensitive to the accumulated spins, and the technique is then used to detect spin accumulation in Pt, Ta and Au thin films. Finally, a dynamic experiment is performed to study the speed of the spin accumulation following a short, 2 ns current pulse in Pt.

2.2 Magnetization-induced second harmonic generation

An optical technique called the magnetization-induced second harmonic generation (MSHG)[15, 16, 17] is proposed as a technique to directly detect the accumulated spins on the surface of a current carrying heavy metal, without requiring a magnetic film grown on top. When light of frequency ω is shined on an amorphous metallic thin film, the reflected light will have the harmonics (2ω, 3ω, 4ω…) of the fundamental (Figure 2.1 (a)), in addition to the predominant fundamental, with each harmonic being less intense than the last. Second (or any even) order nonlinear optical effects are observable only in systems where both space-inversion and time reversal symmetries are broken, and therefore the second harmonic is generated only at the surfaces and interfaces of an amorphous metallic thin film. When the thin film is magnetic, the intensity of the reflected second harmonic becomes a function of the magnetization $\boldsymbol{M}$ at the surfaces and interfaces of the reflector (Figure 2.1 (b)), a phenomenon called magnetization-induced second harmonic generation (MSHG). In other words, second order susceptibility $\chi^{(2)}$ has a crystallographic component χ^{Crys}, and a magnetization dependent component χ^{Magn}, and is a function of $\boldsymbol{M}$ as $\chi^{(2)} = \chi^{Crys} + \chi^{Magn}\boldsymbol{M}$.

The spin-Hall effect leads to the accumulation of spins in a thin layer at the surfaces and interfaces of a current carrying heavy metal wire. The accumulated spins have a net angular momentum, leading to a net (spin) magnetic moment $\boldsymbol{\sigma}$. Since the MSHG signal is only sensitive to the magnetic moments at

surfaces and interfaces, it is an ideal technique for our detection and measurement of the current-induced spin accumulation.

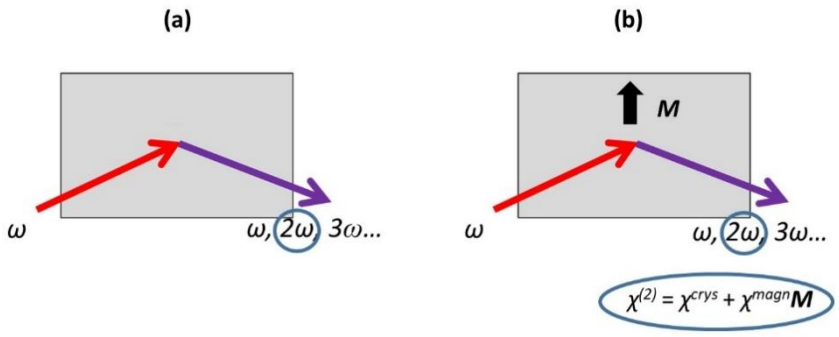

Figure 2.1 Second harmonic generation (SHG) and magnetization-induced second harmonic generation (MSHG).
(a) The light reflected from a surface has harmonics of the incident fundamental (2ω, 3ω, 4ω…). Filtering out frequencies except 2ω enables detection of the SHG intensity. (b) The magnetization $\boldsymbol{M}$ at the surfaces and interfaces of the reflector changes $\chi^{(2)}$, and therefore the SHG, leading to MSHG.

2.3 Sample preparation and fabrication

Thin films of Pt and β-Ta heavy metals, and a Cu control sample, with varying thicknesses of 10 nm – 30 nm, are deposited onto a thermally oxidized silicon substrate with ~300 nm of SiO_2 by radio frequency sputter deposition at a base pressure of 4.7 mT in an AJA sputter chamber. The β-Ta samples are capped with a thin protective 2 nm layer of Ti sputtered in the same chamber to prevent oxidation of the heavy metal surface, and the Cu film is similarly capped by 1 nm of Al. Similar Au thin films are grown by e-beam evaporation. This is done because the MSHG signal is extremely sensitive to surface smoothness and oxidation[15]. Au and Pt films do not need a capping layer as they are noble metals not prone to oxidation.

The sputtered thin films are patterned into wires as follows. The samples are first primed and heated in an oven at 120 ^{0}C to drive off any moisture from the surface. A thin layer of HMDS (hexamethyldisilazane) is then coated onto the surface to ensure adhesion of the photoresist. The positive photoresist OiR 906-12 (Dow Chemical) is spin-coated at 4100 RPM for 30 s, followed by a soft bake at 90 ^{0}C for 1 min. The sample is patterned by exposing it to ultraviolet radiation in the I-line with a dosage of 130mJ cm^{-2} with a Karl Suss MA6 Mask Aligner. Then, the sample is developed with OPD 4262 (Fujifilm) for 45-60s to expose the areas of the heavy metal to be removed, followed by a dip in a water bath for 45 s. These areas are removed by ion milling with Ar ions at base pressures $< 10^{-4}$ Torr. The milling cycles are switched on/off for 20 s/40 s to prevent overheating of the substrate, and an end-point detector is used to confirm when the heavy metal layer is completely etched off, with a few cycles of overetch to ensure complete removal of the heavy metal. For a heavy metal layer with thickness of 20 nm, this will take ~15-20 etching cycles. The photoresist is stripped by dipping the sample in Remover PG (MicroChem) at least 2 hours. At the end of this fabrication step, the heavy metal wire is patterned as a 50 μm ×50 μm square, with the sides of the wire leading to large pads of the same heavy metal film, onto which the Au contacts will be grown.

The Au contacts are patterned by a standard lift-off process with a bilayer photoresist. The sample is first pre-baked at 150 ^{0}C for 5 min to drive off moisture from the surface. LOR-5A (MicroChem) is spin-coated at 4100 RPM for 30s, followed by a bake at 150 ^{0}C for 10 min. The sample is then spin coated with OiR 906-12 and baked at 90 ^{0}C for 1 min, as with the previous lithography step. The sample is exposed in the aligner and developed as before. Au contacts with thickness ~80 nm are deposited through e-beam evaporation, using ~10 nm thick evaporated Ti to improve adhesion of the Au to the sputtered heavy metal film. The Au/Ti contacts are then lifted off by stripping the bilayer photoresist in Remover PG for 3+ hrs or overnight. The LOR-5A upon development forms an undercut that ensures that no sidewalls are formed during this process. A microscope image of the patterned wire is shown in Figure 2.2.

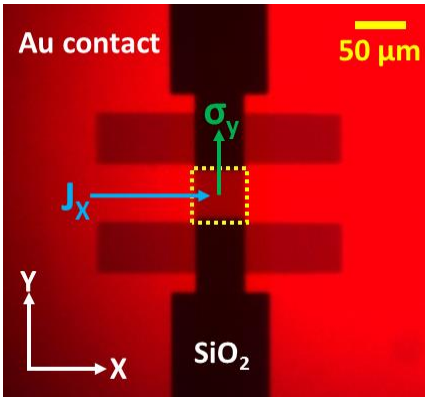

Figure 2.2 Microscope image of a patterned Pt wire for MSHG detection of spin accumulation.
The dotted yellow square indicates the patterned 50 ×50 µm^2 Pt wire with 10 nm thickness. J_X and σ_Y indicate the directions of the charge current and accumulated spin moments at the sample surface, respectively (Figure from ref [18]).

The sample is then attached to a chip carrier, and the leads of the carrier are electrically connected to the Au contact pads with wire bonds.

2.4 MSHG experimental setup and detection of accumulated spins

A schematic of the MSHG experimental setup used to directly detect the accumulated spins in the patterned heavy metal wires is shown in Figure 2.3. The laser used is an 800 nm wavelength, regeneratively amplified Ti:sapphire laser (Coherent RegA 9050) which outputs ~ 70 fs pulses, each of energy up to ~ 1 µJ, at 252 KHz repetition rate. The laser beam is attenuated in power by a half-waveplate – polarizer pair and focused onto the wire to a ~ 30 µm spot with an intensity of 300 µJ/cm^2 using a 5x objective. The polarizer is used to render the incident beam p-polarized. A high-pass (blocks lower wavelengths) red optical filter is placed before the objective to block second harmonics of the fundamental arising from the optical elements before the sample. The reflected light is filtered with two low pass (blocks longer wavelengths) blue filters, such that only the 400 nm second harmonic is allowed through, and the dominant 800 nm fundamental is removed. The weak second harmonic intensity is then passed through another p-polarized analyzer and focused into a sensitive photomultiplier tube (Hamamatsu). The setup also includes a microscope, not shown in the schematic, comprising of a red LED, camera and lenses, to image the samples and ensure proper alignment of

the laser beam on the wire. The electrical signal output of the photomultiplier tube is then amplified and the reflected second harmonic intensity detected using a photon counter (Stanford Research Systems). Since the second harmonic signal is extremely weak, it is crucial to keep ambient light from entering into the photomultiplier tube. Therefore the whole setup is enclosed in a well-sealed black box, with a small opening for the laser beam and sealable doors for user access.

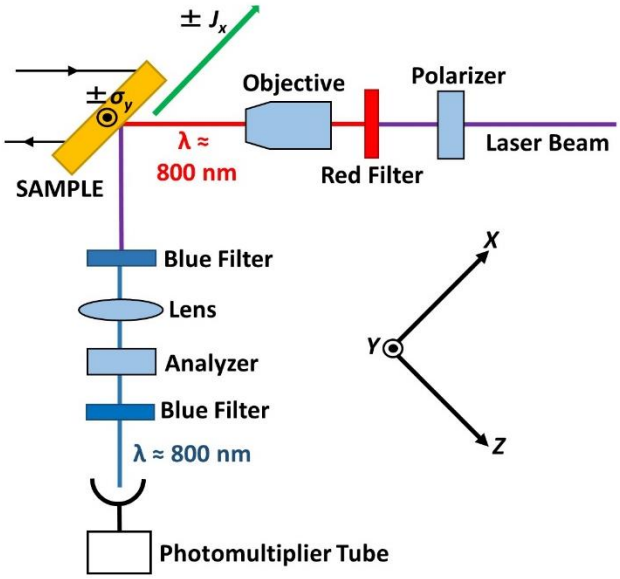

Figure 2.3 Schematic of the MSHG setup.
The charge current J_C and accumulated spin moments σ at the sample surface are along the x- and y-axes, respectively. The signal from the photomultiplier tube is amplified and detected by a photon counter.

For the described configuration of the polarizer and analyzer being both p polarized, the measured MSHG signal is sensitive to the component of magnetization M_Y transverse to the plane of incidence[15, 17]. Since spins accumulate such that their magnetic moment is perpendicular to the direction of the applied charge current, the charge current is applied along the x-axis which is in the plane of incidence, so that the accumulated spin moments are along the y-axis. A function generator (Agilent) is used to apply alternating positive and negative charge current pulses to the sample, with the current pulses being separated by the laser pulse repetition period, and each current pulse being 200 ns wide and ~150 mA in amplitude. The accumulated spins at the sample surface then have a net magnet moment of $\pm\sigma_Y$. The low duty cycle of the current reduces DC heating of the sample by Joule heating.

An output of an electronic delay generator, triggered at the laser repetition rate by a synchronous trigger signal from the RegA, is used to trigger the function generator with a certain delay such that the current pulses arrive at the sample when a laser pulse is incident on it. The photon counter has two channels that are be gated (enabled) independently such that each channel detects the electrical signal from the photomultiplier tube for alternating laser pulses. This, coupled with the alternation of the applied current pulses, enables the two channels of the photon counter to independently measure the second harmonic intensity for spin accumulations along +y and –y respectively. The channels of the photon counter are only gated at a 100 ns window around the photomultiplier signal from a single pulse, rather than the whole laser repetition period, in order to reduce the dark noise background. A

second independent output of the delay generator triggers the photon counter so that it is gating is aligned with the photomultiplier signal.

The intensity of the reflected second harmonic is expected to depend quadratically on the intensity of the incident fundamental, as seen in equation (2.1), where $E(\omega)$ is the electric field of the incident fundamental, $E(2\omega)$ and $P^{(2)}(2\omega)$ the field and polarization of the reflected second harmonic, and $\chi^{(2)}$ is the second harmonic susceptibility.

$$(2.1)\ E(2\omega) \propto P^{(2)}(2\omega) = \chi^{(2)} E(\omega) E(\omega)$$

This quadratic relationship is confirmed for a 10 nm thick Pt wire, without any applied current, for incident intensities up to ~ 500 $\mu J/cm^2$ as shown in Figure 2.4.

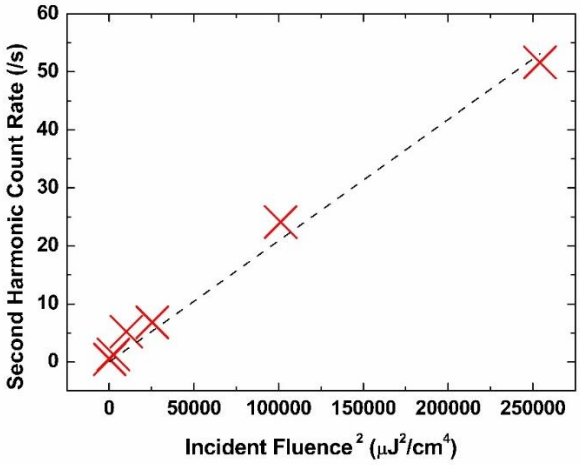

Figure 2.4 Dependence of second harmonic intensity on incident intensity.
The SHG intensity scales linearly with the square of the incident laser intensity (up to a fluences of ~500 $\mu J/cm^2$) for a 10 nm thick Pt film (Figure from Ref [18]).

The magnetic asymmetry A in MSHG experiments with the previously mentioned configuration can be defined by equation (2.2) [15] where $I^{2\omega}(\pm M_Y)$ is the intensity of the reflected second harmonic when the surface magnetization is $\pm M_Y$. The asymmetry term is proportional to, and is a measure of, the surface magnetism. In the case of current-induced spin accumulation, the surface magnetism arises from the magnetic moment of the accumulated spins at the surface $\pm\sigma_Y$. Therefore, $I^{2\omega}(\pm\sigma_Y) = I^{2\omega}(\pm J_X)$ is the intensity of the reflected second harmonic for a net moment of spin accumulation of σ_Y along the $\pm$y axes, corresponding to a charge current J_X applied along the $\pm$x axes.

$$(2.2)\ A = \frac{I^{2\omega}(+M_Y) - I^{2\omega}(-M_Y)}{I^{2\omega}(+M_Y) + I^{2\omega}(-M_Y)} \propto M_Y$$

$$A = \frac{I^{2\omega}(+\sigma_Y) - I^{2\omega}(-\sigma_Y)}{I^{2\omega}(+\sigma_Y) + I^{2\omega}(-\sigma_Y)} = \frac{I^{2\omega}(+J_X) - I^{2\omega}(-J_X)}{I^{2\omega}(+J_X) + I^{2\omega}(-J_X)} \propto \sigma_Y \propto J_X$$

The asymmetry signal A in our experiments is proportional to, and is a measure of the accumulated spin moments, which in turn is proportional to the applied current $(\pm J_X)$ [19] for a given sample.

A ferromagnetic, unpatterned, in-plane magnetized 20 nm thick CoFeB film was used to verify that the setup can detect magnetic signals. Reflected second harmonic intensities were measured for opposite in-plane applied magnetic fields of ± 40 mT, with no current in the sample. An asymmetry signal of ~80% was detected, indicating that the setup is sensitive to magnetic signals.

With a 20 nm thick Pt sample, an asymmetry A of 6.1% was observed for a current density of $J_C = 1.5 \times 10^7$ A/cm^2 with 10 $V_{p\text{-}p}$ driving voltage, indicating that the MSHG setup is capable of detecting magnetic signals from the heavy metal thin film. The measurement is performed 20 times for 1 minute integration time each. Three control experiments were performed on this sample to verify that the magnetic signal arises from the current-induced spin accumulation. First, the sample stage is rotated and the asymmetry A is plotted as a function of θ, the angle between the current direction and the plane of incidence, as shown in Figure 2.5 (a). As can be seen from the fit, the asymmetry varies as the cosine of θ. The magnetic asymmetry A is zero when the current is perpendicular to the plane of incidence (the spins are along the x axis and zero magnetic moment component along the y-axis) and changes sign if the sample is rotated further. The setup being sensitive to M_Y (σ_Y), this proves that the magnetic signal is measured is perpendicular to the current, and that its direction changes with that of the current, as is expected for the current-induced spin accumulation. Secondly, increasing the amplitude of the current pulses leads to a proportional increase in A, as shown in Figure 2.5 (b). This is also expected for the current-induced spin accumulation, as the spin-Hall angle $\theta_{sH} = J_s/J_c$ is constant for a given sample, leading to increased spin accumulation for larger currents. Thirdly, it is important to ensure that the measured signal does not originate from spin polarization due to the Oersted magnetic field generated at the sample surface by the charge current, since this field is also perpendicular to the charge current direction, and scales linearly with the charge current. The amplitude of the current pulse through the film being ~150 mA, the Oersted field at the surface of the film is calculated to be ~1.9mT. However, the asymmetry is unchanged when a larger transverse magnetic field of 40mT was applied along the y-axis using an external magnet, in conjunction with the current. If the asymmetry was arising from the polarization of the spins at the surface of the Pt wire by the Oersted field, the large external applied field would have drowned out any asymmetry signal from the smaller Oersted field. The possibility of the MSHG signal arising from the Oersted field of the current is therefore ruled out, and it is concluded that the asymmetry is a measure of the current-induced spin accumulation in the sample.

The error bars for the experiments mentioned above are obtained by counting over repeated experiments of 1 minute each. Photon counting is a statistical process which leads to a Poisson distribution. Therefore, the error in these measurements is related to the shot noise associated with the photon counting, which is the square root of the total counts. The statistical distribution of second harmonic photon counts for a 10 nm Pt film measured with alternating positive and negative pulses over 250 min, with each measurement lasting 1 minute is shown in Figure 2.6. The two distributions corresponding to the second harmonic photon counts at positive and negative current pulses are Poisson, as is expected., The mean counts per minute for the distributions corresponding to positive and negative current pulses are 135.6 and 104.3 respectively. The standard deviations of the distributions are 11.2 and 10.4 respectively, and are approximately equal to the square root of the mean counts, indicating that the counting process is limited by shot noise.

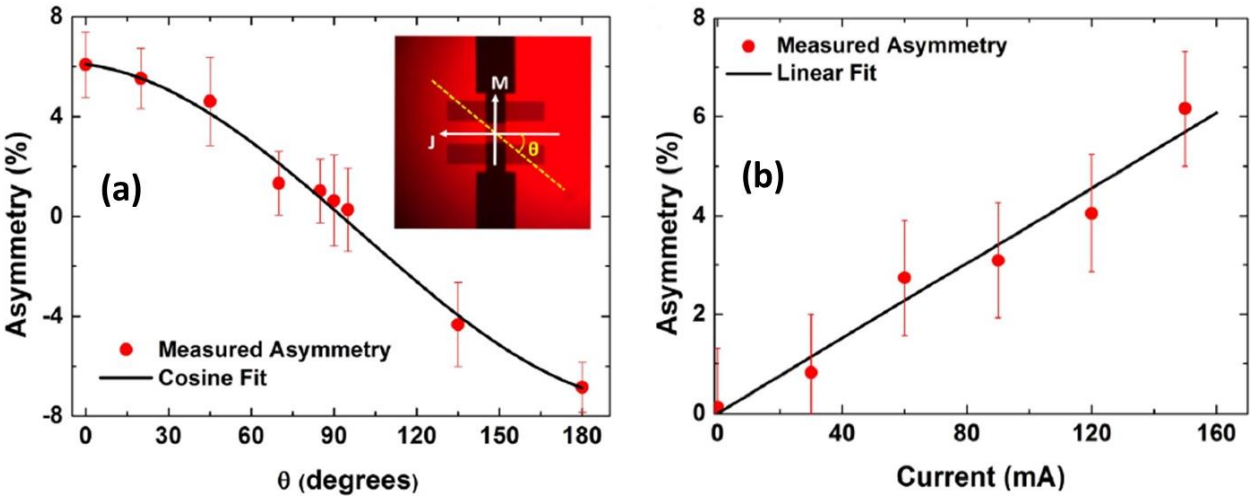

Figure 2.5 Control experiments for MSHG detection of accumulated spins.
(a) Magnetic asymmetry A as a function of the angle θ between the direction of current and the plane of incidence (yellow dotted line in inset). The MSHG signal is sensitive to the component of magnetization transverse to the plane of incidence. The cosine dependence of A on θ indicates that the magnetization is perpendicular to the direction of current. (b) Magnetic asymmetry A as a function of the amplitude of the current pulses. Both measurements are done with a 20 nm Pt wire (Figure from Ref [18])

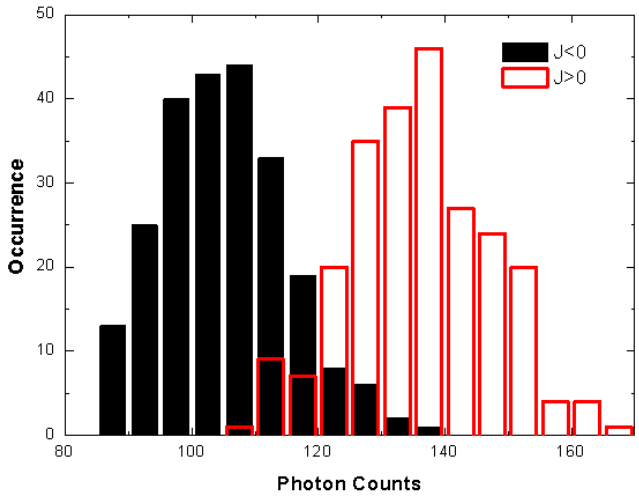

Figure 2.6 Distribution of second harmonic photon counts.
A Poisson distribution of second harmonic photon counts is seen for 20 nm Pt, for positive and negative current pulses. Each of the 250 data points is of 1 minute duration. The standard deviation of the distributions are approximately equal to the square root of the mean counts per minute of the corresponding distribution (Figure from Ref [18]).

2.5 Detection of current-induced spin accumulation in Pt, Ta and Au

The experiment described above to detect the asymmetry from current-induced spin accumulation is repeated for Pt, Ta and Au heavy metal wires of different thicknesses. The asymmetry normalized

with the applied charge current density (A/J_C) is utilized as a measure of the spin accumulation because the spin accumulation scales with J_C for a given sample. Table 2.1 summarizes the normalized asymmetry values for the different heavy metal wires. For all the samples, the current is applied along the x-axis (as indicated in Figure 2.3), with a 10 V_{p-p} driving voltage. The asymmetry measured is then divided by the corresponding current density in order to obtain the normalized asymmetry reported in the table. The asymmetry for all the samples with zero current is found to be zero within the shot noise level.

Sample	Asymmetry/Current density [%.cm-2/(10^7A)]
Pt (10 nm)	5.12 (±0.51)
Pt (20 nm)	4.05 (±0.68)
β-Ta (30 nm)/ Ti (1 nm)	-5.78 (±2.02)
Au (10 nm)	1.10 (±0.04)
Au (20 nm)	0.50 (±0.04)
Cu (10 nm)/ Al (1 nm)	0.11 (±0.16)

Table 2.1 MSHG signal for current-induced spin accumulation in different metallic wires. The magnetic asymmetry A is normalized with respect to the charge current density J_C applied along the plane of incidence and 10 V_{p-p} driving voltage.

Both the Pt platinum samples, with thicknesses of 10 nm and 20 nm, exhibit a high normalized asymmetry signal as is expected from the large spin-Hall angle of Pt[9]. The MSHG signal of the β-Ta sample is expected to arise from the Ta/Ti interface where the spins from the Ta accumulate. Moreover, the normalized asymmetry in the β-Ta sample is large and comparable to that of Pt, and its sign is the opposite to that of Pt, as is expected from the opposite spin-Hall angles in Pt and β-Ta[6, 9]. Although Au is a heavy metal that with high spin-orbit coupling, most previous experiments to measure the spin-Hall effect in Au through conventional techniques that relied on a ferromagnet grown on top of an Au film yielded negligible spin-Hall angles in Au. As can be seen from Table 2.1, the evaporated pure Au films of 10 nm and 20 nm thickness show a non-negligible normalized asymmetry with the same sign as Pt and with a magnitude ~ 20 % of that of Pt. This result is consistent with the previously reported non-negligible spin-Hall angle for Au[20], and the ratio with that of Pt is close to the one reported by the Hoffman group[21, 22].

Cu has a completely filled 3d shell which leads to its low spin-orbit coupling, and therefore Cu is expected to have no current-induced spin accumulation. This is seen from Table 2.1 which shows that the asymmetry in the 10 nm Cu film capped with 1 nm Al is zero within the limits of the experimental noise. The magnitude of the asymmetry in Cu, compared to that of other metals, is consistent with the data of Zhang et al[23]. The photon count rates were of the order of ~ 100 per minute for the Pt and Ta films, and ~1000 per minute for the Au and Cu films. The measurements were integrated over a time period of 20 minutes to obtain adequate signal/noise ratio. The standard error bars in the table are calculated from the shot-noise of the photon counting as described in Section 2.4.

In order to interpret the increase in asymmetry for the Au and Pt samples when decreasing the film thickness, the elements of the non-linear second order susceptibility tensor, $\chi^{(2)}$, are needed. The top and bottom interfaces are expected to have complex susceptibilities of different amplitude and phase. It is assumed that $\chi^{(2)}$[air/Pt] and $\chi^{(2)}$[Pt/SiO_2] will have similar order of magnitude and will be phase shifted by 180° due to opposite symmetries of the metal/insulator interfaces[24, 25]. Under this assumption, for a spin accumulation of opposite orientation on both interfaces, as expected for spin-Hall effect, the SHG fields from the top and bottom interfaces should add constructively. The absorption length for light of a certain wavelength is constant for films of the same material. This then explains the observed increase in the absolute value of the asymmetry in thinner films, as we are more sensitive to the bottom interface as a result of decreased absorption through the film. It must also be noted that the competition between the spin-Hall and the Rashba effects in contributing to the surface spin accumulation[26] may also play a role in determining the thickness dependence of the normalized magnetic asymmetry. The ability of the MSHG technique to directly measure the spin accumulation at the heavy metal surface independently of effective torques on a ferromagnetic layer in contact with the normal metal[26] will be of great value in helping identify the relative roles of spin-Hall and Rashba effects in various material structures.

This experiment, at the time of publication, was the first direct optical observation of current induced spin accumulation on metallic surfaces. Previously, work by van 't Evre et al.[27] had claimed to have detected accumulated spins using the optical technique of magneto-optical Kerr effect (MOKE, which will be discussed in Chapter 3). However, this experiment had worse SNR values compared to the MSHG experiment described here. A possible reason for this can be that the MOKE signal arises from the bulk of the film, leading to a diminished signal that is a function of the convolution of the oppositely oriented spins along the film thickness with the penetration depth of the probe light, while the MSHG signal arises only from the surfaces and interfaces and the signal from the two opposite interfaces of the metal add constructively as described before. Further work by Riego et al.[28] aimed at reproducing MOKE detection of current induced spin accumulation concluded that the detected signal in Ref [27] arose from asymmetric heating in the metallic stacks. Since the publication of the MSHG work detailed in this chapter, other groups have reported direct MOKE detection of accumulated spins[29, 30]. Such direct optical measures of accumulated spins will help elucidate the fundamental properties of various kinds of current induced spin accumulation.

2.6 Dynamics of spin accumulation in Pt

The experiments described in the above sections confirm that MSHG is an effective technique to detect current-induced spin accumulation in heavy metals directly without the need for a magnet grown on top. This then enables the study of inherent properties of the spin-accumulation, independent of its interaction with the magnetization of the grown magnet. Since this thesis explores the speed of magnetic processes in spintronic devices, the MSHG technique is used to study the dynamics and speed of the current-induced spin accumulation in Pt, a heavy metal commonly used in spin-orbit torque devices.

The time dynamics of the spin accumulation was studied in the 10 nm Pt sample for an applied 2 ns wide current pulse. The ns current pulses are applied to the sample as unipolar, 5 V voltage pulses from a fast signal generator (Avtech). The voltage pulse waveform is measured across the sample

contacts with an RF active probe, and the current waveform is estimated based on the measured resistance of the sample. For unipolar pulses, the magnetic asymmetry of the SHG signal is calculated from equation (2.3).

$$(2.3)\ A = \frac{I^{2\omega}(+\sigma_Y) - I^{2\omega}(0)}{2I^{2\omega}(0)} = \frac{I^{2\omega}(+J_X) - I^{2\omega}(0)}{2I^{2\omega}(0)} \propto \sigma_Y$$

The relative time of arrival of the laser and current pulses at the sample is varied using the electronic delay generator that triggers the function generator at increasing delays relative to the amplified laser trigger signal, and at each delay time the magnetic asymmetry is measured from equation (2.3). The results are shown in Figure 2.7. Within the observed noise level, the spin accumulation pulse is seen to follow the current pulse on the time scale of ~50 ps. Similar results were observed in the 20 nm Pt film. The width of the spin accumulation signal is the same as the width of the current pulse, within the limits of the experiment. This indicates that the rise and fall times for the spin accumulation are well below those of the current pulse itself, ~100 ps. It can therefore be concluded that the MSHG is suitable for time-dependent studies of the current induced spin accumulation. However, to better quantify the speed of spin accumulation, we need to use pulse generators capable of supplying shorter, more stable current pulses, and delay generators that can apply finer time delays.

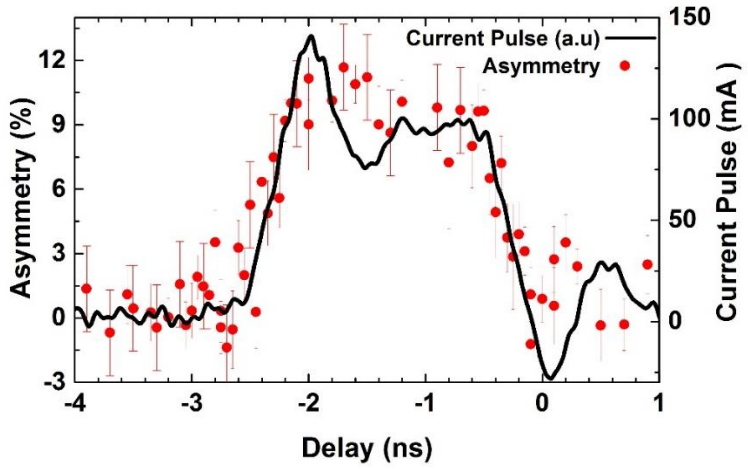

Figure 2.7 Speed of current-induced spin accumulation in Pt.
Spin accumulation at the surface of the 10 nm Pt sample as a function of the delay of the laser pulse relative to the 2 ns current pulse. The "zero" time delay is arbitrary. The current magnitude was estimated from the voltage signal across the sample contacts and separate measurement of the sample resistance. (Figure from Ref [18])

2.7 Conclusion: Towards faster spintronic devices

In this chapter, I have shown that the magnetization-induced second harmonic generation is a promising technique to detect and probe the current induced spin accumulation at the surface of heavy metal thin films. The spin accumulation is verified to be perpendicular to the direction of flow of charge current, and that the measured magnetic asymmetry signal due the spin accumulation is found to scale linearly with the applied charge current density. The surface magnetization due to spin

accumulation is detected in the metals Pt, β-Ta and Au. The sign of the asymmetry in β-Ta and Pt are opposite to each other, and the sign in Au is the same as in Pt. The magnitude of the asymmetry normalized to charge current density is negligible in Cu, and is small in Au, as is expected. The surface/interface sensitivity of MSHG, in addition to the simplicity and the ability to detect spins directly independent of spin transport into an adjacent magnetic layer, makes it a strong candidate to study spin accumulation at metallic surfaces and interfaces.

The dynamics of the spin accumulation in Pt thin films following a short 2 ns current pulse are also reported. These experiments indicate that the spins accumulate within 50 ps of the applied charge current, and that the accumulation speed is outside of the limits of the electronics in the experimental setup. In building an ultrafast spintronic device that operates on the principle of ultrafast heating of the magnetic bit in conjunction with the spin-orbit torque from a heavy metal carrying short ps current pulses, one of the fundamental speed limitations to be considered will be the speed of spin accumulation in these ultrafast spin-orbit torque devices. Such a device will be discussed more in detail in Chapter 7. Previous works have reported conflicting values for spin accumulation length (0.5 nm – 10 nm) and spin accumulation lifetime (0.1 ps – 1 ps) in Pt[31, 32, 33, 34, 35], and these values differ by more than an order of magnitude. Given short enough pulses and more robust electronics, MSHG can potentially be used to directly detect the speed of current-induced spin accumulation in heavy metals used for spin-orbit torque devices.

2.8 References

1. Žutić, I., Fabian, J. & Das Sarma, S. Spintronics: Fundamentals and applications. *Rev. Mod. Phys.* **76,** 323–410 (2004). https://doi.org/10.1103/RevModPhys.76.323
2. Ralph, D. C. & Stiles, M. D. Spin transfer torques. *Journal of Magnetism and Magnetic Materials* **320,** 1190–1216 (2008). https://doi.org/10.1016/j.jmmm.2007.12.019
3. Mihai Miron, I., Gaudin, G., Auffret, S., Rodmacq, B., Schuhl, A., Pizzini, S., Vogel, J. & Gambardella, P. Current-driven spin torque induced by the Rashba effect in a ferromagnetic metal layer. *Nature Mater* **9,** 230–234 (2010). https://doi.org/10.1038/nmat2613
4. Dyakonov, M. I. & Perel, V. I. Current-induced spin orientation of electrons in semiconductors. *Physics Letters A* **35,** 459–460 (1971). https://doi.org/10.1016/0375-9601(71)90196-4
5. Hirsch, J. E. Spin Hall Effect. *Physical Review Letters* **83,** (1999).
6. Liu, L., Pai, C.-F., Li, Y., Tseng, H. W., Ralph, D. C. & Buhrman, R. A. Spin-Torque Switching with the Giant Spin Hall Effect of Tantalum. *Science* **336,** 555–558 (2012). https://doi.org/10.1126/science.1218197
7. Tanaka, T., Kontani, H., Naito, M., Naito, T., Hirashima, D. S., Yamada, K. & Inoue, J. Intrinsic spin Hall effect and orbital Hall effect in 4 d and 5 d transition metals. *Phys. Rev. B* **77,** 165117 (2008). https://doi.org/10.1103/PhysRevB.77.165117
8. Pai, C.-F., Liu, L., Li, Y., Tseng, H. W., Ralph, D. C. & Buhrman, R. A. Spin transfer torque devices utilizing the giant spin Hall effect of tungsten. *Appl. Phys. Lett.* **101,** 122404 (2012). https://doi.org/10.1063/1.4753947
9. Liu, L., Moriyama, T., Ralph, D. C. & Buhrman, R. A. Spin-Torque Ferromagnetic Resonance Induced by the Spin Hall Effect. *Phys. Rev. Lett.* **106,** 036601 (2011). https://doi.org/10.1103/PhysRevLett.106.036601
10. Sih, V., Myers, R. C., Kato, Y. K., Lau, W. H., Gossard, A. C. & Awschalom, D. D. Spatial imaging of the spin Hall effect and current-induced polarization in two-dimensional electron gases. *Nature Phys* **1,** 31–35 (2005). https://doi.org/10.1038/nphys009

11. Stern, N. P., Steuerman, D. W., Mack, S., Gossard, A. C. & Awschalom, D. D. Drift and diffusion of spins generated by the spin Hall effect. *Appl. Phys. Lett.* **91,** 062109 (2007). https://doi.org/10.1063/1.2768633
12. Kato, Y. K., Myers, R. C., Gossard, A. C. & Awschalom, D. D. Observation of the Spin Hall Effect in Semiconductors. *Science* **306,** 1910 (2004). https://doi.org/10.1126/science.1105514
13. Valenzuela, S. O. Spin Hall effect and Spin Orbit Torques. 25 (2014).
14. Ando, K., Takahashi, S., Harii, K., Sasage, K., Ieda, J., Maekawa, S. & Saitoh, E. Electric Manipulation of Spin Relaxation Using the Spin Hall Effect. *Phys. Rev. Lett.* **101,** 036601 (2008). https://doi.org/10.1103/PhysRevLett.101.036601
15. Kirilyuk, A. & Rasing, T. Magnetization-induced-second-harmonic generation from surfaces and interfaces. *J. Opt. Soc. Am. B* **22,** 148 (2005). https://doi.org/10.1364/JOSAB.22.000148
16. Straub, M., Vollmer, R. & Kirschner, J. Surface Magnetism of Ultrathin g-Fe Films Investigated by Nonlinear Magneto-optical Kerr Effect. *PHYSICAL REVIEW LETTERS* **77,** 4 (1996).
17. Gerrits, Th., Silva, T. J. & Rasing, Th. Component-resolved determination of the magnetization by magnetization-induced optical second-harmonic generation. *Review of Scientific Instruments* **77,** 034704 (2006). https://doi.org/10.1063/1.2179414
18. Pattabi, A., Gu, Z., Gorchon, J., Yang, Y., Finley, J., Lee, O. J., Raziq, H. A., Salahuddin, S. & Bokor, J. Direct optical detection of current induced spin accumulation in metals by magnetization-induced second harmonic generation. *Appl. Phys. Lett.* **107,** 152404 (2015). https://doi.org/10.1063/1.4933094
19. Zhang, S. Spin Hall Effect in the Presence of Spin Diffusion. *Phys. Rev. Lett.* **85,** 393–396 (2000). https://doi.org/10.1103/PhysRevLett.85.393
20. Seki, T., Hasegawa, Y., Mitani, S., Takahashi, S., Imamura, H., Maekawa, S., Nitta, J. & Takanashi, K. Giant spin Hall effect in perpendicularly spin-polarized FePt/Au devices. *Nature Mater* **7,** 125–129 (2008). https://doi.org/10.1038/nmat2098
21. Mosendz, O., Vlaminck, V., Pearson, J. E., Fradin, F. Y., Bauer, G. E. W., Bader, S. D. & Hoffmann, A. Detection and quantification of inverse spin Hall effect from spin pumping in permalloy/normal metal bilayers. *Phys. Rev. B* **82,** 214403 (2010). https://doi.org/10.1103/PhysRevB.82.214403
22. Mosendz, O., Pearson, J. E., Fradin, F. Y., Bauer, G. E. W., Bader, S. D. & Hoffmann, A. Quantifying Spin Hall Angles from Spin Pumping: Experiments and Theory. *Phys. Rev. Lett.* **104,** 046601 (2010). https://doi.org/10.1103/PhysRevLett.104.046601
23. Zhang, H. J., Yamamoto, S., Fukaya, Y., Maekawa, M., Li, H., Kawasuso, A., Seki, T., Saitoh, E. & Takanashi, K. Current-induced spin polarization on metal surfaces probed by spin-polarized positron beam. *Sci Rep* **4,** 4844 (2015). https://doi.org/10.1038/srep04844
24. Wierenga, H. A., Prins, M. W. J., Abraham, D. L. & Rasing, Th. Magnetisatization-induced optical second-harmonic generation: A probe for interface magnetism. *Phys. Rev. B* **50,** 1282–1285 (1994). https://doi.org/10.1103/PhysRevB.50.1282
25. Spierings, G., Koutsos, V., Wierenga, H. A., Prins, M. W. J., Abraham, D. & Rasing, Th. Interface magnetism studied by optical second harmonic generation. *Journal of Magnetism and Magnetic Materials* **121,** 109–111 (1993). https://doi.org/10.1016/0304-8853(93)91160-9
26. Kim, J., Sinha, J., Hayashi, M., Yamanouchi, M., Fukami, S., Suzuki, T., Mitani, S. & Ohno, H. Layer thickness dependence of the current-induced effective field vector in Ta|CoFeB|MgO. *Nature Mater* **12,** 240–245 (2013). https://doi.org/10.1038/nmat3522
27. van 't Erve, O. M. J., Hanbicki, A. T., McCreary, K. M., Li, C. H. & Jonker, B. T. Optical detection of spin Hall effect in metals. *Appl. Phys. Lett.* **104,** 172402 (2014). https://doi.org/10.1063/1.4874328

28. Riego, P., Vélez, S., Gomez-Perez, J. M., Arregi, J. A., Hueso, L. E., Casanova, F. & Berger, A. Absence of detectable current-induced magneto-optical Kerr effects in Pt, Ta, and W. *Appl. Phys. Lett.* **109,** 172402 (2016). https://doi.org/10.1063/1.4966276
29. Stamm, C., Murer, C., Berritta, M., Feng, J., Gabureac, M., Oppeneer, P. M. & Gambardella, P. Magneto-Optical Detection of the Spin Hall Effect in Pt and W Thin Films. *Phys. Rev. Lett.* **119,** 087203 (2017). https://doi.org/10.1103/PhysRevLett.119.087203
30. Bansal, R., Behera, N., Kumar, A. & Muduli, P. K. Crystalline phase dependent spin current efficiency in sputtered Ta thin films. *Appl. Phys. Lett.* **110,** 202402 (2017). https://doi.org/10.1063/1.4983677
31. Geresdi, A., Halbritter, A., Tanczikó, F. & Mihály, G. Direct measurement of the spin diffusion length by Andreev spectroscopy. *Appl. Phys. Lett.* **98,** 212507 (2011). https://doi.org/10.1063/1.3593959
32. Feng, Z., Hu, J., Sun, L., You, B., Wu, D., Du, J., Zhang, W., Hu, A., Yang, Y., Tang, D. M., Zhang, B. S. & Ding, H. F. Spin Hall angle quantification from spin pumping and microwave photoresistance. *Phys. Rev. B* **85,** 214423 (2012). https://doi.org/10.1103/PhysRevB.85.214423
33. Azevedo, A., Vilela-Leão, L. H., Rodríguez-Suárez, R. L., Lacerda Santos, A. F. & Rezende, S. M. Spin pumping and anisotropic magnetoresistance voltages in magnetic bilayers: Theory and experiment. *Phys. Rev. B* **83,** 144402 (2011). https://doi.org/10.1103/PhysRevB.83.144402
34. Boone, C. T., Nembach, H. T., Shaw, J. M. & Silva, T. J. Spin transport parameters in metallic multilayers determined by ferromagnetic resonance measurements of spin-pumping. *Journal of Applied Physics* **113,** 153906 (2013). https://doi.org/10.1063/1.4801799
35. Nguyen, M.-H., Ralph, D. C. & Buhrman, R. A. Spin Torque Study of the Spin Hall Conductivity and Spin Diffusion Length in Platinum Thin Films with Varying Resistivity. *Phys. Rev. Lett.* **116,** 126601 (2016). https://doi.org/10.1103/PhysRevLett.116.126601

Chapter 3. Helicity-independent All-Optical Switching in GdFeCo by picosecond laser pulses

From the study of the dynamics of current-induced spin accumulation of Chapter 2, the MSHG technique provided insight that spins accumulate within 50 ps timescales of a short charge current pulse. Irrespective of the speed of spin accumulation, the spin-orbit torque (SOT) switching in conventional spintronic devices is limited by the equilibrium precessional dynamics of magnetization, as discussed in Section 1.5. The fastest known SOT device needed, at best, a 200 ps current pulse to exhibit switching[1]. In order to increase the switching speed of spintronic device, we will turn to the field of ultrafast magnetism – wherein magnetization can be manipulated in picosecond and sub-picosecond timescales by the ultrafast heating by short, intense laser pulses – in the upcoming chapters.

3.1 Helicity-independent all-optical switching in GdFeCo

The field of ultrafast magnetism, discovered in 1996[2] with the demonstration of ultrafast demagnetization of a ferromagnetic Ni thin film following irradiation with a short 100 fs laser pulse, offers the promise of controlling magnetism in unprecedented picosecond (ps) and sub-picosecond timescales. One of the most fascinating phenomena that has been intensely studied towards this end is the helicity-independent all-optical toggle switching (HI-AOS) of the magnetization of ferrimagnetic rare earth-transition metal (RE-TM) alloys by a single short laser pulse. HI-AOS was first demonstrated in thin films of ferrimagnetic GdFeCo[3, 4]. GdFeCo has two unequal and oppositely aligned magnetic sublattices – the Gd sublattice and the FeCo sublattice, as represented by the schematic in Figure 3.1 (a) and exhibits bulk perpendicular magnetic anisotropy. At thermal equilibrium, the magnetic moments of the two sublattices of the ferrimagnet are held opposite to each other by a large negative exchange coefficient $J_{Gd\text{-}FeCo}$. The compensation temperature T_M of this ferrimagnet, at which the sublattices have equal magnitudes of magnetization and the net magnetic moment of the alloy goes to zero, is dependent on the relative composition of the Gd and FeCo sublattices; Gd rich alloys have a higher T_M, and FeCo rich alloys have a lower T_M.

When a thin film of GdFeCo is irradiated with a short fs laser pulse with sufficient energy, its magnetization switches in the opposite direction owing to HI-AOS, irrespective of the polarization of the laser pulse and the presence or absence of an external applied magnetic field. The magneto-optical Kerr effect (MOKE) microscope images of Figure 3.1 (b) indicate this toggle switching of GdFeCo magnetization with each successive pulse (MOKE microscopy will be discussed further in Section 3.2). In these figures, the light gray and dark gray contrasts represent the two opposite magnetizations of the GdFeCo, indicating that the area of the film under the laser beam toggles its magnetization. The toggle switching of GdFeCo has been demonstrated to occur in ultrafast ps and sub-ps timescales. Time-resolved X-ray magnetic circular dichroism (TR-XMCD)[3] experiments of HI-AOS have enabled the study of the magnetization dynamics of the Gd and the FeCo sublattices independently of each other. As seen from Figure 3.1 (c) these experiments show that the magnetization of GdFeCo switches to the opposite direction within a couple of ps of being irradiated with a short ~100 fs laser pulse. The FeCo sublattice demagnetizes first and crosses the zero magnetization line in a few hundred fs.

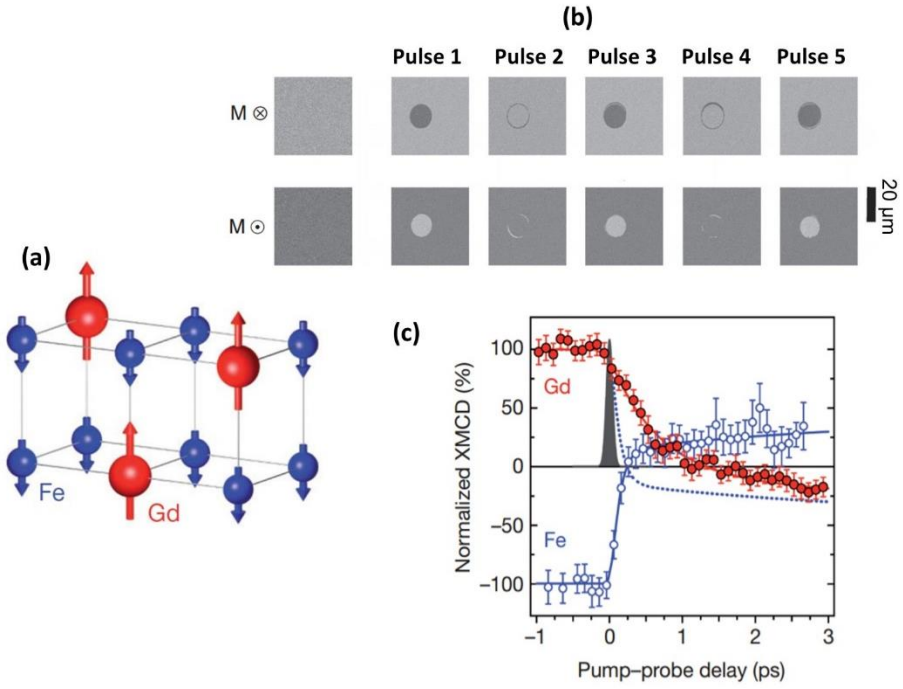

Figure 3.1 Helicity-independent all optical switching in GdFeCo.
(a) Schematic of GdFeCo ferrimagnet indicating the two oppositely aligned Gd (red) and FeCo (blue) sublattices. (b) MOKE microscope images depicting HI-AOS in GdFeCo with individual fs laser pulses. The light gray and dark gray contrasts indicate two opposite magnetization directions. Toggle switching is seen irrespective of the initial magnetization state (top and bottom). (c) Time resolved XMCD data showing the ultrafast reversal of the Gd and Fe sublattice, with a transient ferromagnetic state from ~200 fs to ~1 ps (Figures from Ref [3, 4]).

The faster demagnetization of FeCo compared to the Gd sublattice occurs because the 3d orbitals of Fe and Co, which contribute to the magnetization of the transition metal sublattice, lie at the Fermi level of GdFeCo (Figure 3.2). Therefore the laser pulse is first absorbed by the 3d electrons of sublattice, causing it to demagnetize first. The 4f electrons are the primary contributors for the magnetization of the rare earth sublattice Gd. Since the 4f orbitals of Gd lie farther away from the Fermi level, they are heated indirectly by the laser pulse through the interaction of the orbitals 3d(Fe)-5d(Gd)-4f(Gd). This leads the Gd sublattice to demagnetize slower and switch to the opposite magnetization in a couple of picoseconds. It must be noted that the differing demagnetization rates of the two sublattices leads to a transient ferromagnetic state for a small window (~200 fs to ~1 ps in Figure 3.1 (c)) of time when the two sublattices are aligned parallel to each other. Since HI-AOS occurs in ultrafast timescales and is independent of the polarity (angular momentum) of the triggering laser pulse and the presence of an external applied field, it has been described as an ultrafast thermal effect[3, 4]. As mentioned in Section 1.6, the high switching speed associated with HI-AOS offers the possibility of promising technological applications in high-speed, energy-efficient and non-volatile magnetic memory and logic, with two to three orders of magnitude of higher operating speeds compared to conventional spintronic devices that operate on mechanisms such as external field control[5], spin-transfer- torque[6, 7], or spin-orbit torque[1].

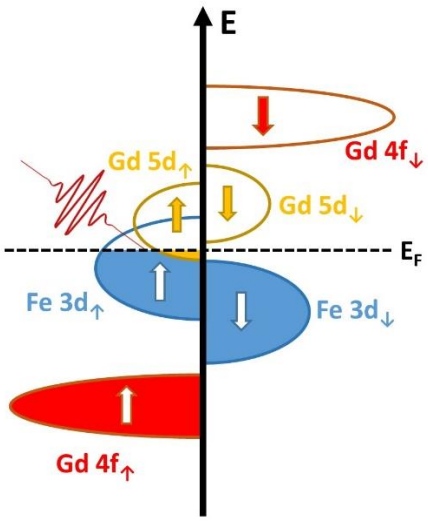

Figure 3.2 Schematic of GdFeCo band structure.
The 3d orbitals of Fe (and Co, not shown) lie at the Fermi level and absorb the optical energy of the laser. The 4f orbitals of Gd lie further away from the Fermi level.

Despite intense study, the mechanisms of HI-AOS remain unresolved due to the rich physics that are found after a sub-100 fs pulsed laser excitation. Ultrafast processes are described by the three temperature model[2], comprising of the electron, phonon (lattice) and spin systems, introduced in Chapter 1. When a magnetic thin film is excited with a short intense laser pulse, the pulse energy is first absorbed by the electronic system of the magnet. In the first hundred femtoseconds, highly nonequilibrium phenomena such as nonthermal carrier excitation [8, 9] and superdiffusive spin currents[10] may occur. In the next few hundred femtoseconds, electrons become thermalized with each other, meaning their distribution can be described by Fermi-Dirac statistics $f(E) = 1/(1+\exp\{(E-E_F)/kT_e\})$, resulting in a high electronic temperature T_e, but remain out of thermal equilibrium with the lattice and spin degrees of freedom[2]. In addition to these non-equilibrium phenomena, the strong dependence of equilibrium magnetic properties on temperature could also play a central role in HI-AOS[11, 12], as it does in heat-assisted magnetic recording (HAMR) technology[11].

The energy absorbed by the metal film and the resulting transient temperature response are known to play a central role in ultrafast demagnetization of single-element ferromagnets[2, 13, 14]. However, due to the large number of mechanisms that may contribute to HI-AOS, it has been difficult to determine the primary role of energy and temperature during HI-AOS. Temperature rise can directly or indirectly facilitate magnetization switching in a number of ways. For example, in HAMR, the lattice temperature T_P of the system is heated close to the critical Curie temperature T_C to reduce the anisotropy before an applied field favors a particular direction for the magnetization upon cooling[11]. In contrast, HI-AOS models for ferrimagnets[3, 4, 15, 16, 17] do require the lattice temperature of the film to not approach the Curie temperature, as that will lead to randomly magnetized domains inside the excited area rather than toggle switching. Instead, these models rely on transient electron temperatures that are out of equilibrium with the lattice to induce the dynamics of the Gd and Fe magnetic sublattices[3].

Despite the centrality of temperature to prevailing theories for HI-AOS, the energy required for switching, and the resulting temperature response of the electrons and phonons remains unclear. This

is largely related to uncertainties in the minimum absorbed fluence required for switching (i.e., critical fluence F_C) and unknown thermal parameters. Peak temperatures and subsequent cooling are determined by F_C, the electron phonon coupling parameter g_{ep}, and the electronic heat capacity C_e. C_e and g_{ep} are generally set by assuming typical values for transition metals. However, reported values for g_{ep} for transition metals vary by an order of magnitude[17, 18]. Owing to these considerations[19], there is considerable uncertainty in the peak electron and phonon temperatures reported in previous studies, and a systematic analysis of these temperatures is required to better elucidate the mechanisms behind HI-AOS.

These aforementioned models of HI-AOS predict the transient electron and phonon temperature response to an applied laser pulse from either the three temperature or two temperature models. In atomistic calculations, T_e is coupled with a random Langevin noise field term η_i of the sublattice i as shown in equation ((3.1).

$$(3.1)\ \eta_i \propto \alpha_i T_e$$

Here, a_i is an effective damping parameter, a channel to dissipate angular momentum. This Langevin noise field is entered into an atomistic calculation of the Landau-Lifshitz-Gilbert equation as follows.

$$(3.2)\ H_i = \eta_i + \frac{\delta E_i}{\delta S_i}$$

$$(3.3)\ \frac{\delta S_i}{\delta t} = -\frac{\gamma_i}{(1+\alpha_i^2)\mu_i}(S_i H_i + \alpha_i S_i [S_i H_i])$$

Here H_i is the effective magnetic field, S_i the reduced atomic localized spin, and γ_i the gyromagnetic ratio of the sublattice i. E_i is the total energy of the sublattice, including the Zeeman, anisotropy and exchange terms.

These models can successfully reproduce the HI-AOS switching behavior through a three-step process. In the first step T_e has to quickly overcome T_C in order for the Langevin noise field (corresponding to thermal excitations of the electrons) to overcome the strong exchange field which at equilibrium holds the two sublattices antiparallel to each other. This induces the independent demagnetization of the sublattices. Due to their different damping (rate of dissipation of angular momentum) and magnetic moments, demagnetization for different lattices will occur at different rates, the Fe demagnetizing faster[3]. The second step involves the cooling of T_e which allows the remagnetization of the completely demagnetized Fe sublattice. At this stage the exchange fields become dominant over the Langevin noise again, and as the Gd demagnetizes toward its equilibrium magnetization (at T_e), conservation of angular momentum induces the switching of the Fe sublattice, leading to the transient ferromagnetic state. The third step consists of the antiparallel alignment of the Gd spins relative to the Fe spins due to the exchange interaction, which becomes dominant over the Langevin noise as the electrons start to cool. However, in these models it is often clearly claimed[3, 4, 20] that initially T_e needs to quickly overcome T_C in order to decouple the sublattices and allow a faster demagnetization of the Fe sublattice. 1000s of kelvin of T_e is required for the Langevin noise term to be high enough to effectively overcome the exchange between the sublattices in the non-equilibrium timescales of a few hundred femtoseconds.

In this chapter, I will detail systematic experiments performed on the HI-AOS of GdFeCo thin films of different compositions to elucidate the roles of electron and phonon temperatures in the HI-AOS process. The > 1000 K T_e required by the HI-AOS models described above imply that HI-AOS of GdFeCo can only be performed by ultrashort sub-100 fs laser pulses. This means that longer ps pulses would require much larger fluences than the damage threshold of the thin film to trigger peak $T_e >$ 1000 K, which negates the possibility of HI-AOS by ultrafast heating in ps timescales. This would then pose an insurmountable barrier for ultrafast spintronic devices operating with short electrical pulses, since it is not possible to generate intense, sub-ps current pulses on chip using existing technologies. Towards that end, this chapter explores experiments performed on the HI-AOS of GdFeCo with laser pulse excitations of varying pulsewidth, ranging from ~55 fs up to 15 ps, and challenges hypotheses of the need for high T_e to trigger HI-AOS.

3.2 MOKE microscope experimental setup for HI-AOS

The switching of the magnetization of GdFeCo thin films by HI-AOS after excitation with individual laser pulses is verified using a magneto-optical Kerr effect (MOKE) microscope, or image MOKE, setup. MOKE microscopy is a robust tool to characterize static magnetization properties, and several static magnetic hysteresis loops reported in this thesis were performed using this setup. In addition to the ease of setup and use, a MOKE microscope has the added advantage of providing spatial information of the magnetization of a film. As is evident by the name, a MOKE microscope operates on the principle of the magneto-optical Kerr effect[21, 22], wherein the complex polarization $\Theta = \theta + i\varepsilon$ (where ε is the Kerr ellipticity and θ the Kerr rotation) of light incident on a magnetic thin film changes upon reflection. The change in ellipticity and rotation of the reflected light is proportional to, and is a measure of, the magnetization of the reflecting sample.

The schematic of the MOKE microscope setup is shown in Figure 3.3 (a). Light from red LED source at 630 nm is rendered p-polarized (electric field in the plane of incidence) by a high extinction ratio (> 1000 : 1) polarizer. The light is then focused onto the back focal plane of the sample objective. The objective collimates the light and illuminates the sample surface evenly at normal incidence. The reflected light from the sample is deviated from the path of incidence using a beam splitter. This light is then passed through an analyzer that is close to the crossed position with respect to the polarizer, and is then focused onto a CCD camera detector to form an image. At the near-crossed position of the polarizer and analyzer, the intensity of light at the camera becomes proportional to the change in rotation of the reflected light, and therefore is a direct measure of the magnetization of the sample[22]. For normal incidence of polarized light, the MOKE is sensitive to the out-of-plane component M_Z of the sample magnetization. This configuration, called polar MOKE, is ideal for the samples reported in this thesis, most of which exhibit out-of-plane magnetization. For an objective of 20×, an area of 125 × 100 μm^2 on the sample surface is imaged by the camera. To achieve large signal to noise ratios, the camera image is integrated for a relatively large time of 500 ms (or even larger, up to 2.5 s, for higher objectives and/or samples with low reflectivity). Care is taken to optimize the exposure time so as to not saturate the camera signal. Since the change in reflected intensity at the camera for opposite magnetizations is small, the contrast in the camera signal for the two magnetization states is at best ~5% of the camera signal. Differential images are made using the data acquisition software to enhance this contrast and to better visualize the magnetic domains and the two magnetic states. An

example of domain formation in a GdFeCo thin film is shown in Figure 3.3 (b) where the light gray and dark gray regions of the image correspond to domains with two opposite magnetization states.

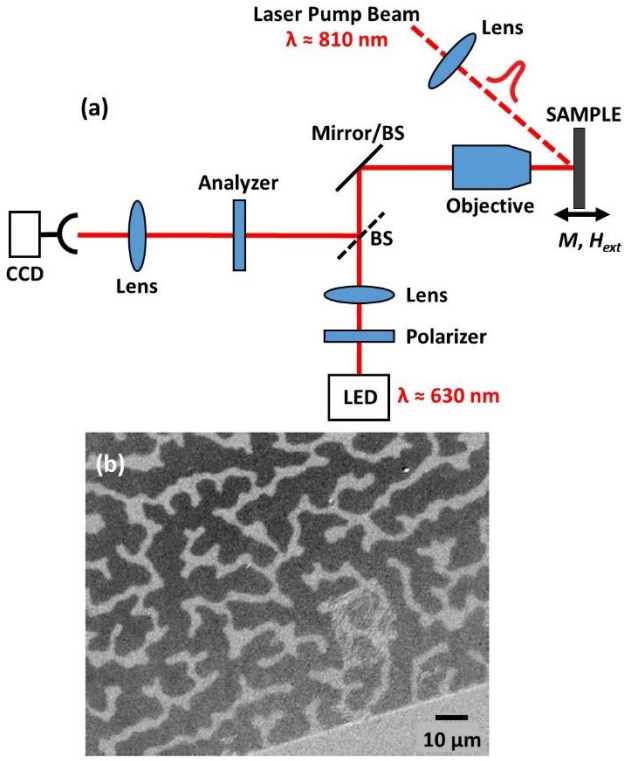

Figure 3.3 MOKE microscopy.
(a) Schematic of a MOKE microscope. A 630 nm LED lamp is used as the source and CCD camera is used as the detector. (BS = Beam splitter) (b) Differential contrast MOKE microscope image of GdFeCo domains. The light and dark gray regions indicate domains with opposite magnetization states (Figure (b) from Dr Yang Yang).

To perform single shot HI-AOS experiments, the exciting laser beam, called the pump, is incident on the sample at 40° to the sample normal. Toggling of the image intensity (image MOKE contrast) in the areas of the sample under the illuminated pump indicate the exhibition of HI-AOS by the sample.

3.3 GdFeCo characterization and HI-AOS with ps pulses

Two $Gd_x(FeCo)_{100-x}$ films with concentrations x = 24.5 % and x = 27.5% are grown by co-sputtering the following stacks on Si/SiO_2(300 nm) substrates: Ta(2.5)/GdFeCo(14)/Ta(3.6)/Ta_2O_5(2.8) (thicknesses in nm). Throughout this chapter, these samples will be referred to as $Gd_{24}FeCo$ and $Gd_{27}FeCo$ respectively. X-ray reflectivity measurements are performed to confirm the layer thicknesses. Polar magneto-optical Kerr effect (MOKE) measurements confirm that the films exhibit out-of-plane magnetic anisotropy, as seen by the square hysteresis loops in the inset of Figure 3.4. The normalized polar Kerr rotation (NPKR) is measured as a function of the sample temperature by heating the sample with an electric heater. A Curie temperature T_C of ~540K is obtained by fitting the NPKR via the phenomenological formula[23] NPKR = $[(T_C - T)/(T_C - 300)]^{0.39}$ (see Figure 3.4), where T is the sample temperature. This Curie temperature is close to previously reported values[24]. It must

be noted that for the 630 nm LED light probe used in the MOKE microscope (and for the 800 nm laser probe used in later sections), the probe is sensitive only to the magnetization of the transition metal sublattice (FeCo) of RE-TM ferrimagnets as these wavelengths are absorbed by electrons in the Fermi level and, from Section 3.1 and Figure 3.2, the Fermi level is populated by the 3d electrons of the FeCo sublattice (the 4f electrons of Gd are far away from the Fermi level). The compensation temperature T_M is measured by monitoring the coercivity and polarity of the magnetic hysteresis via MOKE as the sample is heated. The T_M is the temperature at which the polarity of the hysteresis loop flips. A T_M of ~430 K is observed for sample $Gd_{27}FeCo$. Sample x = 24.5% presented a hysteresis with the opposite polarity to that of x = 27.5% at room temperature (see inset of Figure 3.4), meaning its compensation temperature is below room temperature.

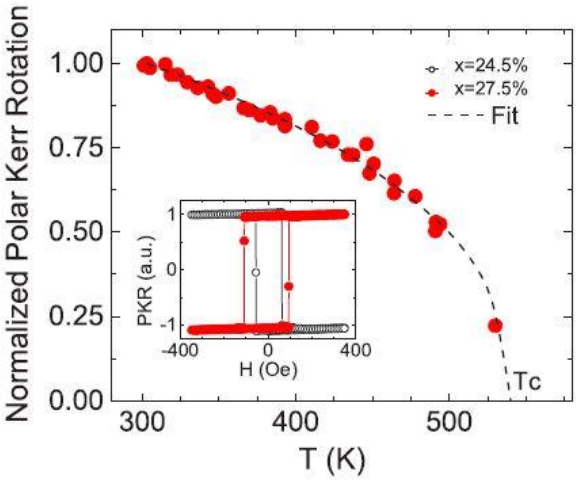

Figure 3.4 Temperature dependence of GdFeCo magnetization.
Normalized Kerr rotation of $Gd_x(Fe_{90}Co_{10})_{100-x}$ with x = 27.5% as a function of temperature. Inset shows square magnetic hysteresis as a function of the out-of-plane external field H, at room temperature, for samples with x = 27.5% and x = 24.5%. The opposite polarities of the loops indicate that they have T_M on either side of the room temperature. (Figure from Ref [19])

A regeneratively amplified 252 kHz repetition rate Ti:sapphire laser (Coherent RegA 9050 system used in Section 2.4) with 810 nm center wavelength is used to generate the high energy laser pump pulses that trigger HI-AOS. The laser pulse duration FWHM is tunable from Δt = 55 fs to Δt = 25 ps by adjusting the final pulse compressor in the chirped pulse amplifier[25]. The RegA 2050 allows the output of single laser pulses. A MOKE microscope setup described in Section 3.2 is used for imaging the sample magnetization after each single laser pulse shot.

In the single-shot experiments, the laser beam is incident with an angle of 40° with respect to the sample normal. The spatial beam profile is obtained by the knife-edge technique[26] and the energy of each pulse is monitored with a fast photodiode connected to a 6 GHz oscilloscope. The photodiode output voltage is calibrated to the laser pulse intensity by obtaining a calibration curve of the photodiode output peak amplitude with respect to the laser power in the repetition mode. An effective index of refraction of $n = 3.7 + 4.2i$ for Ta/GdFeCo/Ta is measured by ellipsometry. To accurately determine the fluence absorbed in the GdFeCo film, a multilayer absorption calculation is performed[27] by calculating the electric field in each layer through the matrix transfer method. The absorption is

then obtained by calculating the divergence of the Poynting vector in the stack. The refractive indices of the layers in the stack used for this calculation are shown in Table 3.1. An absorption of 29% was found in the Ta/GdFeCo/Ta stack. The absorption profile is shown in Figure 3.5.

Layer	Thickness (nm)	Complex refractive index	Absorption by layer (%)
Air	-	1	-
Ta_2O_5	2.8	2.114	0
Ta/GdFeCo/Ta	20	3.7 + 4.2i	29
SiO_2	300	1.4533	0
Si	-	3.696 + 0.0047i	-

Table 3.1 Multilayer absorption calculation parameters and results for the GdFeCo stack.

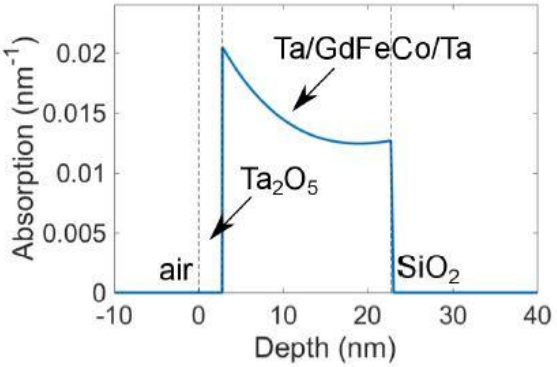

Figure 3.5 Absorption profile in the GdFeCo stack.
The optical absorption as a function of depth is calculated by the matrix transfer method. (Figure from Ref [19])

The magnetization of the film is saturated with an external magnetic field $H \approx \pm 100$ Oe. Following removal of the external field, the film is then exposed to a single linearly polarized laser pulse with Δt = 55 fs. As shown in Figure 3.6 for $Gd_{27}FeCo$, after each laser pulse of the same energy, the magnetization in a small region reliably toggles repeatedly between white (up) and black (down). This observation of helicity-independent toggling of the GdFeCo magnetization is consistent with the helicity-independent AOS reported in Refs [3, 4]. In the absence of domain wall motion, the reversed domain size is determined by the area within the Gaussian laser profile with a fluence above F_C[13]. However, in these films, the domain wall motion reduces the size of the reversed domain in the seconds following laser irradiation. A critical domain size (≈10μm) is observed, below which optically switched domains shrink and collapse after several seconds. Instability of small magnetic domains is a well understood phenomenon that occurs whenever the domain wall energy is larger than the domain stabilizing pinning and dipolar energy terms[28]. In order to minimize the effect of such relaxation mechanisms on the measurement of the critical fluence, the pump diameter (FWHM) is chosen to be relatively large (≈0.16 mm). The absorbed critical fluences F_C, such as those shown in Figure 3.7, are

then obtained by decreasing the pump fluence until no switching is observed. For T = 300 K and Δt = 55 fs, F_C = 0.82 ± 0.16 mJ/cm^2 is found for both GdFeCo samples.

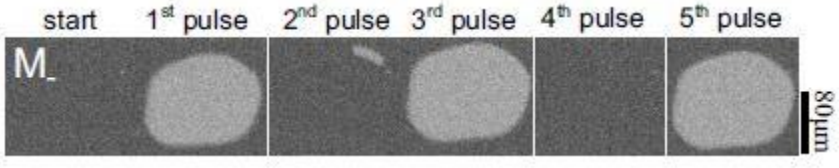

Figure 3.6 MOKE microscopy images of HI-AOS in GdFeCo.
The images, shown here for the $Gd_{27}FeCo$ film initially magnetized along M–, confirm toggle switching with Δt = 55 fs linearly polarized laser pulses (Figure from Ref [19]).

To study the importance of the lattice (phonon) temperature in AOS, the sample is heated by mounting it on a resistive heater, and the critical fluence F_C is recorded as a function of the initial sample temperature T_0. A threshold F_{MD} at which a multidomain pattern is observed is also recorded (see picture #3 in Figure 3.7 (a)). The measurement of this threshold has a large uncertainty due to the stochastic nature of domain nucleation and the instability of the small multidomain patterns. Within experimental accuracy the multidomain thresholds for both samples are equal (see Figure 3.7 (b)). In the case where the whole system reaches T_C, a multidomain magnetization pattern is expected to arise as the sample cools down from the paramagnetic state and is remagnetized randomly. Indeed, the transition from pure AOS to multidomain is observed (pictures #2 and #3 in Figure 3.7 (a)) at a particular threshold fluence F_{MD} (blue crosses in Figure 3.7). Transient temperatures for electrons and the lattice are calculated with the three temperature model[2, 14] (details in Section 3.6), and the threshold at which the transient equilibrium temperature, when the electrons and phonons are back in equilibrium (~few ps to few 10s of ps), exceeds T_C is plotted as a blue dashed line in Figure 3.7. The model will be discussed later in this chapter. Both GdFeCo samples have very similar compositions, resulting in similar total heat capacities. Therefore, their Curie temperatures and transient equilibrium temperature, and thus the multidomain fluence threshold are expected to be similar. Therefore, the demagnetization or multidomain threshold F_{MD} sets a limit above which no AOS can be observed.

As observed from Figure 3.7 (a), the critical fluence for $Gd_{24}FeCo$ is independent of ambient temperature, while the critical fluence of $Gd_{27}FeCo$ decreases by a factor of 2 upon a change in ambient temperature from 300 to 450 K. The different temperature dependence is believed to be related to the difference in energy transfer rates between sublattices in both samples, as has been predicted[16]. A discussion on the energy transfer rates will follow later in this chapter. Importantly, it is to be noted that both samples display a weaker temperature dependence than one would expect if AOS was an equilibrium phenomenon dependent on transient equilibrium phonon temperatures analogous to HAMR. If changes to equilibrium magnetic properties were the primary driver of AOS in a manner analogous to HAMR, the peak lattice temperature reached following laser irradiation at F_C would be a constant and insensitive to ambient temperature. The peak lattice temperature is calculated as $T_P = T_0 + F_C/(d*C)$ where d is the film thickness and C (3×10^6 J/m^3/K for GdFeCo[29]) is its specific heat capacity. At ambient temperatures of 300 and 470 K, the calculated transient temperature rise in the lattice at the corresponding F_C following irradiation is~150 and ~70 K, respectively. Therefore, the peak lattice temperature during AOS varies from 450 to 540 K (~T_C) for ambient temperatures from 300 to 470 K, and is not a constant. Therefore, as expected, we confirm

that unlike in HAMR, heat-induced changes to equilibrium magnetic properties are not the primary drivers of AOS.

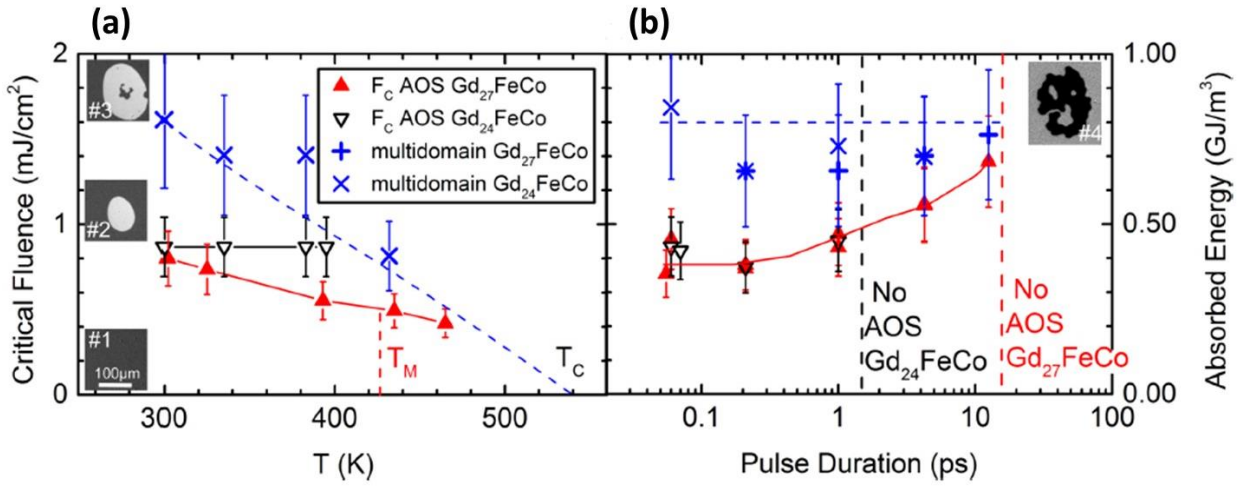

Figure 3.7 Studies of the critical fluence for HI-AOS and multidomain formation in the GdFeCo films.
Critical fluences F_C (for AOS) and F_{MD} (for multidomain state formation) for the $Gd_{27}FeCo$ and $Gd_{24}FeCo$ films as a function of the (a) initial temperature of the sample for Δt = 55 fs laser pulses and (b) the laser pulse duration Δt at room temperature. Solid lines are guides for the eyes. The blue dashed lines are a calculation of the fluence needed to make the lattice reach T_C (see text). MOKE images in (a) show the typical result in each fluence range. From bottom to top: (#1) No switch (ultrafast demagnetization), (#2) AOS, and (#3) multidomain state. The vertical dashed lines in (b) show the limits for observation of AOS in each sample. The right hand image (#4) shows the fully demagnetized state obtained for a Δt = 16 ps pulse of ~1.85 mJ/cm^2 on $Gd_{27}FeCo$ (Figure from Ref [19]).

As discussed in Section 3.1, previous theories on HI-AOS necessitate high peak electron temperatures (T_e > ~1000K) to effectively overcome the exchange between the sublattices and cause GdFeCo to switch. To test the importance of the peak electron temperature, single-shot AOS experiments as a function of the pulse duration (FWHM) Δt are performed (Figure 3.7 (b)). As Δt increases for a fixed laser fluence, the laser peak intensity drops as $1/\Delta t$ resulting in a lower peak T_e. If the peak T_e is a key parameter for AOS as postulated by previous models, as Δt is increased, the critical fluence should increase proportionally. However, only a relatively weak dependence of the critical fluence on the pulse duration is observed (see Figure 3.7 (b)). The energy needed for AOS increases by ~50% as the pulse duration increases by over two orders of magnitude. Similar trends have been reported in the context of helicity-dependent AOS [30, 31] (this type of AOS will be discussed briefly in Chapter 4 and Chapter 5). However, the analysis in these works was made in terms of helicity-induced optomagnetic fields. Furthermore, high critical fluences were reported that would easily heat the lattice above T_C. Such high lattice transient temperatures would result in a random multidomain state instead of a HI-AOS in our GdFeCo samples, as shown earlier. Single-shot HI-AOS is observed in the $Gd_{27}FeCo$ sample for pulses as long as Δt = 15 ps, as shown in Figure 3.7 (b). For Δt > 15 ps, the extrapolated F_C exceeds the multidomain critical fluence F_{MD} indicated in the figure by blue cross points

(experimental data) and blue line (calculated F_{MD}). Beyond $\Delta t > 15$ ps, the result is a fully demagnetized pattern (picture #4 in Figure 3.7 (b)) and no HI-AOS is ever observed for these pulse durations. This is in sharp contrast with the $\Delta t = 55$ fs multidomain state (picture #3 in Figure 3.7 (a)) where the outer part of the Gaussian laser beam, with a lower fluence, does induce HI-AOS.

3.4 Time resolved MOKE experimental setup

An experimental technique called the time-resolved magneto-optical Kerr effect (TR-MOKE)[32] is used throughout this thesis to study the dynamics of the magnetization in timescales from a few hundred femtoseconds up to ~1 ns. The regeneratively amplified Ti: Sapphire laser (Coherent RegA 9050) can output high energy (~6 μJ) pulses as short as 55 fs (can be increased up to 20 ps by increasing the chirp of the laser compressor), with an 810 nm central wavelength and a bandwidth of ~50 nm. The short laser pulses ensure that the laser probe can detect changes in magnetization with a high temporal resolution better than 100 fs. The repetition rate between the pulses can be varied between 10 kHz and 300 kHz, with the standard repetition rate being 252 kHz. The average power of the RegA 9050 at 252 kHz repetition rate is ~1.2 W. The schematic of the TR-MOKE setup used for most of the magnetization dynamics experiments in this thesis is shown in Figure 3.8. The output of the RegA is split into two beams – a low power probe beam and a high power pump beam – by a polarizing beam splitter. A half wave plate placed before the polarizing beamsplitter, when used in conjuction with the polarization of the beamsplitter, enables the adjustment of the relative power between the pump and the probe. The pump and probe beams go through different optical paths before they overlap spatially at the sample surface.

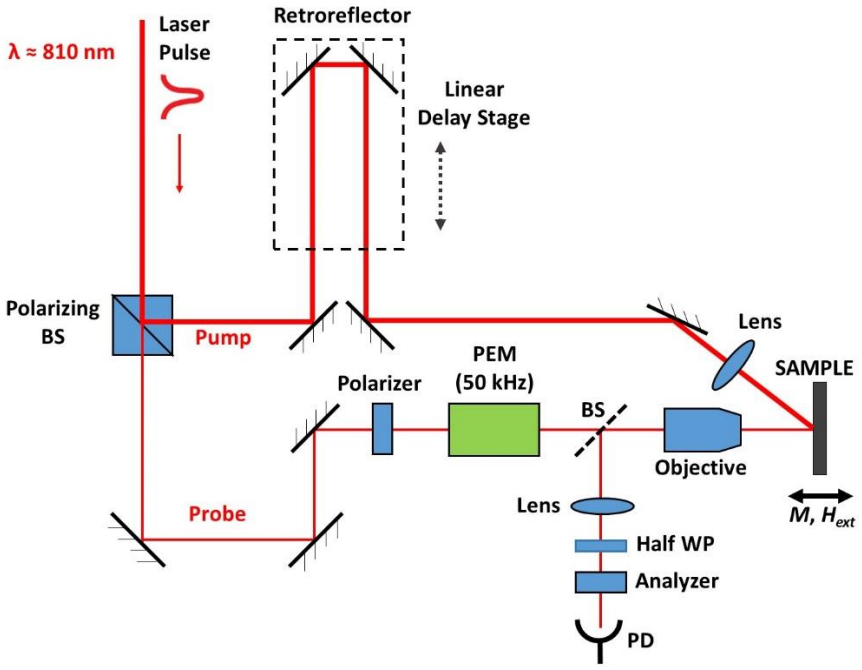

Figure 3.8 Schematic of the time-resolved MOKE pump-probe setup.
The relative time delay between the pump and the probe beams at the sample is varied by passing the pump through a variable linear delay line. The polarizer polarizes the probe at a 45° angle with respect to the PEM optical axis. (BS = beam splitter, PD = photodiode, WP = waveplate)

The probe beam is then passed through another half wave plate and polarizer pair to enable adjustment of the probe power independent of the pump. The polarizer is set such that the probe polarization is at 45° with respect to the plane of the optical table. The polarization of the probe beam is then modulated a photo-elastic modulator (PEM) whose axis is parallel to the horizontal, such that the incoming 45° polarized probe beam has equal s and p components of polarization. The PEM is composed of a birefringent crystal and works on the principle of the photoelastic effect. It can be considered to be a tunable waveplate, and nominally operates at a frequency f = 50 kHz. When a sinusoidal electric field at 50 kHz is applied across the crystal of the PEM, the birefringence of the crystal gets modulated. This causes a modulation in the retardation of the s and p components of the probe beam, which in turn leads to a modulation of the polarization of the beam as it exits the crystal. The probe is then focused onto the sample by an objective with normal incidence to detect the out-of-plane component of the sample magnetization using polar-MOKE, as described for the LED light probe in Section 3.2. The reflected probe from the sample is separated from the normally incident beam using a beam splitter and focused onto a Si photodetector. The Si photodetector signal is measured by a lock-in amplifier that is referenced at f (the PEM modulation frequency) or $2f$ to measure respectively the Kerr ellipticity ε or Kerr rotation θ. The lock-in amplifier integration time is typically set to 300 ms to ensure quick, drift-free measurements and optimal signal-to-noise ratio. The integration time can be increased up to 1-3 s to increase the signal-to-noise ratio for more sensitive measurements. It must be noted that this setup, without the pump beam, is also used to perform static MOKE measurements with the laser probe. In order for the probe to not perturb the magnetization of the sample, the probe power is set low, typically at ~0.5 mW before the objective for 252 kHz repetition rate. A signal of ~1 mV, with SNR of up to 500:1 can be achieved for this configuration (at 252 kHz repetition of the laser) as a best case scenario for the complete switching ($+M_S$ to $-M_S$) of a 20 nm thick GdFeCo film.

The pump is the short, high powered beam that triggers the ultrafast magnetic response in the sample. It is first sent to a retroreflector fixed on to a 220 mm long linear delay stage (Thorlabs DS220). The incident pump beam is tuned to be parallel with the delay stage, and the retroreflector ensures that the reflected beam is parallel to the incident beam. This ensures that the pump propagation direction remains unchanged as the delay stage traverses its length. The delay stage can move the retroreflector along its length, thereby enabling one to change the optical path length that the pump travels before arriving at the sample relative to the pump. The delay stage has a resolution of 0.1 μm which corresponds to a temporal resolution of ~6.7 fs. If the delay stage is set that the pump beam travels the same length as the probe, both the beams overlap temporally at the sample, in addition to being spatially overlapped. The reflected pump is then passed into a half wave plate-polarizer pair to independently set the pump power. The polarizer renders the pump p-polarized. The pump is then focused onto the sample and spatially overlapped with the probe beam using a plano-convex lens fixed at a distance equal to its focal length from the sample surface, and is incident onto the sample at an angle of ~40° with respect to the sample normal. This pump beamline remains unchanged and is used in conjunction with the MOKE microscope in the single shot MOKE microscopy experiments described in Sections 3.2 and 3.3.

As mentioned earlier in this section, laser MOKE experiments are performed by integrating the lock-in amplifier signal for typically 300 ms. In TR-MOKE experiments, this corresponds to ~80,000 pump-probe cycles. In order to reset the original state of the magnet between consequent pump pulses

in switching or large demagnetization experiments, a constant resetting external magnetic field is applied throughout such experiments.

The size of the focused pump and probe beams at the sample surface is set by changing respectively the focal length of the plano-convex lens and the magnification of the probe objective. Another way to do this is to change the spot size of the collimated beam arriving at the pump focusing lens or the objective. The diffraction limited spot size w_f of a focused beam is given by equation (3.4), where w is the beamwidth of the collimated beam before the focusing lens of focal length f and λ is the wavelength of the beam.

$$(3.4)\ w_f = \frac{f\lambda}{w}$$

Equation (3.3) indicates that larger the size of the collimated beam before the focusing lens or objective, smaller is the diffraction limited spot size at the focus, and vice-versa. The size of the collimated pump and probe beams, and therefore the size of the focused spot, can be changed by introducing telescopes on the pump or probe lines. A simple telescope is composed of two plano-convex lenses separated by the sum of their focal lengths, and can be used change the width of a collimated beam before the focusing lens or objective. If w_i and w_o are the widths of the incoming and outgoing beams of a telescope, their relationship is given by equation (3.5) where f_1 and f_2 are the focal lengths of the first and second lenses of the telescope.

$$(3.5)\ w_o = \frac{f_2}{f_1} w_i$$

The spot size of the focused probe beam at the sample is kept much smaller (typically 10x or more) than that of the pump, so that the profile of the pump intensity can be assumed to be constant across the probe spot when the probe is overlapped with the center of the pump spot.

3.5 Time-resolved experiments on HI-AOS of GdFeCo: switching speed with ps laser pulses

Time-resolved pump-probe MOKE measurements, as described in Section 3.4, are performed on both $Gd_{27}FeCo$ and $Gd_{24}FeCo$ samples. For these experiments, a constant, perpendicular external field of 55 Oe is applied to reset the magnetization between pump pulses. The pump beam, incident at 40° with respect to the sample normal, has a spot diameter (FWHM) of ~100 μm, whereas the probe, at normal incidence, is kept much smaller with a spot diameter of ~6 μm. As shown in Figure 3.9, for a fluence of 0.86 mJ/cm^2 the reversal occurs, against the external magnetic field, for both samples. The magnetization of both samples switch (cross the zero magnetization line) in the order of a few ps, as is expected from previously published results in this material. The opposite sign of the signal at negative time delay for samples with T_M above and below room temperature is due to the sensitivity of the 810 nm probe to the FeCo sublattice magnetization. When $T < T_M$ the external field drives the dominant Gd sublattice, whereas at $T > T_M$ the field drives the dominant FeCo[33].

It is important to first verify that the switching behavior is not affected by the presence of the constant external applied field. For this purpose, pump-probe experiments are performed at low pump fluences

with no external field on both samples (blue lines in Figure 3.9). The low pump fluence ensures a small demagnetization of the GdFeCo and no switching. No difference in the Kerr signal is observed with respect to experiments performed with the 55 Oe external field. Moreover, experiments on the low T_M sample $Gd_{24}FeCo$ (black downward triangles in Figure 3.9) at $T > T_M$ where no transition through T_M was possible due to laser heating yielded similar results with and without the constant external field. This means that field induced switching scenarios due to crossing of T_M can be discarded[33]. Both these experiments confirm that the presence of the field does not affect the magnetization dynamics, at least for the first few hundred ps.

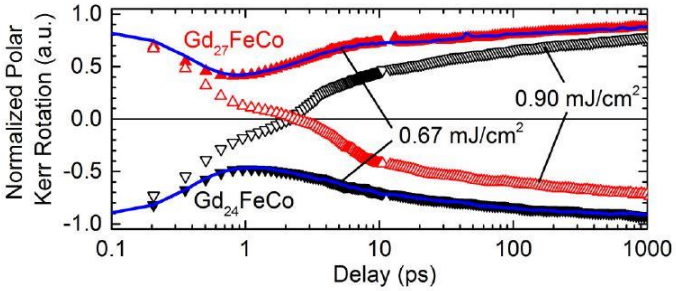

Figure 3.9 Effect of an external resetting field on the magnetization dynamics of GdFeCo. Evolution of the normalized polar Kerr rotation of $Gd_{27}FeCo$ (red upward triangles) and $Gd_{27}FeCo$ (black upward triangles) samples induced by a linearly polarized Δt = 55 fs pump, under a constant perpendicular external field of 55 Oe. At an absorbed laser fluence of 0.67 $mJcm^{-2}$ (less than F_C) the films only undergo demagnetization (filled triangles). The blue lines correspond to the evolutions under no external field for 0.67 $mJcm^{-2}$. They show no difference with respect to the results with the external field during the first nanosecond. Increasing the fluence to 0.90 $mJcm^{-2}$ with the external field yields the switching curves (open triangles). The opposite initial magnetization states of the two samples confirm that they have T_M on either side of the room temperature (Figure from Ref [19]).

TR-MOKE experiments were performed at different pump fluences to confirm that the critical fluence F_C extracted from dynamic and static measurements agree with each other. The fluence dependence of the magnetization evolution in $Gd_{24}FeCo$ at T = 300 K and for Δt = 55 fs is shown in Figure 3.10. The curve at 0.79 mJ/cm^2 presents relatively higher noise at long time delays, which is interpreted as the consequence of the final magnetization state becoming extremely sensitive to small fluctuations in the pump intensity when the fluence approaches the critical fluence F_C. It is concluded from this figure that $F_C \approx 0.8 mJ/cm^2$, which is consistent with the single-shot technique for measuring critical fluences (Figure 3.7).

It was shown in Section 3.3 that longer laser pulses, with pulsewidth up to Δt = 15 ps, can trigger single-shot HI-AOS in $Gd_{27}FeCo$. The surprising result that the critical pump fluence for switching increased by only by 50% even as the Δt increased by more than two orders of magnitude brings into question the validity of previous models for HI-AOS, which postulate that high peak electron temperatures are crucial for HI-AOS. Moreover, this result is of technological interest, as it indicates that Joule heating by intense electrical pulses with pulsewidth less than 15 ps can potentially also trigger HI-AOS in this sample, since the phenomenon is known to be triggered by ultrafast heating. It is therefore imperative to know whether the switching speed of $Gd_{27}FeCo$ is still in the ultrafast regime when it is triggered by the long ps optical pulses.

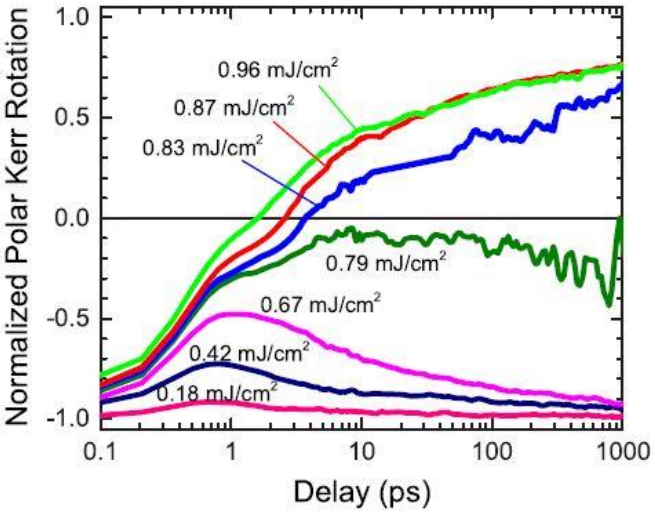

Figure 3.10 Magnetization dynamics of $Gd_{24}FeCo$ for different pump fluences.
The solid lines represent the evolution of the magnetization of $Gd_{24}FeCo$ after a Δt = 55 fs linearly polarized pump pulse, at room temperature. The switching threshold is determined to be close to 0.8mJ/cm^2 (green curve) because of the large noise at longer timescales, agreeing with the single-shot experiments (see Figure 3.7 (a)) (Figure from Ref [19]).

Time-resolved pump-probe experiments are performed on $Gd_{27}FeCo$ at various pump pulse durations in order to see how the switching dynamics are affected by the heating rate of the electronic system. The results of these experiments are shown in Figure 3.11. As a consequence of stretching the pulsewidth at the output of the RegA compressor, the probe pulse duration is also equal to that of the pump, which results in a loss of time resolution and smoothing of the data for longer pulse durations. For longer pulse durations, the HI-AOS fluence window between the critical switching fluence F_C and the multidomain formation threshold fluence F_{MD} reduces, as shown in Figure 3.7 (b), leading to a smaller switched area at the sample. Therefore, the probe is tightly focused through a 50× objective onto a ~2 μm spot at the center of the pump spot for these experiments. A constant ~200 Oe magnetic field is applied to reset the magnetic state of the film between pulses. The pump-probe overlap time $t_0 = 0$ is assumed to be the time at which the temporal peaks of the pump (shown as the gray Gaussean in Figure 3.11) and probe pulses are perfectly overlapped. This is calculated to be the time at which the demagnetization rate $|dM/dt|$ in the switching curves is maximum. As the pump duration increases from Δt = 55 fs to Δt = 10 ps, the switching time (crossing of 0 on the y axis) increases from ~2 ps up to ~13 ps. The switching happens in all cases after all of the energy of the optical pulse is completely deposited in the film. These results show that even with a 10 ps optical pulse trigger, HI-AOS still occurs in a rather ultrafast manner. This releases the constraint on using femtosecond lasers for the study of AOS and for applications.

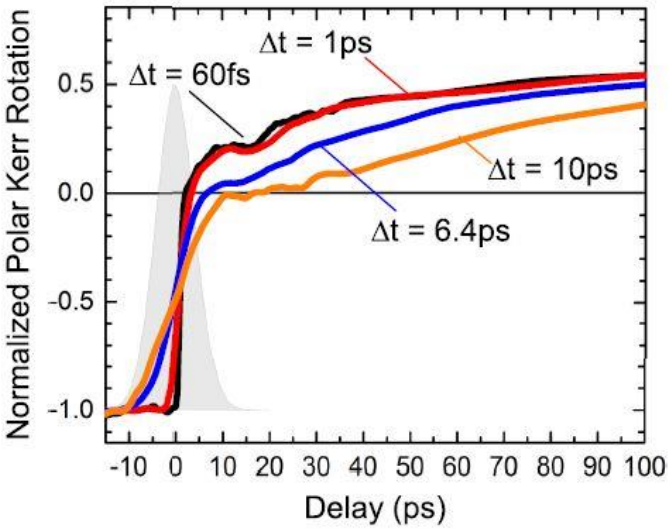

Figure 3.11 Magnetization dynamics of $Gd_{27}FeCo$ for different pump pulse durations. The solid represent the evolution of the magnetization of $Gd_{27}FeCo$ after a linearly polarized pump pulse, at room temperature, for durations Δt = 60 fs, 1 ps, 6.4 ps, 10 ps, at their critical fluences F_C ~0.8, 0.9, 1.0, and 1.6mJ/cm^2, respectively. A 10 ps pump intensity profile is depicted in light grey. The probe duration was kept equal to the pump duration, which results in a loss of resolution and a smoothing of the long pulse duration curves. The switching time (crossing of 0) increases with the pump duration, and always happens after all the energy has been deposited on the film. Zero time delay was set by assuming that the maximum slope of the demagnetization corresponds to the peak of the pump pulse (Figure from Ref [19]).

3.6 Electron and phonon temperatures during HI-AOS with ps pulses

Previous sections of this chapter have shown that ultrafast switching due to HI-AOS occurs in the $Gd_{27}FeCo$ sample with laser pulses as long as 15 ps. An estimate of the peak electron and phonon temperatures following excitation with these long laser pulses is needed to verify that peak T_e of > 1000 K is not essential to trigger HI-AOS in GdFeCo.

The temperature response of the electron, phonon and spin baths of the GdFeCo is calculated using a version of the using the three temperature model[2, 14] (first introduced in Section 1.6) modified to include heat diffusion between the GdFeCo and the substrate. Two layers are assumed: one effective layer of Ta/GdFeCo/Ta with weighted thermal parameters and one of SiO_2. Both layers are assumed to be coupled through an electron conductance of ~200×10^6 Wm^{-2}K^{-1}, which is typical value for sputtered metals on dielectrics[34]. Within the simulation time (~1 ns) no heat reaches the bottom of the SiO_2. Equation (3.6) encapsulates the three equations used in this model.

$$(3.6)\ C_e\frac{dT_e}{dt} = g_{ep}(T_p - T_e) + g_{es}(T_s - T_e) + \Lambda_e\frac{d^2T_e}{dt^2} + P(t,z)$$

$$C_p\frac{dT_p}{dt} = g_{ep}(T_e - T_p) + g_{ps}(T_s - T_p) + \Lambda_p\frac{d^2T_p}{dt^2}$$

$$C_s \frac{dT_s}{dt} = g_{es}(T_e - T_s) + g_{ps}(T_p - T_s) + \Lambda_s \frac{d^2 T_s}{dt^2}$$

Here T_i, C_i and Λ_i are the temperature, heat capacity and heat diffusion coefficient, respectively, of the bath i (i = e, p and s for electrons, phonons and spins respectively), and g_{ij} is the coupling constant between baths i and j. $P(t,z)$ is the absorbed power from the laser, accounting for the absorption profile calculated through a multilayer reflectivity calculation and the temporal Gaussian profile of FWHM Δt.

The electron heat capacity is fixed as $C_e = \gamma T_e$, with $\gamma = 167 \times 10^6$ $Jm^{-3}K^{-2}$ based on first-principles band structure calculations of amorphous $GdFe_2$[35]. The lattice heat capacity C_p is set to 2.3×10^6 $Jm^{-3}K^{-1}$, a weighted average of the lattice heat capacity of Ta and $GdFe_2$[29]. The spin heat capacity C_s in this model as a function of temperature was fixed by subtracting the electronic and lattice heat capacities from the total heat capacity of $GdFe_2$[35]. The electron-spin coupling constant g_{es} is fixed at 10^{17} $Wm^{-3}K^{-1}$and the electron-phonon coupling constant g_{ep} is set to 6×10^{17} $Wm^{-3}K^{-1}$. These two values are set based on thermal transport measurements of Au/GdFeCo metallic bilayers[36].

The spin temperature in this three temperature model calculation is not considered to be a valid descriptor of the thermodynamic state of the spin system. The transient magnetic states that occur following laser irradiation, especially the transient ferromagnetic state where the Gd and FeCo sublattices are parallelly aligned, do not occur in the equilibrium phase diagram of GdFeCo and therefore cannot be described with an effective spin temperature. The sole purpose of the spin temperature in the model is to account for the impact of energy transfer between the electrons and magnetic sublattices on the transient temperature response of the electrons. This channel for energy exchange needs to be considered especially when the system is close to T_C where the magnetic heat capacity C_s can be as large as ~40% of the total heat capacity.

The small increase in F_C as Δt increases implies that the peak electron temperature of the system is not particularly important for HI-AOS. The transient temperature response of the electrons and phonons during HI-AOS with Δt = 55 fs, Δt = 1 ps, and Δt = 12.5 ps pulses at fluences equal to their corresponding critical fluence F_C calculated from the three temperature model are shown in Figure 3.12. As shown in this figure, for Δt = 12.5 ps pulses, T_e will only be heated to ~530 K. Given the ~20% uncertainty of the measured critical fluence, it is not possible to exactly determine whether the peak T_e reaches T_C or not. Despite this open question, this result raises questions on the proposed scenario where very high electron temperatures (1000–2000 K) are necessary for HI-AOS[3, 4, 16, 17].

Given these surprising results, it can be hypothesized that helicity-independent switching is a three-step process where there is no need for high electron temperatures. First, after optical absorption, the energy per Fe spin degree of freedom becomes slightly higher than the energy per Gd spin degree of freedom, as proposed by Wienholdt *et al.*[37]. This leads to Fe becoming hotter and demagnetizing faster. In the second step, the Fe and Gd spins exchange energy and angular momentum on a time scale faster than the time scale of angular momentum dissipation into the lattice. This corresponds to a semiadiabatic process and the dynamics of the system are thus governed by the principle of maximization of entropy as described by the following equation (3.7).

$$(3.7)\ (2J_{FF}S_F - 2J_{FF}S_G + J_{FG}S_F - J_{GG}S_G)dS_F > 0$$

The left side of the equation corresponds to the change in internal energy of the system. J is the exchange constant and S is the total spin angular momentum of sublattices FeCo (F) or Gd (G). In GdFeCo, J_{FF} and J_{GG} are negative, J_{FG} is positive, so that S_F and S_G have initially opposite signs. Conservation of angular momentum ($dSF = -dSG$) is implied.

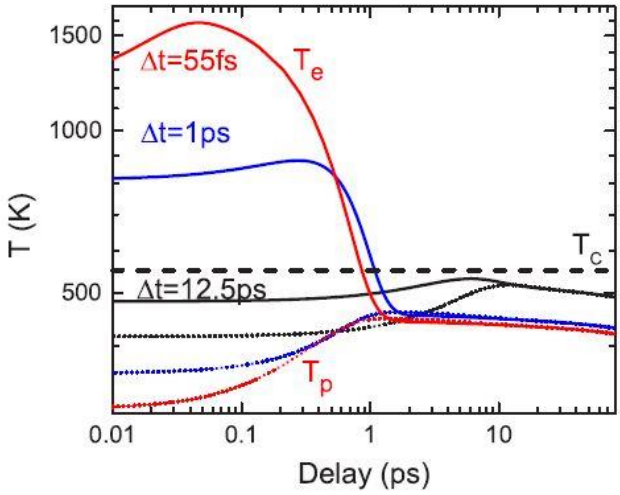

Figure 3.12 Transient electron and lattice temperatures of GdFeCo for different for different pump pulse durations.
Calculated electronic (solid lines) and lattice (dotted lines) temperatures of $Gd_{27}FeCo$ after a Δt = 55 fs pulse at F_C = 0.8 mJ/cm^2 (red), a Δt = 1 ps pulse at F_C = 0.9 mJ/cm^2 (blue), and a Δt = 12.5 ps pulse at F_C = 1.35 mJ/cm^2 (black) according to the three-temperature model. The dashed line indicates T_C. For Δt = 12.5 pulses, T_e gets very close to T_C. Whether T_e needs to reach T_C or not is unclear due to the uncertainties (~20%) of the critical fluences F_C (Figure from Ref [19]).

To fulfill equation (3.7), $|S_F|$ and $|S_G|$ must initially decrease, meaning demagnetization of the sublattices will occur. As the Fe sublattice is initially hotter, the Fe will reach full demagnetization first. With the Fe fully demagnetized (S_F = 0) equation (3.7) implies the switch and growth of the Fe sublattice parallel to the Gd spins, leading to a transient equilibrium ferromagnetic state[37]. In other words, on time scales over which angular momentum is conserved, the temporary equilibrium state will be ferromagnetic because entropy is maximized with ferromagnetically aligned Gd and Fe spins.

In the third and final step, as the system starts to cool down, the equilibrium exchange coupling forces the Gd to switch in order to be antiferromagnetically aligned with the now dominating Fe lattice[3] and both sublattices remagnetize as they cool down. Remagnetization occurs on much longer time scales than demagnetization, so spin angular momentum is not conserved anymore.

In the proposed three-step scenario, the magnetization can switch sign without the electron temperature T_e ever needing to reach the Curie temperature T_C. There are two requirements: (i) the Fe spin system must be preferentially heated with respect to the Gd spins[37] and (ii) the exchange of energy between sublattices should happen faster than the time scales of dissipation of angular momentum into the lattice[38]. Moreover, the lattice temperature should remain below T_C at all times, as it will otherwise obviously result in a multidomain final state. As shown in Figure 3.7 (b) the total energy necessary for HI-AOS is not strongly dependent on the pulse duration, indicating that it is crucial to

deposit a minimum amount of energy (the critical fluence), rather than a minimum peak T_e, on the sample in order to drive sufficient energy and angular momentum transfer between sublattices. The difference in maximum pulse duration that can trigger HI-AOS between samples $Gd_{24}FeCo$ and $Gd_{27}FeCo$ shown in Figure 3.7 (b) resides most probably in the differences in energy transfer rates between the Fe and Gd spin sublattices, which depend on the composition[16].

3.7 Conclusions: towards ultrafast switching with electrical pulses

The work presented in this chapter conclusively show that ultrafast HI-AOS can be triggered in GdFeCo even by relatively long ps pulses. The minimum energy required for switching increases only by ~50% as the pump pulse duration is increased over two orders of magnitude. Surprisingly, even for a long 10 ps pump pulse, the $Gd_{27}FeCo$ sample switches in a relatively ultrafast manner, within 13 ps of the excitation. These surprising results bring into doubt previously proposed models for HI-AOS, which require that the electron temperatures T_e rapidly increase to ~1000-2000 K in the first few hundred femtoseconds irradiation in order for the Langevin noise to overcome the strong exchange coupling between the Gd and FeCo sublattices, thereby enabling them to have a transient ferromagnetic state. The requirement of these models on the excitation being ultrashort (sub-ps) is disproved by the ps pulse results discussed in this chapter. An alternate hypothesis for HI-AOS based on the conservation of angular momentum at short time scales, driven by the semi-adiabatic exchange of spins between the two sublattices in a manner that maximizes entropy, has been proposed.

More interestingly, these results offer the tantalizing prospect of triggering similar HI-AOS processes in a GdFeCo ferrimagnet by electrical pulses rather than by optical pulses. The fact that GdFeCo switches in an ultrafast manner when heated by 15 ps optical pulses offers evidence that heating this material with any impulse in that timescale will lead to ultrafast HI-AOS. Joule heating by intense electrical pulses with durations less than 15 ps should therefore also trigger switching in GdFeCo. CMOS technology capable of supplying intense electrical pulses with ps pulsewidths exists since the late 2000's and offers the potential of integrating an ultrafast magnetic bit on-chip without the need for large, bulky femtosecond laser systems. Experimental work done to develop an Auston-switch and transmission line based prototype to generate large amplitude ps electrical current pulses, and to demonstrate ultrafast magnetization switching in GdFeCo and other magnetic materials will be discussed in Chapter 6 and Chapter 7.

3.8 References

1. Garello, K., Avci, C. O., Miron, I. M., Baumgartner, M., Ghosh, A., Auffret, S., Boulle, O., Gaudin, G. & Gambardella, P. Ultrafast magnetization switching by spin-orbit torques. *Appl. Phys. Lett.* **105,** 212402 (2014). https://doi.org/10.1063/1.4902443
2. Beaurepaire, E., Merle, J.-C., Daunois, A. & Bigot, J.-Y. Ultrafast Spin Dynamics in Ferromagnetic Nickel. *Phys. Rev. Lett.* **76,** 4250–4253 (1996). https://doi.org/10.1103/PhysRevLett.76.4250
3. Radu, I., Vahaplar, K., Stamm, C., Kachel, T., Pontius, N., Dürr, H. A., Ostler, T. A., Barker, J., Evans, R. F. L., Chantrell, R. W., Tsukamoto, A., Itoh, A., Kirilyuk, A., Rasing, Th. & Kimel, A. V. Transient ferromagnetic-like state mediating ultrafast reversal of antiferromagnetically coupled spins. *Nature* **472,** 205–208 (2011). https://doi.org/10.1038/nature09901
4. Ostler, T. A., Barker, J., Evans, R. F. L., Chantrell, R. W., Atxitia, U., Chubykalo-Fesenko, O., El Moussaoui, S., Le Guyader, L., Mengotti, E., Heyderman, L. J., Nolting, F., Tsukamoto, A., Itoh,

A., Afanasiev, D., Ivanov, B. A., Kalashnikova, A. M., Vahaplar, K., Mentink, J., Kirilyuk, A., Rasing, Th. & Kimel, A. V. Ultrafast heating as a sufficient stimulus for magnetization reversal in a ferrimagnet. *Nat Commun* **3,** 666 (2012). https://doi.org/10.1038/ncomms1666

5. Bhatti, S., Sbiaa, R., Hirohata, A., Ohno, H., Fukami, S. & Piramanayagam, S. N. Spintronics based random access memory: a review. *Materials Today* **20,** 530–548 (2017). https://doi.org/10.1016/j.mattod.2017.07.007
6. Lee, O. J., Ralph, D. C. & Buhrman, R. A. Spin-torque-driven ballistic precessional switching with 50 ps impulses. *Appl. Phys. Lett.* **99,** 102507 (2011). https://doi.org/10.1063/1.3635782
7. Rowlands, G. E., Rahman, T., Katine, J. A., Langer, J., Lyle, A., Zhao, H., Alzate, J. G., Kovalev, A. A., Tserkovnyak, Y., Zeng, Z. M., Jiang, H. W., Galatsis, K., Huai, Y. M., Amiri, P. K., Wang, K. L., Krivorotov, I. N. & Wang, J.-P. Deep subnanosecond spin torque switching in magnetic tunnel junctions with combined in-plane and perpendicular polarizers. *Appl. Phys. Lett.* **98,** 102509 (2011). https://doi.org/10.1063/1.3565162
8. Guidoni, L., Beaurepaire, E. & Bigot, J.-Y. Magneto-optics in the Ultrafast Regime: Thermalization of Spin Populations in Ferromagnetic Films. *Phys. Rev. Lett.* **89,** 017401 (2002). https://doi.org/10.1103/PhysRevLett.89.017401
9. Mueller, B. Y. & Rethfeld, B. Relaxation dynamics in laser-excited metals under nonequilibrium conditions. *Phys. Rev. B* **87,** 035139 (2013). https://doi.org/10.1103/PhysRevB.87.035139
10. Battiato, M., Carva, K. & Oppeneer, P. M. Superdiffusive Spin Transport as a Mechanism of Ultrafast Demagnetization. *Phys. Rev. Lett.* **105,** 027203 (2010). https://doi.org/10.1103/PhysRevLett.105.027203
11. Thiele, J.-U., Coffey, K. R., Toney, M. F., Hedstrom, J. A. & Kellock, A. J. Temperature dependent magnetic properties of highly chemically ordered Fe[sub 55−x]Ni[sub x]Pt[sub 45]L1[sub 0] films. *J. Appl. Phys.* **91,** 6595 (2002). https://doi.org/10.1063/1.1470254
12. Stanciu, C. D., Kimel, A. V., Hansteen, F., Tsukamoto, A., Itoh, A., Kirilyuk, A. & Rasing, Th. Ultrafast spin dynamics across compensation points in ferrimagnetic GdFeCo : The role of angular momentum compensation. *Phys. Rev. B* **73,** 220402 (2006). https://doi.org/10.1103/PhysRevB.73.220402
13. Khorsand, A. R., Savoini, M., Kirilyuk, A., Kimel, A. V., Tsukamoto, A., Itoh, A. & Rasing, Th. Role of Magnetic Circular Dichroism in All-Optical Magnetic Recording. *Phys. Rev. Lett.* **108,** 127205 (2012). https://doi.org/10.1103/PhysRevLett.108.127205
14. Kimling, J., Kimling, J., Wilson, R. B., Hebler, B., Albrecht, M. & Cahill, D. G. Ultrafast demagnetization of FePt:Cu thin films and the role of magnetic heat capacity. *Phys. Rev. B* **90,** 224408 (2014). https://doi.org/10.1103/PhysRevB.90.224408
15. Schellekens, A. J. & Koopmans, B. Microscopic model for ultrafast magnetization dynamics of multisublattice magnets. *Phys. Rev. B* **87,** 020407 (2013). https://doi.org/10.1103/PhysRevB.87.020407
16. Barker, J., Atxitia, U., Ostler, T. A., Hovorka, O., Chubykalo-Fesenko, O. & Chantrell, R. W. Two-magnon bound state causes ultrafast thermally induced magnetisation switching. *Sci Rep* **3,** 3262 (2013). https://doi.org/10.1038/srep03262
17. Atxitia, U., Ostler, T. A., Chantrell, R. W. & Chubykalo-Fesenko, O. Optimal electron, phonon, and magnetic characteristics for low energy thermally induced magnetization switching. *Appl. Phys. Lett.* **107,** 192402 (2015). https://doi.org/10.1063/1.4935416
18. Bonn, M., Denzler, D. N., Funk, S., Wolf, M., Wellershoff, S.-S. & Hohlfeld, J. Ultrafast electron dynamics at metal surfaces: Competition between electron-phonon coupling and hot-electron transport. *Phys. Rev. B* **61,** 1101–1105 (2000). https://doi.org/10.1103/PhysRevB.61.1101

19. Gorchon, J., Wilson, R. B., Yang, Y., Pattabi, A., Chen, J. Y., He, L., Wang, J. P., Li, M. & Bokor, J. Role of electron and phonon temperatures in the helicity-independent all-optical switching of GdFeCo. *Phys. Rev. B* **94,** 184406 (2016). https://doi.org/10.1103/PhysRevB.94.184406
20. Mentink, J. H., Hellsvik, J., Afanasiev, D. V., Ivanov, B. A., Kirilyuk, A., Kimel, A. V., Eriksson, O., Katsnelson, M. I. & Rasing, Th. Ultrafast Spin Dynamics in Multisublattice Magnets. *Phys. Rev. Lett.* **108,** 057202 (2012). https://doi.org/10.1103/PhysRevLett.108.057202
21. Florczak, J. M. & Dahlberg, E. D. Detecting two magnetization components by the magneto-optical Kerr effect. *Journal of Applied Physics* **67,** 7520–7525 (1990). https://doi.org/10.1063/1.345813
22. Qiu, Z. Q. & Bader, S. D. Surface magneto-optic Kerr effect. 14
23. Piper, J. D. A. DUNLOP, D. J. & ÖZDEMIR, Ö. 1997. Rock Magnetism. Fundamentals and Frontiers. Cambridge Studies in Magnetism Series. xxi + 573 pp. Cambridge, New York, Port Chester, Melbourne, Sydney: Cambridge University Press. Price £80.00, US $125.00 (hard covers). ISBN 0 521 32514 5. *Geological Magazine* **135,** 287–300 (1998). https://doi.org/10.1017/S0016756898218437
24. Kirilyuk, A., Kimel, A. V. & Rasing, T. Ultrafast optical manipulation of magnetic order. *Rev. Mod. Phys.* **82,** 2731–2784 (2010). https://doi.org/10.1103/RevModPhys.82.2731
25. Pessot, M., Maine, P. & Mourou, G. 1000 times expansion/compression of optical pulses for chirped pulse amplification. *Optics Communications* **62,** 419–421 (1987). https://doi.org/10.1016/0030-4018(87)90011-3
26. Magnes, J., Odera, D., Hartke, J., Fountain, M., Florence, L. & Davis, V. Quantitative and Qualitative Study of Gaussian Beam Visualization Techniques. *arXiv:physics/0605102* (2006). at <http://arxiv.org/abs/physics/0605102>
27. Hecht, E. *Optics*. (Pearson Education, Inc, 2017).
28. Wolfe, R., Malozemoff, A. P. & Slonczewski, J. C. *Applied solid state science: advances in materials and device research*. (Academic Press, 1979). at <http://www.vlebooks.com/vleweb/product/openreader?id=none&isbn=9781483214764>
29. Hellman, F., Abarra, E. N., Shapiro, A. L. & van Dover, R. B. Specific heat of amorphous rare-earth–transition-metal films. *Phys. Rev. B* **58,** 5672–5683 (1998). https://doi.org/10.1103/PhysRevB.58.5672
30. Steil, D., Alebrand, S., Hassdenteufel, A., Cinchetti, M. & Aeschlimann, M. All-optical magnetization recording by tailoring optical excitation parameters. *Phys. Rev. B* **84,** 224408 (2011). https://doi.org/10.1103/PhysRevB.84.224408
31. Vahaplar, K., Kalashnikova, A. M., Kimel, A. V., Gerlach, S., Hinzke, D., Nowak, U., Chantrell, R., Tsukamoto, A., Itoh, A., Kirilyuk, A. & Rasing, Th. All-optical magnetization reversal by circularly polarized laser pulses: Experiment and multiscale modeling. *Phys. Rev. B* **85,** 104402 (2012). https://doi.org/10.1103/PhysRevB.85.104402
32. Zhang, G. P., Hübner, W., Lefkidis, G., Bai, Y. & George, T. F. Paradigm of the time-resolved magneto-optical Kerr effect for femtosecond magnetism. *Nature Phys* **5,** 499–502 (2009). https://doi.org/10.1038/nphys1315
33. Stanciu, C. D., Tsukamoto, A., Kimel, A. V., Hansteen, F., Kirilyuk, A., Itoh, A. & Rasing, Th. Subpicosecond Magnetization Reversal across Ferrimagnetic Compensation Points. *Phys. Rev. Lett.* **99,** 217204 (2007). https://doi.org/10.1103/PhysRevLett.99.217204
34. Wilson, R. B. & Cahill, D. G. Experimental Validation of the Interfacial Form of the Wiedemann-Franz Law. *Phys. Rev. Lett.* **108,** 255901 (2012). https://doi.org/10.1103/PhysRevLett.108.255901

35. Tanaka, H., Takayama, S. & Fujiwara, T. Electronic-structure calculations for amorphous and crystalline Gd 33 Fe 67 alloys. *Phys. Rev. B* **46,** 7390–7394 (1992). https://doi.org/10.1103/PhysRevB.46.7390
36. Wilson, R. B., Lambert, C.-H., Gorchon, J., Yang, Y., Salahuddin, S. & Bokor, J. Electron-phonon interaction during optically induced ultrafast magnetization dynamics of Au/GdFeCo bilayers. *arXiv:1609.00648 [cond-mat]* (2016). at <http://arxiv.org/abs/1609.00648>
37. Wienholdt, S., Hinzke, D., Carva, K., Oppeneer, P. M. & Nowak, U. Orbital-resolved spin model for thermal magnetization switching in rare-earth-based ferrimagnets. *Phys. Rev. B* **5** (2013).
38. Chimata, R., Isaeva, L., Kádas, K., Bergman, A., Sanyal, B., Mentink, J. H., Katsnelson, M. I., Rasing, T., Kirilyuk, A., Kimel, A., Eriksson, O. & Pereiro, M. All-thermal switching of amorphous Gd-Fe alloys: Analysis of structural properties and magnetization dynamics. *Phys. Rev. B* **92,** 094411 (2015). https://doi.org/10.1103/PhysRevB.92.094411

Chapter 4. Helicity-independent All-Optical Switching in GdTbCo alloys

The last chapter elaborated on results on extending the helicity-independent all-optical switching (HI-AOS) of ferrimagnetic GdFeCo alloys up to ~15 ps laser pulse widths. It was shown that the $Gd_{27.5}(Fe_{90}Co_{10})_{62.5}$ sample exhibits HI-AOS of its magnetization in an ultrafast manner within 15 ps of excitation when irradiated with a 10 ps optical pulse. This brought into question previous models of HI-AOS which relied on the requirement of high electron temperatures of 1000-2000 K, which are attainable only with sub-ps excitations. A more thorough understanding of the HI-AOS mechanism is required so that the phenomenon and relevant materials can be better exploited for application in high-speed spintronic devices.

4.1 All-optical switching experiments in Tb-based ferrimagnets

Ever since the report of discovery of ultrafast toggle switching of magnetization in GdFeCo by single laser pulses[1, 2], considerable scientific effort has been poured into triggering magnetization reversal in different magnetic materials using just optical excitations in the absence of a magnetic field. HI-AOS has thus far been observed primarily in the ferrimagnetic alloys GdFeCo[1, 2, 3], GdFe[4], and GdCo[5]. The HI-AOS capabilities of ferrimagnetic GdFeCo have also been extended to a ferromagnetic Co/Pt film grown on top of the ferrimagnet by the exchange coupling, a result that will be discussed in detail in Chapter 5. Lalieu et. al.[6, 7] demonstrated HI-AOS on ferrimagnetic bilayers of Pt/Gd/Co, proving that the ultrafast toggle switching can occur in ferrimagnetic systems that are not alloys.

A second form of all-optical switching of magnetization called the helicity-dependent all-optical switching (HD-AOS), wherein the final switched state of the magnet is set by the helicity (left- or right-circular polarization) of the exciting laser beams, was discovered in Nancy by Lambert et al[8] and Mangin et al[9] in 2014. In these HD-AOS experiments, the magnetic state of the excited thin film relaxes to a randomly demagnetized state if the optical excitations are linearly (or randomly) polarized. Right- and left-circularly polarized optical pulses tend to change the magnetization to opposite final states that are independent of the initial state of the magnet, unlike the toggle switching of HI-AOS where the final state is always the opposite of the initial state. Moreover, it is known that this phenomenon needs multiple (upto hundreds) laser pulses to completely switch the magnetization from one direction to another. Mangin et al[9] demonstrated HD-AOS in a series of samples, including thin films of ferrimagnetic rare earth-transition metal (RE-TM) alloys, multilayers and heterostructures, as well as rare earth-free Co-Ir-based synthetic ferrimagnets. More surprisingly, HD-AOS was exhibited even by ferromagnetic thin films, such as Co/Pt multilayers[8, 10, 11], CoNi/Pd[8] multilayers and FePtAgC[8] granular films. It has been argued that the HD-AOS could arise from two different mechanisms: the inverse Faraday effect[12] or the magnetic circular dichroism[13]. The inverse Faraday effect corresponds to the generation of an effective magnetic field in a material induced by the helicity of light. This magnetic field can cumulatively switch the material along its direction. Reversing the helicity of light reverses the induced magnetic field and thus the switched magnetization direction. The magnetic circular dichroism (MCD) model of HD-AOS explains the magnetization reversal as effect of preferential absorption of light of a particular helicity by spins of a particular orientation (owing to MCD), leading to the cumulative flipping of these spins as more laser pulses are

applied. Nevertheless, the HD-AOS mechanism is known to be different from that of HI-AOS, which occurs because of heating in short ps and sub-ps timescales irrespective of the angular momentum of the excitation. HD-AOS on the other hand needs multiple laser pulses of a certain helicity which makes the overall process quite slow, with timescales of the order of microseconds or longer[10]. This thesis therefore deals primarily with the HI-AOS, and not HD-AOS. Unless otherwise mentioned, the term AOS in this thesis will refer to HI-AOS.

Despite the technological and scientific significance of ultrafast switching of magnetization through the HI-AOS, the phenomenon thus far has predominantly only been reported in Gd-based ferrimagnetic RE-TM alloys and multilayers. Tb ($Z = 65$) is a rare earth element that differs from Gd ($Z = 64$) only by one additional electron in its 4f shell. However, Tb based ferrimagnetic RE-TM systems – at the time of the work outlined in this chapter – exhibited only the slower HD-AOS process. Indeed, HD-AOS was demonstrated in a variety of Tb-based systems such as TbCo alloys[9, 14, 15], TbFe alloys[16] and Tb/Co multilayers and heterostructures[9]. Time-resolved pump-probe experiments by Allebrand et al[17] showed that some TbCo alloys show transient reversal of magnetization, wherein their magnetism reverses for a short period of a few ps following a short laser pulse excitation, after which the magnetization reverts to its original direction. Single-shot AOS was demonstrated in TbFeCo alloys[18], but it required patterning of nanoscale antennas to enhance the optical field, thereby confining the switched region to less than 100 nm in areas near and around the antennas. The switching was strongly influenced by inhomogeneities and control of the uniformity in the switched area under the laser pulse fluence profile could not be achieved. Moreover, the switching speed of TbFeCo was not reported in this work. More recently, HI-AOS was demonstrated in Tb/Co bilayers[19] but switching was observed only for a narrow range of concentrations and laser fluences.

Based on atomistic simulations, Moreno et al[20] argued that ferrimagnetic Tb_xCo_{1-x} alloys satisfy the necessary conditions for HI-AOS, including the presence of a transient ferromagnetic state. It was shown that for short laser pulse durations of ~50 fs, Tb_xCo_{1-x} alloys theoretically exhibit HI-AOS for a range of laser fluences and Tb concentrations. The need for large laser fluences in the simulations, potentially greater than the burning threshold of the samples, is described as a potential reason why experimental evidence of HI-AOS in TbCo alloys is scarce.

Unraveling the reasons for the relative ease of Gd-based RE-TM ferrimagnets in exhibiting HI-AOS as compared to Tb-based ones could help interpret the mechanism of HI-AOS. The major difference between Gd and Tb is the spin-orbit coupling of their 4f shells, whose electrons are the primary contributors to the net magnetization of rare earth atoms. Gd has a half-filled 4f shell ($4f^7$) which leads to its low orbital angular momentum $L = 0$. The 4f shell of Tb ($4f^8$) on the other hand has one completely filled orbital, which leads to a higher orbital angular momentum $L = 3$. Since the spin-orbit coupling of an electron in the 4f shell is $\sim \xi \boldsymbol{L}.\boldsymbol{S}$, where $\boldsymbol{S}$ is the spin angular momentum and ξ the spin-orbit coupling constant[21], Tb is known to have higher spin-orbit coupling than Gd[17]. This is observed physically as the higher anisotropy and damping of Tb compared to Gd[22, 23], as these parameters are intrinsically governed by the spin-orbit coupling[21].

In this chapter, I will introduce work done to disentangle the role of Gd in enabling HI-AOS through static and dynamic experiments performed on thin films of ferrimagnetic $Gd_{22-x}Tb_xCo_{78}$. Starting with pure GdCo, Gd atoms are incrementally replaced by Tb atoms to get samples with progressively larger Tb atomic percentage. The switching characteristics, such as the threshold fluence for switching and

the switching speed, are then studied as a function of the Tb concentration. The effect of anisotropy on HI-AOS is studied by annealing a GdTbCo sample and by using different capping and buffer layers. Atomistic spin dynamics simulations coupled with the two-temperature model are then performed to explain the experimental results, and provide insights into the mechanism of HI-AOS. These simulations, detailed in Section 4.6, show that the differential element-specific damping between the RE and TM sites plays a significant role in the HI-AOS of a ferrimagnetic RE-TM alloy, and indicate that engineering the damping of the system is crucial in uncovering more materials that exhibit HI-AOS.

4.2 Growth and characterization of $Gd_{22-x}Tb_xCo_{78}$ alloys

Amorphous, ferrimagnetic thin-films of Ta(3)/Pt(3)/$Gd_{22-x}Tb_xCo_{78}$(10)/Pt(3) (thicknesses are in nm) heterostructures are sputter deposited using a magnetron sputtering system (AJA International) onto substrates of Si(525mm)/SiO_2(50nm)/SiN_x(300 nm), at an Ar pressure of 1 mtorr, and a background base pressure of 6×10^{-8} torr. The substrates were mounted on a plate rotating at 15 rpm to ensure thickness and compositional uniformity. The GdTbCo films are co-deposited from separate Tb, Gd and Co targets with Pt or Ta over and underlayers grown in situ in the same chamber to ensure the purity of the interfaces. Layer thicknesses are monitored with a quartz mass balance during growth and then confirmed via X-Ray reflectivity analysis. Rutherford backscattering spectrometry is used to confirm the sample composition. All the samples present square hysteresis loops, indicating that they all have perpendicular magnetic anisotropy (PMA).

Energy dispersive spectroscopy images taken with a scanning transmission electron microscope found no evidence of inhomogeneities at the 10 nm scale as had been reported in previous work on GdFeCo[24]. Figure 4.1 shows the elemental mapping of a 15 nm thick $Gd_{10}Tb_{12}Co_{78}$ sample capped with 7nm of Ta taken on an FEI TitanX, operated at 200 kV in STEM mode with an approximate probe size of 3 nm diameter.

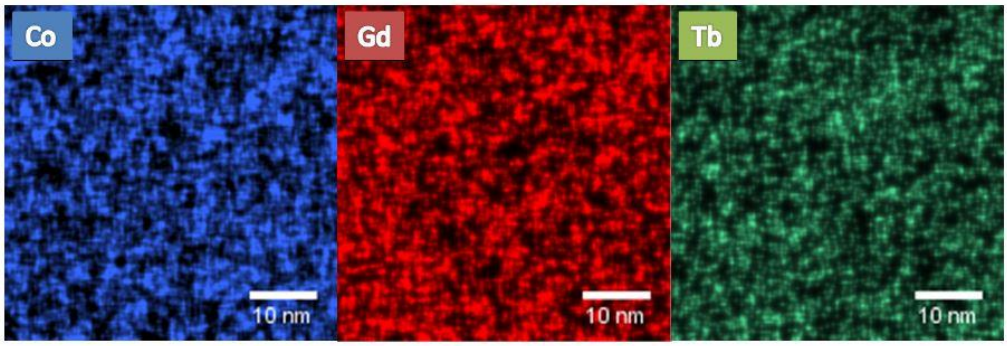

Figure 4.1 Scanning transmission electron microscopy images of GdTbCo.
Scanning TEM images of $Gd_{10}Tb_{12}Co_{78}$(15 nm)/Ta(7 nm) shows no evidence of large range inhomogeneities (Figure from Ref [25]).

The magnetization is then measured with a Quantum Design MPMS SQUID magnetometer as a function of field and temperature to measure the compensation temperature T_M. Room temperature saturation M_s (~100 emu/cm3) and T_M (~400 K) are fairly independent of x, due to the fixed 22 atomic percentage (at.%) RE content. The fairly similar T_M of different films is seen in the

magnetization vs temperature curves shown in Figure 4.2. At room temperature, the magnetization of all the films studied in the $Gd_{22-x}Tb_xCo_{78}$ series is RE dominant. A TM dominant $Gd_{19}Co_{81}$ sample with T_M lower than room temperature was also grown, but its HI-AOS behavior was not studied in detail. A vibrating sample magnetometer (LakeShore) found the Curie temperature of all the films in the $Gd_{22-x}Tb_xCo_{78}$ series to lie above 600 K. This lower limit is given because as the temperature increases the PMA decreases and is eliminated in the 620 - 670 K range[26] above which the films are irreversibly modified by the nucleation of crystallites.

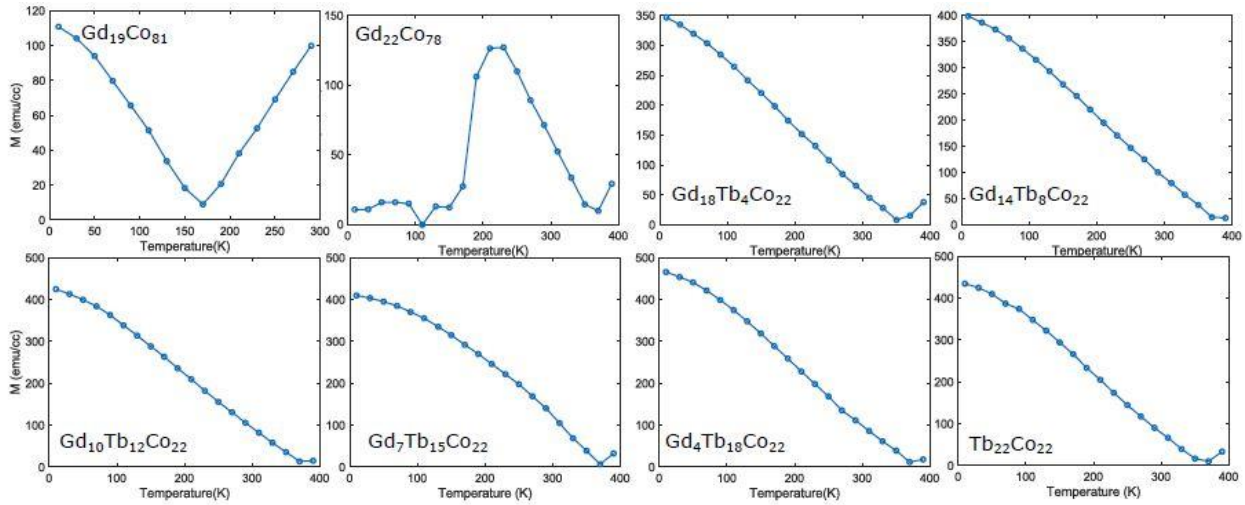

Figure 4.2 Magnetization vs temperature of the GdTbCo films.
Remanent magnetization as a function of temperature after saturating with an out of plane 5 T magnetic field, measured with a SQUID magnetometer. All films in the $Gd_{22-x}Tb_xCo_{78}$ series (all graphs except top left) exhibited a compensation temperature $T_M \sim 400$ K where their remanant magnetization drops to zero. A $Gd_{19}Co_{81}$ film (top left) with a below room temperature also exhibited HI-AOS but its magnetization dynamics were not studied. The $M(T)$ for a-$Gd_{22}Co_{78}$ falls near zero at low temperatures because the perpendicular anisotropy energy is overcome by the shape anisotropy energy $2\pi M_S^2$ (Figure from Ref [25]).

The intrinsic perpendicular magnetic anisotropy constant K_{ui}, (measured from the hard axis hysteresis loops as $K_{ui} = H_K M_S/2 + 2\pi M_S^2$ where is the H_K anisotropy field and M_S the saturation magnetization[21]), for different Gd(Tb)Co samples with different cap and buffer layers is shown in Figure 4.3. For the Ta(3)/Pt(3)/$Gd_{22-x}Tb_xCo_{78}$(10)/Pt(3) sample series, which is the focus of this chapter, K_{ui} increases with increasing Tb at.% x, from 4×10^5 erg/cm^3 for $Gd_{22}Co_{78}$ to 2×10^6 erg/cm^3 for $Tb_{22}Co_{78}$. This is attributed to the larger single ion anisotropy of Tb compared to Gd, owing to its larger orbital angular momentum ($L = 3$ for Tb, and $L = 0$ for Gd) of its 4f orbitals as mentioned in Section 4.1. The effect of growing on Ta or SiN buffer layer, and of capping with Ta or Pt are also shown in Figure 4.3; these over and under layers, particularly Pt, increase the magnetic anisotropy of these thin films, due to interfacial anisotropy effects of the high SOC Pt.

Since the origin of PMA in GdCo is an open question[27], a series of GdCo samples with different cap and buffer layers and Gd/Co concentrations are grown and studied. The K_{ui} of these samples are also included in Figure 4.3. With Pt buffer and cap layers, GdCo has PMA, while with Ta buffer and cap

layers, GdCo exhibits in-plane anisotropy. Moreover, GdCo grown under very clean conditions and without Pt over or underlayers are magnetized in-plane, while slightly worse background pressure or deliberate O introduction yields PMA. A TM rich $Gd_{19}Co_{81}$ film with T_M lower than room temperature, sandwiched by Pt buffer and cap layers, also exhibited PMA. These observations indicate that the PMA in GdCo films studied here arises from an interfacial contribution from heavy metal Pt layers, and also potentially from a slight gettering of residual oxygen in the chamber.

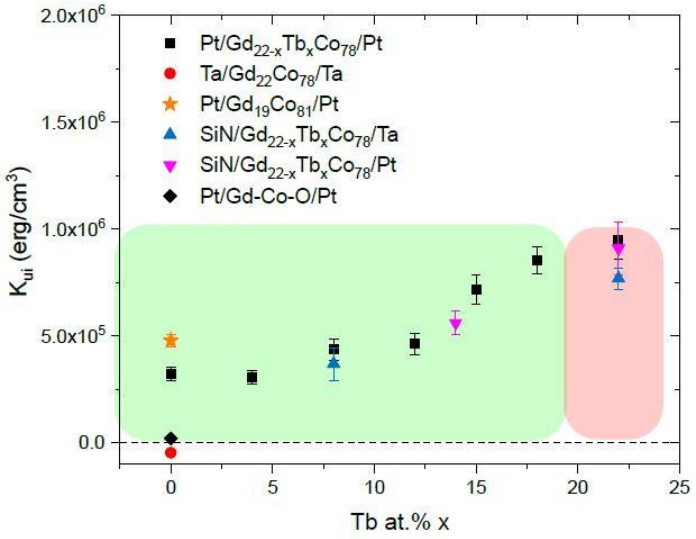

Figure 4.3 Effect of Tb at.% and capping and buffer layers on the perpendicular magnetic anisotropy of GdTbCo films.
The perpendicular magnetic anisotropy constant K_{ui} increases with the Tb at.% x for the $Gd_{22-x}Tb_xCo_{78}(10)$ samples for a given cap and buffer layer. The $Gd_{22}Co_{78}$ film with Ta cap and buffer layers did not exhibit PMA, indicated by its negative K_{ui}. The green and red boxes indicate samples which exhibit HI-AOS (to be discussed in Section 4.3) (Figure from Ref [25]).

4.3 Static studies of HI-AOS in $Gd_{22-x}Tb_xCo_{78}$ alloys

The ability of the samples to exhibit HI-AOS is first verified using the Magneto Optical Kerr Effect (MOKE) microscope setup described in Section 3.2. The magnetization of the samples is initialized at room temperature with an external out of plane magnetic field of ~ 0.7 T using a permanent magnet, fully saturating all samples. The field is then turned off, and the samples are irradiated with ~100 fs full-width half maximum (FWHM) 810 nm optical pulses from a regeneratively amplified Ti-Sapphire laser. The laser beam is p-polarized, and is focused to an elliptical spot with a FWHM of ~(110 × 80) μm^2, incident at an angle of 50° with respect to the sample normal.

MOKE microscope images used to verify single shot toggle switching in each of the films in $Ta(3)/Pt(3)/Gd_{22-x}Tb_xCo_{78}(10)/Pt(3)$ sample series are depicted in Figure 4.4. The first row of this figure indicates that pure $Gd_{22}Co_{78}$, with no added Tb, exhibits HI-AOS, as is expected from previous results. Surprisingly, the other rows of the figure show that HI-AOS is exhibited in all the samples, except the $Tb_{22}Co_{78}$ film without any Gd. Films with as much as 18 at.% Tb (and hence as little as 4 at.% Gd) have deterministic magnetization reversal upon irradiation with a single laser pulse. Moreover, above the critical fluence for switching F_C, the switched area of the film is comparable to

the laser beam spot-size, can be deterministically controlled by the spatial Gaussean profile of the laser pulse fluence, and is not random or small (~100 nm scale) as in the case with previous reports of AOS in TbFeCo[18]. Amorphous $Tb_{22}Co_{78}$ only shows demagnetization, evidenced by the nucleation of random magnetic domains, and this result is also consistent with the absence of HI-AOS reported in other experimental works mentioned in Section 4.1. It must also be noted that all the GdCo samples described in Section 4.2 that have PMA exhibit HI-AOS. The ability to exhibit HI-AOS is unaffected by the buffer layers being either Ta or SiN, and presents evidence that anisotropy K_{ui} alone is not the relevant driving parameter for HI-AOS. Several GdCo films of other RE/TM ratio are also tested, with varying saturation magnetization values M_S, including TM-dominant (low RE/TM ratio) $Gd_{19}Co_{81}$ with T_M below room temperature. These also exhibit HI-AOS, demonstrating that at least over a limited range of M_S, M_S is not a determining factor for the ability to show HI-AOS. The polar MOKE configuration of the MOKE microscope is unable to verify HI-AOS in the GdCo samples with in-plane magnetization. The rest of this chapter will focus on results on the samples in the Ta(3)/Pt(3)/$Gd_{22-x}Tb_xCo_{78}$(10)/Pt(3) series, and the films in this series with $x \neq 0$ and $x \neq 22$ will be simply referred to as GdTbCo.

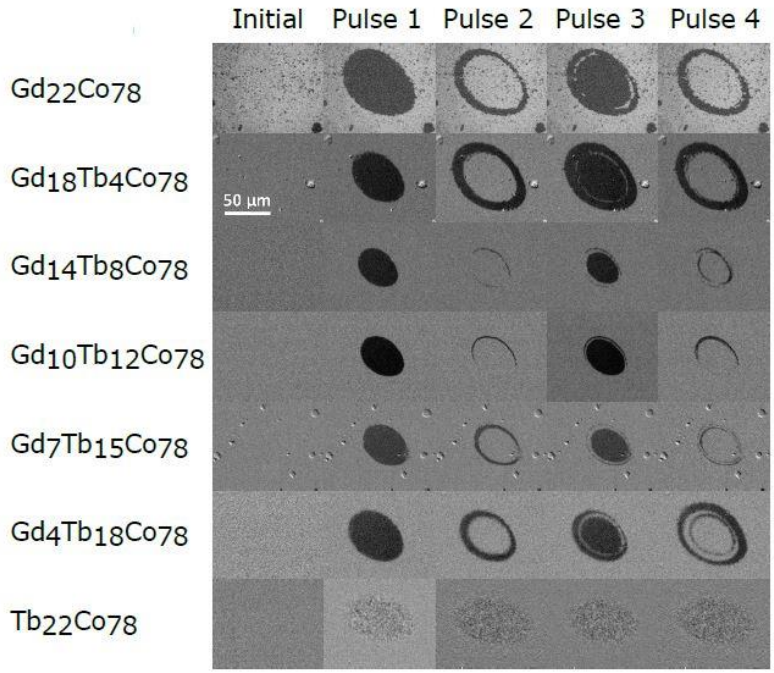

Figure 4.4 MOKE microscopy images of HI-AOS in GdTbCo films.
The toggling of magnetic contrast with each successive laser pulse indicates the ability to exhibit HI-AOS in films with Tb at.% x up to 18% (with just 4% Gd). The films are initialized with an external out-of-plane field of ~0.7 T. The magnetization of the TbCo film breaks up into small domains when irradiated a laser pulse, indicating demagnetization and no HI-AOS (Figure from Ref [25]).

The incident critical fluence for switching the GdTbCo films is measured as described in the previous chapter in Section 3.3. Ellipsometry measurements yield a complex refractive index of ~3.5 + 4.2i for all the Ta/Pt/Gd(Tb)Co/Pt stacks used in this study at the laser wavelength of 810 nm. Multilayer absorption calculations based on the matrix transfer method is used, as in Section 3.3, to calculate the absorption in each of these films. The refractive indices used for this calculation are tabulated in Table

4.1. The calculations result in 41% absorption in all of the films in this series. The resulting absorbed critical fluence F_C, as well as the incident critical fluence, are shown in Figure 4.5. The figure indicates that the F_C increases linearly with the Tb at.% x, from 1.8 mJ/cm^2 for $Gd_{22}Co_{78}$ to 2.5 mJ/cm^2 for $Gd_4Tb_{18}Co_{78}$, the last sample in the series that exhibits HI-AOS. The increasing critical fluence with increasing Tb at.% indicates that the addition of Tb makes it energetically less favorable for a sample to exhibit HI-AOS.

Layer	Thickness (nm)	Complex refractive index	Absorption by layer (%)
Air	-	1	-
Ta/Pt/ $Gd_{22-x}Tb_xCo_{78}$/Pt	19	3.5 + 4.2i	41
Si_3N_4	300	2.01	0
Si	-	3.696 + 0.0047i	-

Table 4.1 Multilayer absorption calculation parameters and results for the GdTbCo stacks.

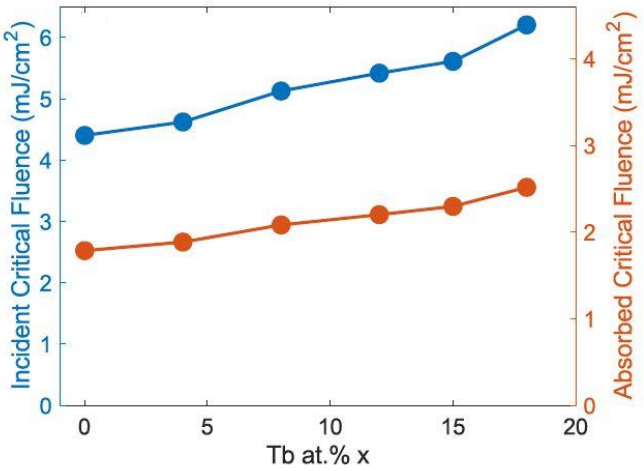

Figure 4.5 Dependence of critical switching fluence on Tb atomic percentage.
The incident critical fluence (orange) and calculated absorbed critical fluence (blue) of the $Gd_{22-x}Tb_xCo_{78}$ films increases as a function of the Tb atomic percentage x. Note the different scales for the blue and orange curves (Figure from Ref [25]).

4.4 Time dynamics of switching in $Gd_{22-x}Tb_xCo_{78}$ alloys

The pump-probe based time-resolved MOKE (TR-MOKE) technique described in detail in Section 3.4 is used to study the dynamics of magnetization of the GdTbCo films as they undergo HI-AOS or ultrafast demagnetization. A constant external out-of-plane field of ~0.7 T is applied to reset the magnetization of the film to its original direction between pump pulses. The characteristics of the pump beam are as described in Section 4.3. The probe beam is incident normal to the sample plane, focused through a 50× objective to focus to a spot (<15 μm) much smaller than the pump.

The magnetization dynamics for different laser fluences presented in Figure 4.6 show that at low absorbed pump fluences below F_C, the magnetization of the $Gd_{14}Tb_8Co_{78}$ film demagnetizes in ~2 ps, after which the external magnetic field ensures remagnetization along the original magnetization direction. At an absorbed fluence of 1.96 mJ/cm^2, the magnetization response at longer timescales is quite noisy, indicating that the final magnetization state is extremely sensitive to small fluctuations in the pump pulse intensity. Following the arguments of Section 3.5, it is concluded from this time-resolved measurement that the critical absorbed fluence $F_C \approx 1.96$ mJ/cm^2 for this sample. This value is in close agreement with the critical fluence measured from static MOKE microscopy measurements on the same sample (Figure 4.5 and Section 4.3). As the pump fluence is increased beyond F_C, the magnetization reverses to the opposite direction in ~2 ps, and recovers approximately 65% of its saturation magnetization in the reversed direction within 10 ps. It must be noted that the dynamics remain fairly similar for the fluences above F_C indicated in this figure. The low fluence (demagnetization) experiments are done with the normal laser repetition rate of 252 kHz. The switching experiments are performed at a lower repetition rate of 100 kHz, as the higher fluences can cause DC heating of the magnetic film at high repetition rates. This is evidenced by the pump-induced reduction of the magnetic signal at negative delays, since the magnetization of a sublattice decreases with temperature in accordance with Curie's law. As with the experiments in Section 3.5, the time-resolved experiments described here at 810 nm wavelength are sensitive only to the Co sublattice of the ferrimagnets.

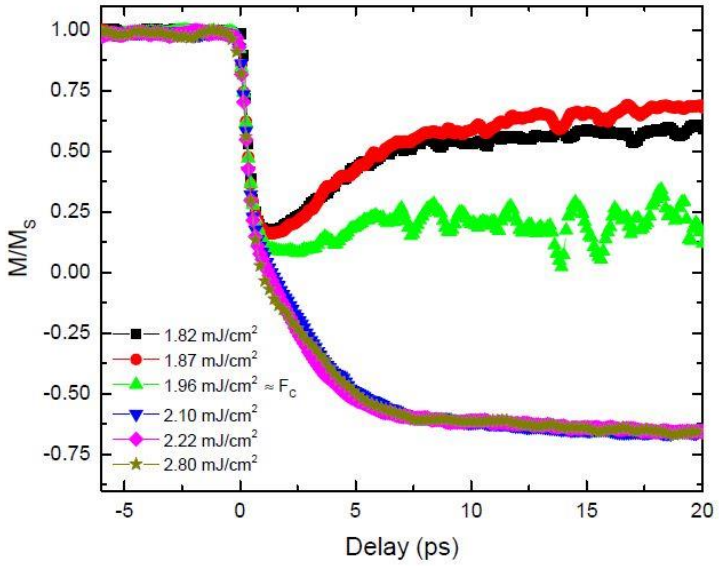

Figure 4.6 Effect of pump fluence on the magnetization dynamics of $Gd_{14}Tb_8Co_{78}$.
The different curves correspond to different absorbed pump fluences. Absorbed pump fluences less than 1.96 mJ/cm^2 lead to demagnetization (followed by remagnetization). The noisy trace at the long time delays for absorbed fluence of 1.96 mJ/cm^2 leads to the conclusion that the critical fluence for HI-AOS $F_C \approx 1.96$ mJ/cm^2, in agreement with static measurements of F_C. Increasing the fluence beyond F_C does not have a significant effect on switching dynamics (Figure from Ref [25]).

Next, the time dynamics of reversal for the different $Gd_{22-x}Tb_xCo_{78}$ films is compared in Figure 4.7 (a). An incident fluence of 6.9 mJ/cm^2 (absorbed fluence of ~2.8 mJ/cm^2) is chosen for all the samples,

as it slightly exceeds the critical fluence of $Gd_4Tb_{18}Co_{78}$, the sample with the highest critical fluence that showed HI-AOS. A constant fluence is used for all the samples because as observed from Figure 4.6, the magnetization dynamics are not affected by increasing the fluence above F_C. Figure 4.7 (a) shows that while the TbCo film only exhibits demagnetization as expected from the static measurements from Section 4.3, the GdCo film and all the GdTbCo films undergo ultrafast HI-AOS. The magnetization reversal process follows a two-step behavior. In the first step an ultrafast demagnetization occurs within the first picosecond post irradiation from the pump pulse. This initial rapid drop of magnetization is a feature that is shared for all the samples in the series. The second stage consists of remagnetization in the opposite direction as the system cools down, except for $Tb_{22}Co_{78}$. $Gd_{22}Co_{78}$ exhibits the fastest remagnetization time; with increasing Tb concentration, the remagnetization systematically slows. The remagnetization rate plateaus with the x = 15% and x = 18% samples exhibiting similar dynamics. This could be due to the increased DC heating of these samples, which were grown during a different sputtering run. The slowing down of the switching dynamics with increased Tb concentration, in addition to the increased critical fluence, provides conclusive proof that the addition of Tb hinders the HI-AOS capabilities of RE-TM ferrimagnetic films. Finally, $Tb_{22}Co_{78}$ completely demagnetizes to 0 magnetization upon irradiation and then recovers its magnetization along its initial direction upon cooling. It is possible that $Tb_{22}Co_{78}$ exhibits a transient switching in the first few ps following irradiation, similar to the behavior reported by Alebrand et al.[17] and modeled by Moreno et al.[20], suggesting that HI-AOS could occur at a higher fluence. Higher fluences are also needed to better resolve the transient switched state, if it exists. However, utilizing higher fluences led to irreversible damage of the sample as the laser ablated or "burned" the sample surface. By 200 ps all samples had remagnetized to about 80% of the saturation value as shown in in the long timescale scan of Figure 4.7 (b). To mitigate DC heating in the films, experiments were performed at 100 kHz repetition rate for GdCo, GdTbCo samples with x < 15%, and TbCo. For the samples with x = 15% and x = 18% which were more prone to heating by the laser pump, the laser repetition rate was fixed at 10 kHz.

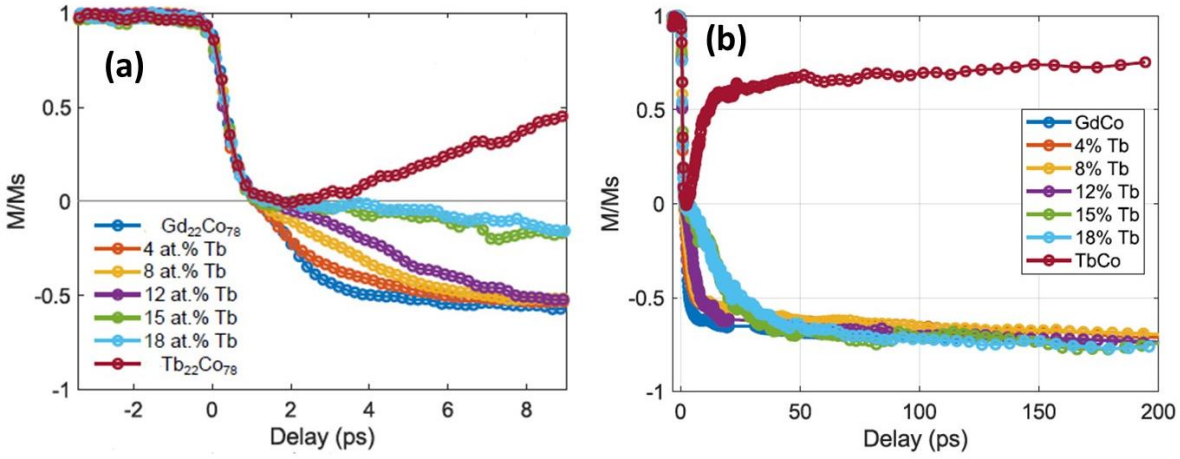

Figure 4.7 Effect of Tb concentration on the magnetization dynamics of GdTbCo films.
(a) Short time scale TR-MOKE measurements show that the HI-AOS reversal is a two-step process for all films (except TbCo). The first initial demagnetization (~1 ps) is similar for all films in the series, including TbCo. The second remagnetization step becomes increasingly slower with increasing Tb.

(b) Longer timescale TR-MOKE measurements indicate ~80% recovery of magnetization within 200 ps of excitation (Figure from Ref [25]).

4.5 Effect of annealing on switching dynamics

Since the anisotropy of a sample depends strongly on annealing, a GdTbCo film is annealed to study the influence of anisotropy on the HI-AOS dynamics. The $Gd_{10}Tb_{12}Co_{78}$ film was annealed at 300 °C for one hour, resulting in a significant reduction of its coercivity H_c as shown in Figure 4.8. The anisotropy K_{ui} is reduced from 4.6 × 10^5 erg/cm^3 to 2.5 × 10^5 erg/cm^3, while maintaining the composition and the saturation magnetization M_S constant as seen in the Figure 4.8. Further annealing at 350 °C eliminated the PMA. The fact that M_S is unchanged by annealing strongly indicates that inhomogeneities such as phase segregation or crystallization have not occurred.

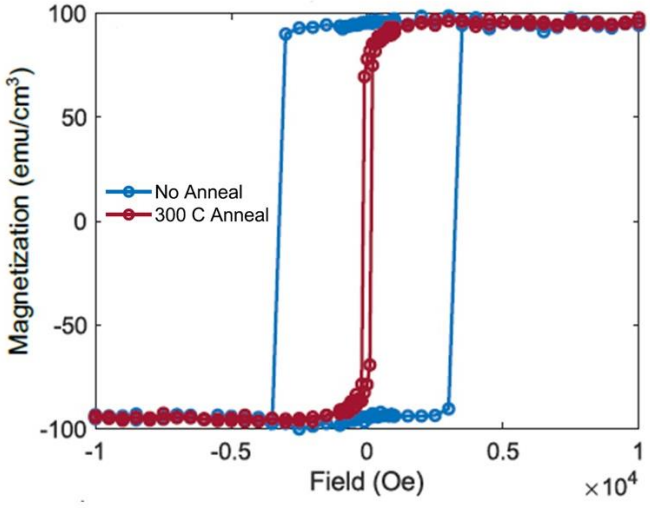

Figure 4.8 Effect of annealing on the anisotropy of $Gd_{10}Tb_{12}Co_{78}$.
Annealing $Gd_{10}Tb_{12}Co_{78}$ at 300°C for 1 hour results in a reduction in coercivity from ~3500 Oe to ~100 Oe, thereby reducing the perpendicular magnetic anisotropy constant K_{ui}. The saturation magnetization M_S remains unchanged (Figure from Ref [25]).

The magnetization dynamics of the film before and after annealing are shown in Figure 4.9 (a). While both the annealed and unannealed films have similar initial demagnetization characteristics, the annealed sample shows a significantly slower remagnetization time. The critical fluence required for switching did not change upon annealing.

Atomistic simulations of the magnetization dynamics of this sample as a function of the damping on the Gd sites α_{Gd} are shown in Figure 4.9 (b). The salient features of these simulations will be detailed in Section 4.6. From Figure 4.9 (b) it can be seen that increased damping on the Gd site α_{Gd} leads to slower remagnetization times, suggesting that the experimentally annealed sample has increased damping, in addition to its reduced anisotropy. Indeed, work from Malinowski et al.[28] showed that introducing local variations of the anisotropy in amorphous CoFeB leads to an increase in the damping parameter. Since the origin of anisotropy in GdTbCo RE-TM alloys is due to a combination of pair-ordering and single ion anisotropy of Tb[29, 30], annealing of a-RE-TM alloys leads to a structural

relaxation of pair-ordering that introduces local anisotropy variations. This in turn leads to higher damping and the slower remagnetization time observed.

TR-MOKE experiments (Figure 4.9 (a)) show that the samples with higher anisotropy (larger Tb at.%) exhibit slower switching dynamics. Atomistic simulations (explained in Section 4.6) with varying anisotropy also support this result. But the annealing study in Figure 4.9 (a) shows that the film with lower anisotropy exhibits slower switching. Moreover, the critical fluence F_C required for switching remains unchanged upon annealing. These observations lead to the conclusion that it is the damping of the system, and not the anisotropy, that is the significant contributor to the ability to exhibit HI-AOS. This is consistent with the observation made in connection with the analysis of various cap and buffer layers (Figure 4.3) that the ability to undergo HI-AOS is not determined by the magnitude of K_u alone. Simulations performed with varying anisotropy also support this conclusion.

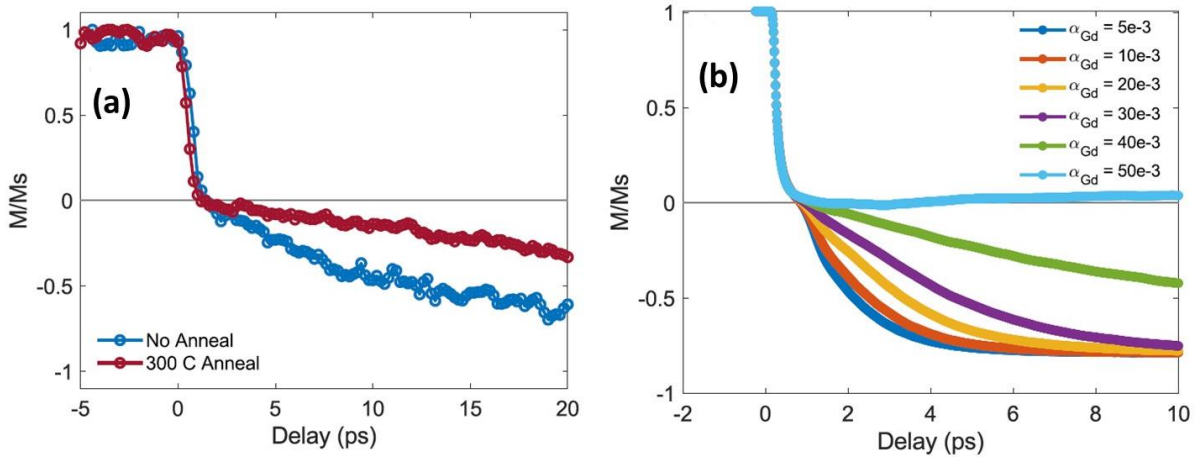

Figure 4.9 Effect of annealing on the switching dynamics of $Gd_{10}Tb_{12}Co_{78}$.
(a) Experimentally measured TR-MOKE switching dynamics of $Gd_{10}Tb_{12}Co_{78}$ in the as grown state (blue curve) and after annealing (red curve) at 300 °C for 1 hour. (b) Atomistic spin dynamics simulation of the time-resolved magnetization dynamics of $Gd_{10}Tb_{12}Co_{78}$ as a function of increasing damping a_{Gd} at the RE Gd site. Increasing a_{Gd} leads to a slower remagnetization time, indicating that annealing leads to a higher damping at the RE sites (Figure from Ref [25]).

4.6 Atomistic simulations of switching dynamics: element specific damping

Atomistic spin dynamics simulations using the VAMPIRE software package[31, 32] combined with a two-temperature model (2TM)[2] were performed to simulate the experimental magnetization dynamics. These simulations were done by our collaborators Sergiu Ruta, Richard Evans and Roy Chantrell at the University of York. The atom level simulation allows to model each atomic type (Gd,Tb,Co) independently and it has been previously used to accurately describe HI-AOS in ferrimagnets. These simulations are carried out as follows. First, energy of the system is described by the spin Hamiltonian, which includes the exchange and anisotropy energies of Gd, Tb and Co, is calculated from equation (4.1).

$$(4.1)\ \mathcal{H} = -\sum_{i<j} J_{i,j} S_i S_j - \sum_i k_{ui} (S_i^z)^2$$

Here the spin S_i is a vector describing the local spin direction. It is normalized to the local atomic spin magnetic moment (μ_S). μ_{Co} = 1.61 μ_B for the magnetic moment on Co sites, μ_{Gd} = 7.63 μ_B for the Gd sites, and μ_{Tb} = 9.34 μ_B for the Tb sites.

The magnetic anisotropy of the sublattice i, k_{ui}, is taken from literature as: 8.07 × 10^{-24} J for Gd, 2.16 × 10^{-22} J for Tb and 3.73 × 10^{-23} J for Co[20]. $J_{i,j}$ is the exchange constant between atomic sites, and is limited to nearest neighbor interactions. The work of Hansen et al.[33] shows that the RE-TM exchange does not depend on the RE concentration, whereas the TM-TM exchange interaction is strongly influenced by the presence of RE. To describe the effect as observed experimentally, the effective Co-Co exchange is taken as described in equation (4.2).

$$(4.2)\ J_{Co-Co}^{eff} = J_{Co-Co}^{bulk} + J_{Co-Tb-Co} \frac{x}{100-x-y} + J_{Co-Gd-Co} \frac{y}{100-x-y}$$

Here x and y = 22 – x are the atomic percentages of the Tb and Gd, respectively.

For GdCo, the equation (4.2) simplifies to

$$(4.3)\ J_{Co-Co}^{eff} = J_{Co-Co}^{bulk} + J_{Co-Gd-Co} \frac{y}{100-y}$$

And for TbCo, the equation (4.2) simplifies to

$$(4.4)\ J_{Co-Co}^{eff} = J_{Co-Co}^{bulk} + J_{Co-Tb-Co} \frac{x}{100-x}$$

The exchange parameters $J_{Co\text{-}Co}$, $J_{Co\text{-}Tb\text{-}Co}$ and $J_{Co\text{-}Gd\text{-}Co}$ used in the simulations are summarized in Table 4.2. Based on these exchange parameters, both the compensation temperature T_M and Curie temperature T_C do not vary with the Tb at.% x in the $Gd_{22-x}Tb_xCo_{78}$ system, with the T_C around 800K and the T_M around 400K. The T_M agrees well with experimental measurements. The ~200 K discrepancy in T_C could be due to the irreversible nucleation of crystallites at high temperatures (T > 600 K) as mentioned in Section 4.2.

	J_{Co-Co}^{bulk}	$J_{Co-Tb-Co}$	$J_{Co-Gd-Co}$	J_{Co-Tb}	J_{Co-Gd}	J_{Gd-Gd}	J_{Gd-Tb}	J_{Tb-Tb}
Exchange energy (10^{21} J)	5.9	-4.4	-5.36	-1.0	-1.25	1.26	1.0	0.82

Table 4.2 Exchange energies in GdTbCo alloys.

Once the Hamiltonian is computed, as with the simulations described in Section 3.1, the on-site effective field B_{eff}^i at site i is computed as the summation of (i) the local field derived from the spin

Hamiltonian and (ii) a random Langevin noise field η_i to model the heat bath (equation (4.5)) using the VAMPIRE software package.

$$(4.5)\ B_{eff}^{i} = -\frac{\partial \mathcal{H}}{\partial S_i} + \eta_i$$

The effective field is then incorporated into the Landau-Lifshitz-Gilbert equation (equation (4.6)) to compute the system dynamics.

$$(4.6)\ \frac{\partial S_i}{\partial t} = -\frac{\gamma_i}{(1+\alpha_i^2)}\left[S_i \times B_{eff}^{i} + \alpha_i S_i \times (S_i \times B_{eff}^{i})\right]$$

a_i and γ_i are the damping and the gyromagnetic ratio at the site i respectively.

The Langevin noise field η_i of equation is a stochastic thermal field due to the interaction of the conduction electrons with the local spins. The stochastic thermal field is assumed to have Gaussian statistics and satisfies the following equations (4.7).

$$(4.7)\ \langle \eta_{i,a}(t)\eta_{i,b}(t')\rangle = \delta_{ij}\delta_{ab}(t-t')2\alpha_i k_B T_e \frac{\mu_i}{\gamma_i}$$

$$\langle \eta_{i,a}(t)\rangle = 0$$

Here k_B is the Boltzmann constant, T_e is the electron temperature and μ_i is the magnetic moment at site i. δ_{ij} is the delta function. The rapid change in thermal energy of the system under the influence of a femtosecond pulse with absorbed power $P(t)$ is modeled by calculating T_e the from the two-temperature model (2TM) as in equation (4.8).

$$(4.8)\ C_e \frac{dT_e}{dt} = g_{ep}(T_p - T_e) + P(t)$$

$$C_p \frac{dT_p}{dt} = g_{ep}(T_e - T_p)$$

Here, T_p is the lattice or phonon temperature, g_{ep} is the coupling constant between the electron and phonon baths, and C_p and C_e are the specific heat capacities of the phonons and electrons respectively. The values of C_e =700 $Jm^{-3}K^{-1}$, C_p=3.0 × 10^6 $Jm^{-3}K^{-1}$and G_{ep}=17 × 10^{17} $Wm^{-3}K^{-1}$ are used in this work, based on previously reported values on GdFeCo[2] and TbCo[20].

The simulated dynamics of HI-AOS of the $Gd_{22-x}Tb_xCo_{78}$ films is shown in Figure 4.10 (a). As can be seen from the Figure 4.10 (a), the simulations are in excellent agreement with the experiments, reproducing the characteristic behavior of a first fast demagnetization that is independent of Tb at.%, followed by increasingly slow remagnetization times with increasing Tb content. The bump in the magnetization following the initial demagnetization step is clearly seen in simulation, and exhibits a more linear character with increasing Tb as seen experimentally. The approximately factor of two discrepancy in the time scales between experiment and simulation is due to both the small size of the

simulated system, which does not allow for domain dynamics to be taken in consideration, and also due to heat dissipation effects which are not included in the simulation.

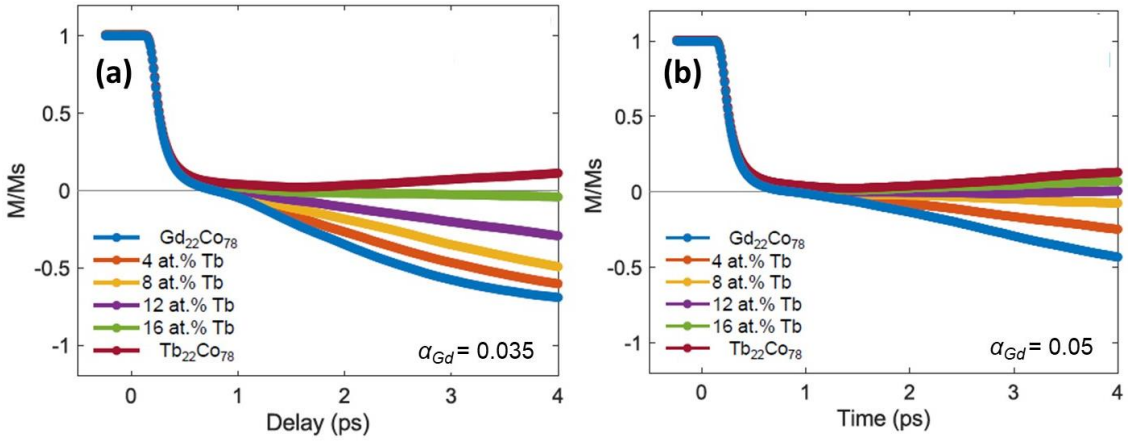

Figure 4.10 Atomistic spin dynamics simulations of HI-AOS in GdTbCo.
(a) Simulations of the dynamics of HI-AOS in $Gd_{22-x}Tb_xCo_{78}$ films qualitatively reproduce the experimentally observed initial quick demagnetization and the second slower remagnetization (that becomes slower with increasing Tb). The simulations agree with the experimental results only when the damping of the RE and TM sites are taken to be different. Here, $a_{Gd} = 0.035$, $a_{Tb} = a_{Co} = 0.05$. (b) The simulations fail to reproduce the experimental observations when the whole system is assigned a single damping $a_{Gd} = a_{Tb} = a_{Co} = 0.05$. The HI-AOS in the samples with higher Tb cannot be seen (Figure from Ref [25]).

Remarkably, the simulations were only able to reproduce the experimental data when the element specific damping of the Gd, Tb and Co sites were assigned separately, rather than when using a net damping of the system as is typically done when simulating such RE-TM ferrimagnetic systems[20, 34, 35]. In the simulations, the Gd/Tb ratio is varied as in the experiments, and the element-specific damping value is fixed at 0.05 for the Tb and Co sites as in Ref. [20]. The magnetism of rare earth elements arise primarily from electrons in the 4f orbital, and the damping of these elements is tied strongly to the spin-orbit coupling of the 4f orbital. Since the 4f orbital of Tb ($L = 3$) has a larger spin-orbit coupling than the 4f orbital of Gd ($L = 0$), it can be expected that the damping of the Gd sites of the GdTbCo alloys is lower than that of the Tb sites. The damping of Gd is taken to be lower than Tb and was varied between 0.005 and 0.05 in order to study its effect on the dynamics. The simulations reported in this Figure 4.10 (a) are performed with element-specific damping values of $a_{Gd} = 0.035$ and $a_{Co} = a_{Tb} = 0.05$. Simulations that are done by assigning the same damping parameter on all elemental sites ($a_{Gd} = a_{Co} = a_{Tb} = 0.05$) were not successful in reproducing the experimentally observed dynamics (Figure 4.10 (b)), especially for the samples with higher Tb at.%. This is consistent with previous experimental and theoretical work on the role of damping in systems doped with RE[22, 36]. The experimental work of Radu et al.[22] on permalloy doped with RE showed increased damping for doping with Tb but no significant increase when doping with Gd. Ellis et al.[36] showed that element-specific damping is required to reproduce the macroscopic damping in such systems.

Figure 4.11 shows the simulation results of critical fluence F_C as a function of Tb concentration and varying Gd damping. The critical fluence for switching in the simulation is determined as the fluence

at which the switching transitions from non-deterministic to deterministic thermally induced switching. The Figure 4.11 shows that increasing the Tb content increases the critical fluence as observed experimentally, for all values of Gd damping. It also shows, that for a given concentration, increasing the damping on the Gd site increases the critical fluence.

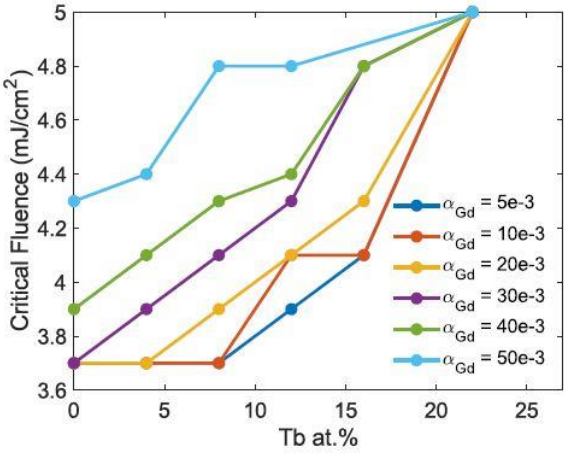

Figure 4.11 Simulated critical fluence for different Tb concentrations.
Simulated critical fluence F_C of $Gd_{22-x}Tb_xCo_{78}$ films as a function of Tb at.% x for different damping values at the Gd site a_{Gd} qualitatively reproduce the observed increase in F_C with x ($a_{Tb} = a_{Co} = 0.05$). F_C also increases as a_{Gd} increases, indicating that lowering the damping at the RE site reduces the threshold switching condition of GdTbCo alloys below the laser ablation limit (Figure from Ref [25]).

The experimental results show increasing critical fluence and remagnetization times with increasing Tb content, implying a larger hindrance to HI-AOS with increased Tb, while post-growth annealing slowed the remagnetization rates. The simulations strongly indicate that the relative element specific damping of the rare earth site compared to the cobalt site – or rather, the differential damping between the RE and TM sites – is the key factor that influences the critical fluence required switching and the speed of remagnetization. As discussed in the model for the annealed sample, at a fixed composition the key parameter that leads to slower remagnetization is the increased elemental damping on the RE site, and not the reduced anisotropy of the film. In simulation the damping constant is a phenomenological parameter that combines a host of diverse effects which ultimately lead to the dissipation of angular momentum from the spin system into the lattice. Increasing the Tb composition leads to a greater spin-orbit interaction in the system, which is considered the intrinsic source of damping[37] and is proportional to ξ^2/W, where ξ is the spin orbital coupling energy and W is the d-band width[38]. Thus, as the system becomes Tb-rich it experiences increased spin-orbit coupling which increases damping and thus leads to the slower dynamics observed in Figure 4.7. For the dynamics observed in the annealed sample, the local spin-orbit coupling is very unlikely to have changed, but an anisotropy change occurs due to the structural relaxation and consequent randomization of local anisotropy axes induced by annealing. This then increases the macroscopic damping. The simulation does not directly account for spin-orbit coupling, but it indirectly simulates the effects of stronger spin-orbit coupling via increases in the damping parameter. As mentioned before, the deterministic switching is independent of the anisotropy and therefore the main contribution of spin-orbit coupling for all optical switching is the damping. Therefore although the simulations reveal the critical role of

damping in modifying the ultrafast magnetization dynamics, it is likely that the underlying physical mechanism is rooted in the spin-orbit interaction. Ferromagnetic resonance (FMR) measurements and polar TR-MOKE experiments with an applied in-plane field to cant the magnetization and induce asymmetric oscillations in the out-of-plane direction were performed to extract the effective damping of the GdTbCo films as a function of the Tb at.%. Unfortunately, neither of these were successful in measuring the damping parameter. The FMR experiments failed owing to the small net magnetization of the films which led to subpar signal to noise ratios. The TR-MOKE experiments were limited by the available magnitude of the applied in-plane field, which was incapable of sufficiently canting the magnetization.

The role of element-specific damping can be explained from the perspective of local angular momentum transfer. Following the results of Bergeard et al.[39] and the hypothesis of Gorchon et al.[3] local transfer of angular momenta between the RE and TM sublattices plays a major role in the ultrafast reversal dynamics of RE-TM ferrimagnets. The 4f orbital of the RE atoms and the 3d orbital of the TM atoms, which mainly contribute to the magnetization of the ferrimagnet, are exchange coupled by the 4f (RE) – 5d (RE) – 3d (TM) exchange. This suggests that in Gd-TM ferrimagnets that easily exhibit HI-AOS, the 4f (RE) - 5d (RE) - 3d (TM) exchange is the dominant channel for spins to transfer angular momentum between sublattices and subsequently reverse their magnetization. Damping can be considered as an overarching factor for the loss of energy from the macroscopic variation of the local magnetization by transfer of energy to coupled phonons, spin waves etc[37]. Since Gd has 4f shell with $L = 0$, its 4f orbital is spherical and angular momentum transfer to the lattice from the spin bath is limited, resulting in both low damping of the RE sublattice and low anisotropy compared to Tb. Adding Tb on the other hand, relaxes this constraint due to the anisotropic 4f orbital from having $L = 3$, which introduces greater spin-lattice coupling via the spin-orbit interaction. This paves a channel for the system to dump angular momentum into the lattice in Tb-rich RE-TM systems. This is reflected in the greater damping of the RE sublattice as assumed by the simulations. Increasing the Tb concentration preferentially increases angular momentum transfer into the lattice with fewer spins participating in the 4f - 5d - 3d exchange, thereby inhibiting switching. Therefore the increased critical fluences and slower magnetization dynamics observed in GdTbCo alloys can be explained by the increased magnitude of the spin-orbit coupling that accompanies increasing Tb content. On the same note, the critical fluence can be linked with the spin wave spectrum, which in the simplest case for a ferrimagnet consists of a ferromagnetic (FM) and antiferromagnetic (AFM) branch. Theoretical work has shown that both modes need to be accessed by the energy from the laser pulse to excite a two-magnon bound state leading to an efficient angular momentum transfer between sublattices[40]. Increased damping on the RE sublattice by the addition of Tb effectively shuts down this exchange, thereby increasing the critical fluence. Thus, as Tb is increased, the increased magnitude of the spin-orbit interaction leads to an increase in damping which can explain the increased critical fluences and the slower magnetization dynamics observed in GdTbCo alloys.

4.7 Time-resolved XMCD measurements of GdTbCo

To fully understand the underlying physics of HI-AOS, particularly in GdTbCo, it is necessary to isolate the individual behavior of each magnetic sublattice. The element specificity of X-rays is exploited in a time-resolved X-ray magnetic circular dichroism (XMCD) experiment to independently study the time dynamics of each element of Gd(Tb)Co films as they undergo HI-AOS. These

measurements are done at the UE56-1_ZPM beamline at BESSY II synchrotron. The facility allows for the excitation of magnetic samples with 100 fs pump laser pulses at 800 nm wavelength at 3 kHz repetition rate, and time-resolved detection of the evolution of magnetization using 100 fs X-ray pulses produced in the synchrotron in the transmission configuration and synchronized with the pump laser. A series of 10 nm thick $Gd_{22-x}Tb_xCo_{78}$ films are grown on thin (300 nm) membranes of SiN. The back of the membrane is deposited with 400 nm of Al for heat conduction. The large energy spectrum (750-1300 eV) of the X-rays available at the beamline conveniently cover the L_3 edge of Co (778 eV) and the M_5 edges of Gd (1190 eV) and Tb (1251 eV).

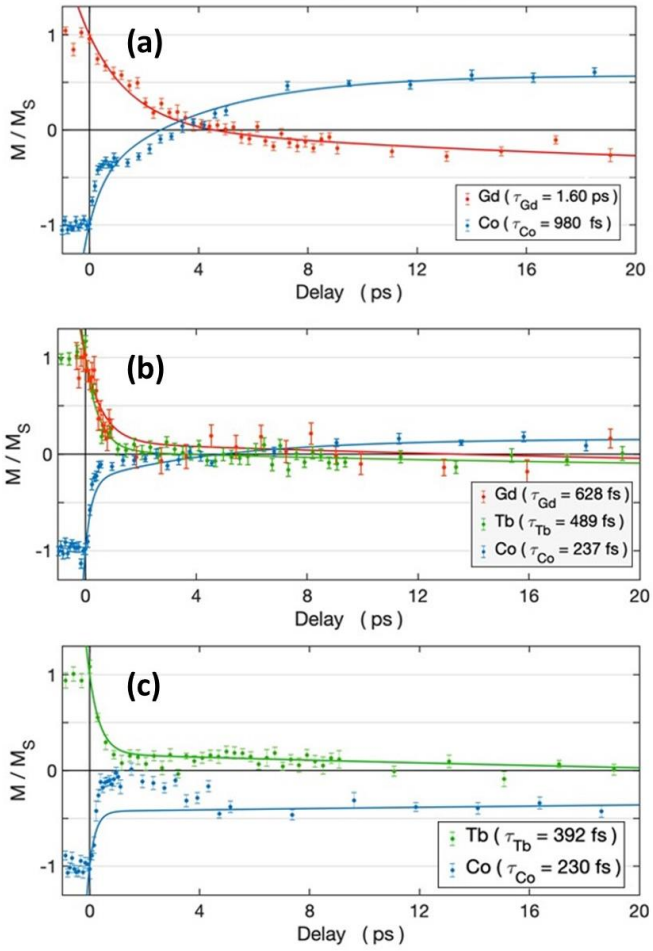

Figure 4.12 Element resolved TR-XMCD measurements of $Gd_{22-x}Tb_xCo_{78}$.
Time resolved dynamics of the Gd, Tb and Co elements in different $Gd_{22-x}Tb_xCo_{78}$ films measured at the UE56-1_ZPM beamline at BESSY II for (a) $Gd_{22}Co_{78}$ (b) $Gd_{10}Tb_{12}Co_{78}$ and (c) $Tb_{22}Co_{78}$. The Gd, Tb and Co traces are depicted in red, green and blue respectively. The measurements are conclusive only for GdCo.

Due to the time constraints of the beam time, only three samples are measured: $Gd_{22}Co_{78}$ (GdCo), $Gd_{10}Tb_{12}Co_{78}$ (GdTbCo) and $Tb_{22}Co_{78}$ (TbCo). The RE concentrations of the GdTbCo sample are chosen such that both Gd and Tb contribute similar magnetic signals. Due to the low signal-to-noise ratio of the TR-XMCD measurements, the experiments are repeated several times, with a complete scan of each element taking up to 12 hrs after optimization of signals. The fs XMCD data measured

at the Gd and Co sites in GdCo, displayed in Figure 4.12 (a), show that Co demagnetizes fastest, followed Gd, similar to Ref [1]. Subsequently, switching occurs on several picoseconds timescale (see e.g. Co), with a clear transient ferromagnetic state of a few ps. However, in GdTbCo (Figure 4.12 (b)) and TbCo (Figure 4.12 (c)) the achieved signal-to-noise ratio does not allow the proper evaluation of timescales and the magnitude of the switching process, especially for the Tb and Gd XMCD data. The GdTbCo data shows Co and Tb switching at the same time, while Gd reverses slower, leading to a transient ferromagnetic state with Co. TbCo shows a weak reversal of Co at long timescales (> 30 ps, not shown). However, these results are not reproducible, and different runs (not shown in figures) at different regions of the same GdTbCo and TbCo samples show different demagnetization timescales, especially for the Gd and Tb sites, leading to ambiguities in the analyses of the data from the beamtime. More comprehensive TR-XMCD experiments with robust samples are necessary in order to better understand the demagnetization and switching timescales of the different elements, and to elucidate the mechanisms behind HI-AOS in GdTbCo and other RE-TM ferrimagnets.

4.8 Conclusions: Engineering of element-specific damping to optimize HI-AOS in materials

In this chapter, I have shown that ferrimagnetic thin films of $Gd_{22-x}Tb_xCo_{78}$ exhibit ultrafast HI-AOS for Tb concentrations up to 18% (with as low as 4% Gd). Starting from $Gd_{22}Co_{78}$, by systematically replacing Gd atoms with Tb atoms such that the RE atomic concentration remains at 22%, the effect of anisotropy, damping, net magnetic moment and other factors on the ability to undergo HI-AOS has been studied. The GdCo and GdTbCo samples switch their magnetization within a few picoseconds of excitation, exhibiting a two-step switching process that includes a first quick demagnetization step (that is independent of Tb concentration), and a second slower remagnetization step. Increased Tb at.% results in an increase of the critical fluence F_C required for switching, and a decrease in the remagnetization speed, proving that the replacement of Gd atoms with Tb results in an increased hindrance to HI-AOS. Annealing of a sample results in slower remagnetization times, which indicates that the damping, and not anisotropy, is the most crucial factor in deciding the ability of a material to switch. Atomistic simulations of the Landau-Lifshitz-Gilbert equation coupled with the two-temperature model are able to reproduce the experimentally observed switching dynamics and critical fluence characteristics, but only when the system is modelled with independent damping parameters on the rare-earth and transition metal sites. These simulations indicate that the differential element-specific damping between the RE and TM sites is the most important parameter that decides the ability of a ferrimagnetic film to show HI-AOS. The low element-specific damping of the Gd site, owing to the low spin-orbit coupling of its half-filled $L = 0$ 4f shell, as compared to the high spin-orbit coupling $L = 3$ 4f shell of Tb, is potentially the reason for the relative ease of HI-AOS in Gd-based RE-TM ferrimagnetic systems. X-ray based time-resolved measurements were inconclusive in disentangling the dynamics of the different elements of the GdTbCo alloys, and more robust samples and experiments are required to completely demystify the HI-AOS mechanism.

Nonetheless, the results in this chapter strongly imply that engineering the differential element-specific damping of the different sublattices of a ferrimagnet will be crucial in uncovering more material systems that undergo HI-AOS. A library of such materials is highly desirable if ultrafast toggle switching, either by short optical or electrical excitations, is to be incorporated into mainstream devices. On another technological note, the increased anisotropy in GdTbCo alloys, due to the large

single ion anisotropy of Tb, can be advantageous for applications in magnetic bits with high PMA and high retention time.

4.9 References

1. Radu, I., Vahaplar, K., Stamm, C., Kachel, T., Pontius, N., Dürr, H. A., Ostler, T. A., Barker, J., Evans, R. F. L., Chantrell, R. W., Tsukamoto, A., Itoh, A., Kirilyuk, A., Rasing, Th. & Kimel, A. V. Transient ferromagnetic-like state mediating ultrafast reversal of antiferromagnetically coupled spins. *Nature* **472,** 205–208 (2011). https://doi.org/10.1038/nature09901
2. Ostler, T. A., Barker, J., Evans, R. F. L., Chantrell, R. W., Atxitia, U., Chubykalo-Fesenko, O., El Moussaoui, S., Le Guyader, L., Mengotti, E., Heyderman, L. J., Nolting, F., Tsukamoto, A., Itoh, A., Afanasiev, D., Ivanov, B. A., Kalashnikova, A. M., Vahaplar, K., Mentink, J., Kirilyuk, A., Rasing, Th. & Kimel, A. V. Ultrafast heating as a sufficient stimulus for magnetization reversal in a ferrimagnet. *Nat Commun* **3,** 666 (2012). https://doi.org/10.1038/ncomms1666
3. Gorchon, J., Wilson, R. B., Yang, Y., Pattabi, A., Chen, J. Y., He, L., Wang, J. P., Li, M. & Bokor, J. Role of electron and phonon temperatures in the helicity-independent all-optical switching of GdFeCo. *Phys. Rev. B* **94,** 184406 (2016). https://doi.org/10.1103/PhysRevB.94.184406
4. Le Guyader, L., El Moussaoui, S., Buzzi, M., Savoini, M., Tsukamoto, A., Itoh, A., Kirilyuk, A., Rasing, Th., Nolting, F. & Kimel, A. V. Deterministic character of all-optical magnetization switching in GdFe-based ferrimagnetic alloys. *Phys. Rev. B* **93,** 134402 (2016). https://doi.org/10.1103/PhysRevB.93.134402
5. El-Ghazaly, A., Tran, B., Ceballos, A., Lambert, C.-H., Pattabi, A., Salahuddin, S., Hellman, F. & Bokor, J. Ultrafast magnetization switching in nanoscale magnetic dots. *Appl. Phys. Lett.* **114,** 232407 (2019). https://doi.org/10.1063/1.5098453
6. Lalieu, M. L. M., Lavrijsen, R. & Koopmans, B. Integrating all-optical switching with spintronics. *Nat Commun* **10,** 110 (2019). https://doi.org/10.1038/s41467-018-08062-4
7. Beens, M., Lalieu, M. L. M., Deenen, A. J. M., Duine, R. A. & Koopmans, B. Comparing all-optical switching in synthetic-ferrimagnetic multilayers and alloys. *Phys. Rev. B* **100,** 220409 (2019). https://doi.org/10.1103/PhysRevB.100.220409
8. Lambert, C.-H., Mangin, S., Varaprasad, B. S. D. C. S., Takahashi, Y. K., Hehn, M., Cinchetti, M., Malinowski, G., Hono, K., Fainman, Y., Aeschlimann, M. & Fullerton, E. E. All-optical control of ferromagnetic thin films and nanostructures. *Science* **345,** 1337–1340 (2014). https://doi.org/10.1126/science.1253493
9. Mangin, S., Gottwald, M., Lambert, C.-H., Steil, D., Uhlíř, V., Pang, L., Hehn, M., Alebrand, S., Cinchetti, M., Malinowski, G., Fainman, Y., Aeschlimann, M. & Fullerton, E. E. Engineered materials for all-optical helicity-dependent magnetic switching. *Nature Mater* **13,** 286–292 (2014). https://doi.org/10.1038/nmat3864
10. El Hadri, M. S., Pirro, P., Lambert, C.-H., Petit-Watelot, S., Quessab, Y., Hehn, M., Montaigne, F., Malinowski, G. & Mangin, S. Two types of all-optical magnetization switching mechanisms using femtosecond laser pulses. *Phys. Rev. B* **94,** 064412 (2016). https://doi.org/10.1103/PhysRevB.94.064412
11. El Hadri, M. S., Pirro, P., Lambert, C.-H., Bergeard, N., Petit-Watelot, S., Hehn, M., Malinowski, G., Montaigne, F., Quessab, Y., Medapalli, R., Fullerton, E. E. & Mangin, S. Electrical characterization of all-optical helicity-dependent switching in ferromagnetic Hall crosses. *Appl. Phys. Lett.* **108,** 092405 (2016). https://doi.org/10.1063/1.4943107
12. Cornelissen, T. D., Córdoba, R. & Koopmans, B. Microscopic model for all optical switching in ferromagnets. *Appl. Phys. Lett.* **108,** 142405 (2016). https://doi.org/10.1063/1.4945660

13. Gorchon, J., Yang, Y. & Bokor, J. Model for multishot all-thermal all-optical switching in ferromagnets. *Phys. Rev. B* **94,** 020409 (2016). https://doi.org/10.1103/PhysRevB.94.020409
14. Kirilyuk, A., Kimel, A. V. & Rasing, T. Laser-induced magnetization dynamics and reversal in ferrimagnetic alloys. *Rep. Prog. Phys.* **76,** 026501 (2013). https://doi.org/10.1088/0034-4885/76/2/026501
15. Alebrand, S., Gottwald, M., Hehn, M., Steil, D., Cinchetti, M., Lacour, D., Fullerton, E. E., Aeschlimann, M. & Mangin, S. Light-induced magnetization reversal of high-anisotropy TbCo alloy films. *Appl. Phys. Lett.* **101,** 162408 (2012). https://doi.org/10.1063/1.4759109
16. Hassdenteufel, A., Hebler, B., Schubert, C., Liebig, A., Teich, M., Helm, M., Aeschlimann, M., Albrecht, M. & Bratschitsch, R. Thermally Assisted All-Optical Helicity Dependent Magnetic Switching in Amorphous $Fe_{100-x}Tb_x$ Alloy Films. *Adv. Mater.* **25,** 3122–3128 (2013). https://doi.org/10.1002/adma.201300176
17. Alebrand, S., Bierbrauer, U., Hehn, M., Gottwald, M., Schmitt, O., Steil, D., Fullerton, E. E., Mangin, S., Cinchetti, M. & Aeschlimann, M. Subpicosecond magnetization dynamics in TbCo alloys. *Phys. Rev. B* **89,** 144404 (2014). https://doi.org/10.1103/PhysRevB.89.144404
18. Liu, T.-M., Wang, T., Reid, A. H., Savoini, M., Wu, X., Koene, B., Granitzka, P., Graves, C. E., Higley, D. J., Chen, Z., Razinskas, G., Hantschmann, M., Scherz, A., Stöhr, J., Tsukamoto, A., Hecht, B., Kimel, A. V., Kirilyuk, A., Rasing, T. & Dürr, H. A. Nanoscale Confinement of All-Optical Magnetic Switching in TbFeCo - Competition with Nanoscale Heterogeneity. *Nano Lett.* **15,** 6862–6868 (2015). https://doi.org/10.1021/acs.nanolett.5b02743
19. Avilés-Félix, L., Olivier, A., Li, G., Davies, C. S., Álvaro-Gómez, L., Rubio-Roy, M., Auffret, S., Kirilyuk, A., Kimel, A. V., Rasing, Th., Buda-Prejbeanu, L. D., Sousa, R. C., Dieny, B. & Prejbeanu, I. L. Single-shot all-optical switching of magnetization in Tb/Co multilayer-based electrodes. *Sci Rep* **10,** 5211 (2020). https://doi.org/10.1038/s41598-020-62104-w
20. Moreno, R., Ostler, T. A., Chantrell, R. W. & Chubykalo-Fesenko, O. Conditions for thermally induced all-optical switching in ferrimagnetic alloys: Modeling of TbCo. *Phys. Rev. B* **96,** 014409 (2017). https://doi.org/10.1103/PhysRevB.96.014409
21. Spaldin, N. *Magnetic Materials: Fundamentals and Applications*. (Cambridge University Press, 2010).
22. Radu, I., Woltersdorf, G., Kiessling, M., Melnikov, A., Bovensiepen, U., Thiele, J.-U. & Back, C. H. Laser-Induced Magnetization Dynamics of Lanthanide-Doped Permalloy Thin Films. *Phys. Rev. Lett.* **102,** 117201 (2009). https://doi.org/10.1103/PhysRevLett.102.117201
23. Russek, S. E., Kabos, P., McMichael, R. D., Lee, C. G., Bailey, W. E., Ewasko, R. & Sanders, S. C. Magnetostriction and angular dependence of ferromagnetic resonance linewidth in Tb-doped Ni[sub 0.8]Fe[sub 0.2] thin films. *J. Appl. Phys.* **91,** 8659 (2002). https://doi.org/10.1063/1.1452708
24. Graves, C. E., Reid, A. H., Wang, T., Wu, B., de Jong, S., Vahaplar, K., Radu, I., Bernstein, D. P., Messerschmidt, M., Müller, L., Coffee, R., Bionta, M., Epp, S. W., Hartmann, R., Kimmel, N., Hauser, G., Hartmann, A., Holl, P., Gorke, H., Mentink, J. H., Tsukamoto, A., Fognini, A., Turner, J. J., Schlotter, W. F., Rolles, D., Soltau, H., Strüder, L., Acremann, Y., Kimel, A. V., Kirilyuk, A., Rasing, Th., Stöhr, J., Scherz, A. O. & Dürr, H. A. Nanoscale spin reversal by non-local angular momentum transfer following ultrafast laser excitation in ferrimagnetic GdFeCo. *Nature Mater* **12,** 293–298 (2013). https://doi.org/10.1038/nmat3597
25. Ceballos, A., Pattabi, A., El-Ghazaly, A., Ruta, S., Simon, C. P., Evans, R. F. L., Ostler, T., Chantrell, R. W., Kennedy, E., Scott, M., Bokor, J. & Hellman, F. Role of element-specific damping on the ultrafast, helicity-independent all-optical switching dynamics in amorphous (Gd,Tb)Co thin films. *arXiv:1911.09803v3 [cond-mat.mtrl-sci]* 8 (2019).
26. Hellman, F., Messer, M. & Abarra, E. N. Coercivity in amorphous Tb–Fe alloys. *Journal of Applied Physics* **86,** 1047–1052 (1999). https://doi.org/10.1063/1.370845

27. Bergeard, N., Mougin, A., Izquierdo, M., Fonda, E. & Sirotti, F. Correlation between structure, electronic properties, and magnetism in Co x Gd 1 − x thin amorphous films. *Phys. Rev. B* **96,** 064418 (2017). https://doi.org/10.1103/PhysRevB.96.064418
28. Malinowski, G., Kuiper, K. C., Lavrijsen, R., Swagten, H. J. M. & Koopmans, B. Magnetization dynamics and Gilbert damping in ultrathin Co48Fe32B20 films with out-of-plane anisotropy. *Appl. Phys. Lett.* **94,** 102501 (2009). https://doi.org/10.1063/1.3093816
29. Hellman, F. & Gyorgy, E. M. Growth-induced magnetic anisotropy in amorphous Tb-Fe. *Phys. Rev. Lett.* **68,** 1391–1394 (1992). https://doi.org/10.1103/PhysRevLett.68.1391
30. Harris, V. G., Aylesworth, K. D., Das, B. N., Elam, W. T. & Koon, N. C. Structural origins of magnetic anisotropy in sputtered amorphous Tb-Fe films. *Phys. Rev. Lett.* **69,** 1939–1942 (1992). https://doi.org/10.1103/PhysRevLett.69.1939
31. Evans, R. F. L., Fan, W. J., Chureemart, P., Ostler, T. A., Ellis, M. O. A. & Chantrell, R. W. Atomistic spin model simulations of magnetic nanomaterials. *J. Phys.: Condens. Matter* **26,** 103202 (2014). https://doi.org/10.1088/0953-8984/26/10/103202
32. VAMPIRE software package. at <https://vampire.york.ac.uk/>
33. Hansen, P., Clausen, C., Much, G., Rosenkranz, M. & Witter, K. Magnetic and magneto-optical properties of rare-earth transition-metal alloys containing Gd, Tb, Fe, Co. *Journal of Applied Physics* **66,** 756–767 (1989). https://doi.org/10.1063/1.343551
34. Lu, X., Zou, X., Hinzke, D., Liu, T., Wang, Y., Cheng, T., Wu, J., Ostler, T. A., Cai, J., Nowak, U., Chantrell, R. W., Zhai, Y. & Xu, Y. Roles of heating and helicity in ultrafast all-optical magnetization switching in TbFeCo. *Appl. Phys. Lett.* **113,** 032405 (2018). https://doi.org/10.1063/1.5036720
35. Iacocca, E., Liu, T.-M., Reid, A. H., Fu, Z., Ruta, S., Granitzka, P. W., Jal, E., Bonetti, S., Gray, A. X., Graves, C. E., Kukreja, R., Chen, Z., Higley, D. J., Chase, T., Le Guyader, L., Hirsch, K., Ohldag, H., Schlotter, W. F., Dakovski, G. L., Coslovich, G., Hoffmann, M. C., Carron, S., Tsukamoto, A., Kirilyuk, A., Kimel, A. V., Rasing, Th., Stöhr, J., Evans, R. F. L., Ostler, T., Chantrell, R. W., Hoefer, M. A., Silva, T. J. & Dürr, H. A. Spin-current-mediated rapid magnon localisation and coalescence after ultrafast optical pumping of ferrimagnetic alloys. *Nat Commun* **10,** 1756 (2019). https://doi.org/10.1038/s41467-019-09577-0
36. Ellis, M. O. A., Ostler, T. A. & Chantrell, R. W. Classical spin model of the relaxation dynamics of rare-earth doped permalloy. *Phys. Rev. B* **86,** 174418 (2012). https://doi.org/10.1103/PhysRevB.86.174418
37. Hickey, M. C. & Moodera, J. S. Origin of Intrinsic Gilbert Damping. *Phys. Rev. Lett.* **102,** 137601 (2009). https://doi.org/10.1103/PhysRevLett.102.137601
38. He, P., Ma, X., Zhang, J. W., Zhao, H. B., Lüpke, G., Shi, Z. & Zhou, S. M. Quadratic Scaling of Intrinsic Gilbert Damping with Spin-Orbital Coupling in L 1 0 FePdPt Films: Experiments and *Ab Initio* Calculations. *Phys. Rev. Lett.* **110,** 077203 (2013). https://doi.org/10.1103/PhysRevLett.110.077203
39. Bergeard, N., López-Flores, V., Halté, V., Hehn, M., Stamm, C., Pontius, N., Beaurepaire, E. & Boeglin, C. Ultrafast angular momentum transfer in multisublattice ferrimagnets. *Nat Commun* **5,** 3466 (2014). https://doi.org/10.1038/ncomms4466
40. Barker, J., Atxitia, U., Ostler, T. A., Hovorka, O., Chubykalo-Fesenko, O. & Chantrell, R. W. Two-magnon bound state causes ultrafast thermally induced magnetisation switching. *Sci Rep* **3,** 3262 (2013). https://doi.org/10.1038/srep03262

Chapter 5. Helicity-independent All-Optical Switching in Co/Pt ferromagnets

The chapters of this thesis so far focused on uncovering the underlying physics behind the phenomena of current-induced spin accumulation in heavy metals and the helicity-independent all-optical switching (HI-AOS) in films of Gd-based rare-earth transition metal (RE-TM) ferrimagnetic alloys. The upcoming Chapter 5 throughChapter 7 will form, loosely, the second part of this thesis and will deal with building up on the discussed results and demonstrating the applications of these phenomena in practical, on-chip spintronic devices.

5.1 Ferrimagnets vs ferromagnets in spintronic devices

Chapter 3 and Chapter 4 discussed in detail the phenomenon of HI-AOS, wherein a thin film of a ferrimagnet, when excited by a short intense laser pulse (with durations ranging from tens of fs up to a few ps, as described in Chapter 3) reverses its magnetization within a few ps of irradiation, irrespective of the polarization of the laser pulse. The magnetization state toggles in an ultrafast manner with each successive optical pulse. The discussion in Section 4.14.1 reports that this phenomenon has thus far only been observed only in RE-TM ferrimagnetic alloys and bilayers, and predominantly only in Gd-based ones. Ferrimagnets have two opposite two unequal and oppositely aligned magnetic sublattices coupled together by a strong exchange field, because of which their net saturation magnetization M_S is quite low, of the order of ~100 emu/cc[1, 2]. On the other hand, ferromagnets – whose magnetic moments all tend to align parallel to each other at saturation – have comparatively larger M_S values. For example, multilayers of Co/Pt, a ferromagnet with perpendicular magnetic anisotropy (PMA) that is commonly used in conventional spintronic devices, have M_S > 1000 emu/cc [3, 4]. An integrated ultrafast spintronic device will ideally need to allow electrical readout of the magnetic state, instead of relying on an optical read. Electrical readouts in spintronic devices are typically done through a magnetic tunnel junction (MTJ – discussed in Section 1.4). In a potential ultrafast spintronic MTJ, the magnetic film that exhibits ultrafast switching would act as the free layer. As a result of its lower net magnetization, an electrical signal from a ferrimagnetic bit is considerably larger than that from ferrimagnetic bit.

From Section 1.4, the two states (parallel and antiparallel magnetization of the free and fixed layers) of an MTJ can be distinguished by a magnetoresistive effect called the tunnel magnetoresistance (TMR). If R_P and R_{AP} are the resistance across the MTJ when the free and fixed layers are aligned parallel and antiparallel, respectively, the TMR is given by TMR = $(R_{AP} - R_P)/R_P$. Larger the TMR, easier the ability to distinguish between the two states of the magnetic bit, and faster the overall circuitry. Standard ferromagnet based spintronic MTJs have high TMR ratios > 100%. CoFeB/MgO/CoFeB MTJs with in-plane magnetized CoFeB have TMR of ~700% at room temperature[5].

Chen et al.[6] demonstrated HI-AOS with subpicosend laser pulses in the GdFeCo free layer of an MTJ structure with a repetition rate of 1 MHz, a speed that was limited only by the laser pulse repetition cycle. The MTJ stack used in this study was Ta(5)/Pd(10)/$[Co(0.6)/Pd(1.5)]_4$/Co(0.8)/MgO(1.8)/GdFeCo(20)/Ta(4) (thicknesses in nm). The Co/Pd multilayer served as the fixed layer of this MTJ. The schematic of this MTJ stack is shown in

Figure 5.1 (a). The magnetoresistance response of this as the GdFeCo free layer is switched by an external applied field and by laser pulses is depicted in Figure 5.1 (b) and (c) respectively. Both these measurements yielded a TMR ratio of ~0.6%, which is almost three orders of magnitude lower than the TMR of ferromagnetic MTJs. Therefore, HI-AOS must be extended to ferromagnets with large net magnetic moments to successfully integrate ultrafast magnetic phenomena with on-chip spintronics with electrical readout.

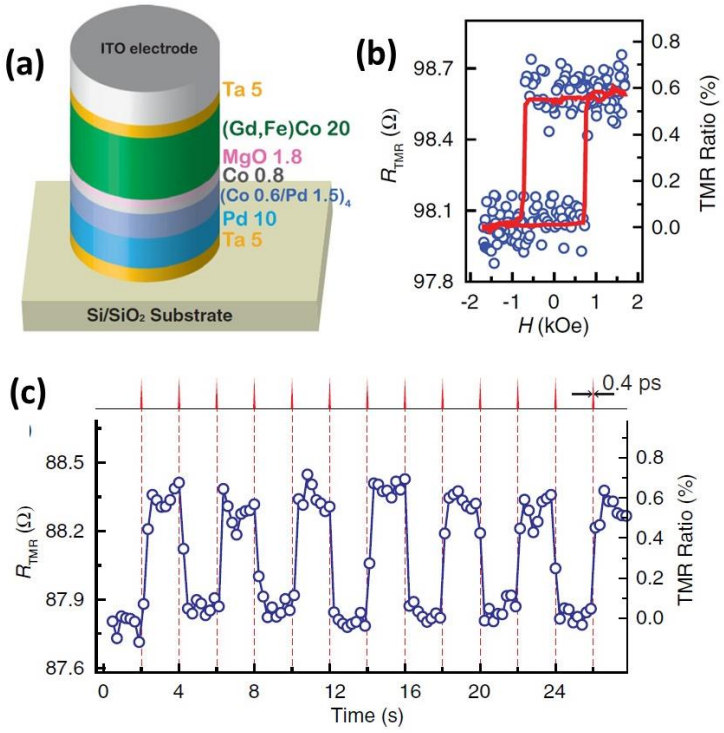

Figure 5.1 TMR of a GdFeCo MTJ.
(a) Schematic of the MTJ stack, thicknesses in nm. Tunnel magnetoresistance (R_{TMR}) and TMR ratio across the stack as the stack is swept by an out-of-plane magnetic field *H* (b) and as the GdFeCo undergoes HI-AOS, triggered by single 0.4 ps laser pulses at 0.5 Hz repetition (Figure from Ref [6]).

5.2 All-optical switching experiments on ferromagnets

At the time of publication of this work detailed in this chapter, ultrafast all-optical switching via the HI-AOS mechanism was observed only in the aforementioned Gd-based RE-TM ferrimagnetic alloys of GdFeCo[7, 8]. Ultrafast HI-AOS has since also been observed in GdFe alloys[9], GdCo alloys[10], bilayers of Pt/Gd/Co[11, 12], Tb/Co bilayers[13] and the GdTbCo alloys[1] discussed in detail in Chapter 4, all of which are also ferrimagnetic systems.

The helicity-dependent all optical switching (HD-AOS) phenomenon, on the other hand is observed in a wider array of magnetic films, including ferromagnets like Co/Pt multilayers, CoNi/Pd multilayers and FePtAgC granular films[14, 15, 16]. A salient feature of HD-AOS is that the orientation of the final magnetic state of the film is independent of its initial magnetization state, and depends only on the helicity or angular momentum (right- or left-circularly polarized) of the applied optical pulses. The

degree of remagnetization along that direction depends on a number of factors, including the number of optical pulses applied[15]. Section 4.1 describes possible mechanisms for HD-AOS. Despite the potential to study and unravel interesting physics from the HD-AOS, the mechanism itself is impractical for application in devices. The repeated pulses needed for switching make the whole process slow (full switching occurs in timescales of μs or ms) and rather inefficient, compared to the ultrafast HI-AOS. Moreover, the dependence of switching on the helicity of light implies that pure Joule heating from short electrical pulses will be incapable of triggering a similar process, making the integration of HD-AOS on-chip infeasible.

Helicity-independent all-optical magnetization reversal by single fs laser pulses was reported in a ferromagnetic PMA Pt/Co/Pt stack by Vomir et al[17]. The magnetic state toggled with each sequential laser pulse, similar to HI-AOS in RE-TM ferrimagnets. However, the magnetization dynamics occurred in quite slow μs rather than ps timescales, indicating that switching occurs through domain nucleation and propagation. Additionally, switching was observed only when the laser spot size was comparable to the intrinsic domain size of the ferromagnetic film (few μm) and the absorbed fluence was less than 4 mJ/cm^2. For larger laser spot sizes and fluences, the magnetization of the irradiated region broke up into random multiple domains. The physics of this switching mechanism remains unclear. Nonetheless, the slow switching speed limits the use of this phenomenon in devices.

In this chapter, I will detail work done in extending the ultrafast, sub-ps HI-AOS capabilities of RE-TM ferrimagnetic alloys on to ferromagnets that can be easily used in a spintronic device for higher electrical readout signal. Co/Pt ferromagnetic multilayers are grown on top of a thin film of ferrimagnetic GdFeCo, in order to couple the switching behavior of the ferrimagnet on to the ferromagnet through the exchange interaction between these two films.

5.3 Depth sensitive MOKE microscopy experimental setup

The stacks studied in this work comprise of a ferromagnetic Co/Pt multilayer grown on top of a thin film of ferrimagnetic GdFeCo. Unlike the surface and interface sensitive MSHG of Chapter 2, the magnetic signal in MOKE microscopy experiments, such as those described in Chapter 3 and Chapter 4, arise from the whole magnetic stack of the film owing to the penetration depth of light in these films being of the order of film thickness. Therefore, MOKE experiments on the ferrimagnet/ferromagnet stacks will yield a magnetic signal that is sensitive to, and is a mixture of, the magnetizations of both the layers. In order to study the magnetic response of the Co/Pt ferromagnet and the GdFeCo ferrimagnet independently of each other, the technique of depth-sensitive MOKE is used[18, 19, 20], which enables one to access the magnetization of each individual film in a magnetic multilayer stack.

The depth-sensitive MOKE microscope setup builds on the MOKE microscope detailed in Section 3.2. As shown in the schematic in Figure 5.2, the depth-sensitive MOKE microscope differs from the regular MOKE microscope (Figure 3.3 (a)) in that it uses a quarter waveplate in front of the polarizer of the incident light. The light is focused by the microscope objective and is incident normal to the sample surface. After the reflection off the sample surface, the light goes through an analyzer, converting polarization changes into intensity changes. Without the quarter waveplate, the magnetic signal is a complex sum $\Theta = \theta + i\varepsilon$ of the Kerr rotation θ and the Kerr ellipticity ε, both of which arise from the net response of all the magnetic films in the stack. When the quarter waveplate angle α is

rotated, it introduces a phase difference between the left- and right-circularly polarized components of the incident beam, and the measured magnetic signal will become a linear combination of θ and ε. At specific quarter waveplate angles α, the rotation and ellipticity responses of a particular film cancel each other, thereby making the net magnetic response of that film effectively zero. The measured magnetic response then will arise only from the other magnetic films of the stack. A mathematical explanation, based on the Jones matrix formalism of different optical and magnetic components, for how the quarter waveplate introduces depth sensitivity will be introduced while discussing depth sensitive TR-MOKE in Section 5.6. A pump laser pulse can be incorporated into this setup to study single shot HI-AOS events.

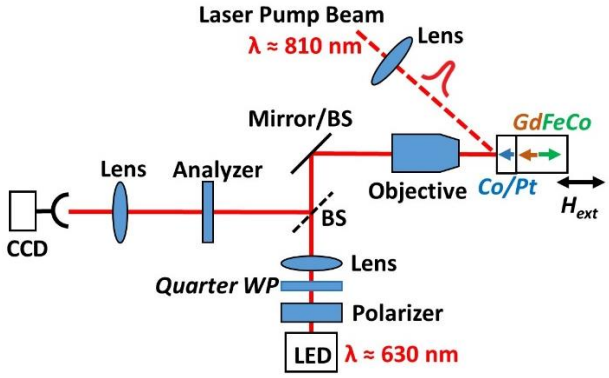

Figure 5.2 Schematic of the depth sensitive MOKE microscope.
The setup is the same as the MOKE microscopy setup (Figure 3.3 (a)) except for the quarterwave plate (QWP) added in front of the polarizer that enables depth sensitivity. The collimating lens for the LED is not shown here. (BS = beam splitter, WP = waveplate)

5.4 Exchange coupled ferrimagnet/ferromagnet stacks

A series of ferrimagnet/ferromagnet stacks is grown by magnetron sputter deposition (same configuration as the samples in Section 3.3) on Si/SiO_2(100 nm) substrates. The stack (shown in the schematic of Figure) is Ta(3 nm)/$Gd_{28}Fe_{65}Co_7$(20 nm)/Co(0.4 nm)/Pt(d)/Co(0.6 nm)/Pt(3 nm). A schematic of this stack is shown in Figure 5.3 (a). The magnetization directions of the Co/Pt ferromagnet and the Gd and FeCo sublattices are indicated by blue, orange and green arrows, respectively. The magnitude and direction of the exchange coupling between the GdFeCo ferrimagnet and Co/Pt ferrimagnet is varied by varying the Pt spacer thickness d. The layer thicknesses are determined from the deposition rate of each material. All of the samples present perpendicular magnetic anisotropy (PMA). Co/Pt is chosen as the ferromagnet for its strong perpendicular magnetic anisotropy even when grown on top of a non-textured film such as GdFeCo and for the possibility of increasing its thickness (number of repeats), all while keeping the perpendicular anisotropy. The transition temperature T_M of the GdFeCo film was found to be below room temperature, indicating that its magnetization is dominated by the FeCo sublattice.

The stacks are characterized by performing hysteresis loops with a regular magneto optical Kerr effect (MOKE) microscope with an applied out-of-plane magnetic field $H_\perp$, as shown in Figure 5.3 (b). The source LED wavelength of 630 nm is sensitive mostly to the FeCo sublattice of the GdFeCo[2]. A strong magnetic signal arises mainly from the thick GdFeCo film, while the signal from the Co/Pt

multilayers is considerably weaker due to the thin layer of Co. The hysteresis loop of a bare $Gd_{28}Fe_{65}Co_7$(20 nm)/Ta(3 nm) film, with a coercivity of ~100 Oe is presented at the top of Figure 5.3 (b). The polarity of magnetization is opposite to that of the Gd dominant $Gd_{27}FeCo$ sample reported in Chapter 3, verifying that the GdFeCo used in these ferrimagnet/ferromagnet stacks is indeed FeCo dominant. Four remnant states are present in the ferrimagnet/ferromagnet samples with Pt spacer thickness d = 4 and 5 nm, and only two in the strongly coupled samples with d = 1.5–3 nm.

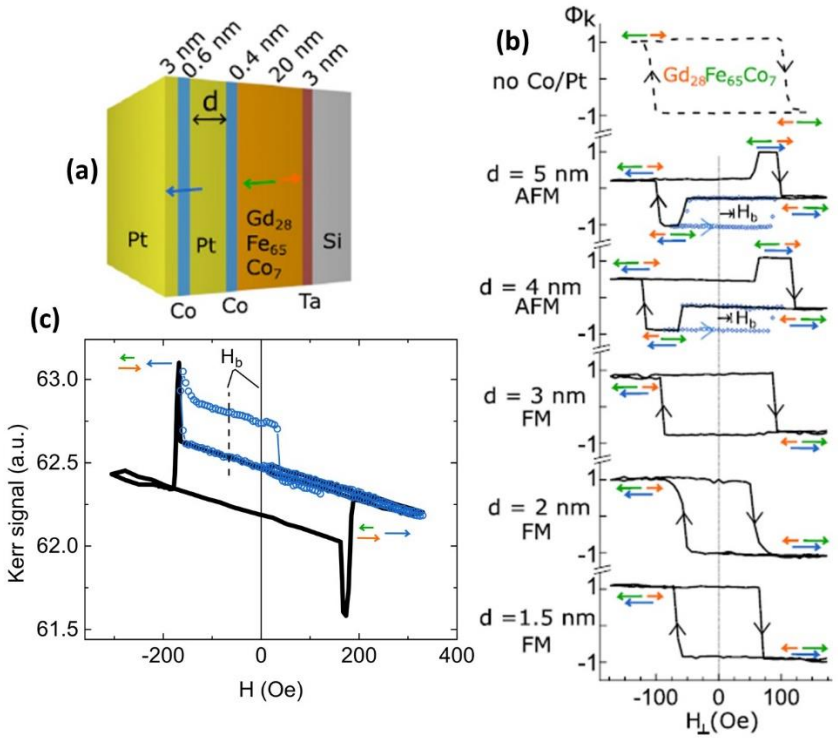

Figure 5.3 Hysteresis loops of the GdFeCo/Co/Pt/Co stacks.
(a) Schematic of the GdFeCo/Co/Pt(d nm)/Co stack series with Pt spacer of thickness d. (b) Magnetic hysteresis loops for bare GdFeCo(20nm)/Ta(3nm) (top) and the GdFeCo/Co/Pt/Co stacks with different Pt spacer. Orange, green, and blue arrows represent Gd, FeCo, and Co/Pt magnetizations, respectively. Minor loops (blue circles) switching only the Co/Pt magnetization, presenting a positive exchange bias H_b, on samples d = 4 and 5 nm. (c) Hysteresis loop (black) and minor loop (blue) for a Gd-rich Si/SiO_2(100nm)/Ta(5nm)/($Gd_{36}Fe_{57.6}$ $Co_{6.4}$)(20 nm)/Pt(4.1nm)/Co(1.2nm)/Pt(5nm) sample. The opposite sign of the exchange bias H_b shift with respect to the one observed in FeCo rich samples indicates that the Co/Pt layer is coupled with the FeCo sublattice instead of the net moment, as expected for interlayer exchange coupling (Figure from Ref [21]).

The magnetic hysteresis loops in Figure 5.3 (b) are also used to characterize the type of the interlayer exchange coupling between the stacks. For the weakly coupled samples with spacer thicknesses d = 4 nm and d = 5 nm, minor hysteresis loops, where only the low coercivity Co/Pt magnetization is switched (blue circles in Figure 5.3 (b)) are performed. The shift of the minor loop seen in these figures correspond to the interlayer bias field H_b. For both samples, this bias field is quite small, ~20 Oe. This

represents an antiferromagnetic (AFM) coupling between the net moments of the GdFeCo and Co/Pt at thick spacers, similar to the reports in Refs. [22, 23, 24]. An RKKY-type of exchange[22, 23, 24] or a dipolar orange peel coupling[22] could explain such AFM coupling. However, in similar stacks with Gd dominant ferrimagnets ($Gd_{36}Fe_{57.6}Co_{6.4}$), H_b has an opposite sign as shown in Figure 5.3 (c), demonstrating that the coupling does not follow the direction of the net moment of GdFeCo, but rather the orientation of the FeCo sublattices. This indicates that the coupling arises from an exchange energy between the sublattices, as a dipole coupling would depend on the net magnetization.

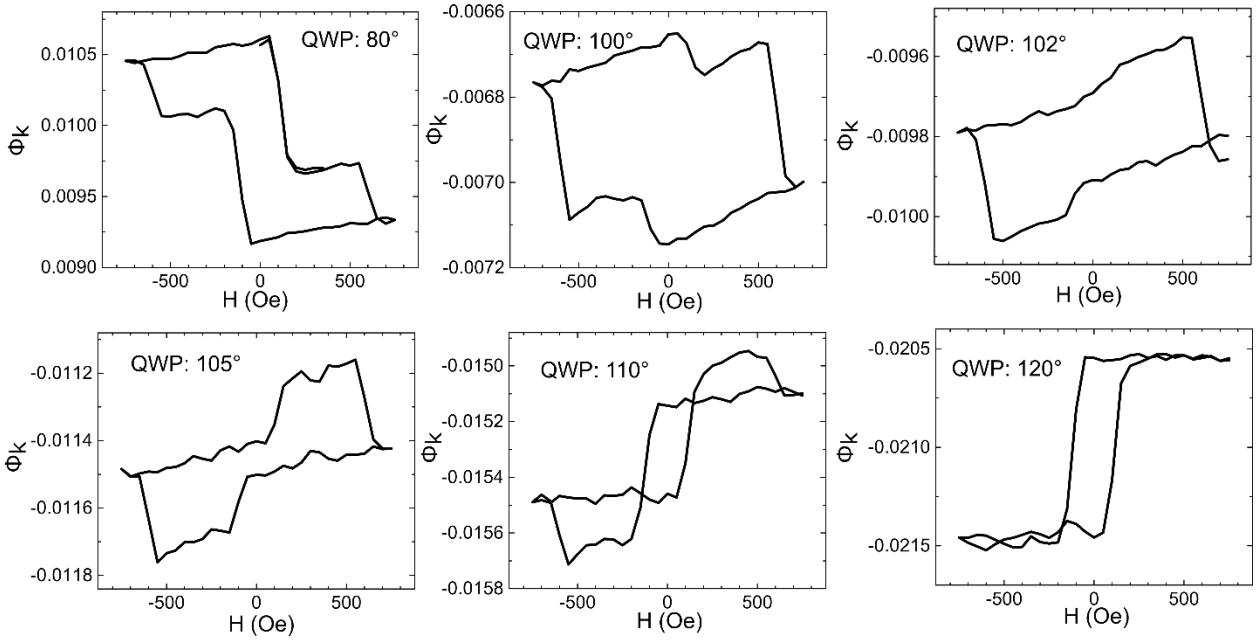

Figure 5.4 Depth sensitive hysteresis loops for different quarter waveplate angles α.
Hysteresis loops are taken using the depth-resolved MOKE microscope setup for the AFM coupled sample $Gd_{28}Fe_{65}Co_7$(20 nm)/Co(0.4 nm)/Pt(4 nm)/Co(0.6 nm)/Pt(3 nm). The microscope is sensitive to the GdFeCo and Co/Pt magnetizations at α = 102° and α = 120° respectively (Figure from Ref [21]).

A quarter wave plate is in the optic path placed after the polarizer to enable the depth-sensitive MOKE microscopy described in Section 5.3. It can be tuned to maximize sensitivity to either the ferromagnet or ferrimagnet layer. The quarter waveplate angles α at which the MOKE response is sensitive to only one layer is determined for all the samples in the series using the weakly coupled d = 4 and 5 nm samples that exhibit two distinct coercivities corresponding to the two magnetic films as follows. For either of these samples, starting at α = 0 (where the magnetic response works just like a regular image MOKE), the quarter waveplate angle is slowly rotated to tune the amplitude of the Kerr signals of the two layers and to minimize the magnetic sensitivity to one of the layers. Hysteresis loops are obtained at different α until a loop with only one coercive field (corresponding to the second layer) is observed. α is further rotated to then reduce the sensitivity to the second layer, until a hysteresis loop with a single coercivity corresponding to the first layer is observed. The hysteresis loops at different α for the d = 4 nm sample is presented in Figure 5.4. From this figure, α = 102° and α = 120° are the two angles at which layer sensitivity to either of the magnetic films is achieved. At each of these two quarter waveplate angles, the polarity of the (single coercivity) hysteresis loops and the direction of the

coercive "jumps" are compared with the hysteresis loop of the bare GdFeCo in Figure 5.4 to identify whether the magnetic response is arising from the GdFeCo layer or from the Co/Pt layer. Moreover, for these weakly coupled samples, the coercivity of the GdFeCo loop is expected to be similar to that of the bare GdFeCo, ~100 Oe, and the signal of this loop is expected to be larger due to its larger thickness. The two quarter waveplate angles corresponding to the Co/Pt and the GdFeCo layers are found to be the same for the d = 4 nm and d = 5 nm samples, and are assumed to remain unchanged for the strongly coupled samples as well. This is because nm scale variations in the nonmagnetic Pt spacer thickness should not influence the complex Kerr rotation. The layer-resolved MOKE hysteresis loops for the GdFeCo (green) and Co/Pt (blue) are shown in Figure 5.5. It must be noted that these hysteresis loops have been corrected for the Faraday effect (slanted hysteresis loops of Figure 5.4) of the objective lens.

As the Pt spacer thickness d of the main (FeCo dominant) series of samples is reduced, the magnetic responses of the GdFeCo and the Co/Pt show the same coercive field (Figure 5.3 (b) and Figure 5.5). This implies the existence of a strong ferromagnetic (FM) coupling between the magnetic moments of the two layers. It can be seen that as d is increased, the sign of coupling changes from FM to AFM coupling, and the coupling strength reduces. The net coupling is therefore attributed to an RKKY-type of exchange as reported in Refs.[22, 23, 24].

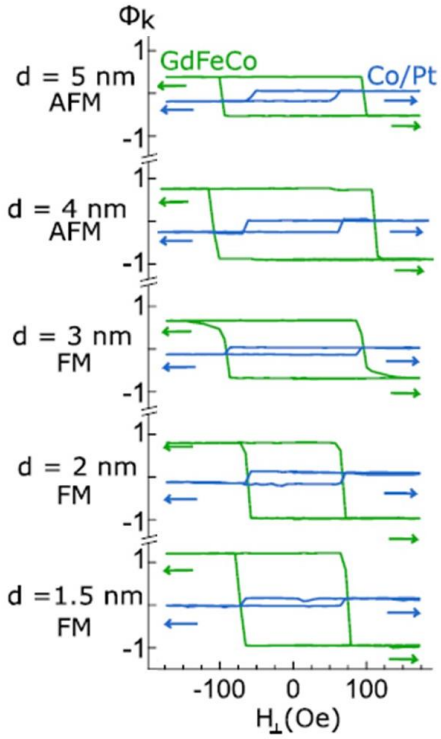

Figure 5.5 Depth resolved hysteresis loops of the GdFeCo and Co/Pt layers.
These are measured for samples in the main $Gd_{28}Fe_{65}Co_7$(20 nm)/Co(0.4 nm)/Pt(d)/Co(0.6 nm)/Pt(3 nm) series. The green and blue curves correspond to the quarter waveplate position for maximum

sensitivity to the FeCo sublattice of GdFeCo and the Co/Pt ferromagnet, respectively (Figure from Ref [21]).

5.5 HI-AOS of ferromagnetic Co/Pt with single optical pulses

The HI-AOS capabilities of the $Gd_{28}Fe_{65}Co_7$(20 nm)/Co(0.4 nm)/Pt(d)/Co(0.6 nm)/Pt(3 nm) stacks is tested with the MOKE microscope (see Section 3.2). The samples are irradiated with linearly polarized pulses from the regeneratively amplified Ti: Sapphire Rega 9050 (Coherent) laser, with a central wavelength of 810 nm and a pulse duration of 70 fs. The pulses are incident at the sample at 40° to the sample normal.

The MOKE micrographs of these single-shot events are presented in Figure 5.6 (a). The contrast in these images has been digitally recolored to better distinguish the four remnant states of the AFM samples. The magnetization of the Co/Pt ferromagnet and the dominant FeCo sublattice of the GdFeCo ferrimagnet are depicted by the blue and green arrows respectively. It must be noted that the magnetizations of these samples are perpendicular to the sample surface; the arrows are presented as pointing to the left or to the right just for clarity of analysis. In the digitally altered single shot images of Figure 5.6 (a), light brown and dark brown colors represent the two opposite configurations where the GdFeCo net magnetization (or the dominant FeCo sublattice) and the Co/Pt magnetization are ferromagnetically (parallel) aligned. Similarly, the white and purple colors represent the two opposite antiferromagnetically (antiparallel) aligned magnetic configurations. The magnetization directions on these regions is assigned and verified by comparing the intensity levels of the MOKE micrograph with the intensity levels of the MOKE microscope hysteresis loops (such as the ones presented in Figure 5.3 (b)) of a given sample for the same microscope configuration.

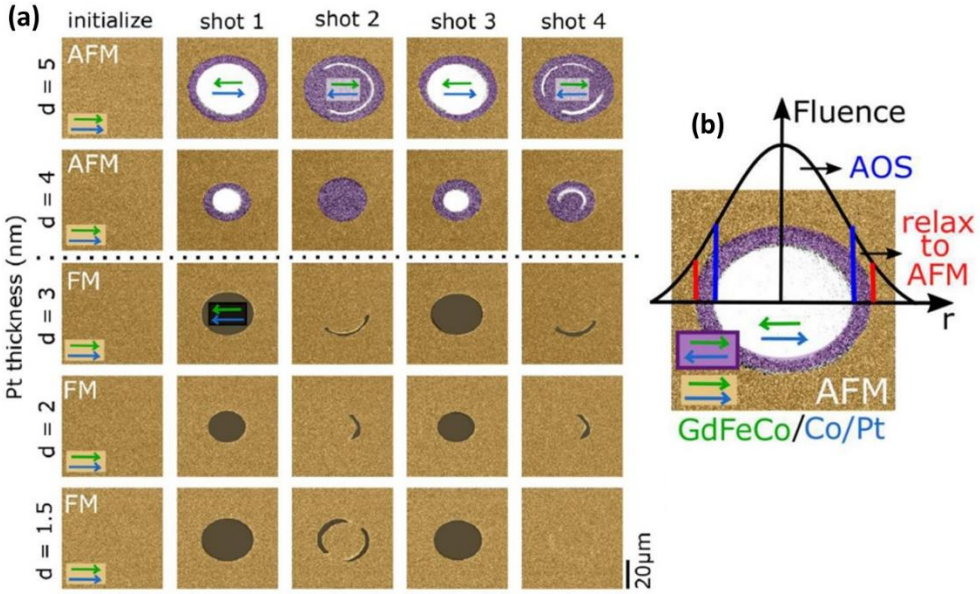

Figure 5.6 Single shot HI-AOS of ferromagnetic Co/Pt.
(a) Digitally re-colored MOKE images of a sequence of HI-AOS events on the GdFeCo/Co/Pt(d nm)/Co stack series. Green and blue arrows represent GdFeCo and Co/Pt magnetizations,

respectively. (b) Laser intensity profile and resulting domain configuration on film d = 5 nm after the first laser shot (Figure from Ref [21]).

The samples are initialized by a positive external magnetic field into a state where the GdFeCo and Co/Pt magnetizations are parallel. This is possible even for the AFM samples with d = 4 nm and d = 5 nm, because as seen from Figure 5.3 (b), the lowest coercivity of these samples (that of the Co/Pt, ~ 70 Oe) is less than the interlayer exchange bias field H_b (~20 Oe). However, this parallel configuration is energetically unfavorable for these two samples as the small H_b tends to align them antiparallel. Once the magnetizations of the ferromagnet and ferrimagnet are initialized to be parallel, the external magnetic field is turned off. The following analysis will be done first for the d = 5 nm sample depicted in the first row of Figure 5.6 (a). After the first single laser shot on this sample, two new regions of different contrasts are observed: a central white circle and the surrounding purple ring. As mentioned previously, these two regions correspond to the two opposite AFM configurations of the sample. The spatial fluence distribution of the laser pulse is assumed to be a Gaussean, as shown in Figure 5.6 (b). In the central white area, the laser intensity is above the critical fluence F_C required for HI-AOS of this stack, and is represented by the blue lines in the Gaussean laser pulse in Figure 5.6 (b). This causes the magnetization of the GdFeCo to reverse, as depicted by the change in direction of the green arrow. The Co/Pt magnetization remains in its original direction, since the reversal of GdFeCo relaxes the sample to a stable AFM state in the central white area. In the surrounding purple ring, the laser intensity (bound by the red and blue lines in the spatial Gaussean of Figure 5.6 (b)) is not high enough to trigger AOS, and therefore the GdFeCo magnetization does not reverse. The Co/Pt layer, however, becomes hot and its coercive field likely reduces. This causes the Co/Pt layer to switch over to the opposite magnetization direction, relaxing the stack to a stable AFM state. This presents a second threshold fluence for the relaxation from an FM state to a more stable AFM state for the samples with d = 4 nm and d = 5 nm. For regions outside the red line in the Gaussean laser pulse of Figure 5.6 (b), the fluences are insufficient to cause any observable changes to the static magnetic state of the film. When the sample is irradiated with a second and subsequent laser pulses, the GdFeCo in the central region switches, and as does the Co/Pt, leading to this region toggling between the two AFM configurations (white and purple). The annular purple ring outside this region remains unchanged with pulses after the first one, since the fluence is insufficient to switch the GdFeCo and the film is already in a stable AFM configuration. Similar switching behavior is observed for the d = 4 nm sample. This experiment is repeated by initializing the sample to an AFM state before irradiation. The ring outside the central switching region is no longer observed with the first (or any subsequent) laser pulse, indicating that this ring arises from the FM initialized sample relaxing to a stable AFM state.

The MOKE micrographs depicting HI-AOS for the FM coupled d = 1.5 nm, 2 nm and 3 nm samples are shown in the bottom three rows of Figure 5.6 (a). The samples are already initialized in their stable FM state, and therefore no annular AFM region is observed upon excitation with a laser pulse as is expected. The first laser pulse switches the magnetization of the GdFeCo in the central region of the pulse. The dark brown region indicates that the magnetization of the Co/Pt is reversed as well, preserving the FM state in this switched region. MOKE images show that successive laser pulses toggle the magnetization between the two opposite FM states. All the samples in the series are irradiated with more than 100 pulses and repeated and reproducible toggle switching is observed. These results present the first observation of single shot all optical toggle switching of magnetization

of a ferromagnetic film. It must be emphasized again that the laser pulses used for these experiments are linearly polarized and therefore the switching is helicity independent.

Multilayer absorption calculations (like the ones used in Chapter 3 and Chapter 4) based on the matric transfer method are performed to calculate the absorbed fluences in the various samples. The absorption per layer is calculated for a beam incident at 40 degrees to normal, with s-polarization, as these are the characteristics of the incident pump. The complex refractive indices used for this calculation and the corresponding absorption percentage of the various layers are tabulated in Table 5.1 for the AFM coupled sample with Pt spacer thickness d = 5 nm. The absorption profile of this sample is shown in Figure 5.7, and the total absorption of this stack is calculated to be 33%.

Layer	Thickness (nm)	Complex refractive index	Absorption by layer (%)
air	-	1	-
Pt	3	2.85 + 4.96i	6.4
Co	0.6	2.50 + 4.84i	1.0
Pt	5	2.85 + 4.96i	8.6
Co	0.4	2.50 + 4.84i	0.5
GdFeCo	20	2.66 + 3.56i	16
Ta	3	1.09 + 3.06i	0.8
SiO_2	100	1.45	0
Si	-	3.70 + 0.005i	-
air	-	1	-

Table 5.1 Multilayer absorption calculation parameters and results for the GdFeCo(20 nm)/Co(0.4 nm)/Pt(5 nm)/Co(0.6 nm)/Pt(3 nm) stack.

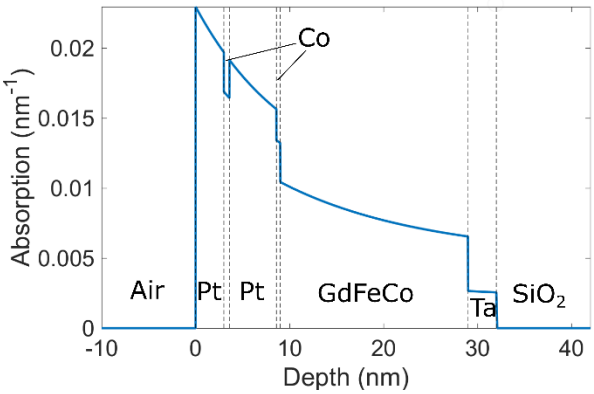

Figure 5.7 Absorption profile of the GdFeCo/Co/Pt/Co stack.

Depicted here is the absorption profile for the AFM coupled GdFeCo/Co/Pt(5nm)/Co/Pt stack obtained from multilayer reflectivity calculations based on the matrix transfer method (Figure from Ref [21]).

Knowing the net absorption of each sample and the threshold incident laser fluence for switching the sample, the absorbed critical fluence F_C can be calculated. The Gaussian profile of the laser intensity then allows the calculation of the threshold absorbed fluence required for the relaxation of an AFM sample from an initialized FM state to a stable AFM state in the purple annular region of Figure 5.6 (a). This threshold fluence and the critical absorbed fluence as a function of the Pt spacer thickness are shown in Figure 5.8. It is observed that F_C remains fairly independent of the Pt spacer thickness, and therefore also of the strength and type of the exchange coupling between the two films.

This Figure 5.8 also shows the transient equilibrium lattice temperature rise ΔT (when the electrons and phonons equilibriate with each other) for each of these samples when they are irradiated with a laser pulse with fluence F_C. ΔT is calculated from $\Delta T = F_C/Ct$ where, C ≈ 2.9 $MJK^{-1}m^{-3}$ is the weighted specific heat capacity of the entire stack (calculated using the specific heat capacity of GdFeCo of 3 $MJK^{-1}m^{-3}$ from Ref [2]) and t is the thickness of the stack.

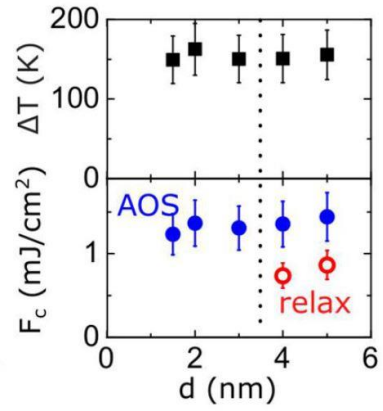

Figure 5.8 Critical fluences for switching and AFM relaxation as a function of Pt spacer thickness.
Absorbed critical fluence F_C for AOS (blue filled circles), fluence for relaxation of parallel states to a stable AFM state (red empty circles), and estimated peak lattice temperature rises ΔT (black squares) as a function of the Pt spacer thickness d (Figure from Ref [21]).

Per laser pulse, equilibrium temperature rises of ΔT = 150 ± 30 K is obtained for all films, irrespective of the type of coupling, since F_C is also observed to be independent of exchange coupling. Given a room temperature of ~300K, the Co/Pt is thus heated to 450 ± 30 K, very close to its expected Curie temperature T_C ~ 470 K[25]. This indicates that for HI-AOS to be possible in the films, the Co/Pt film needs to be almost completely demagnetized. In addition to exchange coupling mediated HI-AOS of these stacks, another possible mechanism that needs to be considered is the switching of Co/Pt by the hot electron spin currents between the layers during demagnetization[26, 27, 28]. If present, spin currents would have opposite signs for parallel and antiparallel alignments, resulting in different critical fluences for switching for the AFM and FM samples. However, as seen in Figure 5.8, the F_C for HI-AOS is the same for AFM and FM coupled films. This implies that spin currents are probably not important to the switching mechanism in these stacks.

5.6 Depth-sensitive time resolved MOKE experimental setup

To study the magnetic properties and the magnetization dynamics of the different layers of a multilayer magnetic stack, depth sensitivity is required. Section 5.3 details how adding a quarter waveplate after the polarizer of the incident LED beam of a MOKE microscope enables depth sensitivity for static measurements. Similarly, adding a quarter waveplate (QWP) to the laser probe path of the pump-probe time-resolved MOKE (TR-MOKE) setup of Section 3.4 enables depth sensitivity[19, 20], and the independent study of the magnetization dynamics of each of the magnetic layers of the stack.

A schematic of the depth-sensitive TR-MOKE setup is shown in Figure 5.9. As can be seen from this figure, the setup is almost exactly the same as a normal TR-MOKE setup (Figure 3.8), except for the quarter waveplate added in front of the 45° probe polarizer, and right before the photo-elastic modulator (PEM). As in the setup in Section 3.4, the PEM modulates the complex polarization $\Theta = \theta + i\varepsilon$ of the probe beam at a frequency of $f = 50$ kHz.

The quarter waveplate "mixes" the Kerr ellipticity ε and Kerr rotation θ of a film of the stack into a linear combination, which then allows the cancellation of magnetic signal from a particular film at a particular quarter waveplate angle. This is understood by using the Jones matrix formalism for the different optical components as follows.

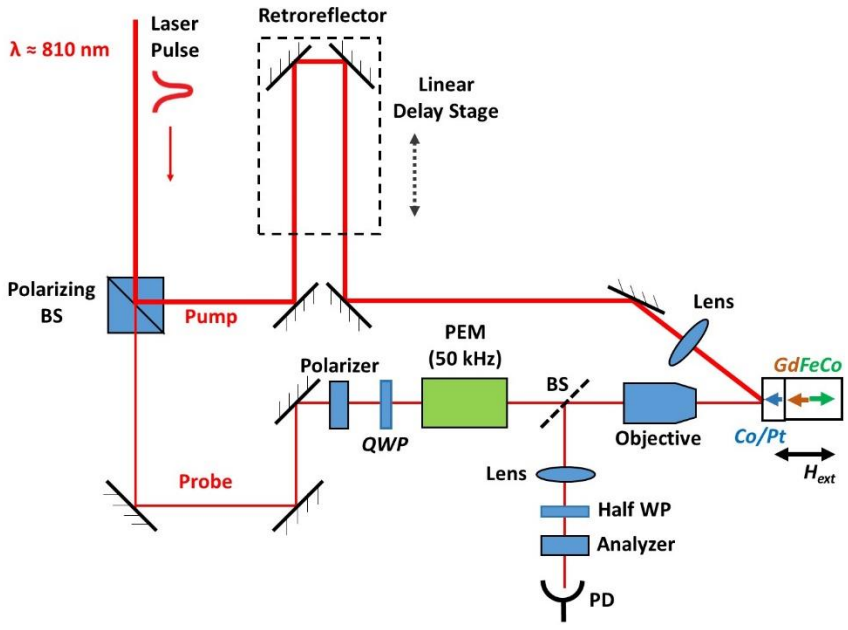

Figure 5.9 Schematic of the depth-sensitive time-resolved MOKE setup.
The main difference of this setup with respect to a regular TR-MOKE setup is the introduction of a quarter waveplate (QWP) before the PEM to enable depth sensitivity. (BS = beam splitter, PD = photodiode, QWP = quarter waveplate)

The polarizer renders the probe 45° polarized before it enters the quarter waveplate. This polarization can therefore be written as $\begin{pmatrix}1\\1\end{pmatrix}$ in the Jones matrix formalism. If α is the angle of the fast axis of the QWP with respect to the plane of incidence, and β is the amplitude of phase modulation of the PEM

(the retardation), the Jones matrices for the QWP and the PEM are then given by equations (5.1) and (5.2).

$$(5.1)\ WP = \begin{pmatrix} \cos\alpha & \sin\alpha \\ -\sin\alpha & \cos\alpha \end{pmatrix} \cdot \begin{pmatrix} 1 & 0 \\ 0 & i \end{pmatrix} \cdot \begin{pmatrix} \cos\alpha & -\sin\alpha \\ \sin\alpha & \cos\alpha \end{pmatrix}$$

$$(5.2)\ PEM = \begin{pmatrix} 1 & 0 \\ 0 & e^{-i*\beta*\sin(\omega t)} \end{pmatrix}$$

Here $\omega = 2\pi f$. The Jones matrices for the Kerr ellipticity ε and Kerr rotation θ of the sample can be written as:

$$(5.3)\ Kerr_{rot} = \begin{pmatrix} \cos\theta & -\sin\theta \\ \sin\theta & \cos\theta \end{pmatrix}$$

$$(5.4)\ Kerr_{el} = \begin{pmatrix} 1 & -i*\varepsilon \\ i*\varepsilon & 1 \end{pmatrix}$$

An analyzer with Jones matrix $A = \begin{pmatrix} 0 & 0 \\ 0 & 1 \end{pmatrix}$ is placed right before the detector.

By multiplying the Jones matrices in order – the 45° polarized beam, the QWP, the PEM, sample Kerr rotation and ellipticity, and the analyzer A – and by separating out the components of ω and 2ω, the final lock-in signals, V_ω and $V_{2\omega}$, at the PEM reference and its second harmonic respectively, can be found. V_ω and $V_{2\omega}$ are of the form

$$(5.5)\ \begin{pmatrix} V_\omega \\ V_{2\omega} \end{pmatrix} \propto \begin{pmatrix} -(\sin 2\alpha)^2 & -\cos 2\alpha \\ -\cos 2\alpha & (\sin 2\alpha)^2 \end{pmatrix} \begin{pmatrix} \theta \\ \varepsilon \end{pmatrix}$$

It can be seen from equation (5.5) that for a QWP angle $\alpha = 0$, the signal locked-in at ω is sensitive to the Kerr ellipticity ε, and the signal locked-in at 2ω measures the Kerr rotation θ, as was mentioned in the MOKE setup of Section 3.5. From equation (5.5), it can be seen that $V_\omega \propto \theta.(\sin 2\alpha)^2 + \varepsilon.\cos 2\alpha$ and $V_{2\omega} \propto \varepsilon.(\sin 2\alpha)^2 - \theta.\cos 2\alpha$. This means that the presence of the quarter waveplate "mixes" the Kerr rotation and Kerr ellipticity signals from the samples for any arbitrary QWP angle α that satisfies $\sin 2\alpha \neq 0$ and $\cos 2\alpha \neq 0$.

For a film with net magnetization M, the total Kerr ellipticity ε and the total Kerr rotation θ are proportional to M. Therefore $\varepsilon = \epsilon M$ and $\theta = \vartheta M$ where ϵ and ϑ are proportionality constants. Focusing only on the first harmonic locked-in signal of equation (5.5), the form of V_ω becomes

$$(5.6)\ V_\omega \propto M[\vartheta(\sin 2\alpha)^2 + \epsilon \cos 2\alpha]$$

Equation (5.6) implies that choosing the right angle α of the quarter waveplate, any linear combination ("mixing") of the Kerr rotation and ellipticity can be obtained. Specifically, there always exist an angle α such that the 2ω signal remains zero, and the magnetic response is annihilated.

For a stack with two magnetic films, like the ferrimagnet/ferromagnet stacks studied in this chapter, the magnetization, Kerr ellipticity and Kerr rotation of the two films can be denoted by M_1 and M_2, ε_1 and ε_2, and θ_1 and θ_2 respectively. Since the Kerr rotation and Kerr ellipticity are proportional to the magnetization, it can be written:

$$(5.7)\ \varepsilon_i = \epsilon_i M_i$$

$$(5.8)\ \theta_i = \vartheta_i M_i$$

ϵ_i and ϑ_i are proportionality constants for each layer i. The total Kerr ellipticity and the Kerr rotation of the stack are given by $\varepsilon = \varepsilon_1 + \varepsilon_2$ and $\theta = \theta_1 + \theta_2$. From the first harmonic locked-in signal of equation (5.6), it can then be seen that

$$(5.9)\ V_\omega \propto M_1[\vartheta_1(\sin 2\alpha)^2 + \epsilon_1 \cos 2\alpha] + M_2[\vartheta_2(\sin 2\alpha)^2 + \epsilon_2 \cos 2\alpha]$$

The right hand side of equation (5.9) can then be solved to find the QWP angles α at which the proportionality constant of the M_1 (or the M_2) term becomes zero. The setup then becomes sensitive only to the magnetization M_2 (or only to M_1), enabling the depth-sensitive, independent detection of the magnetization of a single layer. A similar analysis for the second-harmonic locked-in signal $V_{2\omega}$ yields similar results, but the QWP angles α for layer sensitivity might be different.

The setup discussed so far can work as a depth-sensitive laser MOKE system with the laser beam acting as the probe beam. A pump beam, time delayed with respect to the probe beam by passing it through a retroreflector on a linear delay stage as discussed in detail in Chapter 3, can then be introduced and focused onto the sample overlapping spatially with the probe beam. This then allows the setup to perform layer-resolved (depth-sensitive) time-resolved magnetization experiments.

5.7 Dynamics of magnetization reversal of exchange coupled Co/Pt films

The MOKE micrographs in Figure 5.6 (a) provide clear evidence of the HI-AOS of Co/Pt films with individual laser pulses. However, they cannot provide information on the switching speed of the ferromagnet, and whether ultrafast control over the exchange interaction is achieved. In order to access the fast magnetization dynamics, depth-sensitive time-resolved MOKE measurements (discussed in Section 5.6) are performed.

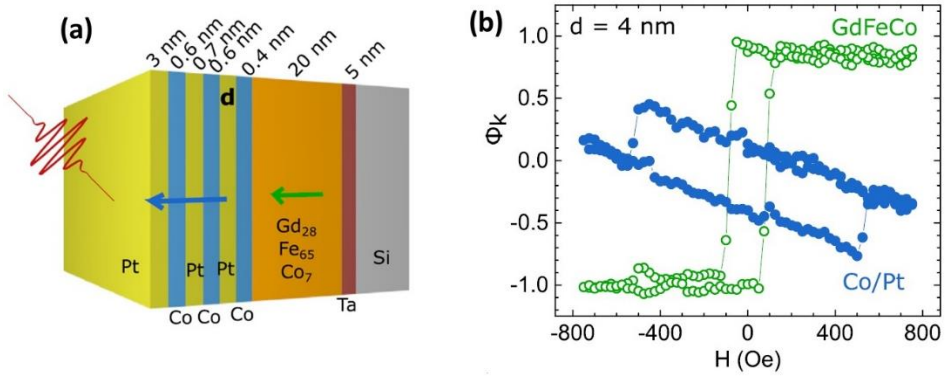

Figure 5.10 GdFeCo/ferromagnet stack used for depth-sensitive TR-MOKE measurements. (a) Schematic of the GdFeCo/Co/Pt(d nm)/$[Co/Pt]_2$ stack series with Pt spacer of thickness d. The additional Co/Pt repeat is added to increase the magnetic signal from the ferromagnet. (b) Depth-sensitive MOKE magnetic hysteresis loops on AFM coupled sample with d = 4 nm (Figure from Ref [21]).

For this purpose, a second series of ferrimagnet/ferromagnet film stacks are grown with the same values of Pt spacer thickness d as the series studied before in the static MOKE microscopy experiments (Sections 5.4 and 5.5). The schematic of films in this series is depicted in Figure 5.10 (a). This series of stacks differs from the previous one by one additional Co/Pt repeat in the ferromagnetic layer, which is included to increase the magnetic signal from the ferromagnet, which is required for time-resolved experiments. The samples presented the same type of exchange coupling as the previous series, with d = 4 nm and 5 nm samples showing AFM coupling, and d = 1.5 nm, 2 nm and 3 nm samples presenting a strong FM coupling. The depth-resolved static MOKE hysteresis loop for the d = 4 nm sample is presented in Figure 5.10 (b). It can be seen that the GdFeCo coercive field (green hysteresis loop) remains unchanged at ~100 Oe. However, the addition of a single Co/Pt repeat increased the coercivity of the ferromagnetic layer from ~70 Oe to ~500 Oe. MOKE microscopy experiments confirmed complete HI-AOS of the ferromagnetic layers in these samples also.

Time-resolved demagnetization measurements were performed on the AFM coupled sample with Pt spacer thickness d = 4 nm (with four remnant states) at a low pump fluence. The experiments were performed and compared for the sample being initialized in the unfavorable parallel (P) magnetization configuration and the energetically favorable antiparallel (AP) configuration. The demagnetization at low fluences is small, and can be recovered by just the magnetic anisotropy field of the layers, allowing both the P and AP configurations to revert back to their original initialized states between pump pulses. The high coercivity of the ferromagnetic film also acts favorably in recovering the original magnetization direction after a small demagnetization. Therefore a resetting magnetic field in between pump pulses is not required for this experiment. The quarter waveplate angles α at which the MOKE is sensitive to either layer are selected from the sample hysteresis loops at different α (see discussion around Figure 5.4).

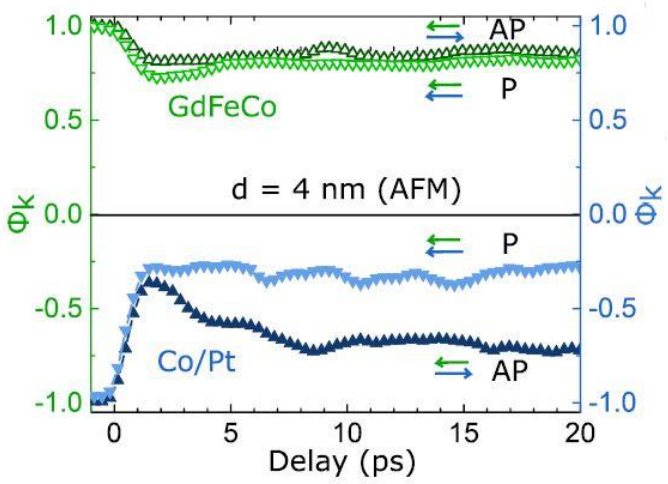

Figure 5.11 Investigation of spin currents in the dynamics of an AFM coupled ferrimagnet/ferromagnet stack.
Depth-sensitive time-resolved demagnetization curves for antiparallel (AP) or parallel (P) initial states of the AFM coupled stack with d = 4 nm. Green and blue arrows represent GdFeCo and Co/Pt magnetizations, respectively. The maximum demagnetization of both layers is the same irrespective

of initial state, suggesting that spin currents do not play a role in the HI-AOS of Co/Pt (Figure from Ref [21]).

The demagnetization dynamics of the Co/Pt ferromagnet (blue) and the dominant FeCo sublattice (green) of the GdFeCo ferrimagnet are shown in Figure 5.11 for both the P and AP starting configurations. The demagnetization of both GdFeCo and the Co/Pt peaks at around ~1–2 ps of delay time, in agreement with the reports where 60–70 fs laser pumps at high intensities were used[2, 29]. The Co/Pt and GdFeCo peak demagnetizations are similar in amplitude for both parallel (P) and antiparallel (AP) cases. The long timescale (2–20 ps) dynamics of the GdFeCo also seems unaffected by the initial state. However, the long timescale dynamics of the Co/Pt magnetization are very different. This result is rather surprising, since the same energy is deposited in the Co/Pt film in both P and AP cases, which should result in a similar spin temperature and magnetization at long time delays[26]. The slower recovery of the magnetization in the parallel case can therefore be attributed to the intrinsic AFM coupling field of the stack that pulls the Co/Pt against the anisotropy field, trying to align it antiparallel with GdFeCo. If spin currents were relevant during demagnetization, they should be maximized during the fast demagnetization (as generated spin current densities are proportional to $|\mathrm{d}M/\mathrm{d}t|$ [26]) and have opposite signs for P and AP cases. As can be seen from Fig, both the P and AP cases of initialization lead to a similar peak demagnetization of Co/Pt. This indicates that spin currents do not play a major role in the switching of the Co/Pt ferromagnet, thereby adding credence to the claim that the ferromagnet is switched by its exchange coupling with the GdFeCo.

To perform time-resolved switching experiments, the magnetizations of both ferromagnet and ferrimagnet layers needs to be reset to their initial directions after each laser pulse, due to the stroboscopic nature of pump-probe experiments. In previous Chapter 3 and Chapter 4, this was done by applying a constant external magnetic field as it was shown that the presence of this field is irrelevant for the switching behavior in the first tens of ps following laser irradiation. However, in the case of the ferrimagnet/ferromagnet stacks presented in this chapter, there is a possibility that an external field might influence the magnetization dynamics, as it cannot be readily assumed that such a field will not compete with the exchange coupling that is believed to be the driving mechanism of switching the ferromagnet. For this purpose, 300 nm thick Au is grown on top of the film by electron beam evaporation, and by photolithography and lift-off (the details of the lithography and evaporation steps are the same as the pattering of Au contacts to the heavy metal wires in Section 2.3), small coils of this film are patterned around the areas where the magnetization dynamics are studied (Figure 5.12 (a)). An amplified waveform generator is used to deliver 1 A, 2 μs wide pulses to these coils, thereby generating an Oersted field in the area of the film enclosed by the coil which resets the magnetization direction. The 70 fs pulse duration pump pulses, at a repetition rate of 54 kHz, are incident at the sample at 40° to the sample normal as in the single-shot MOKE microscopy experiments of Section 5.5. The current pulses applied to the Au coils are synchronized at 54 kHz with the laser repetition, such that their Oersted field resets the film magnetization between successive pump pulses. The low repetition rate of 54 kHz is chosen, just as in Chapter 4, to minimize the DC heating of the sample by the optical and current pulses.

Unfortunately, these time-resolved switching experiments could not be carried on the AFM samples with d = 4 nm and 5 nm, because the coercivity of the Co/Pt layer is larger than the amplitude of the reset magnetic field that could be generated with the patterned coils, and it proved impossible to reset

the film to a stable initial AFM state between pulses. The HI-AOS experiments are thus performed on the sample with thinner d = 1.5 nm Pt spacer, where both layers are strongly FM coupled and present a single and smaller coercivity (H ~ 100 Oe). This sample could be successfully reset to a stable FM state between pump pulses by the field delivered from the patterned Au coils. The incident average power is varied from 40 to 59 mW, and the resulting magnetization dynamics are shown in Figure 5.12 (b).

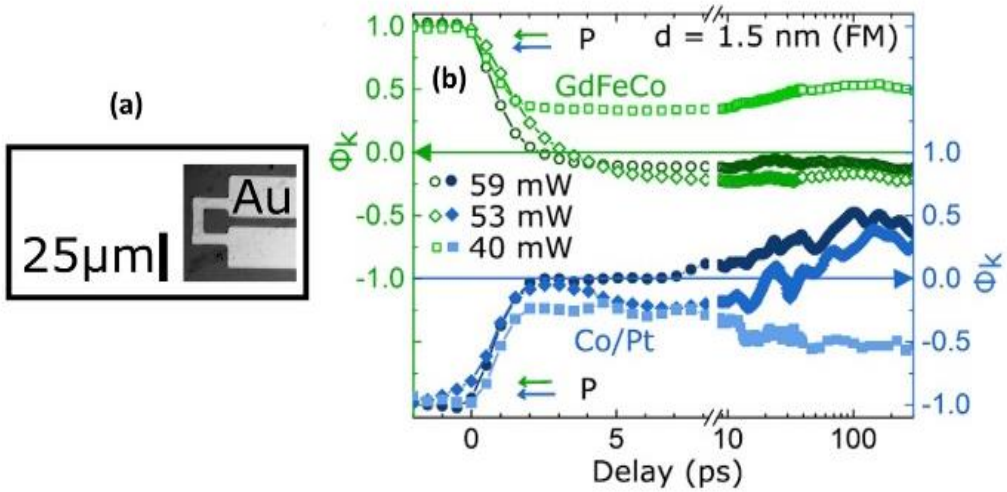

Figure 5.12 Switching dynamics of Co/Pt ferromagnet undergoing HI-AOS.
(a) Microscope image of patterned Au coils around areas of the sample surface where switching dynamics are studied. (b) Depth-sensitive demagnetization and HI-AOS experiments at various pump powers on the FM coupled sample d = 1.5 nm. The Co/Pt ferromagnet reverses its magnetization in ~7 ps after irradiation for an incident laser power of 59 mW (Figure from Ref [21]).

It can be seen that the dynamics of the GdFeCo and Co/Pt layers are quite different. At the lowest incident pump power, 40 mW, only a demagnetization of both GdFeCo and Co/Pt magnetizations is observed, after which they recover along their original initialized direction. Increasing the pump power to 53 mW results in the switching of GdFeCo within ~3 ps, as is expected for this ferrimagnetic alloy. During this time, the Co/Pt demagnetizes nearly completely. The magnetization of Co/Pt then recovers along its original direction over the next 4 ps as the system cools down. As the system cools down, the exchange field induced by the GdFeCo on the Co/Pt also starts to increase. Eventually, the Co/Pt magnetization switches after ~30 ps because of this exchange interaction with GdFeCo. At even higher laser power, 59 mW, the Co/Pt demagnetizes first in similar timescales and remains demagnetized for a few ps, and then grows in the opposite direction, switching in only ~ 7 ps post excitation. The two-steps of the 7 ps switching event of Co/Pt shown in Figure 5.12 (b) – an initial full demagnetization and a subsequent switching – strongly support the idea that the exchange interaction with the GdFeCo is responsible for the reversal of the softened (hot) Co/Pt magnetization. The curves at 53 and 59 mW indicate that the fastest switching occurs when the fluence is such that the temperature of the Co/Pt reaches exactly (or very close to) the Curie temperature T_C. This means that the Co/Pt needs to be almost completely demagnetized for the exchange interaction to switch it. The switching of the magnetization of the Co/Pt multilayers in 7 ps following pump pulse irradiation is the fastest reported switching of a ferromagnet.

5.8 Conclusions: Towards electrical readout of an ultrafast spintronic device

The results presented in this chapter prove conclusively that the exchange coupling arising from a film of ferrimagnetic GdFeCo can extend the HI-AOS capabilities of GdFeCo to a Co/Pt multilayer ferromagnet. By increasing the thickness of the Pt spacer, the sign and magnitude of the exchange coupling between the ferrimagnet and the ferromagnet changes in a manner that is consistent with the RKKY exchange interaction. HI-AOS is observed for all the samples of the series with Pt spacer thickness d ranging from 1.5 nm to 5 nm. The critical fluence F_C required for HI-AOS is independent of the spacer thickness and the type of exchange, indicating that spin currents are not crucial in the switching of the Pt. Time resolved pump-probe experiments on the AFM coupled d = 4 nm sample showed similar peak demagnetization of the Co/Pt ferromagnet for both the parallel and antiparallel initial configuration of the magnetizations, proving that the spin currents do not play a role in the HI-AOS of the ferromagnet. Work by Iihama et al.[28] performed on uncoupled [Co/Pt]/Cu/GdFeCo samples, on the other hand, showed that the Co/Pt ferromagnet switches due to the spin currents generated by the GdFeCo upon laser pulse excitation. A comparative study of the difference between switching the ferromagnet with the exchange field and with spin currents is needed to elucidate the difference between these two HI-AOS mechanisms. Modeling of the HI-AOS of Co/Pt ferromagnets with the exchange field is ongoing.

Time resolved HI-AOS experiments on the strongly ferromagnetically coupled d = 1.5 nm sample showed that the Co/Pt ferromagnet demagnetizes in the same timescale as the GdFeCo ferromagnet, and reverses its magnetization in ~ 7 ps. This is the fastest switching speed reported for a ferromagnet, and is ~10× faster than the fastest reported spin transfer torque (STT) device[30] which was shown to switch with 50 ps current pulses, and ~30× faster than the fastest reported spin orbit torque (SOT) device[31] which needed 210 ps current pulses for switching.

These results indicate that the ultrafast HI-AOS capabilities of GdFeCo can be easily extended to a wider range of ferromagnetic materials by exploiting the exchange interaction with GdFeCo. These magnetic stacks can then be integrated in an ultrafast spintronic device, with the ferromagnet/GdFeCo stack acting as the magnetic bit (typically the free layer of a magnetic tunnel junction). The large magnetization of the ferromagnet, as compared to that of the GdFeCo ferrimagnet, will enable the electrical readout of the MTJ with a large TMR ratio. These large TMR ratios are crucial for easier differentiation of the two magnetic states and for faster electrical readouts. It must be noted that switching a magnetic stack with short optical pulses is not feasible for on-chip integration. Future work will need to focus on (i) ultrafast switching of a coupled ferromagnet/ferrimagnet stack with short electrical pulses for electrical write and (ii) integration of the stack with an MgO barrier and a fixed magnetic layer to form an MTJ for electrical readout.

5.9 References

1. Ceballos, A., Pattabi, A., El-Ghazaly, A., Ruta, S., Simon, C. P., Evans, R. F. L., Ostler, T., Chantrell, R. W., Kennedy, E., Scott, M., Bokor, J. & Hellman, F. Role of element-specific damping on the ultrafast, helicity-independent all-optical switching dynamics in amorphous (Gd,Tb)Co thin films. *arXiv:1911.09803v3 [cond-mat.mtrl-sci]* 8 (2019).

2. Gorchon, J., Wilson, R. B., Yang, Y., Pattabi, A., Chen, J. Y., He, L., Wang, J. P., Li, M. & Bokor, J. Role of electron and phonon temperatures in the helicity-independent all-optical switching of GdFeCo. *Phys. Rev. B* **94,** 184406 (2016). https://doi.org/10.1103/PhysRevB.94.184406
3. Schubert, C. *Magnetic Order and Coupling Phenomena*. (Springer International Publishing, 2014). https://doi.org/10.1007/978-3-319-07106-0
4. Spaldin, N. *Magnetic Materials: Fundamentals and Applications*. (Cambridge University Press, 2010).
5. Ikeda, S., Hayakawa, J., Ashizawa, Y., Lee, Y. M., Miura, K., Hasegawa, H., Tsunoda, M., Matsukura, F. & Ohno, H. Tunnel magnetoresistance of 604% at 300K by suppression of Ta diffusion in CoFeB/MgO/CoFeB pseudo-spin-valves annealed at high temperature. *Appl. Phys. Lett.* **93,** 082508 (2008). https://doi.org/10.1063/1.2976435
6. Chen, J.-Y., He, L., Wang, J.-P. & Li, M. All-Optical Switching of Magnetic Tunnel Junctions with Single Subpicosecond Laser Pulses. *Phys. Rev. Applied* **7,** 021001 (2017). https://doi.org/10.1103/PhysRevApplied.7.021001
7. Radu, I., Vahaplar, K., Stamm, C., Kachel, T., Pontius, N., Dürr, H. A., Ostler, T. A., Barker, J., Evans, R. F. L., Chantrell, R. W., Tsukamoto, A., Itoh, A., Kirilyuk, A., Rasing, Th. & Kimel, A. V. Transient ferromagnetic-like state mediating ultrafast reversal of antiferromagnetically coupled spins. *Nature* **472,** 205–208 (2011). https://doi.org/10.1038/nature09901
8. Ostler, T. A., Barker, J., Evans, R. F. L., Chantrell, R. W., Atxitia, U., Chubykalo-Fesenko, O., El Moussaoui, S., Le Guyader, L., Mengotti, E., Heyderman, L. J., Nolting, F., Tsukamoto, A., Itoh, A., Afanasiev, D., Ivanov, B. A., Kalashnikova, A. M., Vahaplar, K., Mentink, J., Kirilyuk, A., Rasing, Th. & Kimel, A. V. Ultrafast heating as a sufficient stimulus for magnetization reversal in a ferrimagnet. *Nat Commun* **3,** 666 (2012). https://doi.org/10.1038/ncomms1666
9. Le Guyader, L., El Moussaoui, S., Buzzi, M., Savoini, M., Tsukamoto, A., Itoh, A., Kirilyuk, A., Rasing, Th., Nolting, F. & Kimel, A. V. Deterministic character of all-optical magnetization switching in GdFe-based ferrimagnetic alloys. *Phys. Rev. B* **93,** 134402 (2016). https://doi.org/10.1103/PhysRevB.93.134402
10. El-Ghazaly, A., Tran, B., Ceballos, A., Lambert, C.-H., Pattabi, A., Salahuddin, S., Hellman, F. & Bokor, J. Ultrafast magnetization switching in nanoscale magnetic dots. *Appl. Phys. Lett.* **114,** 232407 (2019). https://doi.org/10.1063/1.5098453
11. Lalieu, M. L. M., Peeters, M. J. G., Haenen, S. R. R., Lavrijsen, R. & Koopmans, B. Deterministic all-optical switching of synthetic ferrimagnets using single femtosecond laser pulses. *PHYSICAL REVIEW B* 5 (2017).
12. Lalieu, M. L. M., Lavrijsen, R. & Koopmans, B. Integrating all-optical switching with spintronics. *Nat Commun* **10,** 110 (2019). https://doi.org/10.1038/s41467-018-08062-4
13. Avilés-Félix, L., Olivier, A., Li, G., Davies, C. S., Álvaro-Gómez, L., Rubio-Roy, M., Auffret, S., Kirilyuk, A., Kimel, A. V., Rasing, Th., Buda-Prejbeanu, L. D., Sousa, R. C., Dieny, B. & Prejbeanu, I. L. Single-shot all-optical switching of magnetization in Tb/Co multilayer-based electrodes. *Sci Rep* **10,** 5211 (2020). https://doi.org/10.1038/s41598-020-62104-w
14. Lambert, C.-H., Mangin, S., Varaprasad, B. S. D. C. S., Takahashi, Y. K., Hehn, M., Cinchetti, M., Malinowski, G., Hono, K., Fainman, Y., Aeschlimann, M. & Fullerton, E. E. All-optical control of ferromagnetic thin films and nanostructures. *Science* **345,** 1337–1340 (2014). https://doi.org/10.1126/science.1253493
15. El Hadri, M. S., Pirro, P., Lambert, C.-H., Petit-Watelot, S., Quessab, Y., Hehn, M., Montaigne, F., Malinowski, G. & Mangin, S. Two types of all-optical magnetization switching mechanisms using femtosecond laser pulses. *Phys. Rev. B* **94,** 064412 (2016). https://doi.org/10.1103/PhysRevB.94.064412
16. El Hadri, M. S., Pirro, P., Lambert, C.-H., Bergeard, N., Petit-Watelot, S., Hehn, M., Malinowski, G., Montaigne, F., Quessab, Y., Medapalli, R., Fullerton, E. E. & Mangin, S. Electrical

characterization of all-optical helicity-dependent switching in ferromagnetic Hall crosses. *Appl. Phys. Lett.* **108,** 092405 (2016). https://doi.org/10.1063/1.4943107
17. Vomir, M., Albrecht, M. & Bigot, J.-Y. Single shot all optical switching of intrinsic micron size magnetic domains of a Pt/Co/Pt ferromagnetic stack. *Appl. Phys. Lett.* **111,** 242404 (2017). https://doi.org/10.1063/1.5010915
18. Schäfer, R. Magneto-optical domain studies in coupled magnetic multilayers. *Journal of Magnetism and Magnetic Materials* **148,** 226–231 (1995). https://doi.org/10.1016/0304-8853(95)00218-9
19. Schellekens, A. J., de Vries, N., Lucassen, J. & Koopmans, B. Exploring laser-induced interlayer spin transfer by an all-optical method. *Phys. Rev. B* **90,** 104429 (2014). https://doi.org/10.1103/PhysRevB.90.104429
20. Hofherr, M., Maldonado, P., Schmitt, O., Berritta, M., Bierbrauer, U., Sadashivaiah, S., Schellekens, A. J., Koopmans, B., Steil, D., Cinchetti, M., Stadtmüller, B., Oppeneer, P. M., Mathias, S. & Aeschlimann, M. Speed and efficiency of femtosecond spin current injection into a nonmagnetic material. *Phys. Rev. B* **96,** 100403 (2017). https://doi.org/10.1103/PhysRevB.96.100403
21. Gorchon, J., Lambert, C.-H., Yang, Y., Pattabi, A., Wilson, R. B., Salahuddin, S. & Bokor, J. Single shot ultrafast all optical magnetization switching of ferromagnetic Co/Pt multilayers. *Appl. Phys. Lett.* **111,** 042401 (2017). https://doi.org/10.1063/1.4994802
22. Metaxas, P. J., Jamet, J. P., Ferré, J., Rodmacq, B., Dieny, B. & Stamps, R. L. Magnetic domain wall creep in the presence of an effective interlayer coupling field. *Journal of Magnetism and Magnetic Materials* **320,** 2571–2575 (2008). https://doi.org/10.1016/j.jmmm.2008.03.041
23. Li, X.-X., Bao, J., Lu, L.-Y., Xu, X.-G. & Jiang, Y. Oscillatory antiferromagnetic interlayer coupling in Co/Pt multilayer with perpendicular anisotropy. *Solid State Communications* **148,** 209–212 (2008). https://doi.org/10.1016/j.ssc.2008.08.017
24. Liu, Z. Y., Zhang, F., Li, N., Xu, B., He, J. L., Yu, D. L. & Tian, Y. J. Oscillatory antiferromagnetic interlayer coupling in Co (4 Å) / Pt (t Pt Å) / [Co (4 Å) / Pt (6 Å) / Co (4 Å)] / Ni O (20 Å) multilayers with perpendicular anisotropy. *Phys. Rev. B* **77,** 012409 (2008). https://doi.org/10.1103/PhysRevB.77.012409
25. Metaxas, P. J., Jamet, J. P., Mougin, A., Cormier, M., Ferré, J., Baltz, V., Rodmacq, B., Dieny, B. & Stamps, R. L. Creep and Flow Regimes of Magnetic Domain-Wall Motion in Ultrathin Pt / Co / Pt Films with Perpendicular Anisotropy. *Phys. Rev. Lett.* **99,** 217208 (2007). https://doi.org/10.1103/PhysRevLett.99.217208
26. Malinowski, G., Dalla Longa, F., Rietjens, J. H. H., Paluskar, P. V., Huijink, R., Swagten, H. J. M. & Koopmans, B. Control of speed and efficiency of ultrafast demagnetization by direct transfer of spin angular momentum. *Nature Phys* **4,** 855–858 (2008). https://doi.org/10.1038/nphys1092
27. Battiato, M., Carva, K. & Oppeneer, P. M. Superdiffusive Spin Transport as a Mechanism of Ultrafast Demagnetization. *Phys. Rev. Lett.* **105,** 027203 (2010). https://doi.org/10.1103/PhysRevLett.105.027203
28. Iihama, S., Xu, Y., Deb, M., Malinowski, G., Hehn, M., Gorchon, J., Fullerton, E. E. & Mangin, S. Single-Shot Multi-Level All-Optical Magnetization Switching Mediated by Spin Transport. *Adv. Mater.* **30,** 1804004 (2018). https://doi.org/10.1002/adma.201804004
29. Tsema, Yu., Kichin, G., Hellwig, O., Mehta, V., Kimel, A. V., Kirilyuk, A. & Rasing, Th. Helicity and field dependent magnetization dynamics of ferromagnetic Co/Pt multilayers. *Appl. Phys. Lett.* **109,** 072405 (2016). https://doi.org/10.1063/1.4961246
30. Lee, O. J., Ralph, D. C. & Buhrman, R. A. Spin-torque-driven ballistic precessional switching with 50 ps impulses. *Appl. Phys. Lett.* **99,** 102507 (2011). https://doi.org/10.1063/1.3635782

31. Garello, K., Avci, C. O., Miron, I. M., Baumgartner, M., Ghosh, A., Auffret, S., Boulle, O., Gaudin, G. & Gambardella, P. Ultrafast magnetization switching by spin-orbit torques. *Appl. Phys. Lett.* **105,** 212402 (2014). https://doi.org/10.1063/1.4902443

Chapter 6. Ultrafast spintronics: Switching GdFeCo with ps current pulses

The Chapter 3, Chapter 4 andChapter 5 of this thesis have dealt with the ultrafast response of the magnetization of various magnetic materials to short optical excitations. As mentioned in discussions of these chapters, laser excitations of the sub-ps (and ps) pulse durations are capable of reversing the magnetization of Gd-based rare-earth transition-metal (RE-TM) ferrimagnets, and coupled Co/Pt ferromagnetic films, within a few ps of irradiation, through the helicity-independent all optical switching (HI-AOS). These results provide a positive outlook for the application of this phenomena in ultrafast magnetic devices with switching speeds that are comparable to conventional semiconductor based devices.

However, typical femtosecond or picosecond pulse duration laser systems are bulky. For example, the regeneratively amplified Ti: Sapphire laser RegA 9050 used for most of the studies in this work is ~1.5 × 0.5 × 0.25 m^3 in size, and the entire laser system additionally consists of a Ti: Sapphire laser oscillator (Coherent Mantis) that seeds the RegA and a stretcher-compressor system that stretches and compresses the pulses before and after the RegA respectively. Both of these units are also around the same size as the RegA. The integration of a femtosecond (or picosecond) optical laser with on-chip integration is therefore not feasible. Integrated mode-locked lasers on chip are also infeasible as discussed in Section 1.7. Ideally, the ultrafast magnetic reversal must be triggered by short, high amplitude current pulses that are generated on-chip without the need for an external optical source. This chapter will survey and summarize work performed in our Nanostructures and Nanoelectronics group (Jeff Bokor group at UC Berkeley) and others in demonstrating the control of ultrafast magnetic phenomena without direct optical excitations, with a focus on the ultrafast toggle switching of GdFeCo by short, ps current pulses generated by a photoconductive Auston switch[1].

6.1 Ultrafast demagnetization without direct heating by optical pulses

Prior to the work reported in this chapter, there have been significant studies in triggering ultrafast magnetic phenomena without direct laser irradiation. Eschenlohr et al.[2] demonstrated in 2013 that exciting a 20 nm thin film of Ni capped by 30 nm of Au resulted in ultrafast demagnetization of the in-plane magnetized Ni. The demagnetization was similar to that of a similar reference Ni film without a thick Au capping layer, differing only by a delay in the demagnetization time (Figure 6.1). In this paper, it was estimated that 90% of the optical energy is absorbed by the Au layer, and Ni only absorbs 7% of the light. In comparison, the reference Ni film absorbs 70% of the reference light. Both samples showed a magnetization quenching (demagnetization) of 20% at the same laser fluence. The large demagnetization and delayed response of the Ni/Au sample is attributed to a current from the superdiffusive transport of hot, non-spin-polarized and non-equilibrium electrons generated in the optically excited Au film. This work concludes that direct optical excitation is not a requisite for ultrafast demagnetization. The scenario of interaction of the spins with the laser field[3, 4], which was once proposed as a possible cause of ultrafast demagnetization is therefore discarded. In subsequent years, the calculation of 90% absorption by the Au layer in the Eschenlohr work has been challenged[5]. However, as will be seen from more recent experiments[6, 7, 8] (mentioned in Section 6.2), similar results were observed in the ultrafast magnetization reversal of GdFeCo capped with Au layers as thick as

200 nm, where the optical absorption by the GdFeCo is truly negligible. In this chapter, the ultrafast heating of a magnet by hot, unpolarized, superdiffusive electronic current will be referred to as "remote heating" because the laser pulse does not directly heat the magnetic film studied.

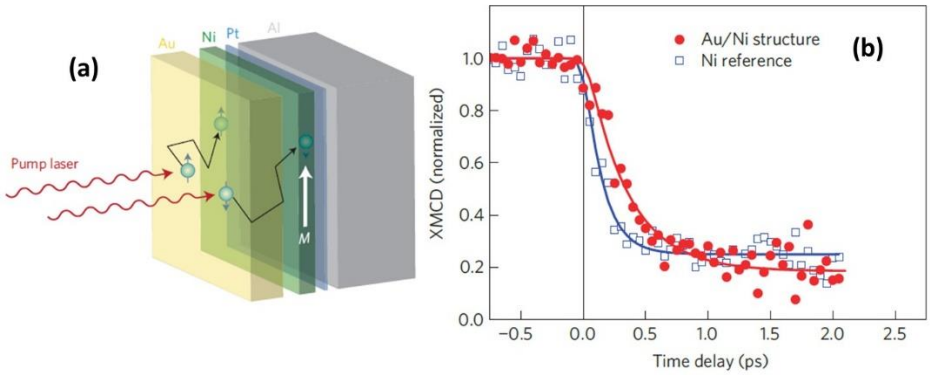

Figure 6.1 Ultrafast demagnetization of Ni by electronic heat currents.
(a) Schematic of the Ni(20 nm)/Au(30 nm) stack used in the work of Eschenlohr et al.[2] The laser pulse excites the top Au layer, generating a superdiffusive electronic current that demagnetizes Ni. (b) The demagnetization dynamics of the Ni in the Ni/Au film (red), compared with that of a reference Ni film (blue). The degree of demagnetization is the same, but the Ni/Au film exhibits a delayed demagnetization (Figure adapted from Ref [2]).

Experiments have also demonstrated high-intensity, free-space THz radiation can also cause ultrafast demagnetization in magnetic thin films. Bonetti et al.[9] excited an amorphous magnetic film of CoFeB with THz pulses generated at 1 kHz repetition rate from a $LiNbO_3$ crystal. The THz pulses had a single cycle transient, and a peak electric field of 15 MV/m, and a spectral density in the range of 0.5-1.5 THz. The CoFeB film demagnetized within ~2 ps of excitation, and the demagnetization percentage increased with the intensity of the THz radiation. Similar work by Shalaby et al.[10] showed ultrafast demagnetization of a 15 nm sputtered Ni film by a ~1 ps wide free space-THz pulse with a peak electric field of 33 MV/m, and spectral range of 1 – 4 THz. Radu et al.[11] in 2017 demonstrated the ultrafast toggle switching of the magnetization of GdFeCo by single free space THz pulses. These experiments on the ultrafast control of magnetic order raise interesting questions on the mechanisms of non-equilibrium energy transfer during ultrafast magnetic processes. Some of these considerations will be discussed briefly in Section 6.8. Nonetheless, these free-space THz experiments indicate that heating magnetic films in the ps timescales will be sufficient to trigger ultrafast demagnetization or even magnetization reversal, echoing the conclusions drawn from the observation of HI-AOS of GdFeCo with ps optical pulses, as discussed in Chapter 3.

6.2 Indirect switching of GdFeCo by electronic heat currents

As mentioned in Section 6.1, the experiment performed by Eschenlohr et al.[2] to demonstrate ultrafast demagnetization of Ni by remote heating from the superdiffusive electronic heat currents generated by a 30 nm thick Au film grown on top underestimated the optical absorption of the Ni film. However, subsequent experiments were able to demonstrate similar results, wherein the magnetic film studied had negligible optical absorption. Vodungbo[6] et al observed that multilayers of ferromagnetic Co/Pd ($[Co(0.4\ nm)/Pd(0.2\ nm)]_{30}$) capped by 40 nm of Al showed ultrafast demagnetization. The 40 nm

cap Al cap is opaque to the infra-red excitation wavelength and is expected to transmit very low optical intensities to the underlying magnet. The dynamics of demagnetization of the capped sample were slower and occurred with a delayed onset compared to an uncapped Co/Pd reference film. The observations were qualitatively in line with theoretical predictions of energy transport from the Al film to the underlying magnetic film by the excited hot electrons of Al. Similarly, Bergeard et al.[12] reported ultrafast demagnetization of ferromagnetic Co/Pt multilayers buried under Cu films with up to 200 nm thickness. The thicker Cu films successfully prevent significant optical absorption by the Co/Pt magnet. As the Cu thickness is increased, the electronic currents take longer to arrive at the magnet, and the demagnetization onset gets delayed as seen in the previously mentioned works. In this experiment, the relaxation length of the excited hot electrons is calculated to be smaller than the Cu cap thickness. Therefore the hot electrons are expected to propagate through the Cu layer without experiencing significant scattering, i.e., the electrons undergo ballistic transport. Moreover, simulations based on the microscopic three-temperature model[13, 14] and modified to incorporate hot electron ballistic transport were able to reproduce the experimental results.

In the Bokor group, remote heating experiments were performed on $Gd_{34}(Fe_{90}Co_{10})_{66}$ (10 nm)/Au(d)/Pt(6 nm) samples[7], where the ferrimagnetic GdFeCo is buried under Au films of varying thickness d and capped with Pt. d is varied between 0 to 200 nm. For films with Au thickness greater than 50 nm, most of the optical energy is absorbed in the Pt and Au layers, leaving the GdFeCo to be excited only by the excited hot electrons. The electronic heat currents were calculated to have a duration of several picoseconds. Fast switching, in ps timescales, by the current of hot electron was observed in all the samples. The presence of the Au overlayer delayed the switching compared to the d = 0 sample, as observed in the other works discussed in this chapter so far. To verify the need of electronic heat currents to cause switching, a similar film $Gd_{34}(Fe_{90}Co_{10})_{66}$ (10 nm)/Au(5 nm)/MgO(3 nm)/Au(75 nm)/Pt(6 nm), where the Au layer is interrupted by a film of MgO, was studied. The insulating MgO prevents electronic heat currents from reaching the GdFeCo. This sample did not show switching, proving that the electronic heat currents indeed cause switching in the GdFeCo/Au films. According to thermal modeling and calculations used in this work, following the optical excitation of the top Pt layer, the Au electron temperature exceeds 1000 K. The high diffusivity of Au electrons allows rapid heat diffusion[15], resulting in picosecond heat currents with intensities as high as a few TWm^{-2} flowing into the GdFeCo, thereby causing it to switch. Analyses of experimental observations of demagnetization delays as a function of the Au thickness led to the conclusion that the electronic heat currents that cause the switching of GdFeCo are diffusive (and not ballistic) in nature, contrasting with the analyses of Bergeard et al.[12].

Similar remote heating experiments on GdFeCo were performed by Xu et al.[8]. Ultrafast magnetization reversal of GdFeCo by a current of excited hot electrons was observed in films of Ta(3 nm)/Pt(5 nm)/Cu(d)/GdFeCo(5 nm)/Ta(5 nm), when a laser pulse excited the Cu side of the sample. The Cu thickness d was varied from 0 to 200 nm. The magnetization dynamics slowed with increasing Cu thickness (Figure 6.2), and the experimental observations were explained as a consequence of the ballistic transport of hot electrons, in agreement with Bergeard et al.[12], but contradicting the analyses of Wilson et al[7]. It is likely that the different thick capping layer materials used (Au vs Cu) could explain the difference in transport properties of the hot electrons.

The studies summarized in Sections 6.1 and 6.2 provide conclusive evidence that direct heating by a laser pulse is not necessary to induce ultrafast demagnetization of a magnetic film, or the ultrafast toggle switching of a GdFeCo ferrimagnet. The free-space THz demagnetization and switching experiments add credence to the results from Chapter 3, in that ps heating stimuli are capable of triggering ultrafast magnetic processes. This is further backed by results on the toggle switching of GdFeCo by remote heating from hot electron currents, which are expected to be a few ps in duration. The remote heating experiments also prove that heating by a short pulse of hot electrons is capable of triggering the toggle switching of GdFeCo. All these results indicate that the ultrafast Joule heating of a magnet from an intense ps wide charge current pulse can potentially induce ultrafast demagnetization, and also toggle switching in Gd-based RE-TM ferrimagnets. Therefore next step towards demonstrating a prototype ultrafast spintronic device will need the excitation of a magnetic film with short charge current pulses, without any optical excitation applied directly on top of the film.

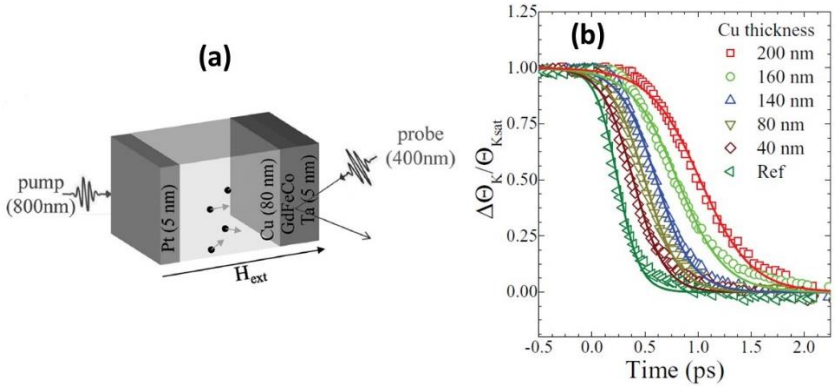

Figure 6.2 Ultrafast toggle switching of GdFeCo by remote heating.
(a) Schematic of the Ta(3 nm)/Pt(5 nm)/Cu(d)/GdFeCo(5 nm)/Ta(5 nm) stack used in the work of Xu et al. The GdFeCo is indirectly excited by a pump pulse on the Cu side. The external field H_{ext} resets the magnetization between pulses during TR-MOKE experiments. (b) Magnetization dynamics of the GdFeCo with different Cu thicknesses. The dynamics exhibit decreased speed and slower onset with increasing Cu thickness (Figure adapted from Ref [8]).

6.3 Generation and propagation of ps electrical current pulses with photoconductive LT-GaAs Auston switches

Low temperature grown GaAs (LT-GaAs) based photoconductive Auston switches[16, 17] are used in the Bokor lab to generate intense, ps wide electrical current pulses. LT-GaAs is extensively used in ultrafast opto-electronics due to its several unique properties, like low carrier lifetime and high mobility.

The LT-GaAs substrates (PAM-Xiamen) used to fabricate the Auston switches comprise of a 1 μm thick layer of LT-GaAs grown on a GaAs substrate by molecular beam epitaxy (MBE) at the relatively low temperature of 200-400°C[18, 19]. The low temperature growth leads to the formation of excess As clusters, which then lead to the mid-gap defect levels in the GaAs (Figure 6.3 (a)). When LT-GaAs is excited by optical pulses, electron-hole pairs are generated. The mid-band defects of LT-GaAs lead to the fast recombination of these excited electron-hole pairs, in the order of 1 ps. This is seen from

time-resolved transient reflectivity (also referred to as time domain thermal reflectance –TDTR for short) experiments performed on LT-GaAs, shown in Figure 6.3 (b). This pump-probe experimental setup is similar to the TR-MOKE experiment described in detail in Section 3.4, except that the reflected probe intensity is sensitive to changes in reflectivity of the sample rather than its magnetization. The pump beam is modulated by either a mechanical chopper (typically at 400 Hz) that provides on-off modulation of the pump intensity. In some cases (say, when using the 80 MHz high repetition rate oscillator laser), the pump intensity can instead be modulated by an electro-optical modulator (EOM) at ~1 MHz. The probe beam is spatially overlapped with the pump on the LT-GaAs, and the reflected probe intensity is detected by a photodector connected to a lock-in amplifier locked in at the reference frequency of the chopper (or EOM) modulation. The signal is therefore sensitive to pump-induced changes to the reflectivity of the sample. The probe does not need any modulation.

These transient reflectivity measurements provide information on the carrier lifetime of LT-GaAs as follows. As seen from Figure 6.3 (b), the transient reflectivity of LT-GaAs quickly changes as it is excited by the pump pulse. The excitation of electrons of LT-GaAs from the valence band to the conduction band by the pump pulse leads to a change in the conductivity, and therefore the refractive index of LT-GaAs. This is observed as a change in its reflectivity. In the next few ps, the electrons and holes start recombining in timescales given by the carrier lifetime of LT-GaAs. As the excited electrons relax back to the valence band, the reflectivity also reverts back to its original value. Therefore, studying the transient tail of such a reflectivity measurement will enable the extraction of the carrier lifetime of LT-GaAs[20, 21]. The LT-GaAs sample measured in Figure 6.3 (b) has a carrier lifetime of ~2 ps.

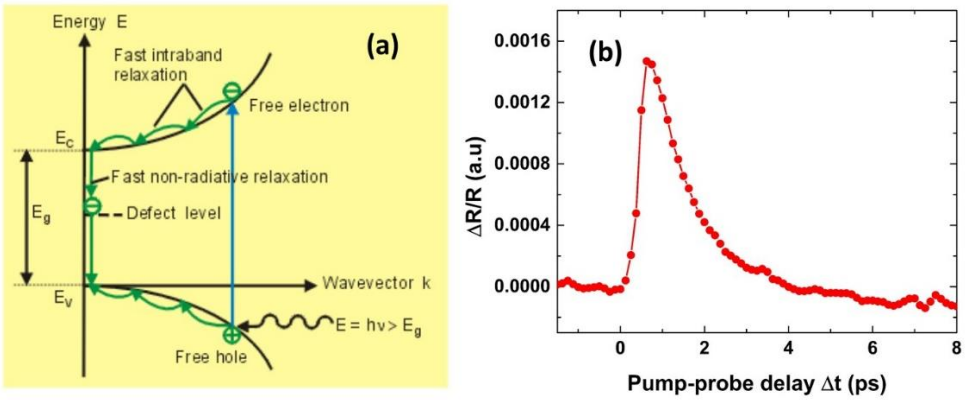

Figure 6.3 Free carrier lifetime in LT-GaAs.
(a) *E-k* band diagram of LT-GaAs depicting a direct bandgap electron-hole pair generation with the absorption of a photon of frequency υ, leading to a fast non-radiative recombination (Fig from Ref [22]). (b) Typical transient thermal reflectivity response of a LT-GaAs film, measured after excitation with a pump laser pulse, indicating short ~2 ps free carrier lifetime.

In addition to its low carrier lifetime, LT-GaAs has a high carrier mobility, and a high resistivity (> 10^8 Ω-cm) when not excited by optical pulses. These qualities make LT-GaAs perfect material for generating short, intense, ps electrical pulses when used as photoconductive Auston switches. An image of a typical photoconductive switch used for ultrafast electrical experiments in this thesis is

shown in Figure 6.4 (a). The Auston switch shown in this Figure 6.4 (a) comprises of two Au electodes with interdigitated fingers making intimate contact with a small rectangular window of LT-GaAs. The LT-GaAs outside the window is covered by a layer of insulating MgO (see Section 6.5 for fabrication details) so that there is no current flow between the electrodes through the semiconducting LT-GaAs in areas outside of the Auston switch. A DC bias voltage (10s of volts) is applied across Auston switch through the two electrodes using a source-meter (Keithley 2400), and the digits of the electrodes amplify the electric field in the LT-GaAs window. The high DC voltage leads to a small leakage current, called the dark current, through the semiconducting LT-GaAs in the Auston switch when there is no optical excitation. When a short laser pulse irradiates the LT-GaAs of the Auston switch, carriers with short (2 ps) lifetime are excited. These carriers then experience the large electric field across the Auston switch, and therefore form a short, ps electrical drift current, which is launched into any electrical circuitry attached with the electrodes of the Auston switch. This train of electrical pulses leads to an average photocurrent (~few μA) that can be measured by the Keithley 2400. The focus of the laser beam and its position on the Auston switch can be optimized by a lens and a steering mirror, respectively, to maximize the photocurrent.

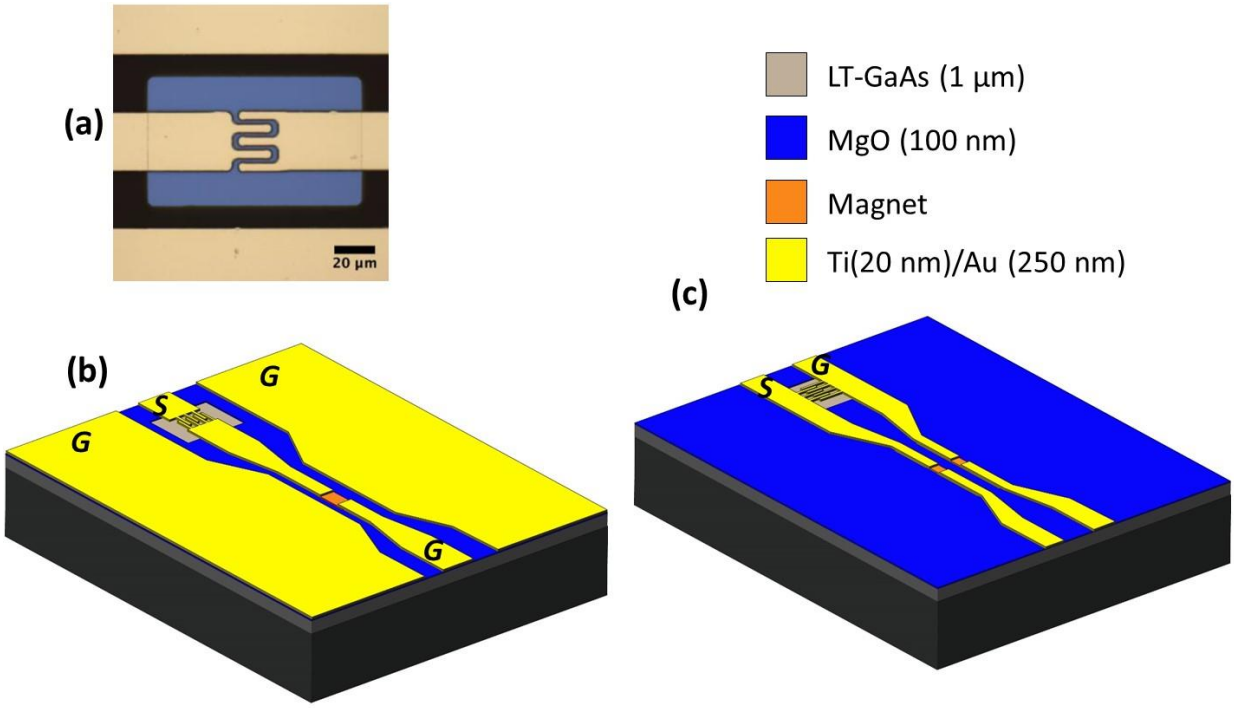

Figure 6.4 Auston switch-transmission line devices for ps electrical pulse generation.
(a) Microscope image of a patterned photoconductive Auston switch in a CPW transmission line. The Au electrodes have interdigitated fingers to enhance the *E* field across LT-GaAs (blue window, figure adapted from Ref [24]). Schematics of the CPW (b) and CPW (c) transmission lines integrated with Auston switches. S and G represent signal and ground for the DC biasing of the transmission lines. The inset of (c) depicts the different layers in (b) and (c).

For the prototype studies demonstrating ultrafast magnetism effects with these short ps electrical currents, laser-pump probe experiments are required, wherein the pump beam triggers the photoconducting Auston switch and generates the electrical pulse, and the probe beam detects the

magnetization dynamics of a magnet triggered by the electrical pulse. In order to spatially separate the sample magnet from the pump beam, the magnetic load is fabricated ~2 mm away from the Auston switch. Short ps electrical pulses are prone to broadening by dispersion while traveling these distances. Therefore low loss transmission lines, both in the ground-signal-ground (GSG) coplanar waveguide (CPW) configuration and the ground-signal (GS) coplanar stripline (CPS) configuration, are designed and integrated with the Auston switch to deliver the ps electrical pulses on to islands of the magnetic film to be studied. Schematics (not to scale) of Auston switch devices with CPS and CPW transmission lines and integrated magnetic loads are shown in Figure 6.4 (b) and (c). The fabrication of these devices will be detailed in Section 6.5. Each chip of these Auston switch/transmission line devices is fabricated to contain 6 – 8 such magnetic devices, with a mix of CPS and CPW configurations.

CPS and CPW transmission lines of varying dimensions were designed. The following will detail only one ideal design for each of these configurations. Near the Auston switch, a typical CPS transmission line used in this study has a ground and signal lines of width 50 μm with a gap of 30 μm. The transmission lines are then tapered over a length of 0.5 mm to a width of 5 μm (the magnetic sample width), with a 6 μm gap, in order to increase the current density delivered to the magnetic sample. The ratio of the widths of the lines and the gap are kept constant throughout the taper in order to preserve the characteristic impedance Z_0 = 60 Ω of the lines. A typical CPW also has a characteristic impedance Z_0 = 60 Ω. The central signal line of the CPW has a width of 30 μm, with 30 μm gaps on either side. This central line is tapered to a width of 5 μm (equal to the magnetic sample width), with 5 μm gaps on either side. The taper of the CPW lines is 0.6 mm long. Again, the ratio of the central line width and gap width is maintained constant throughout the taper to preserve the characteristic impedance. The capacitance, inductance, resistance and conductance per unit length of the transmission line are denoted by *C*, *L*, *R* and *G* respectively. *L* and *C* values are calculated from Ref [23]. The *R* and *G* values for the thick and thin regions of the CPS and CPW transmission lines, are tabulated in Table 6.1.

Transmission line segment	R (Ω/m)	G (S/m)
CPW 5 μm wide	4×10^4	0.14
CPW 30 μm wide	3×10^3	0.014
CPS 5 μm wide	10^4	0.14
CPS 50 μm wide	10^3	0.014

Table 6.1 Resistance and conductance per unit length for different transmission line segments.

6.4 Detection of ps electrical pulses by a THz probe tip

Section 6.3 detailed how the intense, short ps electrical pulses are generated using an LT-GaAs based photoconductive switch, and how they are launched through transmission lines into a magnetic load. These pulses must be detected and characterized, in order to quantify its properties like pulse width

and peak amplitude, and to keep track of spurious effects such as the dispersion from the transmission lines and reflections from various points of the transmission line.

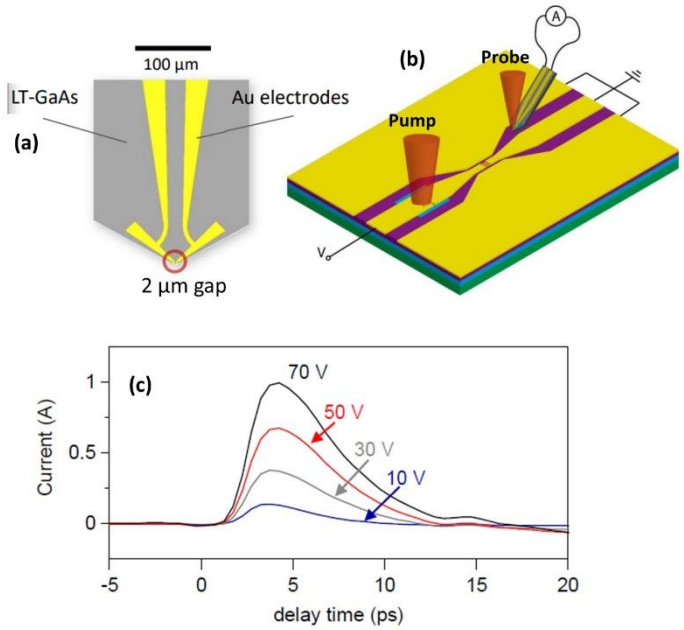

Figure 6.5 Detection of ps electrical pulses.
(a) Schematic of the Protemics Auston-switch based detector tip. A 2µm gap of LT-GaAs acts as the detector. The Au lines transmit the detected signal (From protemics.com). (b) Schematic of ps electrical pulse measurement on a CPW device. The pump laser beam excites the Auston switch of the device, launching electrical pulses. The probe beam is time delayed with respect to the pump and is aligned on the detector tip. (c) Typical measured current profiles for a CPW device at different DC bias voltages, with the detector ~1 mm away from the Auston switch (Figure adapted from Ref [24]).

An LT-GaAs based detector tip (Protemics) is used to characterize the ps current pulses. A schematic of this detector tip is shown in Figure 6.5 (a). This detector also acts as a photoconductive Auston switch (refer to Section 6.3 for the working of Auston switches), and is in a small 2 µm activation region at the tip of the detector. A coplanar stripline (CPS) transmission line is integrated with this detector tip in order to carry electrical signals without dispersion to an externally connected lock-in amplifier (or any other sensitive ammeter). Both the detector tip and the CPS are patterned on a flexible polyethylene terephthalate (PET) cantilever that can be placed in contact with any region of the transmission line where the pulses need to be characterized. A typical configuration for the measurement of ps electrical pulses in an Auston switch-transmission line sample is depicted in Figure 6.5 (b). The pump beam, intensity modulated by either a mechanical chopper or an EOM, irradiates the on-chip Auston switch of the sample and launches electrical pulses towards the magnetic load through the transmission line (CPW in the Figure 6.5 (b)). The detector tip is placed in contact with the CPW, on the gap near where the electrical pulse needs to be characterized. The weak probe beam is focused onto the detector tip. The probe beam excites (or "shorts") the photoconductive switch of the detector tip at certain time delays with respect to the time of arrival of the electrical pulse at the tip, and these delays can be varied by varying the pump-probe delay using the linear delay stage as in any usual time-resolved experiment. The electrical pulse generates an electric field across the

photodetector tip, which then acts similar to the DC voltage bias described for the fabricated on-chip Auston switch in Section 6.3. At a certain time delay, this electrical pulse arrives at the detector tip right when the tip is excited by the probe pulse, thereby launching an electrical signal that is picked up by the transmission line of the detector and measured by the ammeter or lock-in amplifier, locked in at a reference frequency equal to the modulation frequency of the pump. By fine tuning this delay, the probe pulse can "sample" the electric field intensity at different points of time in the electrical pulse. It must be noted that the obtained trace is actually a convolution of the electric field of the current pulse and the detector tip response.

The biasing DC voltage to the on-chip Auston switch is supplied by a Keithley 2400 voltmeter, which can also measure the average photocurrent generated by the Auston switch. Dividing this photocurrent by the pump repetition rate yields the total charge carried by each current pulse. Using the temporal profile of the current pulse measured by the detector tip, and assuming that all the charge of the pulse is contained within this profile, the current of each pulse can be calibrated. Example current profiles measured by the detector tip for different DC bias voltages across the Auston switch for a CPW structure is shown in Figure 6.5 (c).

6.5 Fabrication of Auston switch-transmission line devices

The fabrication of the Auston switch and transmission line devices for triggering ultrafast magnetic processes with electrical pulses involves three (or sometimes four) lithography steps. All of these steps are based on a bilayer photoresist lift-off process, which was first described in Section 2.3. An LT-GaAs chip (~9 × 9 mm^2) is first pre-baked at 150 °C for 5 minutes to remove any moisture that can hinder photoresist adhesion. LOR-5A (MicroChem) is then spin coated at 4100 rpm for 30 seconds using a Headway spinner. This is followed by a bake at 150 °C for 10 minutes. Next, the sample is spin-coated with OiR 906-12 (Dow Chemicals), the I-line photoresist, at 4100 rpm for 30 seconds, and baked at 90 ^{0}C for 1 minute. The post-bake steps drive off moisture from the photoresist and prevent it from sticking to the mask during contact lithography. The pattern for the required layer is patterned by exposing it to ultraviolet radiation in the I-line with a Karl Suss MA6 Mask Aligner, using a 5" chrome mask for the corresponding layer in the high-vacuum contact lithography mode. The exposure time is calculated from the aligner lamp intensity for a total dosage of 130mJ cm^{-2}. However, since the feature sizes that need to be patterned for these samples are quite small, down to 4 μm, most of the layers (except the MgO) must be underexposed by ~2-4% in order to discriminate these small features. Overexposure could result in important features that are in close proximity with each other to merge and cause device failure. For example, the ground and signal lines of the CPS transmission lines near the magnetic load are separated by 6 μm, and the interdigitated fingers of the Auston switch electrodes are separated by 4 μm. Slight overexposure could cause the shorting of these features, rendering the whole device worthless. It is therefore recommended to underexpose the photoresist for these critical layers. After exposure, the bilayer photoresist is developed in an OPD 4262 (Fujifilm) developer for 45 s to 60 s to remove the photoresist in the exposed regions, followed by a dip in a water bath for 45 s. The development of critical features is then inspected under an optical microscope. This is then followed by an O_2 plasma descum at 200 W RF power for 60 s in a YES G500 plasma cleaning system, which removes any remaining organic impurities in the patterned areas where the photoresist has been developed. Next, the required layer is deposited onto the patterned photoresist. The bottom LOR-5A layer forms an undercut during development which ensures that no sidewalls

are formed during thin film deposition. The film deposited on top of the remaining photoresist is lifted off by dipping the sample into a bath of Remover PG (MicroChem) or N-methylpyrrolidone (NMP, MicroChem) for 3+ hrs or overnight. Heating this bath at 60 °C can speed up this process. It must be noted that sonication is not recommended to aid liftoff, as it can easily remove patterned features too, especially the Au electrodes with low adhesion. Lift-off is usually achieved by subjecting the sample to a steady stream of isopropyl alcohol or DI water from a squirt bottle or a water gun over the photoresist stripper bath.

The process of the deposition and patterning of the different layers for the Auston switch-transmission line devices is depicted in the schematic of Figure 6.6 for the CPW transmission line device. It must be noted that the dimensions of this schematic are not to scale, and that the CPS transmission line fabrication follows exactly the same process flow. The three (or four) layers that are deposited during the fabrication of the devices are as follows. First, a 100 nm thick layer of MgO (or any other insulator like AlO_x) is stutter deposited on to the patterned GaAs/LT-GaAs(1 μm) chip by RF-sputtering (AJA sputter system) with an Ar/O_2 ratio of 16:1 at a pressure of 4.7 mT. After lift-off, the whole chip is covered with MgO, except for ~150 × 80 μm^2 windows that serve as openings for the Au electrodes to contact the LT-GaAs and form Auston switches. This MgO layer ensures electrical insulation between the Au electrodes of the transmission lines, except at the Auston switch. The absence of this layer would lead to large leakage dark currents arising from current flow through the semiconducting LT-GaAs.

The second optional step is the deposition of back contact to the devices. A back contact is needed for samples like Pt/Co, where it is essential to ensure direct electrical contact of the transmission lines with bottom Pt film so that current can flow preferentially through the nonmagnetic film and lead to current-induced spin accumulation (this device will be discussed in Chapter 7). ~25 nm of Au is deposited onto the patterned sample (with the MgO layer) by electron beam evaporation (in a CHA solution e-beam evaporator) at base pressures of $\sim 10^{-6}$ Torr. A thin ~5 nm film of Ti is evaporated before the Au to ensure the adhesion of the Au film. The layer thicknesses are monitored by a 6 MHz gold crystal monitor inside the evaporator. After lift-off, the back contact transmission lines with dimensions of 5 × 95 μm^2 coinciding exactly with the thin section of the top transmission lines (which will be deposited last) are left behind on the MgO layer. This step is not required for just Joule heating magnetic samples like the GdFeCo loads mentioned later in this chapter (Section 6.6) where the top transmission line ensures current flow through all the layers of the magnetic stack.

The third step is the deposition of the magnetic islands that will serve as the transmission line loads. The desired magnetic stack is grown by sputter deposition using the same process as the MgO layer. The magnetic stack is then patterned into loads of size 5 × 20 μm^2 overlapping with the bottom transmission line contacts, if exists, with their widths being perfectly aligned.

The fourth and final lithography step is the deposition and lift-off of the top Au transmission lines and Auston switches. A 20 nm thick Ti layer is deposited first to ensure adhesion of Au, followed by a 250 nm thick layer of Au. These layers are evaporated in the e-beam evaporator as with the bottom contacts. The thin 5 μm wide sections of these transmission lines are aligned perfectly with their corresponding bottom contacts. Each of these sections overlaps with a 5 × 7.5 μm^2 region of the magnetic load, thereby exposing an area of 5 × 5 μm^2 of the magnetic load in the final device.

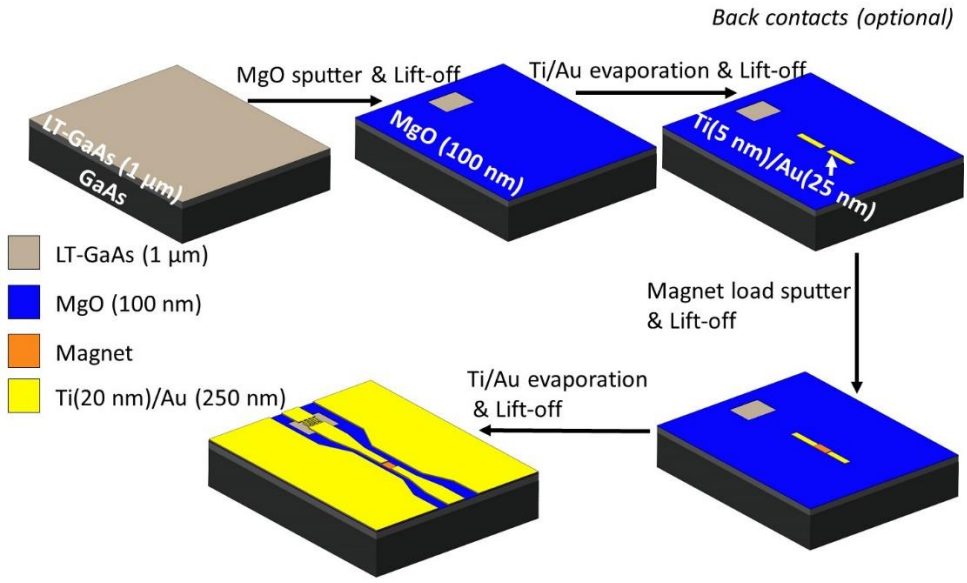

Figure 6.6 Auston switch-transmission line device fabrication flow.
Shown here for only CPW devices, the fabrication process is exactly the same for CPS devices also. The legend indicates the different layers in the final fabricated device.

The fabricated chip is then bonded onto a chip carrier using either silver paste or double sided Kapton tape. The Au pads of the top Au transmission line are then electrically connected to the leads of the chip carrier by wire bonding.

6.6 Toggle switching of GdFeCo with ps electrical pulses

To demonstrate ultrafast toggle switching of GdFeCo, magnetic loads of Ta(5 nm)/$Gd_{63}Fe_{63}Co_7$(20 nm)/Pt(5 nm) are sputter deposited and integrated with the CPS transmission line devices on LT-GaAs substrates[1] through the fabrication process detailed in Section 6.5. The aim of these devices is to heat up the entire stack with Joule heating by having the short ps electrical pulses flow through the films, and therefore these devices do not need a bottom contact. The samples presented perpendicular magnetic anisotropy with a coercive field of 80 Oe at room temperature, and a compensation temperature T_M of ~270 K.

The photoconductive Auston switch is then biased with a DC voltage of 40 V and irradiated with 60 fs, 810 nm central wavelength pump pulses from the regeneratively amplified Ti: Sapphire RegA 9050 laser. A schematic of the device, with pump laser excitation, is depicted in Figure 6.7 (a). The electrical pulses generated are then launched towards the magnetic load through the CPS transmission line and are detected and characterized by the Protemics THz detector tip, as described in Section 6.4. Electrical pulses with pulse durations of 9 ps FWHM, with peak amplitude of current density as high as 1×10^9 Acm^{-2} are detected. The inset of Figure 6.7 (a) shows a current pulse with a peak current density of 7×10^8 Acm^{-2}.

Blank, unpatterned films of the Ta(5 nm)/$Gd_{63}Fe_{63}Co_7$(20 nm)/Pt(5 nm) stack are irradiated with laser pump pulses with pulse durations FWHM (full width at half maximum) ranging from 60 fs up to 10 ps to confirm that they exhibit HI-AOS with optical pulses. The MOKE microscopy images (see Section 3.2 for details of the setup) on the top of Figure 6.7 (b) confirm the helicity-independent all-optical switching (HI-AOS) of the magnetization of the film, as is expected for this material. The corresponding MOKE microscopy images for the patterned GdFeCo loads in the CPS transmission line are shown at the bottom of Figure 6.7 (b). The magnetic contrast of the patterned magnetic load at the center of the transmission lines in these images also toggles between light and dark gray with each successive pulse applied, proving that single ps electrical pulses can also trigger toggle switching of GdFeCo similar to an optical pulse excitation. This result, although quite remarkable for demonstrating the reversal of GdFeCo by ultrafast Joule heating, is expected from the discussions of Sections 6.1 and 6.2.

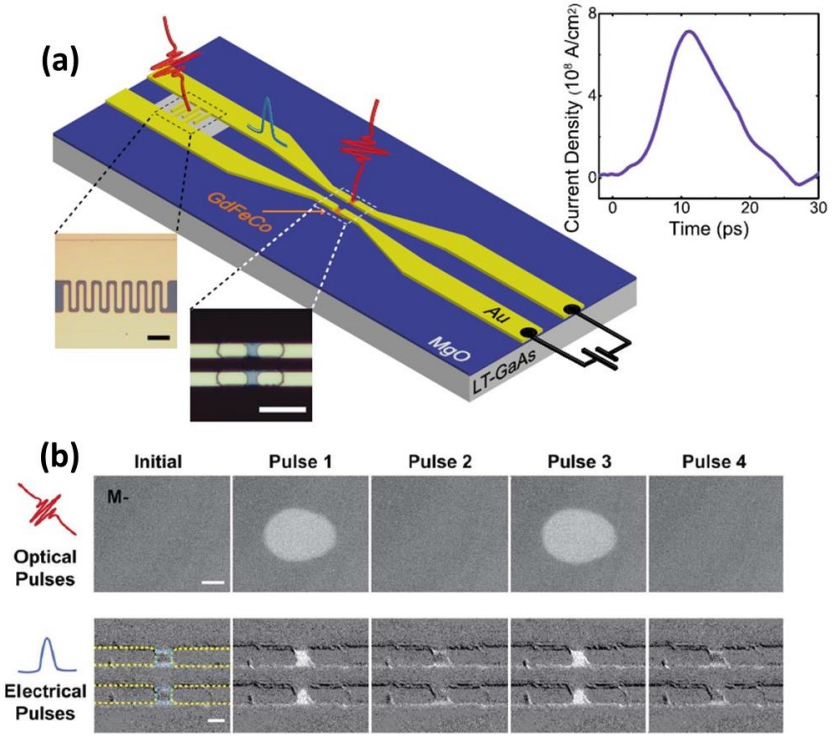

Figure 6.7 Toggle switching of GdFeCo with ps electrical pulses.
(a) Schematic of the Auston switch devices with CPS transmission lines used in Ref [1]. The enlarged pictures are microscope images of the Auston switch (left) and the magnetic load (right). The inset shows the detected current pulse at switching conditions with a peak current density of 7×10^8 Acm^{-2}. (b) MOKE microscope images depicting toggle switching of the magnetization of the Ta(5 nm)/$Gd_{63}Fe_{63}Co_7$(20 nm)/Pt(5 nm) stack by fs optical pulses (top) and by ps electrical pulses (bottom). The magnetic loads in the CPS lines are indicated by the blue squares in the leftmost image. The scale bars represent 5 μm (Figure adapted from Ref [1]).

6.7 Time dynamics of GdFeCo magnetization reversal by ps electrical pulses

It was shown in Section 6.6 that a single, intense ps electrical pulse can reverse the magnetization of GdFeCo by Joule heating[1]. Whether this switching occurs in an ultrafast manner needs to be confirmed. The magnetization of the GdFeCo load is monitored by a weak 60 fs probe pulse focused on to the magnet by a 50× objective. Similar to the TR-MOKE setup of Section 3.4, the time delay between the electrical pulse and the probe pulse at the sample is varied by passing the optical pump beam (that excites the Auston switch) through a linear delay stage. An external out-of-plane magnetic field of ~200 Oe is applied during the measurement to reset the magnetization between pulses.

Starting with a low bias voltage, weak electrical pulses that only cause demagnetization of the GdFeCo are obtained. This is shown by the curves with purple circles in Figure 6.8, where the GdFeCo demagnetizes in ~20 ps, followed by a recovery of magnetization in its original direction. As the bias voltage is increased, the electrical pulse amplitude increases and so does the Joule heating and the energy absorbed in the GdFeCo stack. This increases the degree of demagnetization of GdFeCo, as shown in Figure 6.8. At a high enough absorbed energy, the magnetization of GdFeCo reverses (dark blue squares in Figure 6.8). The magnetization reverses (crosses the $M = 0$ axis) within 10 ps of excitation, indicating that the magnetization reversal of GdFeCo with ps electrical pulses occurs in an ultrafast manner, similar to the HI-AOS of GdFeCo by ps laser pulses (Section 3.5).

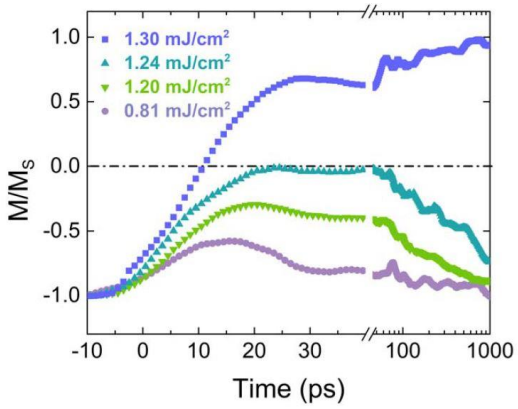

Figure 6.8 Switching speed of GdFeCo for different ps current pulse amplitudes.
Current pulses of different amplitude lead to different absorbed energies at the magnetic load, indicated in the legend (Figure adapted from Ref [1]).

The absorbed energy densities depicted in the legend of Figure 6.8 are with respect to the surface area of the magnetic load, and are calculated in two steps. First, the attenuation of the electrical pulse as it travels along the transmission line to the GdFeCo load is calculated as follows. The Fourier transform of the electrical pulse voltage $V(t)$ is calculated to get the spectrum $\tilde{V}(\omega)$. The energy spectral density is then proportional to $\left|\tilde{V}(\omega)\right|^2$. The voltage for an individual frequency ω at a distance x_0 away from the Auston switch is given by equation (6.1)

$$(6.1)\ \tilde{V}(\omega, x_0) = \exp\left(-\int_0^{x_0} \gamma\, dx\right)\tilde{V}(\omega, 0)$$

Here γ is the propagation constant defined by

$$(6.2)\ \gamma = \sqrt{(R + j\omega L)(G + j\omega C)}$$

R, *G*, *L*, and *C* are the resistance, conductance, inductance and capacitance per unit length of the transmission line. Their values for different wide and thin sections of the transmission line are described in Section 6.3. γ was assumed to vary linearly along the tapered section of the CPS. The energy attenuation for a single frequency ω is given by equation (6.3).

$$(6.3)\ \alpha_1(\omega) = \exp\left(-2\mathrm{Re}\left(\int_0^{x_0} \gamma\, dx\right)\right) \times \frac{Z_1(\omega)}{Z_2(\omega)}$$

Z_1 and Z_2 are the frequency dependent impedances of the 50 μm and 5 μm wide sections of the CPS respectively. These are calculated as

$$(6.4)\ Z_i = \sqrt{(R_i + j\omega L_i)/(G_i + j\omega C_i)}$$

The second step is the calculation of the absorption of the electrical pulse in the GdFeCo load. Multilayer absorption calculations based on the matrix transfer method (introduced in Chapter 3) are used for this. The electromagnetic waves are assumed to travel from the Au CPS into a 5 μm thick layer (equal to the magnetic load length) of the GdFeCo, and reflected back to the Au CPS. The effective complex refractive index of the Au and GdFeCo sections of the CPS are calculated by equation (6.5)

$$(6.5)\ n(\omega) = \mathrm{Conjugate}\left(\frac{\gamma c}{j\omega}\right)$$

Here c is the speed of light. The difference in the complex refractive indices of the Au and GdFeCo sections of the CPS transmission lines arise from the difference in their *R*. The GdFeCo section of the CPS is calculated to have $R = 2.48 \times 10^7\ \Omega/\mathrm{m}$ as opposed to $10^4\ \Omega/\mathrm{m}$ of the Au CPS section. The absorption $a_2(\omega)$ across the GdFeCo load can be then be calculated from the multilayer absorption calculation. The total absorption in the GdFeCo load is then calculated as equation (6.6).

$$(6.6)\ \alpha = \frac{\int \left|\tilde{V}(\omega)\right|^2 \alpha_2(\omega)\alpha_2(\omega)\, d\omega}{\int \left|\tilde{V}(\omega)\right|^2 d\omega}$$

The total pulse of the electrical pulse energy by the Ta/GdFeCo/Pt stack is estimated to be $a = 13\%$. The energy of the current pulse is calculated as $E = \int I(t)^2 Z_0 dt$. Z_0 is the characteristic impedance of the transmission line. The current pulse profile $I(t)$ is measured and calibrated as described in Section 6.4. Knowing *E* and *a*, the energy absorbed by the GdFeCo load can be calculated.

From Figure 6.8, it can be seen that absorbed energy density of 1.3 $\mathrm{mJ/cm^2}$ is required to observe switching of the GdFeCo magnetization in the time dynamics plot, while at 1.24 $\mathrm{mJ/cm^2}$ only exhibits demagnetization. This indicates that the critical fluence for switching is in between these two values, and the numbers are in agreement with the critical fluence for switching with optical pulses (Chapter 3).

Figure 6.9 shows the comparison of the time dynamics of the magnetization reversal with ps electrical pulses and laser pulses of various pulse durations. It must be noted that for a current pulse *I(t)* with a duration of 9 ps FWHM, the Joule heating pulse $I(t)^2$ has a FWHM of 6.4 ps. Therefore the dynamics with the 9 ps current pulse (purple squares in Figure 6.9) are compared with an optical pulse of duration 6.4 ps (orange triangles). The energy density for switching with the current pulse, 1.3 mJ/cm^2, appears to be smaller than that for the 6.4 ps optical pulse (1.65 mJ/cm^2) and even the 1 ps optical pulse (1.40 mJ/cm^2). The energy absorption calculation for the ps current pulses has a large margin of error, and therefore it is likely that the energy differences reported are insignificant. However, the switching with the electrical pulse led to a 70% recovery of GdFeCo magnetization in the opposite direction within just 30 ps of irradiation, while for the optical pulse, the magnetization recovery in this timescale is < 10%. These observations seem to imply that the electrical switching of GdFeCo is more efficient than optical switching. There is a possibility that the additive current-induced spin accumulation arising from the opposite spin-Hall angles of the Pt and Ta layers that flank GdFeCo on either side could exert spin-orbit torques that aid the switching of GdFeCo. But such considerations were shown to be irrelevant for this particular sample, and the maximum possible change in the out-of-plane component of magnetization due to spin orbit torques was calculated to be < 10%[1]. The potential of using the spin orbit torques arising from ps pulses, in addition to ultrafast Joule heating, will be explored in the next chapter.

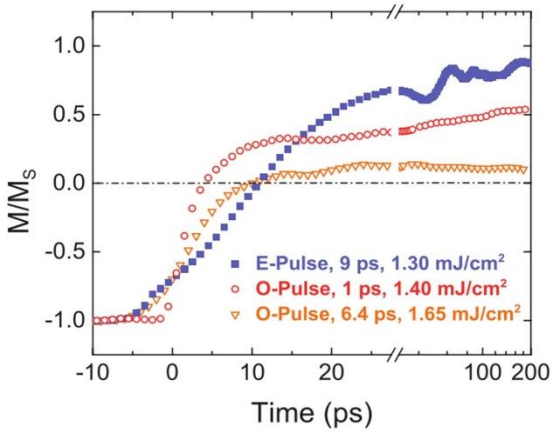

Figure 6.9 Comparison of GdFeCo switching dynamics for excitation with optical and electrical pulses.
The switching with ps electrical pulses (purple squares) recovers 70% of its magnetization within 30 ps of excitation, and appears to be more efficient than switching with comparable ps optical pulses (Figure adapted from Ref [1]).

The switching of GdFeCo with ps electrical pulses showed the potential for high endurance. The sample showed no degradation despite being irradiated for more than 10 hours at the laser repetition rate of 252 kHz. This corresponds to an endurance of > 10^{10} cycles, without any signs of electromigration or other forms of sample damage. This implies that device durability will not be an issue in any potential technology based on ultrafast magnetization reversal with ps electrical pulses. The expected endurance of 10^{10} cycles is several orders of magnitude higher than other competing technologies like resistive RAM, phase change memory, conductive bridge RAM etc.[25]

The energy density required to switch GdFeCo is calculated to be 13 aJ/nm^3. Assuming that this energy density remains constant for magnetic bits of all sizes, a magnetic bit with a cell size of (20 nm)^3, which is typical for magnetic memory, would require a current pulse with a peak current of 3 mA that delivers ~4 fJ of energy for switching. The energy required for switching remains low despite the high current density required because the electrical pulse duration is short. The picosecond electrical switching of GdFeCo can therefore be as energy efficient as the conventional spintronic STT and SOT schemes[26, 27, 28, 29], and yet more than one order of magnitude faster.

6.8 Comparison of excitation with ps electrical pulses vs fs optical pulses: Thermal vs non-thermal distributions

When a magnetic film is irradiated with a laser pulse, the optical energy is first absorbed by a small number of electrons of the film. These few electrons are excited to higher energy levels by a few eV, governed by the optical pulse wavelength. As described in the discussion in Section 3.1 of HI-AOS and other ultrafast magnetic processes, for a short time (~80 – 400 fs) following optical irradiation, the distributions of these eV excited electrons are non-thermal[24, 30], which means that Fermi-Dirac statistics cannot provide a description of the excited electron energies. It is still debated whether this initial non-thermal distribution of electrons plays an important role in the ultrafast demagnetization by laser pulses[2, 14, 31, 32]. Several studies have predicted the initially non-thermal distribution impacts ultrafast demagnetization because electronic scattering rates, which dictate spin flip through mechanisms like the Elliot-Yafet type scattering, depend on both the average energy and total number of electronic excitations[14]. The average energy and total number of excitations can also impact transport phenomena, which is considered by some as an alternative mechanism for the ultrafast demagnetization in metal multilayers[32]. After the first tens or hundreds of fs, the excited non-thermal electrons thermalize with the other electrons in the system, leading to a thermal distribution of electrons that can be described by Fermi-Dirac statistics.

Heating by a ps electrical pulse, on the other hand, leads to a large population of excited electrons with average energies less than 10 meV. This leads to an initial distribution of electrons that is already at thermal equilibrium with itself, and the distribution is said to be "thermal". The average energies of the initial thermal and non-thermal distributions are similar because the thermal distribution has a significantly large number of electrons excited to low energies. Both the thermal (electrical pulse excitation) and non-thermal (optical pulse excitation) initial distributions finally lead to the equilibration of the electron and phonon systems by electron-phonon scattering, in timescales of a few ps after excitation[24]. This is governed by the electron-phonon coupling constant g_{ep}, and the time scale of the thermalization between electrons and phonons[14] can strongly affect magnetization dynamics. g_{ep} depends both on the total number of excited electrons and their average energy.

Wilson et al.[24] showed that the differences in the ultrafast demagnetization of a Co/Pt ferromagnet by an electrical pulse and a laser pulse can be explained by assigning a larger g_{ef} to the case of electrical pulse demagnetization. The larger number of excited electrons in the initial thermal distribution caused by the electrical pulse is attributed as the reason for the increased g_{ep}. It is possible that the difference in initial electron distributions can contribute to the seemingly more efficient switching by the electrical pulse observed in Figure 6.9. More detailed studies are required to understand all the ways the initial electron distribution can affect ultrafast demagnetization and switching. Nonetheless, the ability

induce magnetization reversal in GdFeCo and ultrafast demagnetization in Co/Pt by picosecond electrical heating demonstrates that exciting a nonthermal electron distribution is not necessary for magnetization reversal, consistent with previous studies[7, 30, 33]. However, it is crucial that there be an initial non-equilibrium between the electrons and phonons for the observation of ultrafast magnetic phenomena. This cannot be triggered by heating pulses that are considerably longer than the time it takes for the electrons and phonons to equilibriate, which can vary from a few to few tens of ps. Therefore, one cannot expect ultrafast processes with optical or electrical pulses longer than, say, ~20 ps.

6.9 Conclusions

The different works summarized in this chapter prove that direct interaction with an optical pulse is not necessary to induce ultrafast magnetic processes. Building on the results from Chapter 3 of the HI-AOS of GdFeCo by 15 ps optical pulses, the work presented in this chapter shows that ultrafast toggle switching of GdFeCo can also be achieved from the Joule heating by ps electrical pulses. The electrical pulses were generated using LT-GaAs based photoconducting Auston switches, and delivered to patterned magnetic loads by CPS or CPW transmission lines. The magnetization of GdFeCo reverses within 10 ps when excited with a 9 ps electrical pulse. This result, as well as the evidence of switching of GdFeCo by electronic heat currents in the remote switching experiments, adds weight to the claim from Chapter 3 that peak electron temperatures $T_e > 1000$ K are not necessary for the ultrafast toggle switching of GdFeCo. Moreover, they also show that an initial non-thermal distribution of electrons, which can only be caused by short optical pulses, is not necessary to trigger ultrafast magnetic phenomena.

Switching the GdFeCo magnetization by the 9 ps electrical pulse, in addition to being ultrafast and potentially more efficient than optical switching, proved to be highly reproducible with an endurance $> 10^{10}$ cycles. The energy density required for calculated for switching, 13 aJ/nm^3 is similar to that in conventional spintronic devices that operate on the STT or SOT schemes, while also being up to two orders of magnitude faster than conventional spintronics. It must be noted that the photoconductive switch that relied on laser pulses was used to generate the ps current pulses for experimental convenience. It is currently possible to generate and deliver sub–10-ps current pulses on-chip in conventional complementary metal-oxide semiconductor (CMOS) electronics. For example, a 5-ps gate delay has been demonstrated with 45-nm CMOS technology[34]. Therefore, it should be possible to implement GdFeCo-based ultrafast on-chip memory and logic devices. A memory or logic device would also require an electrical readout. The addition of an oxide tunnel junction to the GdFeCo stack would enable an electrical readout of the magnetic state through the tunnel magnetic resistance (TMR). Coupling the magnetization of the GdFeCo with that of a ferromagnet through the exchange interaction can extend the ultrafast switching characteristics of GdFeCo to the ferromagnet (as described by the experiments in Chapter 5), which can then be used to enhance the TMR ratio of the readout. Such a device will then have an all-electrical read and write mechanism, as is needed for most on-chip electronics. Future work will focus on triggering ultrafast magnetization reversal with electrical pulses generated on-chip, and on the switching of coupled ferromagnet/ferrimagnet stacks by ps electrical pulses.

6.10 References

1. Yang, Y., Wilson, R. B., Gorchon, J., Lambert, C.-H., Salahuddin, S. & Bokor, J. Ultrafast magnetization reversal by picosecond electrical pulses. *Sci. Adv.* **3,** e1603117 (2017). https://doi.org/10.1126/sciadv.1603117
2. Eschenlohr, A., Battiato, M., Maldonado, P., Pontius, N., Kachel, T., Holldack, K., Mitzner, R., Föhlisch, A., Oppeneer, P. M. & Stamm, C. Ultrafast spin transport as key to femtosecond demagnetization. *Nature Mater* **12,** 332–336 (2013). https://doi.org/10.1038/nmat3546
3. Zhang, G. P., Hübner, W., Lefkidis, G., Bai, Y. & George, T. F. Paradigm of the time-resolved magneto-optical Kerr effect for femtosecond magnetism. *Nature Phys* **5,** 499–502 (2009). https://doi.org/10.1038/nphys1315
4. Bigot, J.-Y., Vomir, M. & Beaurepaire, E. Coherent ultrafast magnetism induced by femtosecond laser pulses. *Nature Phys* **5,** 515–520 (2009). https://doi.org/10.1038/nphys1285
5. Khorsand, A. R., Savoini, M., Kirilyuk, A. & Rasing, Th. Optical excitation of thin magnetic layers in multilayer structures. *Nature Mater* **13,** 101–102 (2014). https://doi.org/10.1038/nmat3850
6. Vodungbo, B., Tudu, B., Perron, J., Delaunay, R., Müller, L., Berntsen, M. H., Grübel, G., Malinowski, G., Weier, C., Gautier, J., Lambert, G., Zeitoun, P., Gutt, C., Jal, E., Reid, A. H., Granitzka, P. W., Jaouen, N., Dakovski, G. L., Moeller, S., Minitti, M. P., Mitra, A., Carron, S., Pfau, B., von Korff Schmising, C., Schneider, M., Eisebitt, S. & Lüning, J. Indirect excitation of ultrafast demagnetization. *Sci Rep* **6,** 18970 (2016). https://doi.org/10.1038/srep18970
7. Wilson, R. B., Gorchon, J., Yang, Y., Lambert, C.-H., Salahuddin, S. & Bokor, J. Ultrafast magnetic switching of GdFeCo with electronic heat currents. *Phys. Rev. B* **95,** 180409 (2017). https://doi.org/10.1103/PhysRevB.95.180409
8. Xu, Y., Deb, M., Malinowski, G., Hehn, M., Zhao, W. & Mangin, S. Ultrafast Magnetization Manipulation Using Single Femtosecond Light and Hot-Electron Pulses. *Adv. Mater.* **29,** 1703474 (2017). https://doi.org/10.1002/adma.201703474
9. Bonetti, S., Hoffmann, M. C., Sher, M.-J., Chen, Z., Yang, S.-H., Samant, M. G., Parkin, S. S. P. & Dürr, H. A. THz-Driven Ultrafast Spin-Lattice Scattering in Amorphous Metallic Ferromagnets. *Phys. Rev. Lett.* **117,** 087205 (2016). https://doi.org/10.1103/PhysRevLett.117.087205
10. Shalaby, M., Vicario, C. & Hauri, C. P. Low frequency terahertz-induced demagnetization in ferromagnetic nickel. *Appl. Phys. Lett.* **108,** 182903 (2016). https://doi.org/10.1063/1.4948472
11. Radu, I., Shalaby, M., Hennecke, M., Engel, D., Schmising, C. von K., Tsukamoto, A., Hauri, C. P. & Eisebitt, S. Ultrafast Magnetic Recording With Terahertz Light. in *2019 44th International Conference on Infrared, Millimeter, and Terahertz Waves (IRMMW-THz)* 1–1 (IEEE, 2019). https://doi.org/10.1109/IRMMW-THz.2019.8874387
12. Bergeard, N., Hehn, M., Mangin, S., Lengaigne, G., Montaigne, F., Lalieu, M. L. M., Koopmans, B. & Malinowski, G. Hot-Electron-Induced Ultrafast Demagnetization in Co / Pt Multilayers. *Phys. Rev. Lett.* **117,** 147203 (2016). https://doi.org/10.1103/PhysRevLett.117.147203
13. Beaurepaire, E., Merle, J.-C., Daunois, A. & Bigot, J.-Y. Ultrafast Spin Dynamics in Ferromagnetic Nickel. *Phys. Rev. Lett.* **76,** 4250–4253 (1996). https://doi.org/10.1103/PhysRevLett.76.4250
14. Koopmans, B., Malinowski, G., Dalla Longa, F., Steiauf, D., Fähnle, M., Roth, T., Cinchetti, M. & Aeschlimann, M. Explaining the paradoxical diversity of ultrafast laser-induced demagnetization. *Nature Mater* **9,** 259–265 (2010). https://doi.org/10.1038/nmat2593
15. Choi, G.-M., Wilson, R. B. & Cahill, D. G. Indirect heating of Pt by short-pulse laser irradiation of Au in a nanoscale Pt/Au bilayer. *Phys. Rev. B* **89,** 064307 (2014). https://doi.org/10.1103/PhysRevB.89.064307

16. Grischkowsky, D., Chi, C.-C., Duling, I. N., Gallagher, W. J., Halas, N. H., Halbout, J.-M. & Ketchen, M. B. in *Picosecond Electronics and Optoelectronics II* (eds. Leonberger, F. J., Lee, C. H., Capasso, F. & Morkoc, H.) **24,** 11–17 (Springer Berlin Heidelberg, 1987). https://doi.org/10.1007/978-3-642-72970-6_3
17. Ketchen, M. B., Grischkowsky, D., Chen, T. C., Chi, C., Duling, I. N., Halas, N. J., Halbout, J., Kash, J. A. & Li, G. P. Generation of subpicosecond electrical pulses on coplanar transmission lines. *Appl. Phys. Lett.* **48,** 751–753 (1986). https://doi.org/10.1063/1.96709
18. Warren, A. C., Woodall, J. M., Freeouf, J. L., Grischkowsky, D., McInturff, D. T., Melloch, M. R. & Otsuka, N. Arsenic precipitates and the semi-insulating properties of GaAs buffer layers grown by low-temperature molecular beam epitaxy. *Appl. Phys. Lett.* **57,** 1331–1333 (1990). https://doi.org/10.1063/1.103474
19. Gupta, S., Frankel, M. Y., Valdmanis, J. A., Whitaker, J. F., Mourou, G. A., Smith, F. W. & Calawa, A. R. Subpicosecond carrier lifetime in GaAs grown by molecular beam epitaxy at low temperatures. *Appl. Phys. Lett.* **59,** 3276–3278 (1991). https://doi.org/10.1063/1.105729
20. Korn, T., Franke-Wiekhorst, A., Schnüll, S. & Wilke, I. Characterization of nanometer As-clusters in low-temperature grown GaAs by transient reflectivity measurements. *Journal of Applied Physics* **91,** 2333–2336 (2002). https://doi.org/10.1063/1.1430886
21. Sabbah, A. J. & Riffe, D. M. Femtosecond pump-probe reflectivity study of silicon carrier dynamics. *Phys. Rev. B* **66,** 165217 (2002). https://doi.org/10.1103/PhysRevB.66.165217
22. Bandstructure of LT-GaAs. *BaTop* at <http://www.batop.com/information/PCA_infos.html>
23. Erli Chen & Chou, S. Y. Characteristics of coplanar transmission lines on multilayer substrates: modeling and experiments. *IEEE Trans. Microwave Theory Techn.* **45,** 939–945 (1997). https://doi.org/10.1109/22.588606
24. Wilson, R. B., Yang, Y., Gorchon, J., Lambert, C.-H., Salahuddin, S. & Bokor, J. Electric current induced ultrafast demagnetization. *Phys. Rev. B* **96,** 045105 (2017). https://doi.org/10.1103/PhysRevB.96.045105
25. Wong, H.-S. P. Stanford Memory Trends. at <https://nano.stanford.edu/stanford-memory-trends>
26. Rowlands, G. E., Rahman, T., Katine, J. A., Langer, J., Lyle, A., Zhao, H., Alzate, J. G., Kovalev, A. A., Tserkovnyak, Y., Zeng, Z. M., Jiang, H. W., Galatsis, K., Huai, Y. M., Amiri, P. K., Wang, K. L., Krivorotov, I. N. & Wang, J.-P. Deep subnanosecond spin torque switching in magnetic tunnel junctions with combined in-plane and perpendicular polarizers. *Appl. Phys. Lett.* **98,** 102509 (2011). https://doi.org/10.1063/1.3565162
27. Garello, K., Avci, C. O., Miron, I. M., Baumgartner, M., Ghosh, A., Auffret, S., Boulle, O., Gaudin, G. & Gambardella, P. Ultrafast magnetization switching by spin-orbit torques. *Appl. Phys. Lett.* **105,** 212402 (2014). https://doi.org/10.1063/1.4902443
28. Zeng, Z. M., Khalili Amiri, P., Rowlands, G., Zhao, H., Krivorotov, I. N., Wang, J.-P., Katine, J. A., Langer, J., Galatsis, K., Wang, K. L. & Jiang, H. W. Effect of resistance-area product on spin-transfer switching in MgO-based magnetic tunnel junction memory cells. *Appl. Phys. Lett.* **98,** 072512 (2011). https://doi.org/10.1063/1.3556615
29. Liu, H., Bedau, D., Backes, D., Katine, J. A., Langer, J. & Kent, A. D. Ultrafast switching in magnetic tunnel junction based orthogonal spin transfer devices. *Appl. Phys. Lett.* **97,** 242510 (2010). https://doi.org/10.1063/1.3527962
30. Gorchon, J., Wilson, R. B., Yang, Y., Pattabi, A., Chen, J. Y., He, L., Wang, J. P., Li, M. & Bokor, J. Role of electron and phonon temperatures in the helicity-independent all-optical

switching of GdFeCo. *Phys. Rev. B* **94,** 184406 (2016). https://doi.org/10.1103/PhysRevB.94.184406
31. Schellekens, A. J. & Koopmans, B. Comparing Ultrafast Demagnetization Rates Between Competing Models for Finite Temperature Magnetism. *Phys. Rev. Lett.* **110,** 217204 (2013). https://doi.org/10.1103/PhysRevLett.110.217204
32. Battiato, M., Carva, K. & Oppeneer, P. M. Superdiffusive Spin Transport as a Mechanism of Ultrafast Demagnetization. *Phys. Rev. Lett.* **105,** 027203 (2010). https://doi.org/10.1103/PhysRevLett.105.027203
33. Steil, D., Alebrand, S., Hassdenteufel, A., Cinchetti, M. & Aeschlimann, M. All-optical magnetization recording by tailoring optical excitation parameters. *Phys. Rev. B* **84,** 224408 (2011). https://doi.org/10.1103/PhysRevB.84.224408
34. Mistry, K., Chau, R., Choi, C.-H., Ding, G., Fischer, K., Ghani, T., Grover, R., Han, W., Hanken, D., Hattendorf, M., He, J., Allen, C., Hicks, J., Huessner, R., Ingerly, D., Jain, P., James, R., Jong, L., Joshi, S., Kenyon, C., Kuhn, K., Lee, K., Auth, C., Liu, H., Maiz, J., McIntyre, B., Moon, P., Neirynck, J., Pae, S., Parker, C., Parsons, D., Prasad, C., Pipes, L., Beattie, B., Prince, M., Ranade, P., Reynolds, T., Sandford, J., Shifren, L., Sebastian, J., Seiple, J., Simon, D., Sivakumar, S., Smith, P., Bergstrom, D., Thomas, C., Troeger, T., Vandervoorn, P., Williams, S., Zawadzki, K., Bost, M., Brazier, M., Buehler, M. & Cappellani, A. A 45nm Logic Technology with High-k+Metal Gate Transistors, Strained Silicon, 9 Cu Interconnect Layers, 193nm Dry Patterning, and 100% Pb-free Packaging. in *2007 IEEE International Electron Devices Meeting* 247–250 (IEEE, 2007). https://doi.org/10.1109/IEDM.2007.4418914

Chapter 7. Ultrafast spin-orbit torque switching

Chapters 3 through 6 of this dissertation so far have focused heavily on the ultrafast reversal of magnetization of Gd-based rare-earth transition metal (RE-TM) ferrimagnets (Chapters 3, 4, 6), and of Co/Pt ferromagnetic layers coupled with GdFeCo (Chapter 5), by heating them in short, ps and sub-ps timescales with either optical laser pulses (Chapters 3-5), or with ps electrical pulses (Chapter 6). The magnetization of the films was shown to reverse in ps timescales, up to two orders of magnitude faster than the switching in conventional spintronic devices[1, 2, 3]. It was shown in Chapter 6 that the ultrafast switching of GdFeCo magnetization by ps electrical pulses has comparable energy densities as other spintronic schemes like the spin transfer torque (STT) or the spin orbit torque (SOT), and high endurance and durability ($> 10^{10}$ switching cycles). Moreover, the potential to extend the ps-timescale Joule-heating switching to ferromagnetic films exchange coupled with a GdFeCo film (or any Gd based RE-TM ferrimagnet that exhibits HI-AOS at ps laser pulse durations) can help realize a fully integrated all-electrical ultrafast spintronic device. In such a device, the switching would be caused by ps electrical pulses generated on-chip, and the readout would be done electrically by measuring the tunnel magneto-resistance (TMR) of a magnetic tunnel junction (MTJ) integrated with the ferromagnet. However, the ultrafast magnetization reversal of these magnetic systems follows a "toggle" switching mechanism. The film switches as long as a certain critical amount of energy – either electrical or optical – for a given pulse duration of a short ps or sub-ps heating pulse is supplied, and the final switched magnetic state is always of the opposite orientation of the initial magnetic state. Even in the case of reversal of GdFeCo by ps electrical pulses, the magnetization toggles with each successive pulse applied, irrespective of the polarity of the current.

7.1 Limitations of toggle switching

The toggle switching of magnetization, where no preference for a particular final state is observed for electrical pulses of a given polarity, poses a problem when applied to logic or memory arrays. In the magnetic bit of a spintronic device, the two opposite orientations of the magnetization serve as the 0 and 1 of binary data. Let us assume that in an ultrafast spintronic device, the magnetization of a GdFeCo bit pointing out of the plane of the sample and into the plane of the sample are 0 and 1, respectively. Data is written into the GdFeCo bit by subjecting it to a ps electrical pulse of a certain amplitude. If a "0" needs to be written into that bit, the electrical pulse will result in the desired 0 state only if the previous state of the bit was a "1". If the bit was in a "0" state to begin with, the electrical pulse would cause it to end up with an undesired "1" state. In order to circumvent this limitation of toggle switching, the bits to be written must be checked before each write. A writing electrical pulse must be applied only if the state of the bit is the opposite of its desired final state. Such a "read-before-write" scheme for memory or logic arrays will need additional overheads in terms of control circuitry. These overheads will lead to the whole system being less energy efficient and slower overall, and will adversely impact the speed gains from the ultrafast switching process. An ideal spintronic device requires that its final state be deterministically dictated only by the amplitude and direction of the write pulse, and not by its previous state.

In a conventional spintronic device, operating on the SOT or STT phenomena for example, the final state of the magnetic bit is determined solely by external controllable parameters such as the polarity of the write pulse or the direction of an external applied field, and not by the previous state of the bit.

In an SOT device (see Section 1.3) the accumulated spins following an applied charge current exert a torque onto the magnetization of a magnetic film grown over the current carrying heavy metal wire. Larger the applied current, larger is the accumulated spin moment, and larger is the torque exerted. Let the initial magnetization direction of a magnetic in an SOT device bit be a "0" state. If the current direction, arbitrarily assigned as positive, is such that the exerted damping-like Slonscewski torque (see Figure 1.6 (b)) for the different configurations of spin orbit torques) is opposite to the internal damping torque, at a high enough applied current, the Slonscewski torque exceeds the damping torque, and the magnetization of the bit reverses to a "1" state. The Slonscewski torque from an opposite negative current direction would reinforce the internal damping torque rather than oppose it, causing the magnet to retain its original "0" state. Similarly, if the magnet is initially in the "1" state, the torque from a positive current would aid the damping torque and help retain the original state, while the torque from a negative current would oppose the damping torque and cause the magnetic bit to switch to a "0". In this example of an SOT device, the magnetic bit ends at "0" for negative current pulses and at "1" for positive pulses, irrespective of its starting state, and therefore the bit can be written just by the controlling the current pulse polarity without the need of reading its state prior to the write process.

The work in this chapter aims at extending the effects of SOT to ps timescales and to achieve magnetization reversal by torques from ps electrical pulses. Stacks of PMA Pt/Co/Ta, where the opposite spin-Hall angles of the Pt and Ta layers that flank the magnetic Co on either side lead to an enhancement of the accumulated spin moments in the same direction, are irradiated with ps electrical pulses. The ultrafast Joule heating from the current pulse is expected to lead to an ultrafast loss of magnetic order. The ps timescale spin current pulses arriving at the Co from the Pt and Ta films are expected to aid the heating and demagnetization, and more importantly exert short SOTs on the magnetization of Co. The direction of the torques will reverse upon reversing the direction of the current, a characteristic that can be exploited to switch the magnetic stack in short timescales in a deterministic manner controlled only by the charge current pulse direction. Additionally, such a switching technique offers the possibility of switching any arbitrary magnetic film – including commonly used ferromagnets – deterministically without the need of an underlying Gd-based ferrimagnet. This is advantageous because Gd-based ferrimagnets are expensive and could also be hard to integrate with a standard chip process.

7.2 Speed of spin accumulation

A fundamental speed limit for an ultrafast spintronic device that operates on the principle of the SOT on ps timescales is the speed at which spins can accumulate following a current pulse. Ps electrical currents can exert spin-orbit torques only if spins can accumulate in timescales smaller than the width of the current pulse.

Chapter 2 dealt extensively with the direct detection of the accumulated spins in current carrying wires of heavy metal thin films. It was shown (Section 2.4) that the optical technique of magnetization-induced second harmonic generation (MSHG) was capable of detecting spin accumulation in Pt, β-Ta and Au wires. Such a direct technique does not rely on measuring the response of the magnetization of a magnetic film (grown on top of the heavy metal) to the spin-orbit torque applied by the spins, and can therefore access physics that is unaffected by the magnet and is inherent to the spin

accumulation in the heavy metal. Towards that end, Section 2.6 explored the possibility of measuring the speed of spin accumulation in wires of Pt, the "spin-Hall" heavy metal that yielded the highest magnetic asymmetry signal in the MSHG setup. It was observed that when a 2 ns current pulse is sent through the Pt wire, the spin accumulation pulse follows the current pulse on the time scale of at most ~50 ps, well within the noise level of the measurement (Figure 2.7)[4]. The width of the spin accumulation signal was seen to be the same as the width of the current pulse, within the limits of the experiment, indicating that the rise and fall times for the spin accumulation are well below those of the current pulse itself, ~100 ps. The experiment was unable to better quantify the actual spin accumulation time due to constraints such as the time jitter of the electronic delay generator and the unavailability of sources of short, stable pulses.

The LT-GaAs based Auston photoconductive switch described in Chapter 6 is capable of generating intense < 10 ps duration electrical pulses with peak amplitudes up to ~10^9 Acm^{-2}. The photoconductive switch is triggered by short optical laser pump pulses from the RegA 9050 with a low jitter, and the time delay of the pump pulses with respect to the probe pulses can be finely controlled by the linear delay stage offering a time resolution as small as 6.7 fs. Therefore a photoconductive switch integrated with a Pt transmission line should be capable of generating a stable train of ps electrical pulses needed for the measurement of spin accumulation speed by MSHG. The devices were fabricated with the process detailed in Section 6.5, without the back contact lines or the magnetic load, and using 20 nm thick films of sputter deposited Pt instead of the evaporated Ti(25 nm)/Au(250 nm) thin films for the transmission lines. Current pulses, with ~15 ps duration and densities estimated to be up to 10^8 Acm^{-2} were measured in the patterned coplanar stripline (CPS) transmission lines when the Auston switch was illuminated by pump laser pulses. Since the magnetic asymmetry of the MSHG setup (Equation (2.2)) requires measurement of the reflected second harmonic intensity for spin orientations in two opposite directions, the direction of each consecutive current pulse was reversed by reversing the DC bias voltage across the Auston switch at the laser repetition rate of 252 kHz. The probe beam was focused onto one of the lines (either the ground or signal line) near the Auston switch in order to detect the magnetic signal originating from the spin accumulation as a short electrical pulse passes through the probed area line. Unfortunately, the setup was unable to pick up any magnetic asymmetry signal from the accumulated spins even for DC bias voltages as high as 70 V. Increasing the bias voltage further resulted in irreversible damage of the Pt transmission lines, as shown in Figure 7.1, indicative of electromigration at high current densities.

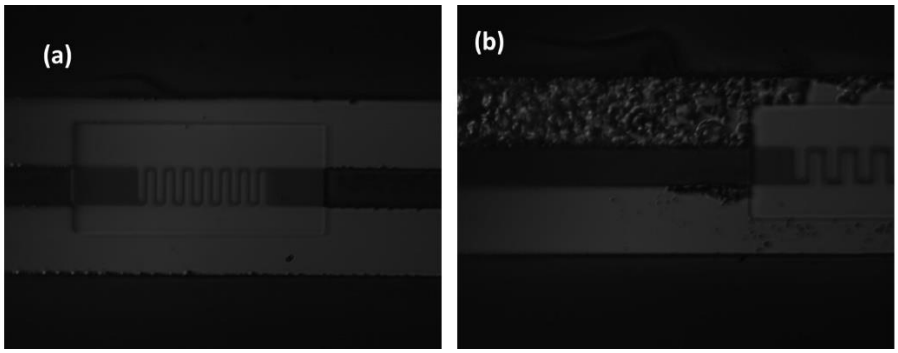

Figure 7.1 Electromigration in Pt transmission lines.

Microscope images of the Pt CPS transmission line for detection of spin accumulation speed before (a) and after (b) application of intense ps electrical pulses. The damage on the transmission line (b) is indicative of electromigration at high DC bias voltages.

Experiments by other groups, however, were capable of estimating the speed of spin accumulation from spin-Hall and other current-induced effects. Kampfrath et al.[5] irradiated stacks of 10 nm in-plane magnetized Fe capped with 2 nm of nonmagnetic Au or Ru with fs laser pulses from the Fe side as depicted in the schematic of Figure 7.2 (a). The spins of the Fe, which are preferentially oriented along its magnetization direction, are excited and a transportation of spin polarization from the Fe to the nonmagnetic cap layer – that is, a spin current – with density J_S begins immediately. To detect the spin current J_S, the inverse spin-Hall effect[6, 7] technique was used to convert J_S into a charge current density J_C following equation (7.1).

$$(7.1)\ J_C = \theta_{SH} J_S \times \frac{M}{|M|}$$

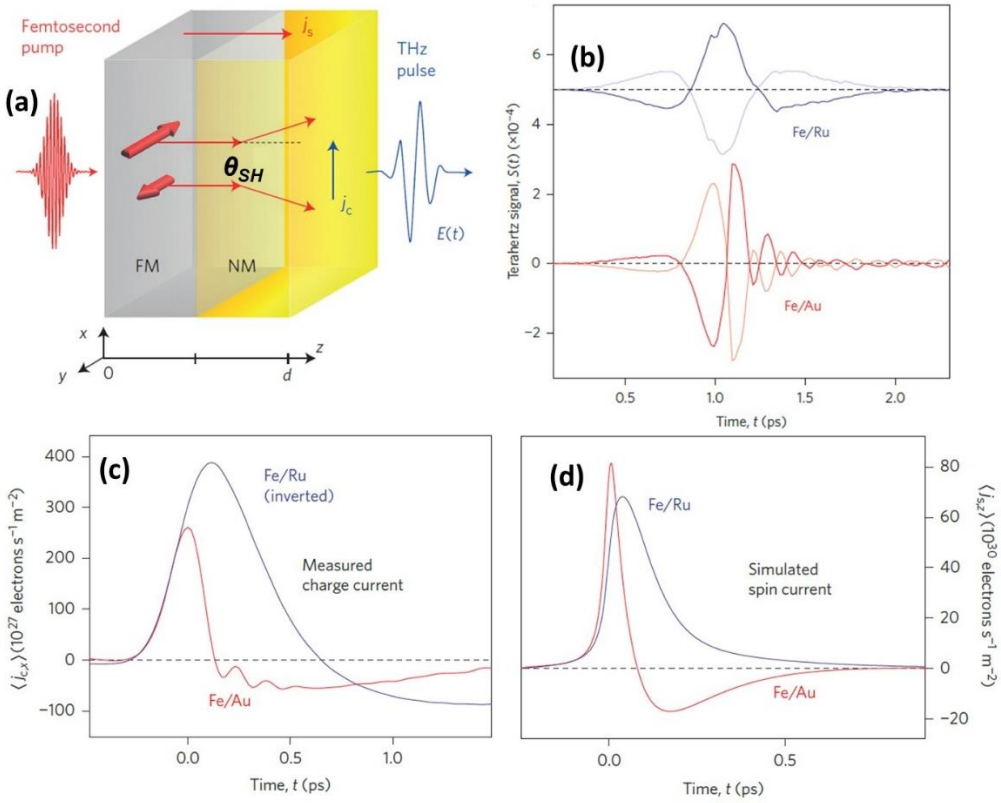

Figure 7.2 THz emission by the inverse spin-Hall effect from ps spin currents.
(a) Schematic of the stack used in Refs [5, 8]. The ferromagnet FM was 10 nm Fe, and the nonmagnet (NM) is 2 nm of Au or Ru. The inverse spin-Hall effect converts the spin current J_S into a transverse charge current J_C. (b) Detected free-space THz radiation from the Fe/Au and Fe/Ru stacks. (c) Calculated transient current pulse J_C. (d) Simulated transient charge current pulse J_S with sub-ps duration (Figures from Refs [5, 8]).

In equation (7.1) θ_{SH} is the spin-Hall angle of the nonmagnetic metal and $\boldsymbol{M}$ is the magnetization of the Fe. $\boldsymbol{M}/|\boldsymbol{M}|$ then represents the orientation of the launched spins, which is parallel to the $\boldsymbol{M}$. The oscillating charge current J_C radiates into free space as a THz pulse, which was measured by the electro-optic sampling of a 250 μm thick <110> oriented GaP crystal. The measured THz signal in the time domain is shown in Figure 7.2 (b) for the Fe/Au and Fe/Ru stacks. The emitted THz spectrum for the Fe/Au sample extended to 20 THz. The z-averaged charge current density, $\langle J_C \rangle = \int_0^d dz J_C/d$, where d = 12 nm is the thickness (z-axis) of the stack, is calculated from spectrum $E(\omega)$ the emitted THz intensity $E(t)$ as equation (7.2).

$$(7.2)\ \langle J_C(\omega) \rangle = -\langle \sigma(\omega) \rangle E(\omega)$$

Here $<\sigma(\omega)>$ is the z-averaged THz conductivity. The charge current transients $<J_C(t)>$ calculated from the emitted THz radiation by equation (7.2) are shown in Figure 7.2 (c). The spin currents $<J_S(t)>$ that lead to $<J_C(t)>$ through the inverse spin-Hall effect can then be calculated from equation (7.1), and are expected to have the same shapes as $<J_C(t)>$ if the spin-Hall angle is assumed to be constant for all frequencies. The spin currents in Figure 7.2 (d) were derived from simulations of superdiffusive spin transport, and were able to qualitatively reproduce the features of $<J_C(t)>$. These observations confirm the interpretation that the emitted terahertz transient is a result of a laser-driven spin current pulse J_S and its transformation into a transverse charge current pulse J_C by the inverse spin-Hall effect. The differences in the responses of the Fe/Ru and Fe/Au stacks were explained to be arising from various electronic differences of the Au and Ru nonmetals.

Further experiments by Seifert et al.[8] were able to build on these results to build highly efficient THz emitters using bilayers of 3 nm thick ferromagnetic CoFeB on 3 nm of a spin-Hall nonmetal. Linearly polarized THz radiation of full-width at 10% amplitude maximum of 30 THz, with no gaps in the spectrum, were emitted by a CoFeB/Ta stack. In order to increase the emitted THz amplitude, optimized trilayer stacks of W(2 nm)/CoFeB(1.8 nm)/Pt(2 nm) were grown. The excited CoFeB launches spin currents J_S in opposite into the Pt and W layers. Since the spin-Hall angles of Pt and W have opposite signs, following equation (7.1), the radiating charge current J_C in both the nonmagnets have the same sign, leading to an enhancement of the emitted THz amplitude. A comparison of the THz radiation $S(t)$ and its spectrum $S(\omega)$ of the trilayer emitter with those of other commonly used THz emitters (non-linear optical crystals of ZnTe <110> and GaP <110>, and a biased Auston photoconductive switch) shows that the THz spectrum of the trilayer emitter is exceptionally smooth and gap-free and has a higher bandwidth than its competitors. It is also characterized by a higher amplitude than that of the GaP and ZnTe crystals at most frequencies in the 2.5 to 15 THz range, and that of the photoconductive switch at frequencies over 3 THz. The time-domain signal $S(t)$ of the trilayer emitter is shorter and has a higher peak amplitude than the other emitters.

The above two experiments prove that a short spin ps current pulse can radiate short THz pulses, with frequencies up to 30 THz. The charge current $<J_C(t)>$ and the simulated spin current $<J_S(t)>$ pulses of Figure 7.2 (c) and (d) show that the radiations arise from extremely short, sub-ps spin current pulses. Importantly, for the work presented in this chapter, this means that the inverse spin-Hall effect – and consequently the spin-Hall effect – will operate at these sub-ps timescales, just like they do in static experiments. Therefore, in an ultrafast SOT device, an applied ps electrical current pulse should

lead to quick spin accumulation within its pulse duration, leading to a ps spin current pulse that can then apply torques onto the magnetic load.

7.3 Quasi-static spin-orbit torque switching of of Ta/Co/Pt ferromagnet

Based on the observations of the previous Section 7.2, it can be concluded that ps current pulses in heavy metal wires will have short spin current pulses due to the spin-Hall (or Rashba) effect. A device in which ps currents are flowed through a wire of heavy metal in contact with a magnet can potentially exert short SOTs onto the magnet, in addition to heating it in ultrafast timescales. For this purpose, stacks of Ta(5 nm)/Pt(3 nm)/Co(1 nm)/Cu(1 nm)/Ta(4nm)/Pt(1 nm) are grown on both glass and LT-GaAs substrates by DC magnetron sputter deposition in an AJA chamber. A schematic of the stack is shown in Figure 7.3 (a). The Ta(5 nm)/Pt(4 nm) layer serves as a buffer, ensuring a well-defined <111> texture for the growth of the Co film and guarantees an interface anisotropy that promotes PMA for Co. The Pt underlayer is also chosen owing to its large spin-Hall angle, which can then exert large spin orbit torques on the magnetization of Co. The Ta(4 nm) layer on the other side of Co is grown because of its large spin-Hall with a sign opposite to that of the Pt underlayer. As mentioned in Section 7.1, this leads to the spin currents arriving at Co from Pt and Ta to have the same orientation of their spin moments, which will result in an enhancement of the SOT on the magnetization of Co[9]. First trials with Pt/Co/Ta stacks (without a thin Cu layer between the Co and Ta) resulted in non-square magnetic hysteresis curves with small remanence indicating a possible large effective Dylazhosinkii-Moriya interaction (DMI) as in Ref [10]. While the DMI is currently an interesting topic of study and can result in the generation of skyrmions (also a hot field of research in the magnetism community) in the Co/Ta interface, such interactions and Skyrmions hinder the PMA of Co and can be detrimental for SOT device applications. In order to obtain two well-defined remanent states at zero applied field, the 1 nm thick Cu layer was inserted to reduce the DMI at the Co/Ta interface. Cu has a long spin-diffusion length, reported to be up to 500 nm[11]. Therefore, spin currents generated in the Ta layer are expected to completely diffuse through the thin 1 nm Cu layer and contribute to the SOT[12, 13]. The choice of the stack was also determined by the necessity of having a top metallic layer (Cu/Ta + Pt capping) in order to get a good electrical contact with the transmission lines (see Sections 6.5 and 7.4 for transmission line fabrication details). Over the course of this chapter, the presence of the Cu layer will be assumed, and this stack will henceforth be referred to as "Pt/Co/Ta". Hysteresis loops performed on the stack with an applied out-of-plane magnetic field, shown in Figure 7.3 (b), yield a square hysteresis with a coercive field of ~50 Oe, confirming PMA in the sample. The Curie temperature T_C of the stack is estimated as ~800 K from the previous experience with extremely similar samples grown and characterized over the years.

The switching of the Pt/Co/Ta sample by SOT is first confirmed for quasi-static conditions with long square current pulses. For this purpose, Hall crossbar structures (shown in Figure 7.4 (a)) are fabricated. An in-plane magnetic field of H_X = 160 mT is applied to break the symmetry, as is required for SOT switching of out-of-plane magnetized stacks[14]. Long, 100 μs duration charge current pulses are applied along the x-axis, parallel or antiparallel to H_X. The corresponding current-driven magnetic hysteresis loop is shown in Figure 7.4 (b), yielding a critical current density J_C for switching the magnetization equal to $\sim 2 \times 10^{11} \mathrm{Am}^{-2}$ and verifying that the magnetization of the stack can be switched by SOT in quasi-DC conditions. As seen from Figure 7.4 (c), the switching current I_C is inversely proportional to the symmetry breaking in-plane field, as is expected for SOT driven switching[15, 16, 17].

It is also observed that the final switched state is independent of the initial state; it depends only on the direction of the current and the in-plane field as is required for a non-toggle deterministically switched device (see the arguments in Section 7.1). When the charge current and the in-plane field are parallel and anti-parallel, the sample switches to a final state of $-M_Z$ and $+M_Z$ respectively (+z being the direction out of the sample plane), in agreement with SOT arising from the combination of the spin Hall effect from both Pt and Ta heavy metals[14, 18].

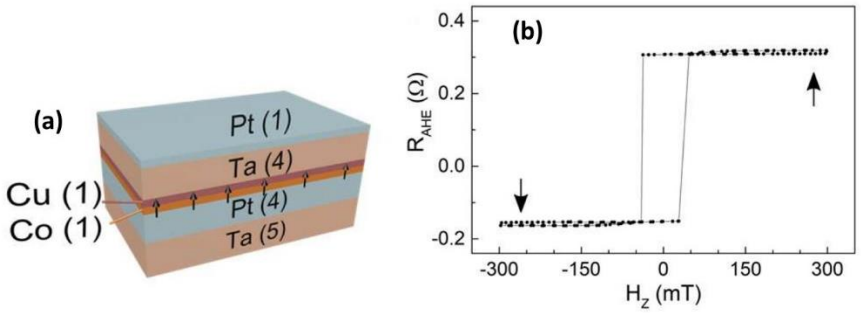

Figure 7.3 Static characterization of the Pt/Co/Cu/Ta stacks.
(a) Schematic of the stack. The Pt and Ta layers exert SOT on the magnetization of Co. The Cu layer reduces the DMI between the Co and Ta. (b) Static hysteresis loops performed with an out-of-plane field on a patterned Hall cross (see Figure 7.4 (a)) of the sample by measuring its anomalous Hall resistance R_{AHE} (Figure from Ref [19]).

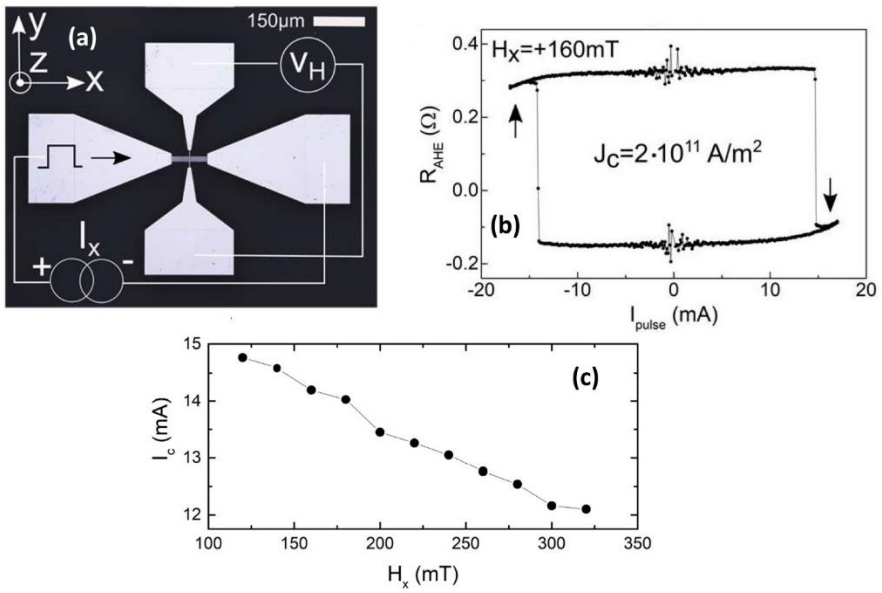

Figure 7.4 Quasi-static SOT switching of the Pt/Co/Ta stack.
(a) Patterned Hall bar using the magnetic stack and gold contact pads. The schematic shows the electrical connections used for the measurement of anomalous Hall resistance ($R_{AHE}=V_H/I$). (b) R_{AHE} as a function of the amplitude of 100 μs current pulses with an in-plane symmetry-breaking field H_X = 160 mT. (c) Critical switching current I_C is inversely proportional to H_X (Figure from Ref [19]).

7.4 Spin-orbit torque switching of Pt/Co/Ta with single ps electrical pulse

Following the switching of the Pt/Co/Ta by SOT from long quasi-DC current pulses, the next logical step is to speed up the switching by utilizing short ps pulses instead. From the discussions of Section 7.2, it can be concluded that ps current pulses will lead to short ps timescale spin current pulses from the Pt and Ta layers that can potentially apply a high enough SOT on Co to switch its magnetization.

Low temperature GaAs (LT-GaAs) Auston photoconductive switches (their working principle is detailed in Section 6.3) are used to generate high-intensity ps pulses. The pulses are delivered to patterned loads of the Pt/Co/Ta magnets by transmission lines in the coplanar waveguide (CPW, ground-signal-ground) configuration. A schematic of the device is shown in Figure 7.5. The fabrication process of these devices is the same as that detailed in Section 6.5, except that these devices have a layer of SiO_2 instead of MgO to provide electrical insulation between the lines. The 100 nm thick SiO_2 layer is sputter deposited in an AC 450 (Alliance Concept) sputtering system in the presence of 20 sccm Ar and O_2 flow at a base pressure of 6.1×10^{-3} mbar. At the end of the fabrication process, a $5 \times 4\ \mu m^2$ area of the magnetic load is exposed under the top transmission line for each CPW device.

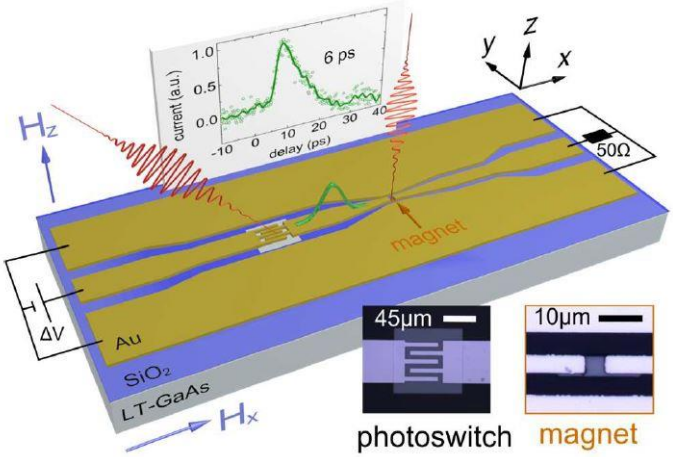

Figure 7.5 Picosecond electrical pulse generation for ultrafast SOT.
Setup for the generation of ps electrical pulses includes an LT-GaAs based Auston switch and CPW waveguide. Pulses with duration 6 ps (inset) are generated. The magnified images indicate the Auston switch (left) and the patterned magnetic load (right). The out-of-plane field H_Z is used to reset the magnetization between pulses during time-resolved measurements (Figure from Ref [19]).

In order to generate the picosecond pulses the Auston switch side of the transmission lines (left side of the schematic in Figure 7.5) is contacted with a CPW 40GHz GBB probe tip. The sample side of the lines (right side of schematic) is contacted with another CPW 40GHz GBB tip, with an add 50Ω resistor to close the circuit. A constant voltage bias ΔV, that can be between -50V and +50V, is applied through the left tip via a Keithley 2400 voltage source, while reading the average current. A small dark (i.e. leakage) current due to the finite switch resistance (>10 MΩ) when no laser pulse is incident on the Auston switch. The photoswitch is then irradiated with a pump beam of 1.5 mW average power (0.3 μJ per pulse) from a 5 kHz amplified laser system (Coherent Legend at the Institut Jean Lamour at Nancy, France). The pump pulses have a duration of 30 fs and a central wavelength of 800 nm, and are focused onto the switch by a 15 cm focal length lens to a beam size (FWHM

diameter) of ~ 300 μm. When the switch is irradiated, a photocurrent is generated. The pump steering mirror is finely tuned to optimize the average photocurrent indicated by the Keithley 2400. Following the pulse detection scheme outlined in Section 6.4, a free-standing Teraspike detector tip (different from the Protemics model tip of Section 6.4) is placed on top of the Au transmission line to measure the generated ps pulses. For this measurement, the pump beam is modulated at 300 Hz with a mechanical chopper, and the lock-in amplifier (Stanford Research Systems 865A) is referenced to this modulation frequency. Exciting the photoconductive switch with the 1.5 mW power pump pulses resulted in intense current pulses with a pulse duration τ_P of 6 ps (see inset of Figure 7.5). These pulses then propagate along the Au CPW and are focused into the Pt/Co/Ta magnetic load by the impedance matched taper.

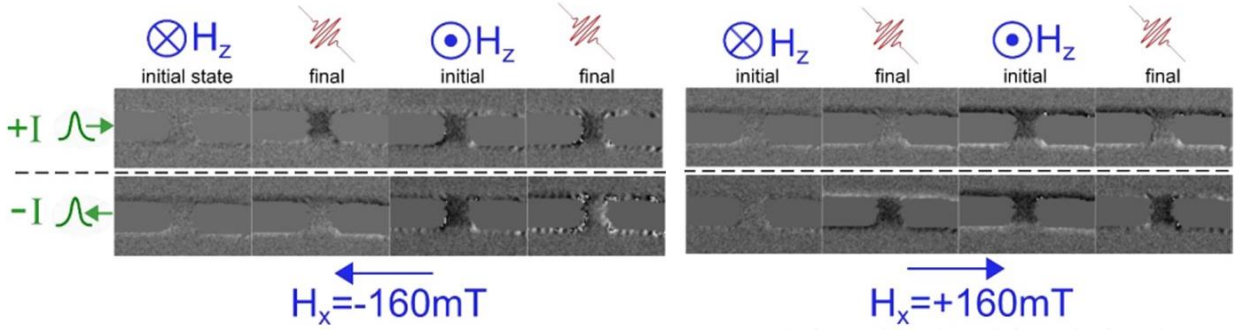

Figure 7.6 Single shot SOT switching of Pt/Co/Ta by 6 ps electrical pulses.
MOKE micrographs depict the switching of magnetization by single 6 ps electrical pulses via SOT. The four quadrants show two before-pulse and two after-pulse images under different combinations of the in-plane field and current directions. The inversion of the final state with current or in-plane field is a clear signature of SOT switching. The final state is always independent of the initial state. Bias voltages used for switching were slightly above the critical threshold (ΔV ~ 40 V). Light (dark) grey indicates magnetization down (up) (Figure from Ref [19]).

Figure 7.6 shows polar magneto optical Kerr effect (MOKE) micrographs of the initial and final states after excitation by a single 6 ps electrical pulse in various configurations, with a symmetry breaking in-plane field of magnitude $|H_X|$ = 160 mT and a DC bias voltage ΔV = 40 V across the lines . Each of the four quadrants represent different combinations of the current pulse and symmetry breaking in-plane field H_X directions. In each case, the magnetization is initialized by an applied out-of-plane field which is turned off prior to applying the electrical pulse. Details of the MOKE microscope are in Section 3.2. A 50× objective is used to focus the 630 nm wavelength LED probe light normally onto the sample surface. The light gray and dark gray colors of the magnetic load in the images of Figure 7.6 indicate magnetization of $-M_Z$ and $+M_Z$ respectively. As with the quasi-static SOT experiments (Section 7.3), it is again observed that parallel (antiparallel) current pulses and field result in a final magnetization state of $-M_Z$ ($+M_Z$), which is expected by the symmetries of the SOTs in the prepared Pt/Co/Ta stack. Multiple successive pulses of the same polarity were injected, no difference in the final state was seen confirming non-toggle SOT mediated switching. The experiment (initial saturation + single shot) was successfully repeated at the switching voltage ΔV = 40 V for n = 35 times. This leads to an estimate of >91% switching probability with a 95% confidence interval (as per the "rule of three", $P > 1 - 3/n$), confirming the deterministic behavior of the reversal. As soon as the

voltage magnitude $|\perp V|$ is decreased below 40 V, no more reversal is observed for any $|H_X|$. Again, when the in-plane field is reduced below $|H_X| = 120$ mT, no reversal is seen, likely requiring higher current densities, as also observed by Garello et al.[1]. The higher current densities were not explored in this work, in order to avoid the risk of degradation or permanent damage of the photoswitch or the magnetic load. To confirm repeatability of these measurements, similar experiments were performed on the same sample stack in other sets of devices (including those in CPS waveguides and different Auston switch designs). Similar switching characteristics were observed in these separate devices.

7.5 Time dynamics of the ultrafast SOT from ps electrical pulses

To measure the ultrafast magnetic response to the current pulses, time-resolved MOKE measurements are needed. The pump laser beam is aligned on the Auston switch and the probe on the Pt/Co/Ta magnetic load for these measurements, as in the experiments of Section 6.7. Unfortunately, technical limitations prevented the measurement of the time resolved switching dynamics using the 5 kHz Coherent Legend amplified laser system used for the ps SOT switching experiments of Section 7.4 and Figure 7.6. The signal-to-noise ratio of laser MOKE experiments depends strongly on the power of the laser probe beam. On the MOKE setup at Nancy used for this work, measurements require a minimum probe laser power of ~60 μW to resolve Kerr rotations of 100 μrad. The full amplitude of the hysteresis ($2M_S$, M_S being the saturation magnetization) of the sample is ~485 μrad, so 60 μW would allow resolution of the dynamics with an SNR of less than approximately 5:1 without accounting for other issues such as laser drift and sample vibrations. At a 5 kHz repetition rate, the high per pulse energy of 12 nJ for 60 μW power causes damage to the sample when focused to dimensions smaller than the sample size of 5×4 μm^2. An 80 MHz oscillator laser at IJL, Nancy was instead used to measure the magnetization dynamics. The oscillator outputs ~250 fs-duration pulses centered at 780 nm. Time-resolved pump-probe measurements of the switching dynamics are not yet possible with this 80 MHz laser system, since the per pulse power is not high enough to generate intense enough current pulses even after irradiating the switch with almost the full pump power and applying the strongest in-plane field available in the setup. Probing the switching dynamics was also not possible with our 5 kHz amplified laser system. Possible solutions would be to make the sample area bigger and defocus the beam, or to use a higher repetition rate laser, such as the 252 kHz Coherent RegA at Berkeley.

Low pump and current pulse intensity time-resolved MOKE measurements are performed with the aforementioned 80 MHz oscillator laser under various configurations of current pulse and in-plane magnetic field direction. 3.6 ps-duration electrical pulses are obtained with this system (inset in Figure 7.7 (a)). In these experiments, the change in the out-of-plane component of the magnetization ($\perp M_Z$) is monitored via polar-MOKE with a time-delayed probe pulse, focused on the magnetic load to a small ~1 μm spot with a 50 × objective. The measurements are done with no out-of-plane field, since at small excitations the sample naturally relaxed back between pulses, as is typical with low-excitation optical pump-probe experiments. The typical magnetic response to the pulses is shown in Figure 7.7 (a).

The zero delay time, i.e. the arrival of the electrical pulse at the magnetic load, by monitoring the time-domain thermoreflectance (TDTR) response, shown in Figure 7.7 (b). This measurement is similar to the experiment described in Section 6.3 to determine the carrier lifetime of LT-GaAs by monitoring

its transient reflectivity. The black TDTR curve of Figure 7.7 (b) indicates the time at which the reflection of the magnetic load changes when it is heated by the ps electrical pulse, thereby allowing the determination of zero delay time. Further work is needed to fully interpret the TDTR response.

From the dynamics under zero in-plane field (black symbols in Figure 7.7 (a)), the response of the Co magnetization to the current pulse is instantaneous, and starts at delay t = 0 set for the system by the TDTR measurement (Figure 7.7 (b)). For both initial starting states of the magnetization $+M_Z$ and $-M_Z$, the out-of-plane magnetization abruptly decreases and then slowly recovers. The decrease of $|M_Z|$ is due to two mechanisms. First, the SOT pulls the magnetization towards the plane, thereby reducing its out-of-plane component. Second, the picosecond charge current induces Joule heating which leads to an ultrafast loss of magnetic order (ultrafast demagnetization)[20, 21]. The latter and the subsequent slow cooling of the sample by heat diffusion explain the slow recovery at long time delays (350 ps; see black curve in Figure 7.7 (a)).

The magnetization dynamics under applied in-plane magnetic fields are depicted by blue and red symbols in Figure 7.7 (a). At negative time delays, the magnetization is tilted in the $x\hat{z}$ plane, along the effective field H_{eff}, which is the vector sum of H_X, the demagnetization field and the anisotropy field H_A of the sample at negative delays. The magnetization is therefore not fully saturated along $\hat{z}$, unlike in the zero field case (black symbols in Figure 7.7 (a)). The addition of an in-plane field breaks the symmetry of the system and, together with the injected spin polarization σ_Y (which depends on the sign of the current pulse), determines the sign for the observed coherent precession. A parallel (antiparallel) in-plane field and current induces a first large precession of the magnetization towards $-M_Z$ ($+M_Z$), regardless of the initial up or down state, as expected from SOT and in perfect agreement with the result of the quasi-static SOT switching experiments from Section 7.3 and single shot experiments of Section 7.4.

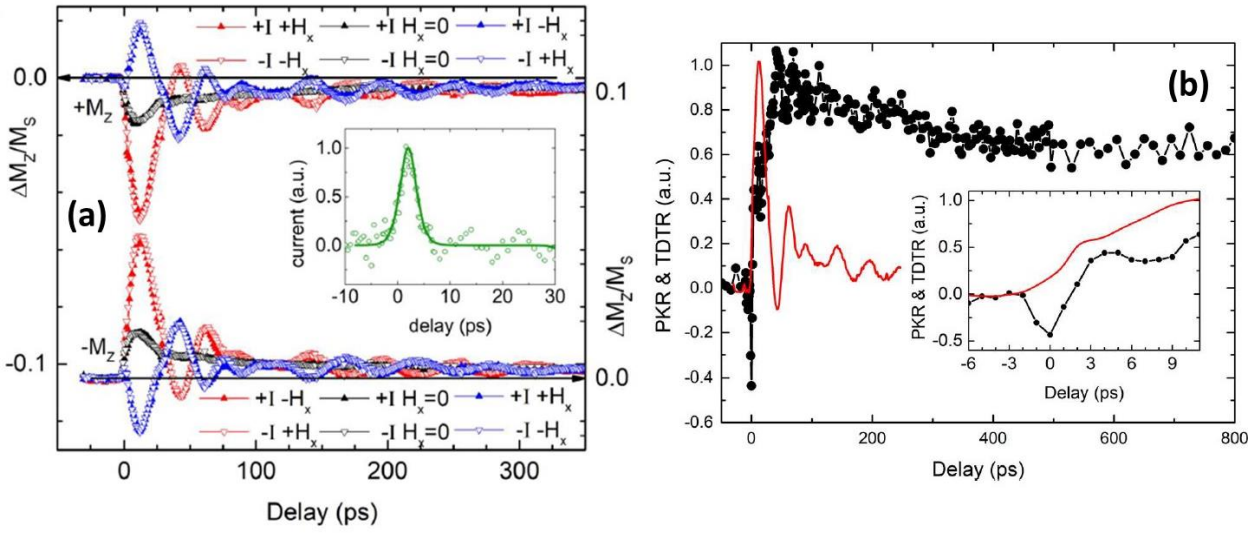

Figure 7.7 Dynamics of magnetization of Pt/Co/Ta due to SOT from 3.6 ps current pulses. (a) The dynamics include spin orbit torques and thermal effects (demagnetization). The phase and sign of the torques is dependent on the in-plane field (H_X) and current direction, as expected from SOT. Without the symmetry-breaking in-plane field the oscillations disappear (black curves). Experiments were done after $\pm Mz$ saturation of the sample, under H_X = 0 mT, H_X = ±160 mT and

a bias voltage of $\Delta V \sim 30$ V. Inset represents the electrical pulse detected. The solid green line is a fit of current trace with a sech^2 function of 3.7ps (FWHM). (b) Time-domain thermoreflectance (TDTR) in black and polar MOKE (PKR) response in red. The electrons immediately respond to the heat pulse (negative peak at time-zero). The magnetic dynamics (red) equally start at the arrival of the pulse with no noticeable delay (Figure from Ref [19]).

7.6 Modeling of the ultrafast SOT dynamics

A simple Landau-Lifishitz-Gilbert (LLG) macrospin model, with the added effects of SOTs and ultrafast Joule heating, was developed to explain the experimentally observed time dynamics[19]. The LLG equation used incorporates both the field-like and damping-like spin-orbit torques (described in Section 1.5) as follows.

$$(7.3)\ \frac{d\vec{M}}{dt} = -\gamma\mu_0\left(\vec{M}\times\vec{H}_{eff}\right) + \frac{\alpha}{M_s}\left(\vec{M}\times\frac{d\vec{M}}{dt}\right) - \theta_{SH}^{DL}\frac{C_s}{M_s}\left(\vec{M}\times\left(\vec{M}\times\vec{\sigma}\right)\right) + \theta_{SH}^{FL}C_s\left(\vec{M}\times\vec{\sigma}\right)$$

where

$$C_s = \frac{\mu_B}{q_e}\frac{J_c}{d_0}\frac{1}{M_s}$$

Here, γ is the gyromagnetic ratio, μ_0 is the vacuum permeability, α is the damping parameter, M_S is the saturation magnetization, $\vec{\sigma}$ is the direction of spin-polarization, θ_{SH}^{DL} is the damping-like spin Hall angle, θ_{SH}^{FL} is the field-like spin Hall angle, J_C is the current density, d_0 is the thickness of the magnetic layer, q_e is the charge of the electron and μ_B is the Bohr magneton. The effective field H_{eff} in the first term consists of a magneto-crystalline anisotropy field H_A, a demagnetization field, and any applied external field, and is given by equation (7.4).

$$(7.4)\ \vec{H}_{eff} = \begin{bmatrix} H_x \\ H_y \\ H_z + \left(\frac{2K_z}{\mu_0 M_s} - M_s\right)m_z \end{bmatrix}$$

Here H_X, H_Y and H_Z, are the x, y, and z-components of the external field, K_Z is the perpendicular anisotropy constant, and $\vec{M} = M_s[m_X \quad m_Y \quad m_Z]^T$. The $-M_S m_Z$ term in the z-direction is the demagnetization field due to thin-film shape anisotropy, and $H_A = \frac{2K_z}{\mu_0 M_s}m_z$.

The temperature evolution of the stack from Joule heating is calculated from the heat diffusion equation (equation (7.5)).

$$(7.5)\ C\frac{dT}{dt} = \Lambda\frac{d^2T}{dx^2} + q(t)$$

Here, T is the temperature of the stack, C is its heat-capacity per unit volume, Λ the thermal conductivity, and $q(t)$ is the volumetric heating from the electrical pulse. Based on literature values of the heat capacity of metals[22] in the Pt/Co/Ta stack and the thickness of each layer, an average value

for $C \sim 2.6$ $Jm^{-3}K^{-1}$ is estimated for the multilayer stack at room temperature. Λ is fixed according to the Wiedemann-Franz Law[23] as $\Lambda = L_0 T/\rho_e \sim 9$ $Wm^{-1}K^{-1}$ where ρ_e is the measured electrical resistivity of the film.

The heating from the electrical pulse is calculated from Ohm's law as $q(t) = \rho_e J(t)^2$ where $J(t)$ is the charge current density. Using equation (7.5) to model the temperature response of the stack to Joule heating makes the assumption that electrons, phonons, and spins are in thermal equilibrium with one another. Such an assumption is not always valid on picosecond time-scales, and nonequilibrium between thermal reservoirs can drive ultrafast magnetic phenomena[20]. However, such nonequilibrium effects in the Pt/Co/Ta SOT switching experiment should be small due to the 4-6 ps electrical pulse duration (following the discussions of Section 6.8), together with the strong thermal coupling between electrons and phonons in the Co layer[24]. The picosecond time-scale for heating is much greater than the electron-phonon relaxation time in transition metals[25]. Therefore, the temperature nonequilibrium $\Delta T_{ep}(t)$ between electrons and phonons can be estimated by assuming a quasi-steady-state condition where rate of heat absorption of electrons equals the rate of heat-loss to the phonons. In other words, $q(t) \sim g_{ep} \Delta T_{ep}(t)$ where g_{ep} is the electron-phonon volumetric energy transfer coefficient[21] which is taken from Ref [24].

The effects of the temperature-evolution after electrical heating is added to the LLG equation (7.3) by allowing M_S and K_Z in these equations to evolve in time based on the predictions of the thermal model described in equation (7.5). Based on Ref [26], the temperature dependencies of the magnetization and magneto-crystalline anisotropy are assumed to be to be described by equations (7.6) and (7.7).

$$(7.6)\ M_s(T) = M_s(0)[1 - (T/T_c)^{1.7}]$$

$$(7.7)\ K_z(T) = K_z(0)[M_s(T)/M_s(0)]^3$$

Here, T_C is the Curie temperature, $M_S(0)$ is the magnetization at absolute zero, and $K_Z(0)$ is the anisotropy constant at absolute zero.

Using all these equations, the experimental magnetization dynamics (Figure 7.7 (a)) of the Pt/Co/Ta stack when excited by a low intensity current pulse can be modeled. The spin Hall angle of the stack is set as $\theta_{SH}^{DL} = \theta_{SH}^{FL} = 0.3$ from Ref [9], and M_S is measured from vibrating sample magnetometry (VSM) measurements. The damping and anisotropy at room temperature are determined using optically excited time-resolved MOKE measurements[27]. To solve for the dynamics, the left hand side of the LLG equation (7.3) is first set as $d\vec{M}/dt = 0$ and is solved for the equilibrium orientation of the moment, $\vec{M}(t < 0) = \vec{M}_0$. The stable solution to $d\vec{M}/dt = 0$ is identified by choosing the solution with the lowest free energy. A finite-difference scheme is then used to evolve $\vec{M}(t)$ forward in time in response to a charge current $J_C(t)$. The magnetization is evolved forward in time with time-increments of $\Delta t = 1$ fs (it is verified that the results are unchanged with smaller time-increments). A number of electrical reflections of the current pulses from the end of the transmission lines were seen affect the dynamics, and these reflections needed to be included in $J(t)$ in the simulations. The resulting best fits are shown in Figure 7.8. The quality of the fit is remarkable for such a simple model.

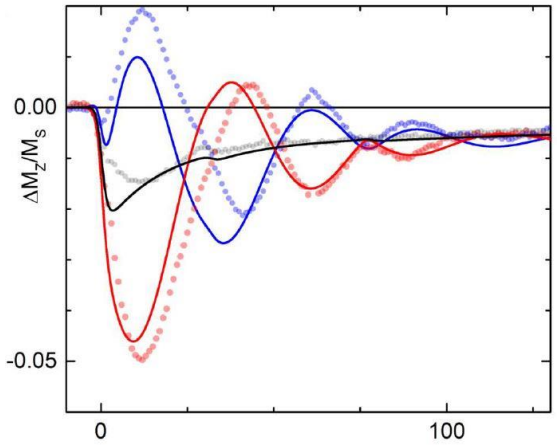

Figure 7.8 Simulation of the ps SOT on Pt/Co/Ta stack.
Macrospin simulation (lines) including ultrafast demagnetization and SOTs on top of the $+M_Z$ experimental data (circles). All data is normalized by the saturation magnetization M_S at room temperature (Figure from Ref [19]).

The dynamics for the blue and red curves on Figure 7.8 are described according to the macroscopic model, and as depicted in the schematics of Figure 7.9 as follows. At negative time delays ($\Delta t < 0$) the magnetization $\boldsymbol{m}$ is initially in its equilibrium position, along $H_{eff}(\Delta t < 0)$ (Figure 7.9 (a)). H_{eff}, as stated before, is the vector sum of H_X, the demagnetization field and the anisotropy field H_A. As soon as the current pulse arrives, a damping-like SOT [28] $\boldsymbol{\tau_{DL}} \sim \boldsymbol{m} \times \boldsymbol{m} \times \boldsymbol{\sigma_y}$ (third term in the right hand side of equation (7.3)) brings the magnetization towards the y axis, along which the accumulated spins $\boldsymbol{\sigma_y}$ are oriented (seen by the initial drop in $|\measuredangle M_Z|$ on blue and red curves in Figure 7.8) as shown in Figure 7.9 (b). At the same time, heating changes the effective field by decreasing H_A, thereby changing the angle (and magnitude) of the effective field to $H_{eff}(\Delta t > 0)$. As $\boldsymbol{m}$ is torqued away from its initial position, precession around the newly evolving effective field begins by the so called thermal anisotropy torque $\boldsymbol{\tau_{Heff}}$ as shown in Figure 7.9 (c). The two current polarities will lead to a 180° phase difference in the precessional dynamics, resulting in opposite $\measuredangle M_Z$ (red and blue trajectories in Figure 7.8 and Figure 7.9). It is interesting to note that a field-like SOT [28] $\boldsymbol{\tau_{FL}} \sim \boldsymbol{m} \times \boldsymbol{\sigma_y}$ (last term in the right hand side of equation (7.3)) dominated SOT cannot reproduce the initial drop in $\measuredangle M_Z$ that leads to a kink close to $\measuredangle t = 0$ on the blue curve. It is therefore concluded that the SOT switching in the Pt/Co/Ta stacks is predominantly caused by damping-like torque, in good agreement with reports on similar structures[9].

Even though the LLG model describes the overall dynamics, its predictions do not agree with certain features of the data. In particular, the model does not match the dynamics of the black trace at $H_X = 0$ between 3 and 10 ps. A possible explanation is inhomogeneous broadening in the effective damping, consistent with prior pump/probe studies of dynamics of perpendicularly magnetized films[29]. In addition to inhomogeneities in anisotropy, it is possible that there are spatial inhomogeneities in the excitation, either due to the (spin) current or hot spot distribution. More experimental and theoretical work will be required to better understand the discrepancies. Experimental data on the switching dynamics will also elucidate the mechanism of switching, and help verify the various assumptions of the simulation.

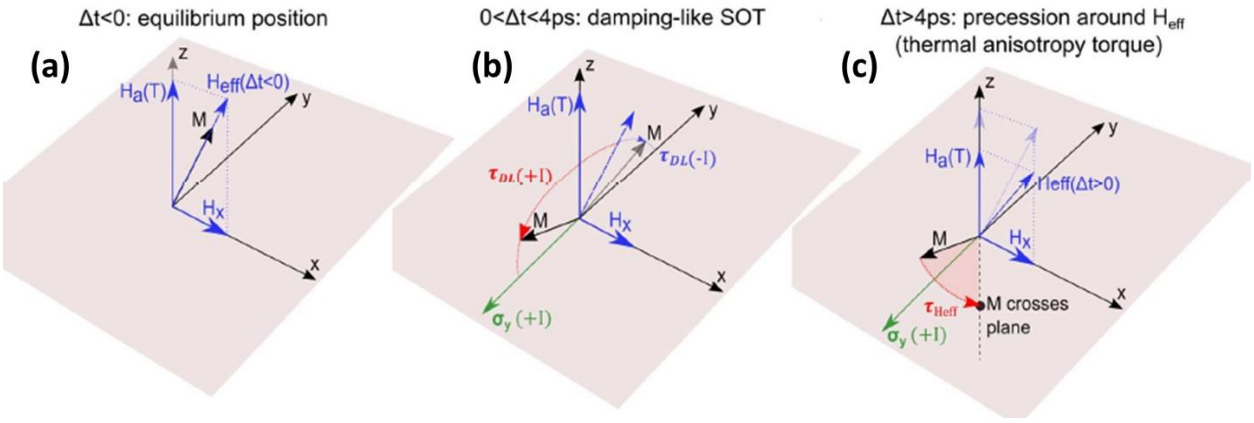

Figure 7.9 Schematics of effect of SOT from ps current pulses on the magnetization of the Pt/Co/Ta stack.
(a) The magnetization $\boldsymbol{M}$ is along H_{eff} at negative time delays. (b) Soon after the current pulse arrives, the damping-like SOT τ_{DL} tries to align $\boldsymbol{M}$ towards σ_y. (c) At longer timescales (after the current pulse) the anisotropy torque τ_{Heff} causes precessions of $\boldsymbol{M}$ around the evolving $\boldsymbol{H_{eff}}$(Figure from Ref [19]).

As stated before, the macrospin approximation is used in this work, i.e. the properties in the LLG equation (7.3) are assumed to be independent of position. Time-resolved measurements performed by focusing the probe beam at different spots on the magnetic load showed no position-dependence, as seen in Figure 7.10. This observation confirms that the macrospin approximation used in the simulations of Figure 7.8 are valid.

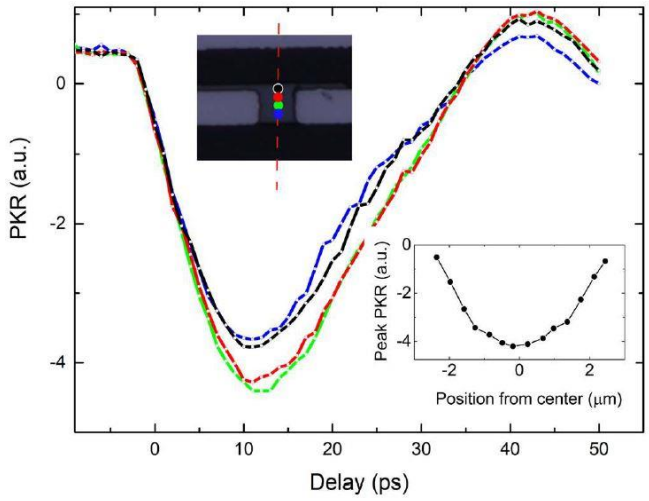

Figure 7.10 Verification of the validity of the macrospin approximation.
Spatial dependence of dynamics measured as a function of the probe spot position along the width of the magnetic load. Inset on the top shows the different probe positions for the different traces. Inset on the bottom shows the demagnetization peak (at 11ps) as a function of the y position (across the sample width). The signal drops as close to the edges because the probe no longer fully overlaps the magnet. The probe width is about 1.5 μm (FWHM), and the sample width is 4 μm. The dynamics are extremely similar across the surface of the sample. Experiments along the length of the magnet (x direction) also showed no major differences (Figure from Ref [19]).

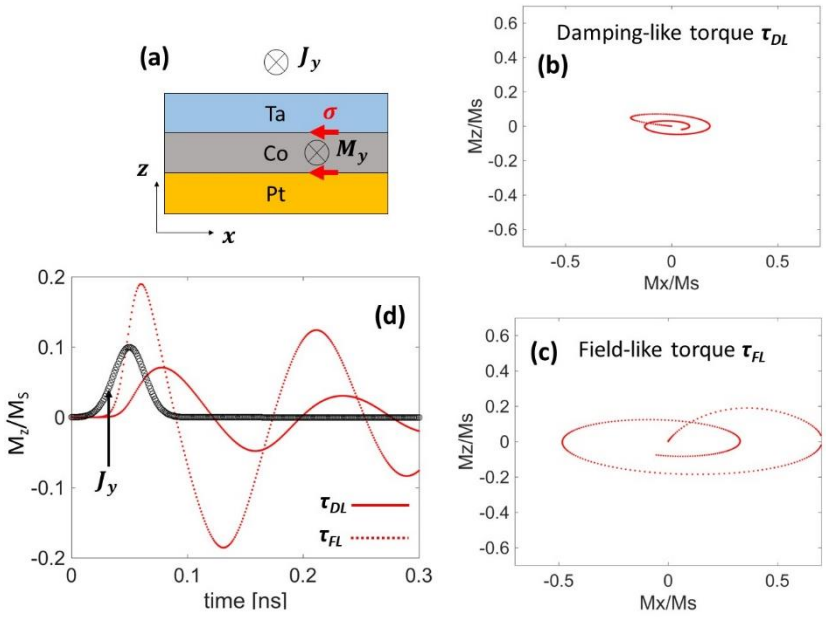

Figure 7.11 Simulations of field-like and damping-like SOTs from a ps current pulse for an in-plane magnet.
(a) Schematic of the toy model sample with in-plane magnetization along the y-axis. Current J_Y is applied along the y-axis, leading to spin accumulation $\boldsymbol{\sigma_X}$ along the x-axis. Simulation of trajectory of $\boldsymbol{M}$ along the x- and z-axes if the SOT is purely a (b) damping-like torque or (c) field-like torque. (d) Simulation of the evolution of M_Z for the two types of SOT for a 50 ps wide charge current J_Y (Figure from Dr Jon Gorchon).

The time-resolved measurements of the ultrafast SOT in the Pt/Co/Ta stack and the corresponding simulations of the dynamics presented in this section led to the determination that the damping-like torque $\boldsymbol{\tau_{DL}}$, and not the field-like torque $\boldsymbol{\tau_{FL}}$, is the dominant SOT acting on the Co layer in the Pt/Co/Ta stack. There has been considerable debate on the relative strengths and utilities of these two torques in various material systems[30, 28, 31]. Triggering the magnetization of a film with the SOT from short electrical pulses and measuring the precessional dynamics can prove to be an effective tool to disentangle the effects of these two torques on any magnetic film. For example, assume a magnetic film of Pt/Co/Ta with Co magnetized in-plane in the y-direction as shown in the schematic of Figure 7.11. Let a short charge current pulse with density J_Y be applied along a wire of this stack, parallel to the magnetization direction. The accumulated spins will then be along the x-axis, with a moment $\boldsymbol{\sigma_X}$. If the damping-like torque ($\boldsymbol{\tau_{DL}} \sim \boldsymbol{m_Y} \times \boldsymbol{m_Y} \times \boldsymbol{\sigma_X}$) is dominant in this structure, the magnetization will first be torqued along the x-direction, as shown by the simulated evolution of M_X vs M_Z in Figure 7.11. This simulation is done using the same LLG equation (7.3) as before, but without any added heating effects. On the other hand, if the damping-like torque ($\boldsymbol{\tau_{FL}} \sim \boldsymbol{m_Y} \times \boldsymbol{\sigma_X}$) is dominant over $\boldsymbol{\tau_{DL}}$, the magnetization will first be torqued along the z-direction (Figure 7.11). The simulated time-evolution of M_Z for both cases is shown in Figure 7.11. The field-like torque results in an early increase in M_Z, while this is delayed for the damping-like torque as the magnetization precesses in ps timescales after the initial increase along M_X. Therefore, by carefully studying the amplitude and phase the precessions of M_X, M_Y, and M_Z, the relative contributions of the two SOTs in any magnetic structure can be determined.

7.7 Energy consumption and endurance in the ultrafast SOT device

The current carried by each electrical pulse that triggered SOT switching of the Pt/Co/Ta stack could not be correctly estimated from the average photocurrent using the method described in Section 6.4. It is likely that there is a significant background current at longer time delays that lead to the breakdown of the calculations. However, an upper limit to the current pulse amplitude can be estimated from the total energy stored in the photoconductive Auston switch before it is excited by a pump laser pulse. The Auston switch comprises of interdigitated electrodes (IDE), and can therefore be modelled as an IDE capacitor, whose capacitance is approximated as $C_{IDE} = (N\text{-}1)\varepsilon_0\varepsilon_r A/d$ where $N = 5$ is the number digits of the electrodes, ε_r is the effective relative permittivity due to LT-GaAs substrate and air (measured as 15), ε_0 the vacuum permittivity, A is the surface area of an electrode and d is the center-to-center distance between electrodes. This is a crude approximation for C_{IDE}, which assumes that the electric field between two adjacent electrodes arises from the entire area A of the electrodes and is mostly concentrated in the LT-GaAs underneath the electrodes (rather than in the air above)[32]. The distance that the electric field travels between the electrodes is also (simplistically) approximated to be the center-to-center distance d between the electrodes. A capacitance of about ~10 fF is estimated for the photoconductive switch from this method. Capacitance on GaAs Auston photoconductive switches in Ref [33] is used as a second tool to approximate the C_{IDE}. The electrodes of the Auston switch used for the work in this chapter have a length $L = 50$ μm, width $W = 6$ μm and a gap $S = 6$ μm, and are on a substrate with thickness $t = 375$ μm, yielding $W/t = S/t \approx 1/50$. From Ref [33], the gap capacitance per unit length of the Auston switch electrodes can then be approximated to be $C_g \sim$ 1 pF/cm. The capacitance of the Auston switch is then approximated as[33] $C_{IDE} \approx NLC_g \approx 25$ fF, in reasonable agreement with the initial simplistic model. As a third verification, it is also well known that the RC time constant due to the capacitance of the photoswitch limits the pulse duration of the generated pulses[34], which means an upper bound for the capacitance can be given by RC < 3.7 ps (the smallest measured pulse duration in the CPW transmission lines). Here, the characteristic impedance Z_0 of the line plays the role of the resistor. The CPW line impedance is designed[35, 36] to be $Z_0 = 70$ Ω, which means the capacitance is at most around 53 fF, consistent with the previous estimations of C_{IDE}. This upper-bound value is taken as the capacitance of the switch to calculate the upper-bound energy dissipation in our experiments.

For threshold bias voltage for SOT switching, found to be $\measuredangle V = 40$ V, the energy stored in the photoconductive switch is at most $\frac{1}{2}C_{IDE}\Delta V^2 \sim 50$pJ, using the RC upper bound for C_{IDE}. In a worst case scenario, it can be assumed that all the energy stored in the switch capacitor is completely dissipated at the magnetic load. This means that a pump laser pulse fully discharges the switch, and the ensuing laser pulse is transmitted along the CPW with no radiative losses, no transmission loses, no reflections, and a perfect absorption at the magnet. For the magnetic load dimensions, this corresponds to an energy density of ~150 MJ/m^3. The energy dissipation by Joule heating for a Gaussian current pulse is $E = \int J(t)^2 \rho \cdot dt = 0.75. J_P^2 \rho_e \tau_p$, where ρ_e (= 81 μΩ-cm) is the measured resistivity of the magnet and J_P is the peak current density. This allows the estimation of the maximum peak current density for switching with $\tau_P = 6$ ps pulses to be about $J_{C,P} \sim 6 \times 10^8$ Acm^{-2}. Assuming the energy density to switch a magnetic bit remains independent of the sample size, a cubic magnetic bit with cell size (20 nm)^3 would require an energy of ~1.2 fJ and a current of ~2.5 mA to induce SOT switching. Although the current pulse amplitude required is quite high, as with the ultrafast toggle

switching of GdFeCo by electrical pulses (Section 6.7), the total energy requirement is low due to the short pulse duration. Therefore, the energy requirements in this ultrafast SOT regime compare extremely favorably with state of the art, ns and sub-ns switching SOT results[37, 38] and other types of memory[38], even though the Pt/Co/Ta stack is non-optimized and has relatively large dimensions. The energy required for this device will be compared with other conventional STT and SOT devices in Figure 8.1. The reduction in anisotropy and ultrafast demagnetization of the magnet caused by the ps Joule heating from the 6 ps pulse is likely to be favoring SOT switching in this device, leading to its remarkably low energy requirement. However, further studies need to be done to verify the energy estimation technique used in this work, and it is also possible that the energy density for ultrafast SOT switching may not remain the same at nanoscales.

The Auston switch is irradiated by the 5 kHz laser for hours ($> 10^8$ pulses) at switching conditions in order to characterize the device (for example, pulse shape characterization) with no noticeable degradation of the switching behavior or magnetic properties of the stack. This means that an ultrafast SOT device will have an endurance of at least 10^8 cycles, and compared favorably with other competing technologies like resistive RAM, phase change memory, conductive bridge RAM etc.[38]

7.8 Conclusions

In this chapter I have shown that the spin-orbit torque from an intense, short 6 ps current pulse can reverse the magnetization of a Pt/Co/Ta stack integrated with an Auston switch-transmission line device. Experimental work by other groups were analyzed to show that the current-induced spin-accumulation can operate at the short ps timescales of the current pulses. Single shot experiments performed with a MOKE microscope confirmed the SOT switching. When the charge current and the symmetry-breaking in-plane field are parallel (anti-parallel), the sample switches to a final state of $-M_Z$ ($+M_Z$), in agreement with SOT arising from the combination of the spin Hall effect from both Pt and Ta heavy metals. The final switched state of the magnet does not depend on its initial state. Therefore this technique can be used to design an ultrafast non-toggle spintronic device, where the switched state is not simply the opposite of its initial state, and can be set deterministically by the direction of the applied current pulse.

Time-resolved measurements of the precessional dynamics induced by low intensity current pulses showed that the magnetization responds instantaneously to the heating and SOT pulses. The dynamics include an ultrafast demagnetization from the Joule heating of the magnet, and precessions that tend towards $-M_Z$ ($+M_Z$) when the current pulse and the in-plane field are parallel (anti-parallel). Simulations based on the macrospin modeling of the LLG equation were able to qualitatively reproduce the observed dynamics, and confirmed that the damping-like torque is dominant over the field-like torque in the magnetic system. Future work on studying the dynamics of SOT switching by ps current pulses can confirm that the magnetization reversal occurs in short timescales, and can further elucidate the exact mechanism of switching.

The endurance of the magnetic sample was found to be quite high, at least 10^8 switching cycles. The energy density for SOT switching with 6 ps electrical pulses was found to be at worst 150 MJm^{-3}, leading to a low switching energy of 1.2 fJ for a typical $(20\ nm)^3$ bit, which compares favorably with other conventional spintronic devices.

Finally, it must be noted that the ultrafast SOT switching was demonstrated in a common ferromagnetic system without the need for exotic magnetic materials like Gd-based RE-TM ferrimagnets. Similar experiments can be done to also deterministic demonstrate ultrafast SOT switching in any magnetic material. This can be useful in making an MTJ with a large TMR ratio, with the switching ferromagnet layer acting as the free layer. The flexibility to extend the observations of this work to a wide range of magnets will be advantageous for integrating an ultrafast SOT device on-chip with other conventional technologies like CMOS.

7.9 References

1. Garello, K., Avci, C. O., Miron, I. M., Baumgartner, M., Ghosh, A., Auffret, S., Boulle, O., Gaudin, G. & Gambardella, P. Ultrafast magnetization switching by spin-orbit torques. *Appl. Phys. Lett.* **105,** 212402 (2014). https://doi.org/10.1063/1.4902443
2. Rowlands, G. E., Rahman, T., Katine, J. A., Langer, J., Lyle, A., Zhao, H., Alzate, J. G., Kovalev, A. A., Tserkovnyak, Y., Zeng, Z. M., Jiang, H. W., Galatsis, K., Huai, Y. M., Amiri, P. K., Wang, K. L., Krivorotov, I. N. & Wang, J.-P. Deep subnanosecond spin torque switching in magnetic tunnel junctions with combined in-plane and perpendicular polarizers. *Appl. Phys. Lett.* **98,** 102509 (2011). https://doi.org/10.1063/1.3565162
3. Lee, O. J., Ralph, D. C. & Buhrman, R. A. Spin-torque-driven ballistic precessional switching with 50 ps impulses. *Appl. Phys. Lett.* **99,** 102507 (2011). https://doi.org/10.1063/1.3635782
4. Pattabi, A., Gu, Z., Gorchon, J., Yang, Y., Finley, J., Lee, O. J., Raziq, H. A., Salahuddin, S. & Bokor, J. Direct optical detection of current induced spin accumulation in metals by magnetization-induced second harmonic generation. *Appl. Phys. Lett.* **107,** 152404 (2015). https://doi.org/10.1063/1.4933094
5. Kampfrath, T., Battiato, M., Maldonado, P., Eilers, G., Nötzold, J., Mährlein, S., Zbarsky, V., Freimuth, F., Mokrousov, Y., Blügel, S., Wolf, M., Radu, I., Oppeneer, P. M. & Münzenberg, M. Terahertz spin current pulses controlled by magnetic heterostructures. *Nature Nanotech* **8,** 256–260 (2013). https://doi.org/10.1038/nnano.2013.43
6. Valenzuela, S. O. & Tinkham, M. Direct electronic measurement of the spin Hall effect. *Nature* **442,** 176–179 (2006). https://doi.org/10.1038/nature04937
7. Saitoh, E., Ueda, M., Miyajima, H. & Tatara, G. Conversion of spin current into charge current at room temperature: Inverse spin-Hall effect. *Appl. Phys. Lett.* **88,** 182509 (2006). https://doi.org/10.1063/1.2199473
8. Seifert, T., Jaiswal, S., Martens, U., Hannegan, J., Braun, L., Maldonado, P., Freimuth, F., Kronenberg, A., Henrizi, J., Radu, I., Beaurepaire, E., Mokrousov, Y., Oppeneer, P. M., Jourdan, M., Jakob, G., Turchinovich, D., Hayden, L. M., Wolf, M., Münzenberg, M., Kläui, M. & Kampfrath, T. Efficient metallic spintronic emitters of ultrabroadband terahertz radiation. *Nature Photon* **10,** 483–488 (2016). https://doi.org/10.1038/nphoton.2016.91
9. Woo, S., Mann, M., Tan, A. J., Caretta, L. & Beach, G. S. D. Enhanced spin-orbit torques in Pt/Co/Ta heterostructures. *Appl. Phys. Lett.* **105,** 212404 (2014). https://doi.org/10.1063/1.4902529
10. Woo, S., Litzius, K., Krüger, B., Im, M.-Y., Caretta, L., Richter, K., Mann, M., Krone, A., Reeve, R. M., Weigand, M., Agrawal, P., Lemesh, I., Mawass, M.-A., Fischer, P., Kläui, M. & Beach, G. S. D. Observation of room-temperature magnetic skyrmions and their current-driven dynamics in ultrathin metallic ferromagnets. *Nature Mater* **15,** 501–506 (2016). https://doi.org/10.1038/nmat4593

11. Kimura, T., Hamrle, J. & Otani, Y. Estimation of spin-diffusion length from the magnitude of spin-current absorption: Multiterminal ferromagnetic/nonferromagnetic hybrid structures. *Phys. Rev. B* **72,** 014461 (2005). https://doi.org/10.1103/PhysRevB.72.014461
12. Nan, T., Emori, S., Boone, C. T., Wang, X., Oxholm, T. M., Jones, J. G., Howe, B. M., Brown, G. J. & Sun, N. X. Comparison of spin-orbit torques and spin pumping across NiFe/Pt and NiFe/Cu/Pt interfaces. *Phys. Rev. B* **91,** 214416 (2015). https://doi.org/10.1103/PhysRevB.91.214416
13. Ostwal, V., Penumatcha, A., Hung, Y.-M., Kent, A. D. & Appenzeller, J. Spin-orbit torque based magnetization switching in Pt/Cu/[Co/Ni] $_5$ multilayer structures. *Journal of Applied Physics* **122,** 213905 (2017). https://doi.org/10.1063/1.4994711
14. Liu, L., Lee, O. J., Gudmundsen, T. J., Ralph, D. C. & Buhrman, R. A. Current-Induced Switching of Perpendicularly Magnetized Magnetic Layers Using Spin Torque from the Spin Hall Effect. *Phys. Rev. Lett.* **109,** 096602 (2012). https://doi.org/10.1103/PhysRevLett.109.096602
15. Miron, I. M., Garello, K., Gaudin, G., Zermatten, P.-J., Costache, M. V., Auffret, S., Bandiera, S., Rodmacq, B., Schuhl, A. & Gambardella, P. Perpendicular switching of a single ferromagnetic layer induced by in-plane current injection. *Nature* **476,** 189–193 (2011). https://doi.org/10.1038/nature10309
16. Cubukcu, M., Boulle, O., Drouard, M., Garello, K., Onur Avci, C., Mihai Miron, I., Langer, J., Ocker, B., Gambardella, P. & Gaudin, G. Spin-orbit torque magnetization switching of a three-terminal perpendicular magnetic tunnel junction. *Appl. Phys. Lett.* **104,** 042406 (2014). https://doi.org/10.1063/1.4863407
17. Lo Conte, R., Hrabec, A., Mihai, A. P., Schulz, T., Noh, S.-J., Marrows, C. H., Moore, T. A. & Kläui, M. Spin-orbit torque-driven magnetization switching and thermal effects studied in Ta\CoFeB\MgO nanowires. *Appl. Phys. Lett.* **105,** 122404 (2014). https://doi.org/10.1063/1.4896225
18. Baumgartner, M., Garello, K., Mendil, J., Avci, C. O., Grimaldi, E., Murer, C., Feng, J., Gabureac, M., Stamm, C., Acremann, Y., Finizio, S., Wintz, S., Raabe, J. & Gambardella, P. Spatially and time-resolved magnetization dynamics driven by spin–orbit torques. *Nature Nanotech* **12,** 980–986 (2017). https://doi.org/10.1038/nnano.2017.151
19. Jhuria, K., Hohlfeld, J., Pattabi, A., Martin, E., Córdova, A. Y. A., Shi, X., Conte, R. L., Petit-Watelot, S., Rojas-Sanchez, J. C., Malinowski, G., Mangin, S., Lemaître, A., Hehn, M., Bokor, J., Wilson, R. B. & Gorchon, J. Picosecond Spin Orbit Torque Switching. *arXiv:1912.01377 [cond-mat, physics:physics]* (2020). at <http://arxiv.org/abs/1912.01377>
20. Beaurepaire, E., Merle, J.-C., Daunois, A. & Bigot, J.-Y. Ultrafast Spin Dynamics in Ferromagnetic Nickel. *Phys. Rev. Lett.* **76,** 4250–4253 (1996). https://doi.org/10.1103/PhysRevLett.76.4250
21. Wilson, R. B., Yang, Y., Gorchon, J., Lambert, C.-H., Salahuddin, S. & Bokor, J. Electric current induced ultrafast demagnetization. *Phys. Rev. B* **96,** 045105 (2017). https://doi.org/10.1103/PhysRevB.96.045105
22. *Coatings, Systems, and Composites*. (Springer US, 1973). https://doi.org/10.1007/978-1-4757-6836-7
23. Wilson, R. B. & Cahill, D. G. Experimental Validation of the Interfacial Form of the Wiedemann-Franz Law. *Phys. Rev. Lett.* **108,** 255901 (2012). https://doi.org/10.1103/PhysRevLett.108.255901
24. Verstraete, M. J. *Ab initio* calculation of spin-dependent electron–phonon coupling in iron and cobalt. *J. Phys.: Condens. Matter* **25,** 136001 (2013). https://doi.org/10.1088/0953-8984/25/13/136001

25. Allen, P. B. Empirical electron-phonon λ values from resistivity of cubic metallic elements. *Phys. Rev. B* **36,** 2920–2923 (1987). https://doi.org/10.1103/PhysRevB.36.2920
26. Lee, K.-M., Choi, J. W., Sok, J. & Min, B.-C. Temperature dependence of the interfacial magnetic anisotropy in W/CoFeB/MgO. *AIP Advances* **7,** 065107 (2017). https://doi.org/10.1063/1.4985720
27. Koopmans, B., Ruigrok, J. J. M., Longa, F. D. & de Jonge, W. J. M. Unifying Ultrafast Magnetization Dynamics. *Phys. Rev. Lett.* **95,** 267207 (2005). https://doi.org/10.1103/PhysRevLett.95.267207
28. Garello, K., Miron, I. M., Avci, C. O., Freimuth, F., Mokrousov, Y., Blügel, S., Auffret, S., Boulle, O., Gaudin, G. & Gambardella, P. Symmetry and magnitude of spin–orbit torques in ferromagnetic heterostructures. *Nature Nanotech* **8,** 587–593 (2013). https://doi.org/10.1038/nnano.2013.145
29. Lattery, D. M., Zhu, J., Zhang, D., Wang, J.-P., Crowell, P. A. & Wang, X. Quantitative analysis and optimization of magnetization precession initiated by ultrafast optical pulses. *Appl. Phys. Lett.* **113,** 162405 (2018). https://doi.org/10.1063/1.5046683
30. Hoffmann, A. Spin Hall Effects in Metals. *IEEE Trans. Magn.* **49,** 5172–5193 (2013). https://doi.org/10.1109/TMAG.2013.2262947
31. Ou, Y., Pai, C.-F., Shi, S., Ralph, D. C. & Buhrman, R. A. Origin of fieldlike spin-orbit torques in heavy metal/ferromagnet/oxide thin film heterostructures. *Phys. Rev. B* **94,** 140414 (2016). https://doi.org/10.1103/PhysRevB.94.140414
32. Oberländer, J., Jildeh, Z., Kirchner, P., Wendeler, L., Bromm, A., Iken, H., Wagner, P., Keusgen, M. & Schöning, M. Study of Interdigitated Electrode Arrays Using Experiments and Finite Element Models for the Evaluation of Sterilization Processes. *Sensors* **15,** 26115–26127 (2015). https://doi.org/10.3390/s151026115
33. Bell, B. A., Perrey, A. G. & Sadler, R. A. Gallium arsenide (GaAs)-based photoconductive switches for pulse generation and sampling applications in the nanosecond regime. *IEEE Trans. Instrum. Meas.* **38,** 92–97 (1989). https://doi.org/10.1109/19.20004
34. Auston, D. H., Johnson, A. M., Smith, P. R. & Bean, J. C. Picosecond optoelectronic detection, sampling, and correlation measurements in amorphous semiconductors. *Appl. Phys. Lett.* **37,** 371–373 (1980). https://doi.org/10.1063/1.91947
35. Gupta, K. C., Garg, R. & Bahl, I. J. *Microstrip lines and slotlines*. (Artech House, 1979).
36. Erli Chen & Chou, S. Y. Characteristics of coplanar transmission lines on multilayer substrates: modeling and experiments. *IEEE Trans. Microwave Theory Techn.* **45,** 939–945 (1997). https://doi.org/10.1109/22.588606
37. Garello, K., Yasin, F., Couet, S., Souriau, L., Swerts, J., Rao, S., Van Beek, S., Kim, W., Liu, E., Kundu, S., Tsvetanova, D., Croes, K., Jossart, N., Grimaldi, E., Baumgartner, M., Crotti, D., Fumemont, A., Gambardella, P. & Kar, G. S. SOT-MRAM 300MM Integration for Low Power and Ultrafast Embedded Memories. in *2018 IEEE Symposium on VLSI Circuits* 81–82 (IEEE, 2018). https://doi.org/10.1109/VLSIC.2018.8502269
38. Wong, H.-S. P. Stanford Memory Trends. at <https://nano.stanford.edu/stanford-memory-trends>

Chapter 8. Conclusion

8.1 Summary of dissertation

From the work presented in this dissertation, it can be concluded that the newly formed field of ultrafast spintronics offers great promise to speed up existing spintronic devices. An ultrafast spintronic device combines the advantages of two previously disparate subfields of magnetism: spintronics (its low power consumption and ease of integration on-chip with other technologies) and ultrafast magnetism (its ability to manipulate magnetism in unprecedented picosecond timescales). The experiments performed and analyzed in this thesis can also help unravel the characteristics of phenomena like current-induced spin accumulation, spin orbit torques (SOT) and ultrafast helicity-independent all optical switching, and the complex mechanisms at play behind them.

The magnetization-induced second harmonic generation (MSHG) was shown to be an effective technique for detecting the current-induced spin accumulation directly on the surfaces of high spin orbit coupling heavy metal wires. The tool was then used to study the dynamics of spin accumulation. Although MSHG was unsuccessful in resolving the speed of spin accumulation, its effectiveness in studying the characteristics of the accumulated spins without their interaction with a ferromagnet was demonstrated.

Extensive HI-AOS experiments on Gd-based ferrimagnets were performed to understand the underlying mechanism and pulse duration limits of the intriguing phenomenon. The ability to switch GdFeCo with 15 ps optical pulses was demonstrated, which brought into question existing theories of HI-AOS that require high electron temperatures of the order of 1000-2000K. More importantly, this result indicates that Joule heating by a ps electrical current pulse should also be able to trigger similar ultrafast switching events in GdFeCo. Atomistic spin dynamic simulations of the HI-AOS of GdTbCo alloys revealed that the differential element-specific damping of the rare earth (RE) and transition metal (TM) sites of RE-TM ferrimagnetic systems is the most critical factor that determines the ability to exhibit HI-AOS.

The HI-AOS capability of a ferrimagnetic GdFeCo film was extended to ferromagnetic Co/Pt films by exploiting the RKKY exchange interaction between the two layers. The ultrafast HI-AOS of Co/Pt has important implications for application, because conventional spintronic devices need ferromagnetic bits to have a larger signal for electrical readout through the tunnel magnetoresistance (TMR).

Finally, building on the observation of HI-AOS of GdFeCo with ps optical pulses, it was shown that Joule heating by ps electrical can also successfully trigger ultrafast magnetic processes. A Co/Pt ferromagnet was delivered with 6 ps electrical pulses by integrating it with an Auston photoconductive switch and a transmission line. It was shown that the spin orbit torque arising from a 6 ps electrical pulse is successful in switching the magnetization of the Co/Pt in a deterministic manner, wherein the final switched state is controlled by the current pulse direction and is independent of the previous state of the device. The energy efficiency of switching was shown to be comparable to other conventional spintronic devices. The energy and switching speed of this device, in comparison with other conventional STT and SOT devices is shown in Figure 8.1 (updated from Figure 1.10 to include the ultrafast SOT device). This demonstration of deterministic, efficient, ultrafast SOT switching of a

ferromagnet will open the door for further research into faster and more efficient ultrafast spintronic devices. As mentioned in Section 1.7, the STT and SOT data points in Figure 8.1 were taken from Ref [1], which cherry-picked data from separate reports of devices with different sizes, materials, configurations etc. For a fixed device structure with a fixed size, the write energy is expected to increase with decreasing switching current pulsewidth τ_P, especially for τ_P < ~0.5 ns (see Section 1.7). This makes the reduction of the switching energy density in the ultrafast SOT device by ~5× compared to the conventional SOT devices in the figure even more remarkable. Since the switching by ultrafast SOT is a non-equilibrium process (unlike conventional SOT), it is likely that the combination of ultrafast Joule heating and the ultrafast SOT in this device accounts for the reduced energy. However, the estimated energy in this work needs to be verified by other independent techniques.

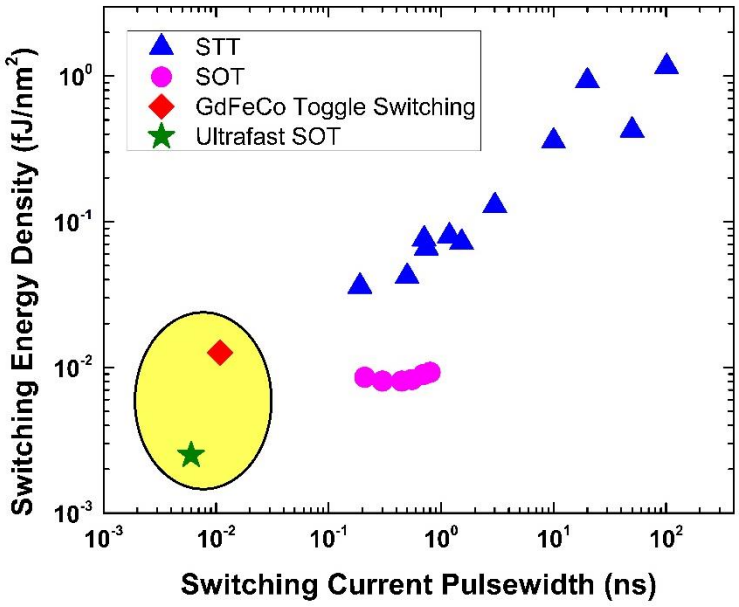

Figure 8.1 Switching energy and switching current pulse durations of ultrafast spintronic devices.
The extremely low switching energy for the ultrafast SOT device (green star) was calculated from the energy stored in the Auston switch (Section 7.7) and needs to be verified by other techniques. It is likely that the combined effect of SOT and ultrafast Joule heating results in the estimated low energy (Figure adapted from data of Refs [1, 2, 3]).

8.2 Future work and outlook

The ultrafast magnetization reversal experiments shown in this dissertation were all done on relatively large μm sized magnets. Effort must be put into demonstrating ultrafast SOT switching (or even toggle switching) by ps electrical pulses in nanoscale magnetic loads. The energy requirements for switching at these small sizes must be carefully studied and analyzed. Work by El-Ghazaly et al.[4] demonstrated the HI-AOS (with optical pulses) of GdCo nanodots, down to 200 nm in size. Interestingly, it was observed that smaller dots recover their magnetization in the opposite switched direction faster than larger ones. Experiments must be performed to verify this behavior for switching with ps electrical pulses.

Immediate future work will focus on verifying whether the magnetization reversal triggered by the SOT from 6 ps electrical pulses occurs in ultrafast timescales.

The ps electrical pulse experiments presented in this thesis were performed using Auston photoconductive switches that were triggered by laser pulses. While this is acceptable for the demonstration of a proof-of-concept prototype, a commercial device must be all-electrical and not rely on bulky laser systems. Future work must therefore also focus on generating these intense ps electrical pulses on-chip using CMOS transistors. From the estimation of Chapter 7, cubic bit of size $(20\ nm)^3$ will require a peak current of ~2.5 mA for SOT switching by a 6 ps wide electrical pulses, assuming that the energy required for switching scales with volume from μm to nm scales (an assumption that also needs to be verified). This current would require fairly bulky CMOS transistors, so any analysis should also include the energy dissipation and spatial density of these transistors.

All these results must then be updated to include an MTJ stack on top of the magnetic bit to enable the electrical readout of the bit, finally resulting in an all-electrical ultrafast spintronic device. Device performance must be characterized and rigorous circuit design and analysis must be performed to understand the performance of a large number of these devices in a circuit or system.

Going by the energy consumption and current pulse width for an individual ultrafast SOT device, ultrafast spintronics holds the promise to be applicable as an MRAM to potentially replace the volatile SRAMs and DRAMs cache memory units high up in the memory hierarchy of a computer system. The low energy dissipation, non-volatility and high speed of these devices can make them integral parts of fast, energy efficient technologies, and can thereby aid humankind in its quest to face the monumental problems of the future.

8.3 References

1. Wong, H.-S. P. Stanford Memory Trends. at <https://nano.stanford.edu/stanford-memory-trends>
2. Yang, Y., Wilson, R. B., Gorchon, J., Lambert, C.-H., Salahuddin, S. & Bokor, J. Ultrafast magnetization reversal by picosecond electrical pulses. *Sci. Adv.* **3,** e1603117 (2017). https://doi.org/10.1126/sciadv.1603117
3. Jhuria, K., Hohlfeld, J., Pattabi, A., Martin, E., Córdova, A. Y. A., Shi, X., Conte, R. L., Petit-Watelot, S., Rojas-Sanchez, J. C., Malinowski, G., Mangin, S., Lemaître, A., Hehn, M., Bokor, J., Wilson, R. B. & Gorchon, J. Picosecond Spin Orbit Torque Switching. *arXiv:1912.01377 [cond-mat, physics:physics]* (2020). at <http://arxiv.org/abs/1912.01377>
4. El-Ghazaly, A., Tran, B., Ceballos, A., Lambert, C.-H., Pattabi, A., Salahuddin, S., Hellman, F. & Bokor, J. Ultrafast magnetization switching in nanoscale magnetic dots. *Appl. Phys. Lett.* **114,** 232407 (2019). https://doi.org/10.1063/1.5098453